



N° d'ordre NNT : 2022LYSE1047

THESE de DOCTORAT DE L'UNIVERSITE DE LYON

opérée au sein de
l'Université Claude Bernard Lyon 1

Ecole Doctorale N° accréditation
Electronique, Electrotechnique et Automatique (ED EEA)

Spécialité de doctorat : Électronique, Micro et nanoélectronique, Optique et Laser
Discipline : Sciences Exactes

Soutenue publiquement le 25 Mars 2022,
par :

M. BERNARDO José Antonio

A new approach for the optimization of Implantable NMR micro-probe for In-vivo Application: Alzheimer's disease

Devant le jury composé de :

M. Rousseau Lionel	Dr. Ingénieur Process (HDR) – Université Paris Est (ESIEE)	Rapporteur
M. Zaim Wadghiri Youssef	Professeur Université de New York (School of Medicine)	Rapporteur
M. Hebrard Luc	Professeur Université de Strasbourg – Laboratoire Icube	Examinateur
Mme Petiet Alexandra	Chercheuse CENIR – ICM Paris	Examinatrice
Mme Chaix Carole	Directrice de Recherche CNRS – ISA Lyon	Examinatrice
M. Morell Christophe	Professeur Université Lyon 1 – ISA Lyon	Examinateur
Mme Fakri-Bouchet Latifa	Maitre de Conférences (HC-HDR); Université de Lyon - ISA	Directrice de thèse
M. Gontrand Christian	Professeur INSA de Lyon - INL	Co-directeur de thèse

Acknowledgements

My thesis was carried out at ISA laboratory of Lyon, with Claude Bernard University. First, I would like to thank the director of the ISA, Mr. Christophe MORELL, for all supports during the three years of my thesis.

I express all my gratitude to my research work, supervisor Mrs. Latifa FAKRI-BOUCHET, as well as Mr. Christian GONTRAND, from INL laboratory, for all their support and wise advice, otherwise my thesis work would not be achieved with a great quality.

I warmly thank Mr. Lionel ROUSEAU for his availability, his advice and the interest showed in my thesis subject as well as for the achievements made at Cleanroom of l'ESIEE Paris, during the prototype manufacturing. I would also like to thank Sir. Stephane ROQUES and all the members of the cleanroom, at Icube laboratory, Strasbourg for their help in the characterization of microprobe prototypes.

I would like to thank, Mr. Youssef ZAIM WADGHIRI, from NYU school of Medicine, (University of New York), and Mr. Lionel ROUSEAU from l'ESIEE, Paris for accepting to examine my thesis manuscript.

Thanks to Mr. Luc HEBRARD from University of Strasbourg, Mrs. Alexandra PETIET from ICM Paris, and Mrs. Carole CHAIX, from CNRS, ISA Lyon for accepting to be jury on my thesis work.

I would like to thank of course all the professionals of ISA, all my doctoral colleagues more particularly those who shared this work with me: Abel RANGEL TREJO, Adam ADEWOLU and Leticia KONADU. The scientific exchanges with my team, the project partners and collaborators during the years of my thesis contributed to my personal training, enriched my scientific and techniques knowledge which really helped me in the achievement of this work.

Finally, I dedicate this work to all my family. I express my gratitude to my mother Rebeca Paulo PEDRO, my lovely girlfriend Marion DEROIN, my Brother Manuel Pedro BERNARDO and friends. During the last three years, you were always in my heart, and some were available to support me and help me to overcome my difficulties.

“Ose savoir!”

- By : Emmanuel Kant

List of Acronyms

AD : Alzheimer's disease

AC : Alternative Current

AI : Artificial Intelligence

ADS : Advanced Design Systems

ANN : Artificial Neuronal network

BP : Basal Prosencephalon

BP : Back Propagation

CAD : Computer Aided Design

CST MWS : Computational Simulation technology Microwave Studio

CSF : Cerebral Spinal Fluid

DUT : Device Under test

DC : Direct Current

DL : deep Learning

Ex-Vivo: outside of a living body

EM : Electromagnetics

EMF : Electromotive Force

EMF: Electromagnetic Field

EEG : Electroencephalogram

FDG : Fluorodeoxyglucose

FP : Forward Propagation

FFP : Feed Forward Propagation

FID : Free Induction Decay

FIT : Finite Integration Technique

FWHM : Full Width at Half Maximum

GABA : Gamma-AminoButyric Acid

GUI : Graphical User Interface

In-Vivo : inside of a living body

In-Vitro : in glass testing

LTD : Latero Dorsal Tegmental

LW : Lorentzian width

LOD : Limit Of detection

LIGA : Röntgenlithographie Galvanoformung Abformung

NMR : Nuclear Magnetic Resonance

NAA : N-Acetyl aspartic acid

NN : Neural network

MEMS : Micro-Electro-Mechanical System

MEK : Methyl Ethyl Ketone

MIBK : Methyl Isobutyl Ketone

MRS : Magnetic Resonance Spectroscopy

MRI : Magnetic resonance Imaging

MCI : Mild Cognitive Impairment

MW : Microwave

MIMO : Multiple Input and Multiple Output

ML : Machine Learning

MAE : Mean Absolute Error

MAPE : Mean Absolute Percentage Error

MSE : Mean Square Error

RMSE : Root Mean Square Error

RAE : Relative Absolute Error

RSE : Relative Square Error

RH : Relative humidity

PET : Positron Emission Tomography

PPT : PedunculoPontine Tegmental

PCB : Printed Circuit Board

PVD : Physical Vapour Deposition

PEEK : Polyether Ether Ketone

PDMS : Poly Dimethyl Siloxane

ROI : Region Of Interest

RF : Radio Frequency

RMSE : Root Mean Square Error

SNR : Signal to Noise Ratio

SPICE : Simulation Program with Integrated Circuit Emphasis

TL : Transmission Line

TSV : through Silicon Vias

VSWR : Voltage Standing Wave Ratio

3D - TLE : 3 Dimensions Transmission Line Extractor

RLC : Resistance Inductance capacitance

UV : Ultraviolet

VNA : Vector Network Analyser

THESIS SUMMARY FRENCH VERSION

Résumé de thèse

Mots clefs : Micro-probe, Micro-bobine, Spectroscopie RMN, Maladie d'Alzheimer, Biomarqueurs, Réseau de Neurons Artificiels (RNA), Facteur de Q, Rapport Signal sur Bruit (RSB ou SNR), Intelligence Artificiel (IA).

La maladie d'Alzheimer (MA) est l'une des maladies neurodégénératives les plus fréquentes chez les personnes âgées. Selon le dernier rapport mondial sur la MA, près de 55 millions de personnes vivent avec la démence de la MA. En France, plus d'un million de personnes souffrent de cette démence, et cela arrive parfois, avant l'âge de 65 ans. La perte de mémoire est souvent le premier symptôme de la MA qui permet d'orienter le diagnostic ; il s'agit donc d'un enjeu de santé publique.

Cette maladie neurodégénérative résulte de la progression de deux principales lésions cérébrales : l'accumulation anormale de protéines appelées peptide β amyloïdes (plaques séniles) et de protéines τ conduisant à la dégénérescence des neurones. L'évolution progressive de la MA peut donc être détectée 20 ans avant l'apparition des symptômes de démence (phase prodromique), par le biais des certains marqueurs fonctionnels et/ou métaboliques. Malheureusement, le diagnostic formel de la MA ne peut être obtenu que par autopsie du cerveau post-mortem. Il convient de noter que les marqueurs qui reflètent l'évolution de la maladie peuvent être biochimiques ou anatomiques.

L'objectif majeur de la recherche clinique actuelle sur la MA est d'améliorer la détection précoce et présymptomatique du dysfonctionnement des neurones. Ainsi, le domaine de la recherche sur la MA est très actif, et plusieurs essais de traitements ont déjà été effectués. Par exemple, les essais visant à nettoyer les plaques séniles ont été mis en place, mais les résultats n'ont pas été concluants jusque-là. Une raison possible serait que les patients qui ont participé à l'essai étaient à un stade trop avancé de la maladie. L'origine de la MA et sa progression ne sont donc pas encore très bien comprises, un diagnostic précoce devrait permettre de mieux comprendre cette pathologie et de mettre en place les traitements pharmacologiques actifs nécessaires pour ralentir la maladie, si possible avant qu'elle n'ait un impact sur la qualité de vie du patient.

Actuellement, malgré les efforts pour diagnostiquer la MA grâce aux techniques de neuro-imagerie par les méthodes de suivi de l'inflammation (atrophie) de l'hippocampe par Imagerie par Résonance Magnétique (IRM) fonctionnelle ou structurelle, ou encore le suivi des

biomarqueurs du liquide céphalo-rachidien ou le suivi des biomarqueurs sanguins, toutefois le diagnostic de la MA est actuellement de façon tardive. Il faut noter que certaines de ces méthodes de diagnostic ne fournissent pas d'informations reproductibles.

Pour notre étude, nous avons choisi la technique de Spectroscopie RMN (SRM) pour suivre l'évolution des biomarqueurs (métabolites cérébraux) qui pourraient éventuellement être représentatives de la MA, grâce à un modèle animal (la souris ou le rat). La Résonance Magnétique Nucléaire (RMN) est une méthode d'analyse très puissante pour identifier des échantillons chimiques et biologiques. Au cours des 20 dernières années, elle est devenue un outil incontournable pour le diagnostic des maladies ; ainsi la SRM semble être un bon candidat pour notre recherche en raison de la capacité de la technique à quantifier la concentration de certains métabolites dans une zone d'intérêt très précise. Néanmoins, l'obtention de spectres RMN *in vivo* de haute résolution constitue un véritable enjeu méthodologique. En effet, la principale limitation de la RMN est sa sensibilité en termes du rapport signal sur bruit (SNR) qui décroît lorsque l'on cherche à augmenter la résolution spatiale. Pour tenter de s'affranchir de cette limitation du SNR, sans une trop forte pénalisation en termes de résolution spatiale ou de temps d'acquisition, il est judicieux d'améliorer l'aimantation transversale moyenne mesurée pendant la réception du signal et également la sensibilité de détection.

Plusieurs stratégies ont été proposées dans la littérature, visant à améliorer la sensibilité RMN:

1. L'augmentation de l'intensité du champ statique B_0 , puisque la sensibilité RMN en spectroscopie varie comme $B_0^{7/4}$. Des aimants supraconducteurs avec des champs statiques de 4,7 T (200 MHz) jusqu'à 23,3 T (1 GHz) sont désormais utilisés en spectroscopie « conventionnelle ».

2. L'amélioration de la sensibilité de détection par :

- L'amélioration du couplage magnétique entre l'antenne assurant la réception du signal RMN et l'échantillon par l'adaptation de la taille du capteur avec celle de l'échantillon. Le facteur de remplissage est ainsi augmenté ($\eta \approx 1$) et par conséquent, le SNR est augmenté et la sensibilité de mesure sera améliorée, grâce à une sensibilité optimale du capteur RF.

- La réduction des sources de bruit thermique par le refroidissement de l'antenne de détection RMN.

3. La réduction de la largeur de raie : la mise en rotation rapide de l'échantillon autour d'un axe à $54,7^\circ$ de la direction du champ (*Magic Angle Spinning*) est utilisée depuis longtemps pour réduire l'élargissement dipolaire dans les milieux solides.

4. L'utilisation de réseaux d'antennes : ici, on ne joue plus sur des facteurs physiques, mais sur des éléments techniques et instrumentaux puisqu'il s'agit de superposer les signaux de capteurs indépendants.

Dans ce travail de thèse, notre stratégie portait sur l'amélioration de l'antenne de détection en termes de rapport signal sur bruit (SNR). Comme on le sait, le SNR est lié à deux principaux paramètres qui peuvent être améliorés : d'une part, le champ magnétique B_1 en adaptant la taille de la micro-bobine à celle de l'échantillon, et d'autre part, la résistance équivalente R de l'antenne qui peut être minimisée. Par ailleurs, nous pouvons également apporter un soin particulier au processus de microfabrication des antennes.

Pour cette étude, nous avons appelé micro-antenne RMN, la micro-probe associée à son circuit d'adaptation et d'accord. La micro-probe est la partie micro-bobine associée à la micro-ligne de transmission (TL) et aux différents types de connectiques. Les connectiques permettent de relier le centre de la micro-bobine à la ligne de transmission, et également la ligne de transmission au circuit d'accord et adaptation.

La Figure. 1 montre le premier prototype de micro-antenne RMN implantable, fabriquée par notre équipe. Cette micro-antenne a été conçue, pour être un outil d'analyse implantable de manière chronique pour des applications *in vivo* assurant la reproductibilité des mesures par spectroscopie RMN haute résolution. Plus précisément, pour suivre la variation des métabolites cérébraux (biomarqueurs) dans des petits volumes à faible concentration en utilisant des modèles animaux (rat ou souris).

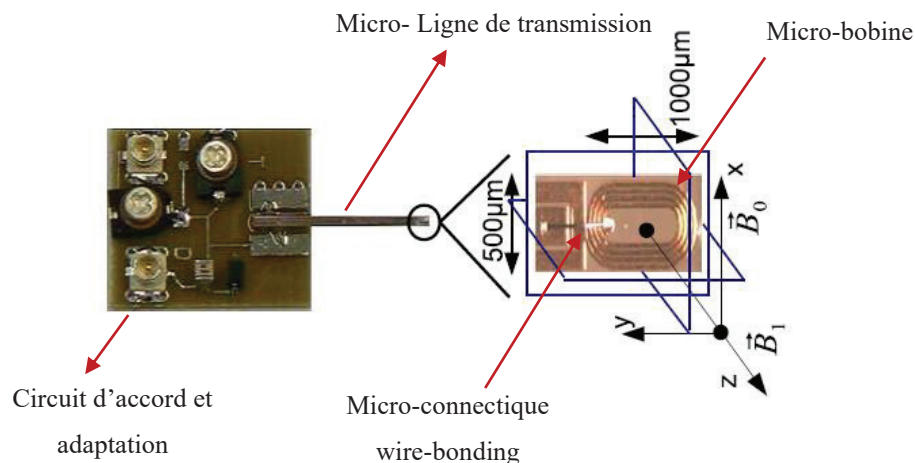


Figure. 1: Le premier prototype de la micro-antenne fabriquée par notre équipe.

Devant cette nécessité d'examiner par spectroscopie RMN de faibles quantités de matière, dans notre équipe, nous voulons explorer une région précise dans un ensemble beaucoup plus vaste ; ce qui nous a orientés vers le choix d'antenne implantable. L'objectif de plusieurs thèses

a été donc de développer et optimiser la micro-probe RMN implantable, pour la détection des métabolites cérébraux en vue du diagnostic précoce de la maladie d'Alzheimer.

Par ailleurs, le principal inconvénient de la micro-probe réside dans sa faible sensibilité en termes de Rapport Signal sur Bruit (SNR) due à la résistance globale de la micro-bobine et à celle de la ligne de transmission et de la partie de connectique (*wire-bonding or underpass & vias*), y compris la résistance supplémentaire correspondante au bruit de couplage élevé entre la partie active de la micro-probe (micro-bobine) avec l'échantillon. Notre première approche pour la réalisation de la micro-probe pour des applications *in vitro* a été présentée dans les thèses de N. Baxan (2008) et A. Kadjo (2011). Les tests *in vivo* n'ont pu être réalisés qu'avec un travail complémentaire d'optimisation (conception et simulations) de la sensibilité de la micro-probe, en termes de son facteur de qualité et SNR . Ce point est d'une extrême importance, car les signaux sources sont si faibles qu'ils sont comparables au bruit thermique, qui peut être lié à la résistance de la micro-antenne. Pour améliorer ses pertes résistives et plus particulièrement celles dues à sa connectique (*wire-bonding*), J. Trejo Rosillo (2014) a proposé dans sa thèse une nouvelle façon de connecter le centre de la micro bobine avec la micro-probe (*underpass & vias*). De même, T. Cong Troung (2014) a développé une méthode d'optimisation des micro-bobines RMN par une approche physique. Malgré ces améliorations, le facteur de qualité est resté faible (par exemple, $Q = 1,4$) ; insuffisant pour les applications *in vivo* attendues.

D'autre part, nous pouvons améliorer les performances de la micro-probe en optimisant son processus de fabrication. La tâche de fabrication nécessite plusieurs étapes coûteuses en temps et argent, surtout quand il s'agit d'explorer la fabrication des prototypes avec différentes dimensions, différents matériaux et les comparer expérimentalement. La simulation permet de s'en affranchir et d'examiner différents scénarios de systèmes sans avoir recours à l'expérimentation, puis de sélectionner les principaux paramètres pour obtenir les performances requises. Elle peut également fournir des tendances de données significatives et réaliser des comparaisons entre les prototypes possibles et guider le processus de fabrication.

La micro-probe peut être considérée comme un microsystème complexe multiparamétriques. Le nombre de paramètres augmente la complexité de l'étude analytique, d'une part et rend la fabrication très sophistiquée et coûteuse, il nous a fallu recourir aux outils de simulations, puis aux outils de prédictions. Par conséquent, l'objectif de ma thèse a été de proposer une nouvelle approche pour optimiser la micro-probe NMR implantable (micro-bobine + micro-ligne de transmission (TL) + connectiques). La Figure. 2 montre le dessin du

nouveau prototype optimisé et fabriqué. Sur la Figure. 2, nous avons également la description de chacune des parties et leurs dimensions respectives.

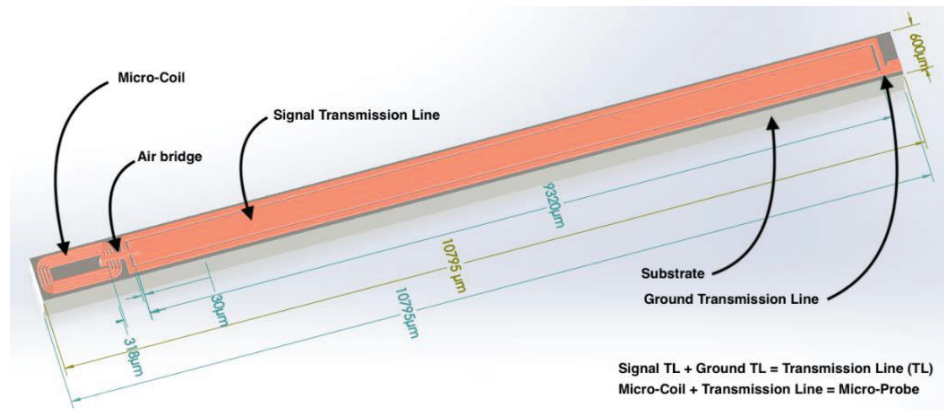


Figure. 2: Le prototype de la micro-probe aux dimensions optimisées : version avec une connectique type *air-bridge*

Pour la réalisation de ce nouveau prototype de micro-probe, nous avons reparti notre approche en deux parties principales :

1. Simulation de performance en termes de facteur de qualité et SNR
2. Prédiction des performances des nouveaux prototypes de micro-probe par le biais d'un modèle de l'IA.

Pour cela, nous avons développé une nouvelle plateforme « maison » 3D - TLE (Transmission Line Extractor) en collaboration avec l'INL (Institut de Nanotechnologie de Lyon). 3D-TLE est une plateforme créée sur MATLAB GUI (Graphical User Interface), qui peut générer un réseau SPICE (Simulation Program with Integrated Circuit Emphasis). Elle peut extraire automatiquement les impédances équivalentes de tout type de composant ou dispositifs de différentes géométries et de matériaux quelconques. Cet extracteur est 100 % compatible avec le simulateur de base SPICE, et avec le logiciel de modélisation ADS (Advanced design system).

Sur la Figure. 3, nous avons le schéma blocs des différentes étapes pour la simulation des performances de différentes géométries et dimensions de la micro-probe.

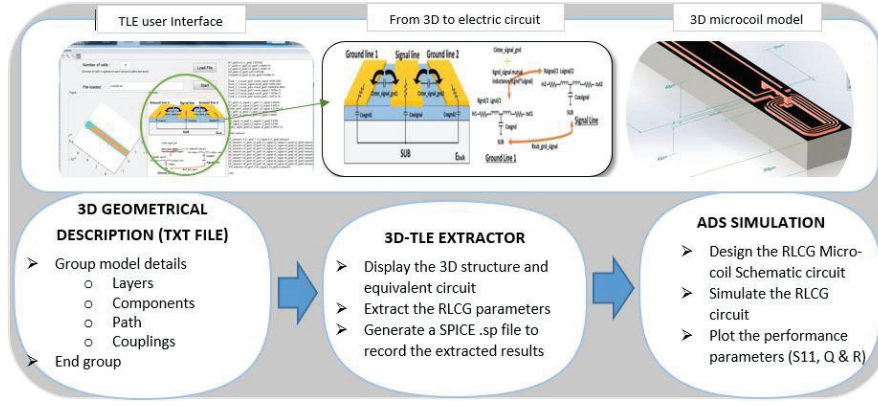


Figure. 3: Schématisation des principales étapes des simulations de micro-probes.

Le principe consiste à créer d'abord, un fichier *.txt* avec tous les paramètres géométriques du système, les propriétés des matériaux et le couplage entre les différentes parties constituant le système. Ensuite, un fichier *spice* est généré avec les paramètres électriques (*RLC*), avec lequel la performance en termes de facteur Q et SNR ont été simulé par ADS et calculé analytiquement.

Pour ce travail, nous avons simulé quatre géométries de micro-bobines (rectangulaire, ellipsoïdale, carrée et circulaire), deux types de substrats (Verre et Silicium) dans la gamme de fréquences de travail de 200 à 900 MHz. Pour chaque géométrie, nous disposons de plusieurs largeurs et longueurs de bobines (correspondant aux diamètres extérieurs des micro-bobines) d'une valeur variant de 500 μm à 1000 μm , ainsi que de tous les autres paramètres géométriques que nous allons voir dans la suite de cette thèse (voir Figure. 4).

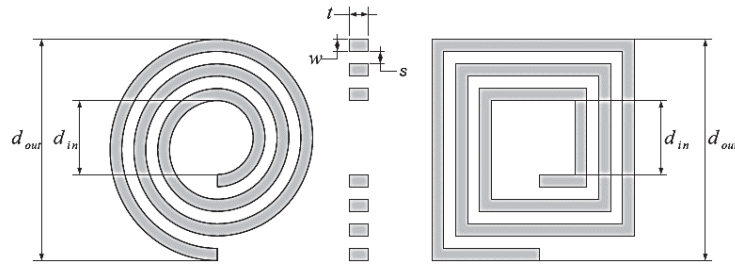


Figure. 4: Une micro-bobine circulaire et carrée à trois spires (d_{out} : diamètre extérieur, d_{in} : diamètre interne, w : largeur du conducteur, t : épaisseur du conducteur et s : distance de séparation entre deux conducteurs)

Dans l'étude des performances de la micro-probe, nous avons proposé un circuit électrique qui modélise complètement la micro-probe, aussi bien avec un substrat de Verre qu'avec un substrat de Silicium (Figure. 5), tenant compte de la contribution respective de chacune de ses parties constitutives.

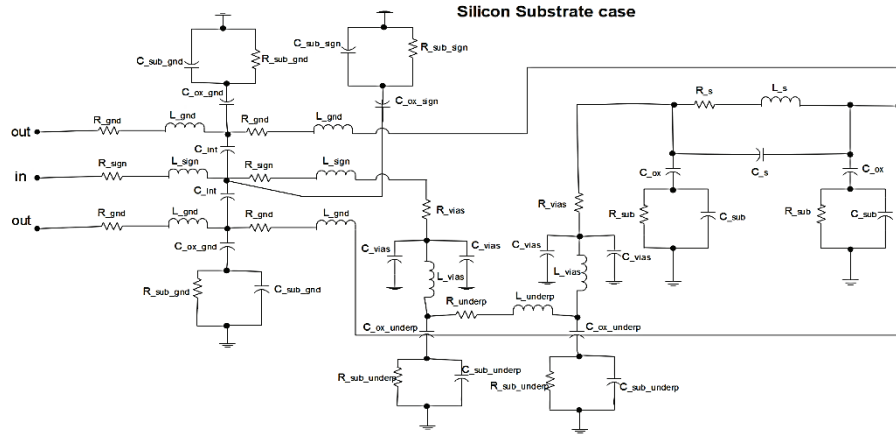


Figure. 5: Le modèle électrique de la micro-probe sur un substrat de silicium (modèle complet)

Les paramètres de performances (RLQ), de notre modèle électrique ont été calculés analytiquement dans la gamme de fréquences de fonctionnement des micro-antenne allant de 200 MHz à 900 MHz . Les résultats analytiques ont également été validés avec des résultats de simulations sur ADS (Tableau. 1) et des mesures après fabrication des prototypes de micro-probes. Notre modèle électrique nous a permis également d'étudier la contribution de chaque partie et estimer les pertes résistives introduites.

Working frequency		300MHz						500MHz					
Electrical parameters		R [Ω]		L_{self} [nH]		Q		R [Ω]		L_{self} [nH]		Q	
Model Type		Calc.	Sim.	Calc.	Sim.	Calc.	Sim.	Calc.	Sim.	Calc.	Sim.	Calc.	Sim.
Complete model	Glass	0.77	0.73	26.80	26.80	65.87	69.10	1.03	0.79	27.57	27.55	83.76	110.20
	Silicon	0.78	0.91	26.88	28.01	65.31	59.06	1.06	1.48	27.77	33.24	81.97	70.69

Tableau. 1: Les paramètres électriques RLQ du meilleur modèle de micro-probe à 300MHz et 500MHz .

Nous avons également, simulé le champ magnétique généré par la micro-probe complète, grâce au logiciel COMSOL Multiphysics ; c'est un logiciel de simulation basé sur la Méthode de calcul par Elément Finie (FEM). La conception du modèle 3D a été effectuée par SOLIDWORKS, qui est un logiciel basé sur la technique de modélisation Computer Aided Design (CAD). La simulation du champ magnétique a été réalisée en utilisant le module RF, et le module Live Link for SOLIDWORKS afin de connecter (importer) le modèle 3D de la micro-probe dans COMSOL Multiphysics.

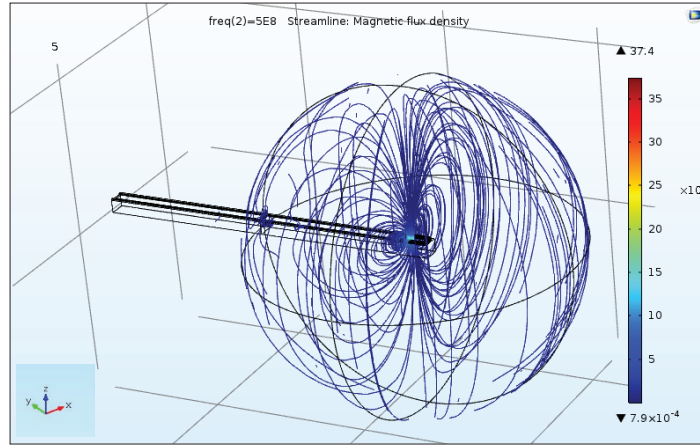


Figure. 6: Vue 3D des lignes de champ magnétique de la micro-probe : Bobine rectangulaire

L'objectif de cette simulation était d'étudier comment varie la composante (B_z) du champ généré par la micro-probe selon sa direction perpendiculaire (axe Oz). Sur la Figure. 6, on montre une approche de notre système complet, c'est-à-dire la micro-probe dans un volume sphérique de 0.6 cm de diamètre, centré sur la surface de la partie active de la micro-probe (micro-bobine rectangulaire), on voit également, les lignes de champ générés dans le volume à une fréquence de 500 MHz .

La Figure. 7 montre que le champ magnétique généré par la micro-probe à 300 MHz est plus faible que celui à 500 MHz au centre ($z = 5850\text{ }\mu\text{m}$). Cette simulation a été réalisée pour une conception de la micro-probe sur le substrat de silicium.

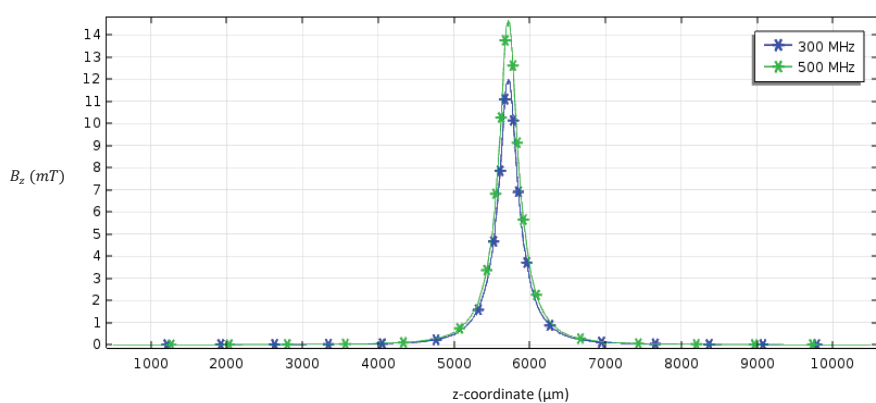


Figure. 7: Variation de la composante z du champ magnétique en fonction de la direction perpendiculaire (y) de la micro-probe.

Nos approches de simulations nous ont permis de déterminer les critères de performance optimal pour les prototypes de micro-probes (voir Figure. 2) et de le valider par la modélisation à l'aide du logiciel ADS. Cependant, ce travail de simulation est très chronophage et il reste difficile de déterminer l'impact de chaque partie qui constitue le dispositif (micro-probe).

L'idée première était de trouver une méthode efficace, pour exploiter et traiter les ensembles de données issues des différentes simulations (Figure. 8). L'autre idée est de, construire un modèle d'optimisation qui pourrait être généralisé à l'optimisation de tout système complexe multiparamétrique comme le nôtre (voir Figure. 9).

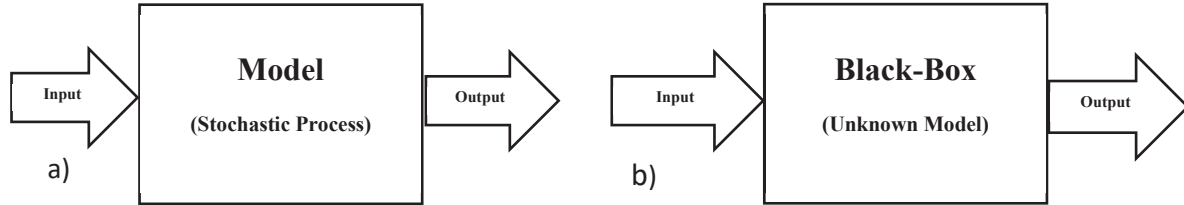


Figure. 8: Le parallèle entre la modélisation Classique et l'approche Machine Learning.

La Figure.8 montre le parallèle entre la méthode classique de simulation et la méthode avec une approche IA. Pour la suite de ce rapport, on s'est focalisé sur l'approche IA qui constitue la deuxième partie de l'approche utilisé pour la réalisation du nouveau prototype de la microprobe.

Le machine Learning (ML) c'est un champ de l'IA qui permet aux programmes des ordinateurs d'exécuter des tâches sans être explicitement programmé pour la réaliser. Cela est possible par l'apprentissage de l'algorithme en utilisant une expérience de l'ensemble de données.

Un modèle ANN qui est une des branches de ML nécessite un grand jeu de données correspondant aux entrées et à leur cible (sorties). Dans le jeu de données, pour notre étude, nous pouvons noter les prédicteurs et les cibles comme suit :

- **Prédicteurs (X)** : $[D_{out} \ D_{out}^* \ w \ t \ s \ n \ w_{und} \ t_{und} \ h_{vias} \ w_{sign} \ w_{gnd} \ \rho \ \varepsilon \ f]$; qui représentent les caractéristiques d'entrée utilisées pour alimenter le modèle pendant l'entraînement et les tests de prédiction.
- **Cible (Y)** : $[R_{probe} \ Q_{probe}]$; qui sont les données de sortie, utilisées comme référence pour le processus d'apprentissage du modèle.

Pour notre étude, nous avons considéré que notre système peut être défini comme un problème 4D (dimension), comme le montre la Figure. 9. Les dimensions correspondent aux performances de la microsonde (facteur Q et résistance), aux paramètres géométriques du système, aux propriétés électriques des matériaux, et la quatrième dimension correspond à la fréquence de travail.

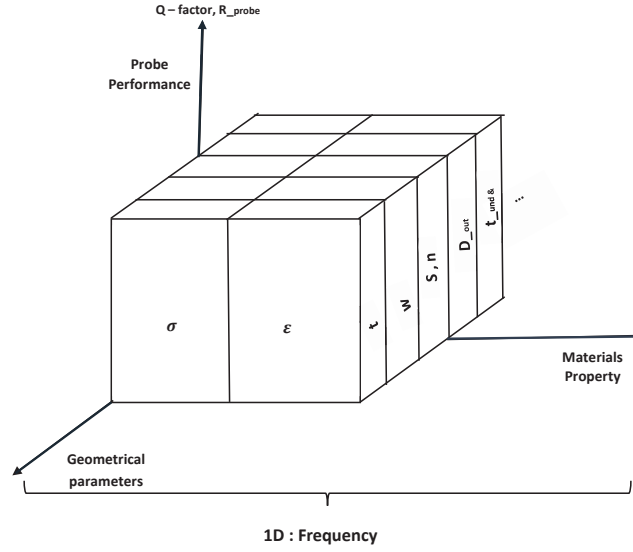


Figure. 9: Le modèle tenseur de notre système multiparamétrique.

Les méthodes de régression de Machine Learning sont utilisées pour prédire les valeurs continues tel que le prix des appartements dans une ville, d'une grandeur physique tel que la température d'un système, le facteur de qualité du système dans notre cas. L'ensemble de données du système peut être caractérisé par deux types de variables : les variables dépendantes et les variables indépendantes.

Les variables indépendantes peuvent être liées à la cause des états d'un système ou à la caractéristique du système pour prédire l'évolution (conventionnellement dénotées par X : Prédicteurs). La variable dépendante peut être considérée comme l'état final du système ou la cible, comme le but final de l'étude ou la tentative de prédiction (conventionnellement dénotée par Y : Target). Certes, pour notre jeu de données, les cibles de la simulation sont bien connues, qui correspondent aux performances de la microsonde en termes de facteur Q et de résistance R , ainsi que les prédicteurs du système, qui sont les paramètres géométriques, les propriétés électriques du substrat, le domaine de fréquence.

Dans cette section, nous présenterons sur la Figure. 10, la méthodologie d'entraînement d'un modèle de prédiction des performances de la microsonde. En outre, nous avons exploré l'outil Deep Learning à partir de l'APP GUI de Matlab (*nnstart*).

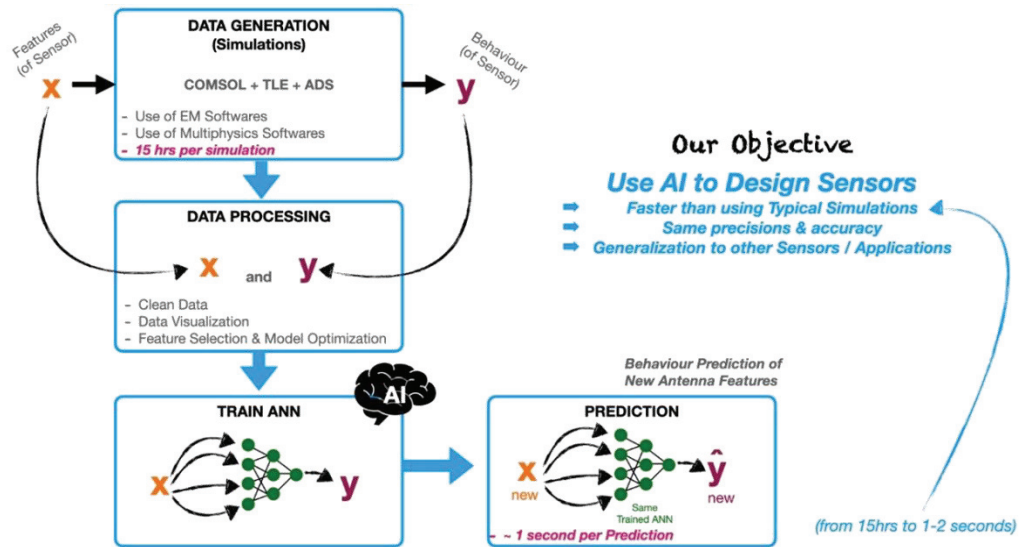


Figure. 10: Le schéma block représentant la procédure de l'approche IA pour la prédiction des performances de la microsonde.

Le principe de la méthodologie de notre approche consiste en plusieurs étapes :

- Génération de données à partir des simulations de performance de la microsonde.
- Pré-traitement des données pour voir la distribution des données, sélectionner les paramètres optimaux et nettoyer les données si nécessaire.
- Entraîner le modèle d'IA, en sélectionnant l'algorithme de d'optimisation des paramètres et hyperparamètres optimaux pour atteindre une bonne précision pour la généralisation du modèle.
- Tester le modèle avec de nouvelles données et évaluer sa précision.

Grâce aux données de simulations réalisées à l'aide de la plateforme 3D-TLE, nous avons développé un modèle par l'approche IA, basé sur une architecture de machine Learning, Réseau Artificiel de Nuerons (RAN) pour démontrer la possibilité de prédire les critères de performance de la micro-probe (facteur Q et résistance R) à partir de sa géométrie, de la nature de son substrat, et de sa fréquence de travail. Le modèle ANN a été entraîné et testé à travers le jeu de données généré par les simulations (6621 observations). Pour ce faire, nous avons utilisé la boîte à outils de MATLAB, Application GUI *Deep Learning* (Figure. 11).

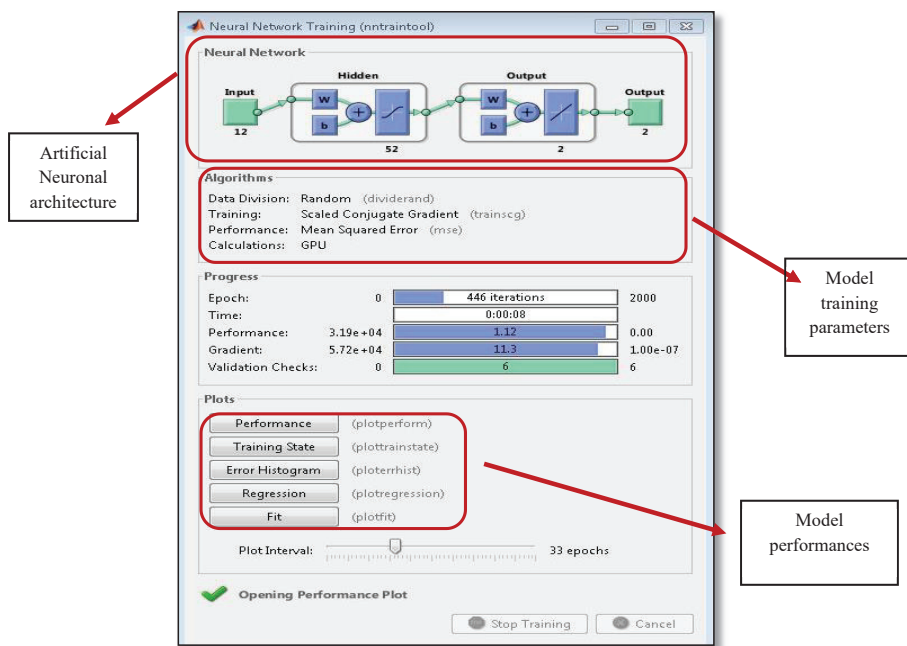


Figure. 11: Interface de l'outil d'entraînement du modèle IA.

Pour trouver le meilleur modèle pour entraîner les données, nous devons définir la forme du modèle (architecture du réseau de neurones), sélectionner les meilleures caractéristiques de nos données, plus précisément identifier quels prédicteurs sont importants, et régler plusieurs paramètres de l'architecture (nombre de neurones dans les couches cachées, la profondeur du réseau, définir les fonctions d'activation pour chaque couche) afin de trouver les hyperparamètres optimaux. En général, c'est un travail d'itération qui est effectué pour trouver le meilleur ajustement pour nos données par rapport au modèle (hyperparamètres optimaux).

Suite à l'essai de plusieurs architectures, avec un réseau peu et très profond, notre modèle choisi est l'architecture *Shallow* qui correspond à une architecture ayant une seule couche cachée. Cependant, intuitivement, elle ne semblait pas être le meilleur choix au vue de sa simplicité en comparaison avec d'autres l'architectures et de la complexité du problème. L'optimisation du nombre de neurones dans la couche cachée a été réalisée grâce à un script développé sur MATLAB. Nous avons fait 1000 itérations pour trouver le nombre optimal de neurones dans la couche cachée (hyperparamètre), et 500 itérations pour trouver les paramètres optimaux pour le réseau.

Pour évaluer la qualité de notre modèle, il était important de diviser nos données (jeu des données). Nous les avons donc répartis aléatoirement de la manière suivante : 70 % de nos données ont été utilisés pour l'entraînement, 15 % pour la validation et 15 % pour le test.

En général, il est souhaitable qu'un modèle puisse tenir compte de la tendance des données, sans s'adapter au bruit dans les données. L'ajustement du bruit est appelé « surajustement » (*overfitting*). L'utilisation de données de validation pendant le processus de training nous a permis d'éviter l'*overfitting*. Pour les données de validation, il existe deux approches : la validation croisée (*cross validation*) et la méthode de validation *hold-out*, celle qui a été retenue pour l'entraînement de notre modèle. Notre modèle entraîné nous a permis de prédire le facteur de qualité et la résistance, pour 60 observations. Sur les figures qui suivent, nous avons l'allure du facteur de Qualité et l'allure de résistance de la micro-probe, dans les cas de données de tests (Figure. 12).

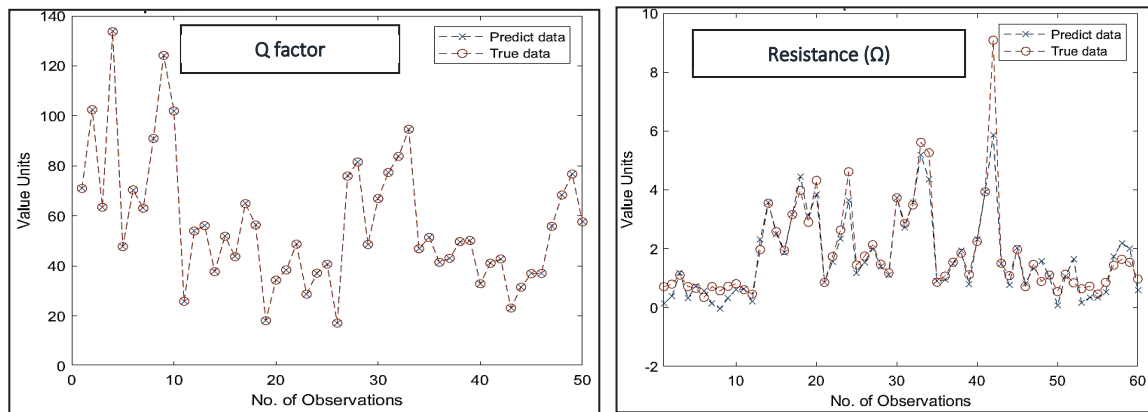


Figure. 12: Prédiction du facteur Q et résistance R de la micro-probe en fonction du nombre d'observations, superposée aux valeurs réelles.

On peut noter sur la Figure. 12 que les prédictions de notre modèle sont en accord avec les vraies valeurs de chaque paramètres (le facteur Q et la résistance R). Les performances du test des modèles IA, en termes de la métrique $RMSE$ et $\langle R^2 \rangle$ sont résumés dans le tableau suivant :

Targets	ANN	RMSE	$\langle R^2 \rangle$ (%)
[R_probe Q_probe]	12 : 125 : 2	0.738	96.56
[Q_probe]	12: 52 : 1	0.032	99.79
[R_probe]	12 : 44 : 1	0.042	91.34

Tableau. 2: Les performances de différentes architectures ANN

A la lumière de ses résultats encourageants, nous avons conçu les *layout* des masques dédiés au process de fabrication de micro-probes. Nous avons prévu des masques pour différents types de connectique « *underpass & vias* », « *wire-bonding* » et « *air-bridge* », au total deux masques

comme défini par le cahier de charge. La fabrication de la micro-probe optimisée a été des prototypes de micro-probe sur une plaquette (*wafer*) de Verre ont été fabriqués avec une connectique telle que le *wire-bonding*. La fabrication de la micro-probe optimisée a été réalisée en salle blanche de l'ESIEE (École Supérieure d'Ingénieurs en Électrotechnique et Électronique) à Paris.

Les prototypes optimisés et fabriqués sont présentés dans les figures que suivent :

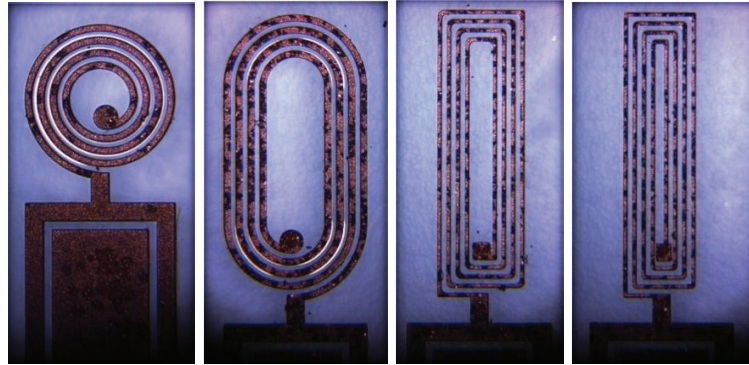


Figure. 13: Les mages des micro-bobines fabriquées dans le substrat de Verre. Géométries : circulaire ($500 \times 500 \mu m^2$), ellipsoïdale ($1000 \times 500 \mu m^2$), rectangulaire ($1000 \times 300 \mu m^2$, $1000 \times 250 \mu m^2$)

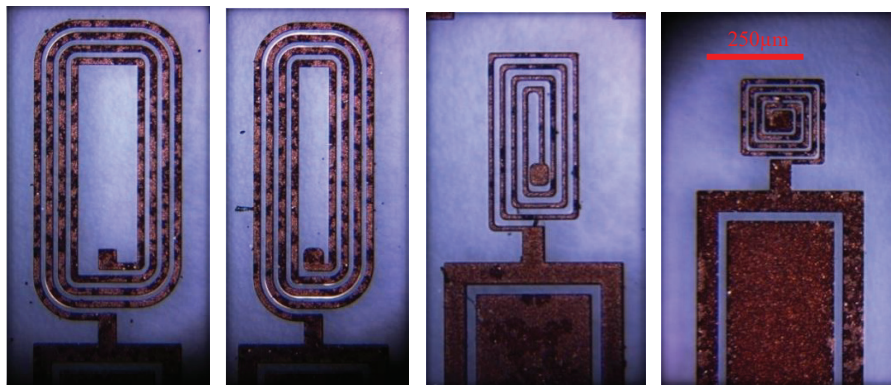


Figure. 14: Les mages des micro-bobines fabriquées dans le substrat de Verre. Géométries : rectangulaire ($1000 \times 500 \mu m^2$, $1000 \times 400 \mu m^2$, $500 \times 250 \mu m^2$), carré ($250 \times 250 \mu m^2$)

Les géométries des micro-bobine fabriquées sur un substrat de Silicium et de Verre, par électrodéposition du cuivre. Les images ont été réalisées par microscopie optique avec un objectif de grossissement de 10.

Nous avons également caractérisé les micro-probes fabriquées dans le substrat de verre. Les Figure. 15 & Figure. 16 montrent les mesures au profilomètre, des épaisseurs de la partie micro-bobine et la partie ligne de transmission. Les mesures ont été réalisés sur les prototypes issus du premier essai de fabrication des micro-probes avant optimisation du process de fabrication.

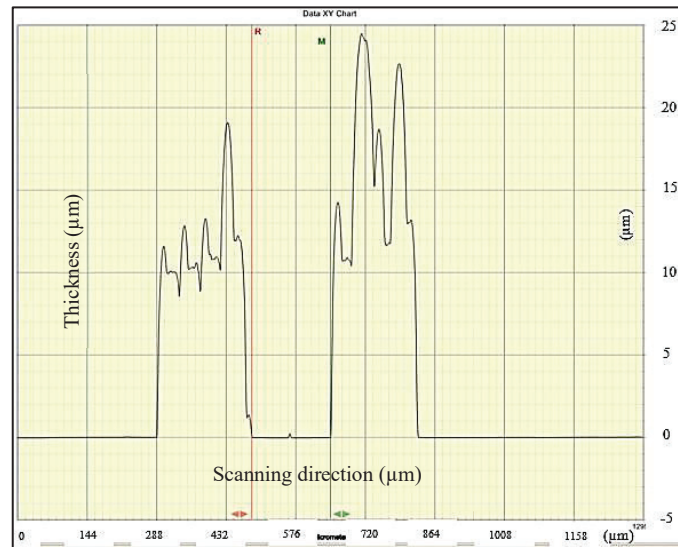


Figure. 15: Courbes de balayage de la surface de la micro-bobine

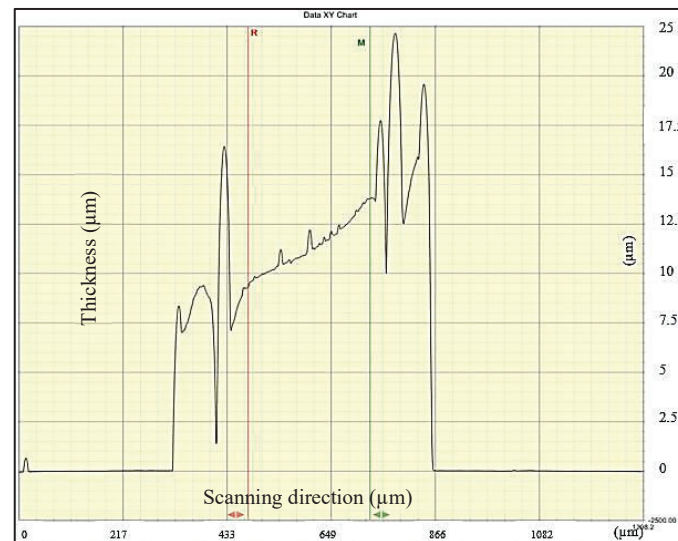


Figure. 16: Courbes de balayage de la surface de la micro-ligne de transmission

Sur la Figure. 17, nous avons les résultats des épaisseurs des micro-probes, pour différentes positions sur le wafer de verre, issu de la fabrication après optimisation du process. On a choisi les sept positions stratégiques sur le wafer, dans l'objectif de sonder l'épaisseur des micro-probes déposés dans différentes parties du wafer.

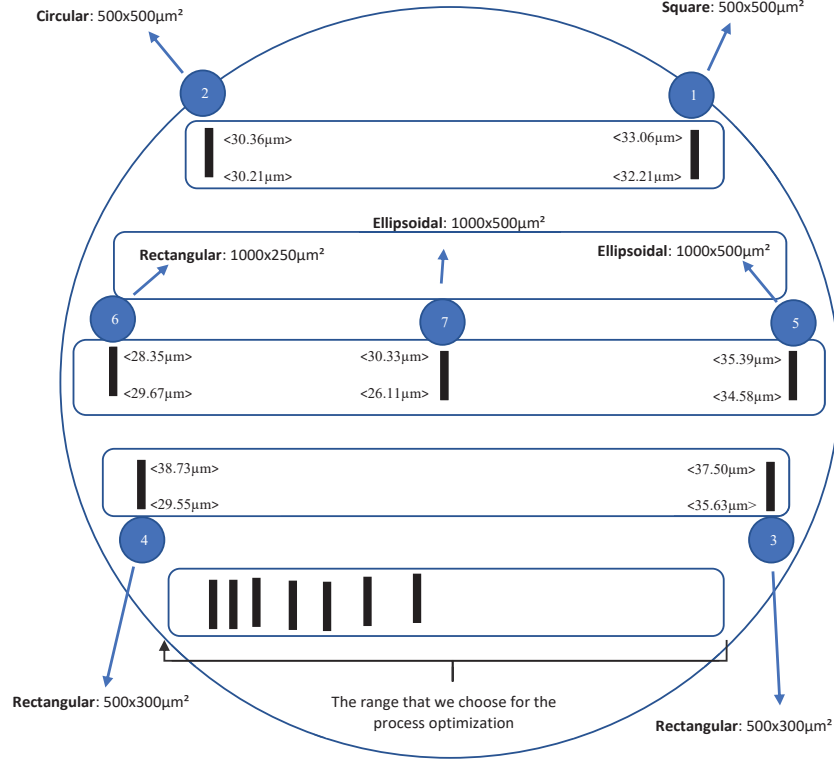


Figure. 17: Cartographie de l'épaisseur sur différentes parties du wafer de verre (Processus de fabrication optimisé).

En conclusion, nous avons optimisé le processus de fabrication de la micro-probe, dans l'objectif de respecter le cahier des charges défini dans le projet (manuscrit de thèse, chapitre IV, paragraphe IV.1.1). Les résultats préliminaires de caractérisation (morphologique et électrique) obtenus avec le prototype fabriqué sur des substrats de verre ont été rapportés. Nous avons fabriqué des *Micro-probes* avec des micro-bobines de très petite dimension de l'ordre de $250 \times 250 \mu\text{m}^2$ avec une épaisseur d'environ $t = (27,10 \pm 1,37) \mu\text{m}$ (Figure. 17). Dimensions atteintes pour la première fois. Nos résultats de caractérisation sont très prometteurs en vue des prochaines applications *in vivo*. A titre d'exemple, le 1^{ère} essai de fabrication (micro-probe d'épaisseur $t = (18,90 \pm 5,25) \mu\text{m}$, Figure. 15 & Figure. 16), nous a permis d'estimer la résistance du prototype sans connecteur, dans un substrat de verre à $R = (3,897 \pm 0,193) \Omega$, et avec un connecteur, soudé dans un PCB on a estimé à $R = (6,12 \pm 0,12) \Omega$.

L'approche IA, plus particulièrement ANN associée à 3D-TLE, est une méthode que nous avons développée pour généraliser l'optimisation de notre système multiparamétrique très complexe (micro-probe). Notre modèle ANN a été entraîné pour prédire le facteur Q de la micro-probe avec une précision de test de 99,67 % ($RMSE = 0,032$), la prédiction de la

résistance avec une précision de 91,34 % ($RMSE = 0,042$), grâce au jeu de données générées par le travail de simulation réalisé au préalable.

Pour finir, notre travail montre qu'à l'avenir nous pourrions concevoir et fabriquer avec précision n'importe quel type de micro-sonde ou sonde optimisée en fonction des performances souhaitées, de la fréquence de travail et du type de substrat. Cela avec un temps de calcul de 2 *minutes* au lieu de 15 *heures*. Ainsi, cette nouvelle approche d'optimisation utilisant des outils d'IA combinés à des outils de simulation (travail d'optimisation multiparamétriques) implique un progrès dans la recherche biomédicale basée sur le développement de micro-capteurs RMN utilisés pour l'exploration du cerveau, le diagnostic précoce et le suivi du traitement.

Table of contents

Acknowledgements

List of Acronyms

Résumé de thèse.....	1
Table of contents.....	18
List of captions of the figures and tables.....	22
Abstract.....	29
Résumé.....	30
Introduction	31
Chapter I : Alzheimer Disease and NMR spectroscopy : Overview.....	35
I.1. Alzheimer Disease (AD).....	36
I.1.1. Introduction of AD as a public health issue.....	36
I.1.2. AD markers and diagnosis methods	37
I.1.3. The objectives of the presents study and hypothesis	39
I.2. NMR spectroscopy	41
I.2.1. Principle of the NMR.....	41
I.2.2. The effect of the static magnetic field B0	41
I.2.3. The Radiofrequency (RF) magnetic field	44
I.2.4. The detection of signals	45
I.2.5. The NMR instrumentation	47
I.3. NMR antennas and their criteria of performance	49
I.3.1. Stat-of-the-art of the surface antennas	49
I.3.2. NMR antenna miniaturization.....	53
I.3.3. The performance criteria of the NMR antennas	59
I.3.3.1. Noises	59
I.3.3.2. S11 Parameter of NMR antenna.....	60
I.3.3.3. Q – Factor of the NMR antenna	61
I.3.3.4. Signal Noise Ratio (SNR)	62
I.4. Sensitivity and Limit of detection of the NMR experiments.....	64
I.4.1. The sensitivity of the NMR experiment	64
I.4.2. Limit of Detection (LOD)	64
I.5. In-vivo implantation made by our team	65
I.5.1. Advantages of the Implanted micro-antennas.....	65
I.5.2. Previous implantations of the Micro-coil in a rat model	67
Conclusion.....	69
Chapter II : Modelling of the magnetic field and resistive loss of the microantenna.....	70
II.1. Review of the previous micro antennas: 1st and 2nd prototypes	71
II.1.1. The micro-coil and transmission line modelling	71
II.1.2. Limitations of the previous designs.....	73

II.2. The design and modelling of the microprobe.	74
II.2.1. Simulation of the magnetic field	75
II.2.2. Electrical parameters of the micro-coil (RLC)	76
II.2.2.1. The length modelling of the four micro-coil geometries	77
II.2.2.1.1. Rectangular and square micro-coil shape	77
II.2.2.1.2. Circular micro-coil shape Rectangular and square micro-coil shape	78
II.2.2.1.3. Ellipsoidal micro-coil shape	78
II.2.2.2. The resistance of rectangular conductor	79
II.2.2.3. Skin effect and proximity effect approach	79
II.2.2.4. Skin effect for a micro-conductor	80
II.2.2.5. Resistance modelling with skin and proximity effect	81
II.2.2.6. The self and mutual inductance.....	82
II.2.2.7. The capacitor of the microprobe model	83
II.2.3. Summary of electrical and magnetic parameters of the micro-coils	84
II.2.4. The impact of the geometrical parameters	85
II.2.5. Design limitation of the smaller micro-coils	87
II.3. Simulation of the magnetic field generated by the microprobe using COMSOL Multiphysics.....	90
II.3.1. Electromagnetic principle of the approach	90
II.3.2. Simulation of substrate impact to the magnetic field	90
II.3.3. The magnetic field generated by the complete microprobe prototype	93
Conclusion.....	97
Chapter III : 3D Electrical model of the microprobe and prediction of performance.. ...	98
III.1. 3D – TLE (Transmission Line Extractor)	99
III.1.1. The principle of 3D -TLE	99
III.1.2. The model of Underpass & Vias (TSV - Through Silicon Vias).....	100
III.1.3. Substrate losses in the high-frequency domain.....	102
III.2. The electrical circuit of the implantable NMR microprobe	103
III.2.1. The RLC electrical circuit and PI model	103
III.2.2. Our proposed microprobe electrical circuit	106
III.2.3. The electrical parameters (RLC) of the microprobe extracted by 3D-TLE..	110
III.2.4. Results of the Q factor and S11 parameters of the simulation of models.....	111
III.2.5. Results of the microprobe modelled on glass and silicon substrate (RLQ) ..	112
III.3. Prediction of the microprobe performances: Artificial Intelligence approach	118
III.3.1. Introduction.....	118
III.3.2. Traditional simulation method for microprobe model.....	118
III.3.3. Machine Learning Approach	120
III.3.3.1. Deep Learning (DL) architecture.....	121
III.3.3.2. The principle of an Artificial Neuron	122

III.3.3.3. The loss function and descendent gradient of a Logistic regression	124
III.3.3.4. Vectorization of the mathematical model of a neuron.....	125
III.3.3.5. The principle of an Artificial Neuronal Network	128
III.3.3.6. Feed Forward propagation and Backpropagation	129
III.3.4. The evaluation metrics of a trained model.....	131
III.3.4.1. Mean Absolute Error (MAE).....	131
III.3.4.2. Mean Absolute Percentage Error (MAPE)	132
III.3.4.3. Mean Square Error (MSE).....	132
III.3.4.4. Root Mean Square Error (RMSE)	132
III.3.4.5. Relative Absolute Error (RAE).....	132
III.3.4.6. Relative Squared Error (RSE).....	133
III.3.5. Model training for the prediction of the micropore performance	133
III.3.5.1. The assumption of the ANN model to the generated data	134
III.3.5.2. The pre-processing of our generated dataset	136
III.3.5.3. The architecture used for our model training.....	139
III.3.5.4. The testing of Backpropagation algorithms and activation function	141
III.3.5.5. The results of the optimization of model parameters of LM algorithms	145
Conclusion.....	149
Chapter IV : Manufacturing of the optimized microprobes and their characterization in cleanroom	150
IV.1. Microprobe cleanroom manufacturing process	151
IV.1.1. Specifications of the microprobe prototype fabrication.....	151
IV.1.2. The main steps for the microprobe fabrication	155
IV.1.2.1. Stage 1: Thin film deposition (Sputtering and evaporation).....	156
IV.1.2.2. Stage 2: Ultra Violet (UV) Photolithography	157
IV.1.2.3. Stage 3: Copper electroplating	160
IV.1.2.4. Stage 4: The photoresist and seed layer removing (Lift-Off)	161
IV.1.2.5. Stage 5: Electroless gold plating.....	162
IV.1.3. Characterization of the fabricated microprobes: 1 st trial	162
IV.1.3.1. Morphological characterization	163
IV.1.3.2. Electrical parameters measurement.....	166
IV.1.4. Optimization of Micro-manufacturing process.....	168
IV.1.4.1. Photolithography Optimisation	168
IV.1.4.2. Electroplating Optimization	170
IV.1.5. Manufactured microprobe after the optimization process	172
IV.1.6. Characterization of the optimized prototype.....	173
IV.1.6.1. Measurement of the thickness on different sides of the wafer...	174
IV.1.6.2. Electrical characterization of the fabricated microprobes.....	180
Conclusion	182
General Conclusions and Discussions	183
Bibliography	185
APPENDICES	197

<i>A.1. Maxwell's equations</i>	<i>198</i>
<i>A.2. Mesh.....</i>	<i>199</i>
<i>A.3. Syntaxes of the .txt file to model TL part on a silicon substrate.....</i>	<i>200</i>
<i>A.4. Syntaxes of the .txt file to model underpass & vias within the silicon substrate.....</i>	<i>201</i>
<i>A.5.Netlist of SPICE file (.sp), with the results of the TL and Underpass & vias modelling within a silicon substrate</i>	<i>202</i>
<i>A.6. The sequences of Microprobe Simulation for data-generating</i>	<i>203</i>
<i>A.7. The Microprobe characteristics for data simulated</i>	<i>203</i>
<i>A.8. Data regularization methods for generalization of the model</i>	<i>204</i>
<i>A.9. Epoch.....</i>	<i>204</i>
<i>A.10. Algorithm selected for the optimization of the final model.</i>	<i>205</i>
<i>A.11. Prediction of Resistance and Q factor using completely different dataset for three trained models.....</i>	<i>207</i>
<i>B.1. Scientific papers</i>	<i>208</i>
<i>B.2. International Congress papers with published proceedings: [O] [eP]:</i>	<i>208</i>
<i>B.3. Presentation in a national conference and congress, Oral [O]/Posters [P] [eP]</i>	<i>209</i>

List of captions of the figures and tables

Fig. I. 1. Natural progression of biological markers of AD [2].....	37
Fig. I. 2. The spectrum of cerebral metabolites of the rat [28].....	39
Fig. I. 3. Anatomy of the main cholinergic pathways in the rat brain [35].	40
Fig. I. 4. Magnetic atomic nuclei behaviour, before and after setting it into the magnetic field	42
Fig. I. 5. Energy diagram describing the distribution of the nucleon quantum stats at two different energy levels, before and after setting into the static magnetic field B_0 [37]	42
Fig. I. 6. The principle of emission and reception of FID signal. a) The rotating of magnetization M induces a EMF into the S loop; b) The signal at point P is proportional to the magnetic field B_1 [43].....	45
Fig. I. 7. The plot of $\xi(t)$, detected NMR signal in the time domain, FID [43].....	47
Fig. I. 8. An implantable planar micro-antenna (with ellipsoidal micro-coil): first prototype developed by our team [57].....	51
Fig. I. 9. A DUT (Device Under Test) with two ports	60
Fig. I. 10. Comparison of the LOD of a commercial antenna with the rack trace antenna [58]	66
Fig. I. 11. (a) Micro-antenna implantation inside the ROI, using a stereotaxy device, (b) representing amagnetic anchoring screw and the micro-antenna site (Dorsal plans of rat skull) [56].	67
Fig. I. 12. <i>In vitro</i> NMR spectrum of 10 brain metabolites in aqueous solution using the planar micro-antenna (prototype developed by our team)	67
Fig. II. 1. Micro antenna prototype (the 1st fabricated by our team) [56].	71
Fig. II. 2. Design and dimensions of the 2 nd prototype of the micro-probe [80].....	72
Fig. II. 3. Block diagram of our methodology to develop the new optimized microprobe prototype.....	74
Fig. II. 4. The four geometries of micro-coil designed in CST MWS	75
Fig. II. 5. Plot of magnetic field (B_z) variation as a function of z-direction.....	76
Fig. II. 6. Circular and square micro-coil shape with three spiral turns (dout : outer diameter, din : inner diameters, w : width of wireline, t : the thickness of wire and s : separation distance between two wires) [43]	77
Fig. II. 7. Ellipsoidal micro-coil shape with four spiral turns [43]	78

Fig. II. 8. Conductor wire, with rectangular surface cross-section [43].....	79
Fig. II. 9. Skin effect phenomena illustration in the case of a rectangular (a) and ellipsoidal (b) conductor surface section. The blue area represents the surface cross-section region where the current is going to pass-through	81
Fig. II. 10. Coplanar line structure for two close wires with the rectangular surface [43].....	82
Fig. II. 11. The four modelled geometries: $n = 4, t = 40 \mu m, w = 22 \mu m, s = 20 \mu m$..	84
Fig. II. 12. Variation of the magnetic field as a function of the z-direction for different dimensions of rectangular micro-coil.....	85
Fig. II. 13. B_z variation as a function of the z-direction, for different dimensions of the square micro-coil	86
Fig. II. 14. Representation of the limiting external diameter as a function of the geometric parameters of the μ coil.....	88
Fig. II. 15. a) The micro-coil modelled on the substrate inside a rectangular system. b) 3D view of the magnetic field variation on the parallel and perpendicular plan against micro-coil	92
Fig. II. 16. Lines of the magnetic field generated by the micro-coil: 2D view (a) situated at $z = 600 \mu m$ and 3D view (b)	92
Fig. II. 17. Profile of the z magnetic field component from several working frequencies.	93
Fig. II. 18. Magnetic field z component as a function of the z-direction for substrates types .	93
Fig. II. 19. The 3D layout of the proposed microprobe: new prototype (Coil Needle) with rectangular coil.....	94
Fig. II. 20. 3D view of the microprobe magnetic field lines	95
Fig. II. 21. Magnetic field z component as a function of microprobe parallel direction (Ox)	95
Fig. II. 22. Magnetic field z component as a function of microprobe perpendicular direction (Oz).....	96
Fig. III. 1. User Interface of 3D-TLE (Transmission Line Extractor).....	99
Fig. III. 2. 3D-TLE extraction tool environment [98]	100
Fig. III. 3. 3D Compact model of the TSV as defined in 3D-TLE [96].....	101
Fig. III. 4. The electrical model of the TSV orientation according to its I (1) /O (2) ports [99] [98]	101
Fig. III. 5. Electrical circuit that models the micro-coil (RLC model).....	104
Fig. III. 6. The electrical circuit that models the micro-coil on the silicon substrate (PI Model)	105

Fig. III. 7. Model PI block diagram.....	105
Fig. III. 8. The electrical circuit modelling the microprobe on a glass substrate (complete model)	107
Fig. III. 9. Block diagram of the electrical circuit of microprobe on a glass substrate	108
Fig. III. 10. The electrical circuit modelling the microprobe on a silicon substrate (complete model).....	108
Fig. III. 11. S11 parameters of the microprobe electrical model from the silicon substrate (a) and the glass (b).....	111
Fig. III. 12. S11 parameters of the complete model of microprobe on a silicon and glass substrate.....	112
Fig. III. 13. Q-factor variation of both complete electrical models of NMR micro-probe	112
Fig. III. 14. Resistances variation from electrical models of microprobe on a glass substrate a) and silicon b)	113
Fig. III. 15. The variation of Resistance a) and Inductance from complete electrical models of microprobe on a glass substrate and silicon	113
Fig. III. 16. The statistical study of RLQ parameters, comparing different models of microprobe modelled on a glass and silicon substrate, for 300 MHz	114
Fig. III. 17. The statistical study of RLQ parameters, comparing different models of microprobe modelled on a glass and silicon substrate, for 500 MHz	115
Fig. III. 18. A statistical study of Q-factor variation from microprobe operating at 300MHz and 500MHz for both substrate cases.....	116
Fig. III. 19. Block diagrams of the classic simulation methodology for microprobe parameters optimization [43]	119
Fig. III. 20. (a) Traditional method vs (b) Machine Learning approach	119
Fig. III. 21. Machine Learning Workflow [116]	120
Fig. III. 22. Two categories of machine learning techniques: Supervised and unsupervised learning [117]	121
Fig. III. 23. Human neuron (a) versus a standard mathematical model of a neuron (b) [124] [125]	122
Fig. III. 23. Representation of the standard activation functions	123
Fig. III. 25. Artificial Neural networks are organized in layers consisting of a set of interconnected nodes	128
Fig. III. 26. Schematic procedure of the AI approach to predict the microprobe performances	134

Fig. III. 27. The tensor model of our multiparameter system	135
Fig. III. 27. The analogy of tensors dimensions [135]	135
Fig. III. 29. Block diagrams of the simulation methodology: TLE user interface and 3D design of the microprobe with its dimensions	136
Fig. III. 30. The histogram of the dataset predictors	137
Fig. III. 31. The boxplot of the predictor with the targets (Resistance and Q factor of microprobe)	138
Fig. III. 32. The plot of the targets (Q – factor and micro-coil Resistance): four types of geometry.....	139
Fig. III. 33. The plot of the targets (Q – factor and Microprobe Resistance): four types of geometry.....	139
Fig. III. 34. ANN architecture for Microprobe dataset training model	140
Fig. III. 35. The microprobe Q factor and Resistance R prediction, using the optimal number of neurons according to the evaluation of RMS from training, validation and testing	143
Fig. III. 36. The microprobe Q factor and Resistance R prediction, using the min and max RMSE of the testing model according to the trial of training with different weights and bias parameters	144
Fig. III. 37. ANN architecture for Microprobe dataset training model	145
Fig. III. 38. The RMSE variation in terms of the number of neurons in the hidden layer	145
Fig. III. 39. (a) The performance variation as a function of epoch (train, validation and test) (b) The error histogram for the Rprobe training model.....	146
Fig. III. 40. A plot of the regression of the (a) Training dataset, (b) the validation and (c) Test dataset.....	146
Fig. III. 41. The prediction and the true value of the Q factor and Resistance of the microprobe	147
Fig. III. 42. RMSE performance of the optimal trial.....	147
Fig. III. 43. The microprobe global Q factor and Resistance R prediction, after trial number optimization.....	148
 Fig. IV. 1. Layout designed for <i>wire-bonding</i> mask fabrication.....	 153
Fig. IV. 2. Layout designed for <i>underpass & vias</i> and <i>airbridge</i> mask fabrication.....	154
Fig. IV. 3. The <i>underpass and vias</i> layer of the designed layout.....	154

Fig. IV. 4. Layout design for the glass wafer: geometries, description of the number of the microprobes for each raw	155
Fig. IV. 5. Sputtering equipment type SCM 600 (ALCATEL).....	156
Fig. IV. 6. Seed layer preparing process a) Glass substrate and b) silicon substrate	156
Fig. IV. 7. The main step of UV photolithography (Mask patterns etching)	157
Fig. IV. 8. The spin coating, (a) before and (b) after the photoresist spreading out	158
Fig. IV. 9. UV photolithography equipment (a): wafer mask alignment to the light exposure) and (b): the wafer after photoresist cleaning up	159
Fig. IV. 10. (a) The microscope to characterize the micro-coil shape, (b) Rectangular micro-coil geometry after the photoresist development and cleaning up	159
Fig. IV. 11. (a) Electro-planting system, (b) bath with an electrolyte solution, (c) preparing the wafer to fix in the cathode part.....	160
Fig. IV. 12. The representation of the wafer after Cu electrodeposition.....	160
Fig. IV. 13. Wafer before (a) and (b) after photoresist and seed layer removing	161
Fig. IV. 14. Wafer before (a) and (b) after photoresist and seed layer removing	161
Fig. IV. 15. The prototype ended up after the electroless process	162
Fig. IV. 16. (a) The microscope (b) The optic profilometer	163
Fig. IV. 17. Checking different defects of the first prototype manufactured: short-circuit, residual resin	164
Fig. IV. 18. Profile of the micro-coil surface scanning.....	164
Fig. IV. 19. Profile of the micro-path surface scanning	165
Fig. IV. 20. Profile of the microprobe surface scanning	165
Fig. IV. 21. Two-point micro-structure resistance measurement.....	166
Fig. IV. 22. Digital multimeter (KEITHLEY 2100, 1kV3A, 6.5 digits) used for Resistance measurement.....	166
Fig. IV. 23. Then microprobe set up on the PCB, and the NANO VNA connected with a microprobe.	167
Fig. IV. 24. The geometries suitable for the performance measurements.....	167
Fig. IV. 25. (a) Ten prepared wafers, (b) the optimized mask	168
Fig. IV. 26. Spin coating section, placing the photoresist.....	169
Fig. IV. 27. The thickness of the deposited resin and the copper layer at the different parts of the wafer.....	171
Fig. IV. 28. The geometry of some manufactured micro-coil: circular ($500 \times 500 \mu m^2$), ellipsoidal ($1000 \times 500 \mu m^2$), rectangular ($1000 \times 300 \mu m^2$, $1000 \times 250 \mu m^2$)	172

Fig. IV. 29. The geometry of some manufactured micro-coil: rectangular ($1000 \times 500 \mu m^2$, $1000 \times 400 \mu m^2$, $500 \times 250 \mu m^2$), square ($250 \times 250 \mu m^2$).....	172
Fig. IV. 30. The geometry of some manufactured micro-coil: square ($500 \times 500 \mu m^2$, $250 \times 250 \mu m^2$, $400 \times 400 \mu m^2$), micro-transmission line.	172
Fig. IV. 31. The geometry of some manufactured micro-coil: micro-coil: square ($1000 \times 1000 \mu m^2$, $250 \times 250 \mu m^2$, $400 \times 400 \mu m^2$).....	173
Fig. IV. 32. The seven-microprobes selected for the resin removing and their classification according to their observation using a microscope.	174
Fig. IV. 33. Microprobe thickness mapping on different parts of the wafer support.....	175
Fig. IV. 34. Confocal Raman Microscopy images of the microprobes selected for the wafer mapping.....	176
Fig. IV. 35. Microprobe fabricated in the glass substrate, with a connector on a PCB support, by <i>wire-bonding</i> connecting wire.....	180
Fig. IV. 36. Measure of S_{11} parameters from four geometries of microprobe	180
Fig. IV. 37. Measure of the resistance and inductance from four geometries of microprobe	181
Table I. 1. Value of gyromagnetic ratios of specific atomic nuclei of interest	43
Table I. 2. Review of all planar microprobe for NMR applications	54
Table I. 3. Summary of our team works, geometrical dimensions, electrical parameters analysis, and materials for μ manufacturing and its application.....	57
Table II. 1. Micro-coil layout and dimension of the optimal geometries [37].....	72
Table II. 2. Summary of electrical and magnetic parameters from each micro-coil geometry at 300 MHz	84
Table II. 3. The electrical and magnetic parameters of each rectangular micro-coil at 300 MHz , for different dimensions	86
Table II. 4. The electrical and magnetic parameters of each square micro-coil at 300 MHz , for different dimensions	87
Table II. 5. Geometric parameters with the limiting diameter for the feasibility.....	89
Table II. 6. Geometrical configurations to be manufactured, $n = 4$ and $t = 40 \mu m$	89
Table II. 7. The physical properties of the substrate material used for our simulations, at room temperature.....	91
Table II. 8. Magnetic field z component as a function of microprobe perpendicular direction (Oz).....	96

Table III. 1. The electrical parameters (RLC) from different parts and according to their dimensions.....	110
Table III. 2. The RLQ parameters from different models of microprobe, performed at 300MHz, although 500MHz	114
Table III. 3. The RLQ electrical parameters from the best model of micro-probe, all of them tuned at 300 MHz and 500 MHz	117
Table III. 4. List of the algorithms and models performance obtained during the testing of algorithms.....	142
Table III. 5. The performance from different ANN architecture for three target cases	148
Table IV. 1. The microprobe geometry, dimensions and characteristics: <i>wire-bonding</i>	152
Table IV. 2. The microprobe geometry, dimensions and characteristics: <i>underpass & vias and airbridge</i>	152
Table IV. 3. The measurement of RLQ parameters of microprobe on 300 MHz (1 st trial of microfabrication).....	167
Table IV. 4. Fundamental parameters of the photolithography process optimization	169
Table IV. 5. Photoresist planting (AZ 125 NXT – 10A).....	169
Table IV. 6. Standards parameters specifications of AZ 125 NXT – 10A photoresist.....	170
Table IV. 7. Parameters of the Oxygen plasma section to clean up the wafer before the copper electroplating	170
Table IV. 8. The setting parameters for the electroplating of the copper layer.....	171
Table (IV. 9.1 to IV. 9.7) show the measurements of the cooper thickness from different areas of the wafer (microprobe n° 1 to n° 7).	176
Table IV. 11. The measurement of the microprobes RL parameters at 300 MHz and 500 MHz	181
Table IV. 12. The measurement of the microprobes RL parameters at 300 MHz and 500 MHz	181

Abstract

Keywords: NMR micro-antenna, Micro-probe, Sensitivity processing, Artificial Neural Network (ANN), NMR Spectroscopy, Alzheimer Disease, Biomarkers, Micromanufacturing.

Alzheimer disease (AD) is one of the most frequent neurodegenerative diseases in older people. According to the latest world AD report, nearly 55 million people live with this dementia. AD results from the progression of two brain injuries: Abnormal accumulation of proteins called peptide β amyloid (senile plaques) and tau proteins (neurons degeneration). However, AD progressive evolution can be detected 20 years before the onset of dementia symptoms (prodromic phase), by certain functional and metabolic markers. Unfortunately, AD is still facing a late diagnosis. NMR spectroscopy (MRS) appears to be a good candidate for AD biomarkers assessment due to its ability to quantify cerebral metabolites concentration in a very precise area of interest (ROI). Unfortunately, the NMR main disadvantage is its sensitivity. Several works from the literature report some approaches to improve this sensitivity. In this thesis work, our strategy is to improve the NMR receiver (RF antenna) in terms of Signal to Noise Ratio (*SNR*). As known, the *SNR* is related to the two main parameters that can be enhanced; on the one hand, the magnetic field B_1 by adapting the micro-probe size to the sample, and on the other hand, the equivalent Resistance R which can be minimized. In addition, we can also improve the antenna microfabrication process.

For this study, we have named NMR micro-antenna, the micro-probe associated with its matching and tuning circuit. The micro-probe is the micro-coil part associated with a micro-Transmission Line (TL) and the different connecting types. Usually, the micro-probe manufacturing task is time-consuming and expensive if we have to explore all prototypes dimensions and compare them experimentally. So, simulation makes possible the examination of different scenarios without experiments to then select the main parameters for the required performances. It can also provide meaningful data trends and guide the manufacturing process of the micro-device. In this work, we propose a new approach to optimize an implantable NMR micro-probe. We developed a platform (3D-TLE: Transmission Line Extractor) associated with Advanced Design System (ADS) software to extract the *RLC* parameters of the micro-probe design. Thus, we obtained a complete electrical circuit to model any micro-probe shape using any type of substrate. The simulations were carried out for four types of micro-coil (square, circular, rectangular and ellipsoidal), with two types of substrates (glass and silicon respectively), at the frequency range of 200 MHz to 900 MHz. In the case of rectangular micro-coil ($1000 \times 500 \mu m^2$), the global resistive loss was around $R = (3.897 \pm 0.193) \Omega$, taking into the account the contribution of the different parts of the micro-probe. Furthermore, we also developed an AI model, in particular an Artificial Neural Network (ANN), which we trained with the dataset generated by micro-probe simulations (6621 observations). Our trained ANN predicted the micro-probe *Q* factor with an accuracy of 99.67 % (*RMSE* = 0.032), and the Resistance with an accuracy of 91.34 % (*RMSE* = 0.042).

Based on previous results, we fabricated the different micro-probe prototypes on a glass and silicon substrate. Thanks to the also optimized fabrication process, we reached very small micro-coil dimensions up to $250 \times 250 \mu m^2$, never achieved before. Our work shows that we can accurately design and fabricate any optimal micro-probe or probe through the required performances, working frequency and substrate type with less computing time (2 minutes instead of more than 15 hours). Thus, this new optimization approach using AI tools combined with simulation tools (multi-parameter optimization work) implies a breakthrough in biomedical research towards NMR micro-detector used for brain exploration, early diagnosis, and treatment follow up.

Résumé

Mots-clefs : Micro-antenne RMN, Micro-sonde, Sensibilité, Réseau Neuronal Artificiel, Spectroscopie RMN, Maladie d'Alzheimer, Biomarqueurs, Microfabrication.

La maladie d'Alzheimer (MA) est l'une des maladies neurodégénératives les plus fréquentes chez les personnes âgées. Selon le dernier rapport mondial sur la MA, près de 55 millions de personnes vivent avec cette démence. La MA résulte de la progression de deux principales lésions cérébrales : L'accumulation anormale de protéines appelées peptide β amyloïde (plaques séniles) et de protéines tau (dégénérescence des neurones). Cependant, l'évolution progressive de la MA peut être détectée jusqu'à 20 ans avant l'apparition des symptômes de démence (phase prodromique), par le biais de certains marqueurs fonctionnels et/ou métaboliques. Malheureusement, le diagnostic formel de la MA ne peut être obtenu que par autopsie du cerveau post-mortem. La Spectroscopie RMN (SRM) semble être un bon candidat pour l'évaluation des biomarqueurs de la MA en raison de sa capacité à quantifier la concentration des métabolites cérébraux dans une zone d'intérêt (ROI) très précise. Cependant, le principal inconvénient de la RMN est sa sensibilité. Plusieurs approches d'amélioration de cette sensibilité ont été proposées dans la littérature. Dans ce travail de thèse, notre stratégie consiste à améliorer le récepteur RMN (antenne RF) en termes de rapport signal sur bruit (*SNR*). Comme on le sait, le *SNR* est lié à deux principaux paramètres qui peuvent être améliorés : d'une part, le champ magnétique B_1 en adaptant la taille de la micro-sonde à celle de l'échantillon, et d'autre part, la résistance équivalente R de l'antenne qui peut être minimisée. Par ailleurs, nous pouvons également apporter un soin particulier au processus de microfabrication des antennes.

Pour cette étude, nous avons appelé micro-antenne RMN, la micro-sonde associée à son circuit d'adaptation et d'accord. La micro-sonde est la partie de la micro-bobine associée à la micro-ligne de transmission (TL) et aux différents types de connectiques. En général, la fabrication de la micro-sonde est longue et coûteuse, quand il s'agit d'explorer plusieurs prototypes de dimensions et matériaux différents et les comparer expérimentalement. La simulation permet d'en affranchir et examiner tous les scénarios possibles sans expérimentations, puis de sélectionner les principaux paramètres pour obtenir les performances requises. Elle peut également fournir des tendances de données significatives et guider le processus de fabrication. Dans ce travail, nous avons proposé une nouvelle approche pour optimiser une micro-sonde RMN implantable. Nous avons développé une plateforme (3D-TLE : Transmission Line Extractor) associée au logiciel Advanced Design System (ADS) pour extraire les paramètres *RLC* de la micro-sonde. Nous avons ainsi proposé un circuit électrique complet permettant de modéliser n'importe quelle forme de micro-sonde et son type de substrat. Nous avons effectué des simulations pour quatre types de micro-bobine (carrée, circulaire, rectangulaire et ellipsoïdale), avec deux types de substrat (verre et silicium), dans une gamme de fréquences de 200 MHz à 900 MHz. Dans le cas de la micro-bobine rectangulaire ($1000 \times 500 \mu m^2$), la perte résistive globale, en tenant compte la contribution des différentes parties de la micro-sonde a été estimée à $R = (3,897 \pm 0,193) \Omega$. En outre, nous avons également développé un modèle d'IA, en particulier un réseau neuronal artificiel (RNA), que nous avons entraîné avec le jeu de données généré à partir des simulations réalisées au préalable (6621 observations). Notre RNA a pu prédire le facteur *Q* de la micro-sonde avec une précision de 99,67 % (*RMSE* = 0,032), et la Résistance avec une précision de 91,34 % (*RMSE* = 0,042).

En se basant sur ces résultats, nous avons fabriqué les différents prototypes de micro-sondes sur substrat de verre et de silicium. Grâce à l'optimisation du processus de fabrication, nous avons pu fabriquer des micro-bobines de très petites dimensions de l'ordre de $250 \times 250 \mu m^2$, dimensions jamais atteintes auparavant.

Notre travail montre qu'à l'avenir nous pourrions concevoir et fabriquer avec précision n'importe quel type de micro-sonde ou sonde optimisée en fonction des performances souhaitées, de la fréquence de travail et du type de substrat. Cela avec un temps de calcul de 2 minutes au lieu de 15 heures. Ainsi, cette nouvelle approche d'optimisation utilisant des outils d'IA combinés à des outils de simulation (travail d'optimisation multi-paramétriques) implique un progrès dans la recherche biomédicale basée sur le développement de micro-capteurs RMN utilisés pour l'exploration du cerveau, le diagnostic précoce et le suivi du traitement.

Introduction

Alzheimer disease (AD) is one of the most frequent neurodegenerative diseases in older people. According to the latest world AD report, nearly 55 million people live with this dementia [1]. AD results from the progression of two brain injuries: Abnormal accumulation of proteins called peptide β amyloid (senile plaques) and tau proteins (neurons degeneration). However, AD progressive evolution can be detected 20 years before the onset of dementia symptoms (prodromic phase) by certain functional and metabolic markers [2]. Unfortunately, AD is still facing a late diagnosis.

For our study, we chose the NMR Spectroscopy (MRS) technique to follow the evolution of biomarkers (brain metabolites) that can possibly be representative of AD, using an animal model (mouse or rat). Nuclear Magnetic Resonance (NMR) is a very powerful analytical method to identify chemical and biological samples. Over the last 20 years, it has become an essential tool for the diagnosis of diseases. MRS seems to be a good candidate for our research because of the technique's ability to quantify the concentration of certain metabolites in a very precise area of interest (ROI). Nevertheless, obtaining high resolution in vivo NMR spectra is a real methodological challenge. Unfortunately, the NMR main disadvantage is its sensitivity.

Several strategies have been proposed in the literature, to improve the NMR sensitivity:

1. Increasing the static field strength B_0 , as the NMR sensitivity in spectroscopy varies as $B_0^{\frac{7}{4}}$ [3]. Superconducting magnets with static fields from 4.7T (200 MHz) to 23.3T (1 GHz) are now used in "conventional" spectroscopy.
2. The improvement of the detection sensitivity by:
 - Improving the magnetic coupling between the antenna receiving the NMR signal and the sample by adapting the size of the sensor to that of the sample [4]. The filling factor is thus increased ($\eta \approx 1$) and consequently, the SNR is also increased and the measurement sensitivity will be improved, thanks to an optimal sensitivity of the RF sensor [5].
 - The reduction of thermal noise sources by cooling the NMR detection antenna.
3. Reduction of the linewidth: the rapid rotation of the sample around an axis at 54.7° from the field direction (Magic Angle Spinning) [6] has been used for a long time to reduce the dipole broadening in solid media [7].

4. The use of antenna arrays: here, we no longer play on physical factors, but on technical and instrumental elements since it is a question of superimposing the signals of independent sensors [8] [9].

In this thesis work, our strategy is to improve the NMR receiver (RF antenna) in terms of Signal to Noise Ratio (*SNR*). As known, the *SNR* is related to the two main parameters that can be enhanced; on the one hand, the magnetic field B_1 by adapting the micro-probe size to the sample, and on the other hand, the equivalent Resistance R which can be minimized. In addition, we can also improve the antenna microfabrication process.

For this study, we called NMR micro-antenna, the microprobe associated with its matching and tuning circuit. The microprobe is the part of the micro-coil associated with the micro-transmission line (TL) and the different types of connectors. The connecting wire allow linking the center of the micro-coil with the transmission line, and another one that will connect the transmission line with the tuning and adaptation circuit. Our implantable NMR microprobe (also called needle coil) should lead to an analysis tool that ensures high-resolution spectroscopic measurements reproducibility and encourages an *in vivo* application. More specifically, to monitor the variation of cerebral metabolic markers in small volume with low concentration by NMR spectroscopy using animal models (rat or mouse).

Our first approach performed *in vitro*, presented in the thesis of N. Baxan (2008) and A. Kadjo (2011), could not be achieved *in vivo* without a complementary work (design and simulations) for the optimization of the microprobe sensitivity (*SNR*). This is of crucial importance because the source signals are so small that they are comparable to thermal noise (sensitivity of the microprobe), which can be linked to its resistance. To overcome these resistive losses of the micro-antenna proposed by N. Baxan, and its connecting wire (*wire-bonding*), a new way have been proposed to connect the centre of the micro-coil with the micro-track (*Underpass & vias*) (thesis of J. Trejo Rosillo (2014)). Likewise, T. Cong Troung (2014) developed a method for optimizing NMR micro-coils using a physical approach. Despite these improvements, the quality factor remained low (e.g., $Q = 1.4$) and insufficient for the expected *in vivo* applications.

We aim to develop an NMR implantable microprobe, leading to an accurate analysis of metabolites biomarkers for *in vivo* applications (in particular, early diagnosis of Alzheimer's disease). Therefore, the objective of my thesis is to propose a new approach to optimize an implantable, biocompatible NMR microprobe specially designed for the target application which requires a high resolution and highest sensitivity.

In the following of my thesis document, I have divided my work in four chapters:

Chapter 1 presents the general context of the project (an introductory part to Alzheimer disease earlier diagnostic), the problematic and the thesis objectives. We briefly introduced the main NMR principles, the NMR signal detection, the state-of-the-art of NMR planar antennas, and the micro-antennas, the definition of microprobe performance parameters, and then we finalized this chapter with a review from previous work carried out by our team, based on the optimization of such microprobes and its prospect for *in vivo* applications.

In chapter 2, we presented the numerical modelling of the microprobe in terms of the magnetic field and resistive losses calculations through commercial software such as COMSOL Multiphysics, Computational Simulation Technology Microwave Studio (CST MWS) for Electromagnetic (EM) simulation and MATLAB *script* developed for RLC (Resistance – Inductance – Capacitance) calculations. We compared our results with the previous works done by our team.

In chapter 3, a new method to model the microprobe in terms of resistive loss was proposed through an original electrical model. We have introduced a new platform for electrical parameters extraction (3D-TLE: Transmission Line Extractor). We have demonstrated the possibility of designing a high-performance microprobe thanks to an Artificial Neural Network (ANN) model, trained using our dataset set from simulation works.

Finally, **in chapter 4**, we presented the main steps of microprobe fabrication and the manufacturing process optimization for our prototype. Some results of the microprobe prototypes fabricated on glass and silicon substrate were reported and their characterization (morphological and electrical). The microprobe layout was designed with *underpass & vias*, *wire bonding & vias*, and *air-bridge* connecting wire, so we fabricated them and validated their performances according to our simulation work and analytical calculations.

Chapter I

Alzheimer Disease (AD) and Nuclear Magnetic Resonance Spectroscopy (MRS): Overview

This chapter aims to present an overview of the project thesis; we begin by introducing Alzheimer's disease, the markers and diagnosis methods, and the present study hypothesis for earlier detection of AD biomarkers. We also report a brief introduction to the NMR principle and its sensitivity.

We report the antenna criteria of performance, the state-of-the-art of planar NMR antennas. We reviewed the work about the NMR micro-antenna optimization previously performed by our team to enhance its performances in terms of SNR and Q factor, for *in vivo* applications. Moreover, according to our team previous results, we presented the *In vivo* implanting pertinence for Magnetic Resonance Spectroscopy (MRS), representing a crucial starting point (hypothesis) for this project.

I.1. Alzheimer Disease (AD)

I.1.1. Introduction of AD as a public health issue

Alzheimer disease (AD) is one of the most frequent neurodegenerative diseases for older people. According to the latest world AD reporting, almost 55 million people live with this dementia [1]. In France, more than 1 million people suffer from AD dementia, and it occurs before the age of 65. Memory loss is often the first symptom of AD that helps orient the diagnosis; therefore, the late diagnosis is a public health concern.

This neurodegenerative disease results in the progression of two brain injuries: Abnormal accumulation of proteins called peptide β amyloids (senile plaques) and tau protein (neurons degeneration). Therefore, the disease's progressive evolution can be detected 20 years before the dementia symptoms (prodromic phase) appear. Note that biomarkers reflecting the state of the disease can be biochemical or anatomical.

The major goal of current clinical research in AD is to improve early detection and presymptomatic detection of neuron dysfunction [10]. So, the AD research field is very active, and several treatments test are currently underway. Trials aimed at cleaning the main lesions observed in the brains of people with AD (the amyloid plaques) have been set up, with an unsuccessful result so far. No improvement in symptoms has been observed even though the amount of plaques is decreasing. A possible reason for this failure is that the patients who participated in the trial were too advanced in their disease. Today, more and more prevention trials are underway in which these plaques are targeted at very early stages of the disease when symptoms are very mild or even non-existent [11].

The AD origin and its progression are not yet very well understood. An earlier diagnosis should help understand this pathology and lead to an implementation of necessary active pharmacological treatments to slow down the disease, if possible, in its earlier stage.

I.1.2. AD markers and diagnosis methods

Since 2007, several organizations have proposed some AD criteria for diagnosis. Some propose to integrate the imaging technique such as neuroimaging biomarkers (MRI – Magnetic Resonance Imaging, PET scan – Positron Emission Tomography) and CSF markers (Cerebral Spinal Fluid) analysis rather make diagnosis founded on the cognitive tests. Then biomarkers were included as diagnostic criteria for AD, such as Amyloid β and abnormal Tau protein. All these-criteria are not yet ready to be used as AD biomarkers in the clinical routines; nonetheless, it represents a crucial asset for the research progress [12].

AD is a progressive disease, but the clinical impacts are provided too late on the dementia stage of the disease; As illustrated in Fig.I.1 AD occur up to 20 years before the onset of dimension symptoms through certain markers such as amyloid β , functional and metabolic markers, atrophy from whole brain, hippocampe, Entorhinal cortex and temporal neocortex. We can note their evolution in different regions of AD stage, particularly in Mild Cognitive Impairment (MCI) where we can distinguish a high evolution of these markers.

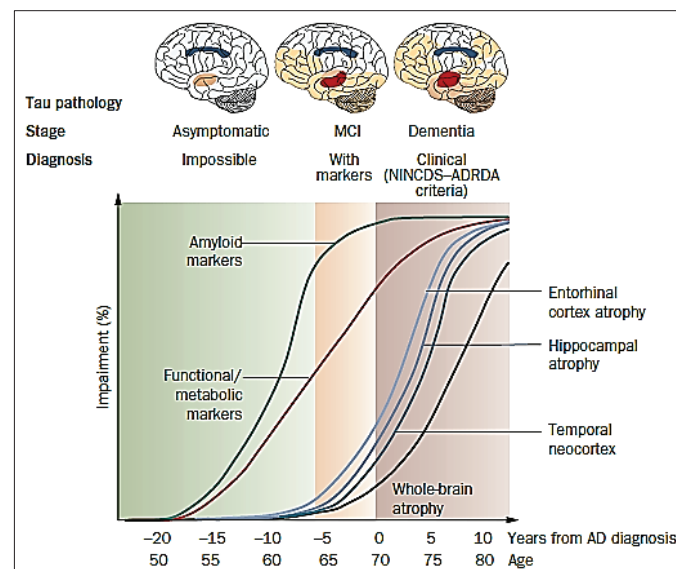


Fig. I. 1. The representation of natural progression of biological markers of AD [2]

A very common approach used by the scientific community is the MCI as a prodromal phase, defined as a traditional stage between normal ageing and dementia, and grouping together subjects suffering from mild cognitive disorders. Subjects with these characteristics have a higher risk of developing AD later [13]. Therefore, in Fig. I. 1, we have a theoretical model of the natural progression of cognitive and biological markers of AD. So, we can highlight two points: Some markers are sensitive to disease in MCI and useful for early

diagnosis and others to disease progression (dementia state) to surrogate markers in a clinical trial.

AD is characterized by an accumulation of amyloid β peptides and some transformation in the cerebral region through the structural abnormal tau protein; these transformations in the long-term causes hypometabolism and cortical atrophy. Cortical atrophy represents a morphological biomarker; its variation is mainly detected in the dementia stage, although amyloid β and tau protein markers have the advantage of occurring earlier than any metabolic, structural and obviously before clinical changes. So, the biomarkers aim to provide quantitative information about the metabolites (molecular) and morphological changes occurring in the subject's brain during these transformations.

There are several tools and methods available to measure the Alzheimer disease markers, such as:

- **Amyloid Positron Emission Tomography (PET):** This imaging technique quantifies amyloid plaque deposition in the brain. From the literature, there are several studies of deposit of amyloid β to measure the AD progression with PET technique [14] [15] [16]. A study to predict and relate the possibility of a patient in MCI that will be in AD dementia stage. The study was performed under 19 months of monitoring, with a sensitivity of 96 % and achieved specificity 42 % [17].
- **Fluorodeoxyglucose (FDG) Positron Emission Tomography (PET):** This PET modality allows mapping cerebral hypometabolism due to pathological neuronal loss. The results reporting the performance of this technique varies very often according to the application, but most recent work has reported the capacity of the FDG PET technique to predict. They had a sensitivity variation from 56 % to 100 %, with a specificity of 24 % to 100 % [18].
- **Cerebral Spinal Fluid (CSF):** Analysis of CSF collected by lumbar puncture allows quantification of the concentration of amyloid-beta peptides $A\beta_{40}$ and $A\beta_{42}$ and of the Tau protein, these concentrations being respectively lower and higher in patients with AD. The best performance achieved with this technique for six months of study is a sensitivity of 81 % for predicting the AD conversion [19].
- **Magnetic Resonance Imaging (MRI):** This structural imaging technique aims to measure focal brain atrophy due to pathological neuronal loss. A Structural MRI study carried out on six months was performed with 81% accuracy for the AD conversion prediction [20]. Others confirm with a similar precision of about 75 % [21].

As we can see in the previous paragraph, the field of neuroimaging markers has made revolutionary advances, and we have different neuroimaging modalities being applied to AD detection. Moreover, the authors are interested in combining different markers and test neuroimaging techniques to predict the possibility of AD conversion in the MCI area. However, neuroimaging is expensive and technically challenging [22].

I.1.3. The objectives of the presents study and hypothesis

Despite the efforts to diagnose AD thanks to neuroimaging techniques (structural, functional and molecular) by monitoring hippocampus inflammation (atrophy) using functional or structural Magnetic Resonance Imaging (MRI) [23] [24], cerebrospinal fluid biomarkers [25] or monitoring blood biomarkers [26], but the AD is still facing a late diagnosis. Note that some of these methods do not provide reproducible information [27].

Magnetic Resonance Imaging (MRI) and Magnetic Resonance Spectroscopy (MRS) techniques are based on the same physical principle (section I.2); MRS consists of NMR (nuclear magnetic resonance) peaks representing different brain metabolites. MRI produces images based on proton signals from water content in the brain tissue, whereas MRS reports the chemical shift in the nuclei in a given region of interest (ROI) of the brain. In MRS, a small volume of tissue (a voxel) is selectively excited in a magnetic field, and the free induction decay (FID) is recorded to produce an MR spectrum [22].

For our study, we have to monitor the AD evolution in the dementia stage of the disease through an animal model. MRS seems to be a good candidate for our research due to the technique's ability to quantify certain metabolites concentrations in a very precise area of interest. So, in the following figure (Fig. I. 2), we have the spectrum of rat cerebral metabolites.

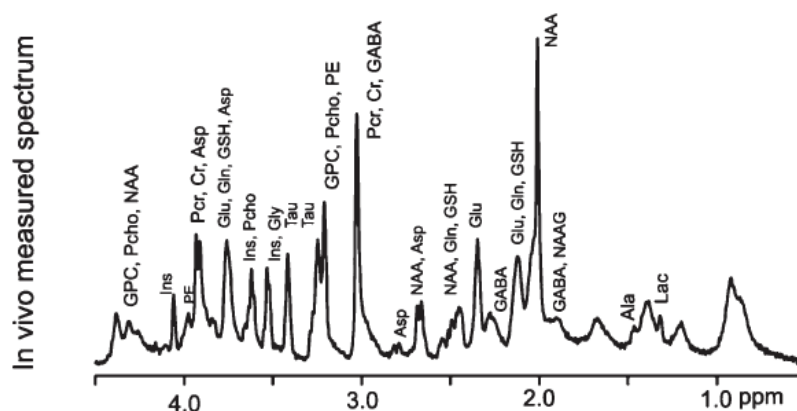


Fig. I. 2. The spectrum of cerebral metabolites of the rat [28]

The area under each NMR peak corresponds to the concentration of that particular metabolite. Differences in the peak area of metabolites in the rat brain provide a measure of the level of neurochemical processing, which is reflective of the pathophysiologic state. Moreover, the cerebral metabolites and also their concentration in the specific ROI are very well known [29] [28]. The point is to quantify the concentration of these metabolites and lead to a possibility of monitoring their variation, distinguishing the abnormal changes corresponding to neurodegenerative diseases such as Alzheimer's disease.

Paul Francis and co-workers examined the original cholinergic hypothesis of AD in a review [30]. Their study describes the biochemical changes of neurotransmitter markers occurring in the patient's brain with AD. Although, several studies focused on neurodegenerative diseases that result in disruptions of the cholinergic innervation network. Cholinergic system deficiency is found mainly in patients with Alzheimer's disease [30] [31], with neocortical electroencephalogram (EEG) activity [32], Parkinson [33] and with epilepsy [34].

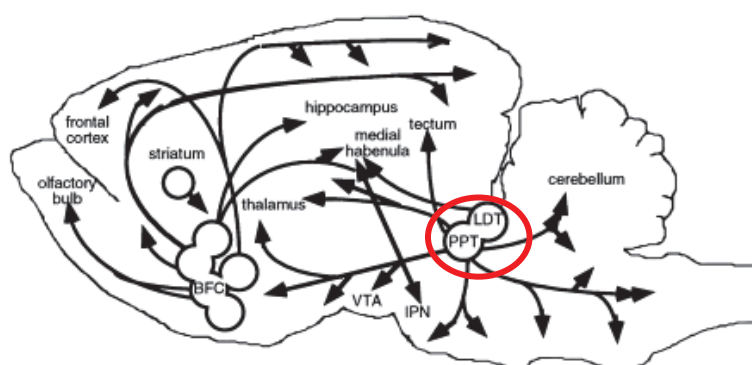


Fig. I. 3. Anatomy of the main cholinergic pathways in the rat brain [35].

The anatomy of the main cholinergic pathways in the brain of a small animal, such as a rat, is shown in Fig. I. 3. It has been highlighted that a significant number of brain nuclei are at the origin of cholinergic innervation. More specifically, there are two areas, the Latero Dorsal Tegmental (LDT) nucleus and the Pedunculo Pontine Tegmental (PPT), where this cholinergic innervation can be specifically targeted. The main source of the cholinergic influx of the cortex and hippocampus is the Basal Prosencephalon (BFC). At the same time, the LDT and PPT areas mainly innervate the brain stem and Mesencephalon (middle brain) [35].

Therefore, it is fundamental to investigate the LDT region by NMR spectroscopy. This should allow monitoring the evolution of the metabolic concentration of neurodegenerative diseases and lead to early diagnosis the AD. This area is about 9 *mm* deep from the skull and occupies a volume of about $1.3 \times 1.2 \times 1 \text{ mm}^3$. In terms of NMR spectroscopy, this volume region is about 2 μL representing our ROI [36].

However, detecting the brain metabolites in the areas of a small volume in the order of about $2\mu L$ in LDT & PPT tissues is a significant challenge for the MRS technique.

I.2. NMR spectroscopy

I.2.1. Principle of the NMR

Nuclear Magnetic Resonance spectroscopy (MRS) is one of the most common analytical methods used to detect analytes with a low concentration. This technique makes it possible to obtain exact information on a sample with a small volume. That can be done by using localized NMR spectroscopy, which improves the technique's performance for low concentrations.

NMR technique consists of analysing the variation of the nuclei magnetization from a substance under the action of two applied fields: The static magnetic field B_0 and the RadioFrequency (RF) field B_1 .

The atomic nuclei are composed of protons and neutrons (nucleons). Each of both has a spin which we represent by a spin angular momentum, and we associate with the magnetization vector:

$$\mu = \gamma_s \hbar \sqrt{s(s+1)} \quad (I.1)$$

With: $\hbar = 1.055 \times 10^{-34}$ (SI) being the normalized Planck's constant and γ_s the gyromagnetic ratio.

The quantum spin number takes the following values: $s = 0, \frac{1}{2}, 1, \frac{3}{2}, 2, \frac{5}{2}, \dots$. We can define a nuclei magnetic quantum number m_s allowing to determine the orientation of an orbital. The quantified quantum number m_s can take the value within the interval $-s < m_s < +s$.

For example, nuclei having the spin number $s = \frac{1}{2}$, we have two possible spin states: Spin up $|\uparrow\rangle$ and spin down $|\downarrow\rangle$ ($m_s = \frac{1}{2}$ and $m_s = -\frac{1}{2}$). Hence, in the equilibrium state, the two states have the same energy, and the overage sum of the magnetic momentum of each atom is equal to zero. These possible states are crucial to define the energy of an atom or molecule subjected to a static magnetic field, as we will see in the following section.

I.2.2. The effect of the static magnetic field B_0

When atoms are under a static magnetic field B_0 following the axes Oz (Fig.I.5), we can calculate the magnetic potential energy by the following formula:

$$E_{ms} = \epsilon - \gamma_s \hbar m_s B_0 \quad (I.2)$$

Where:

E_{ms} represent the Zeeman energy and ϵ is the ground states energy of the atom or molecule.

The previous energy equation designates the separation of an atomic level of defined energy for an atom or a molecule into several sublevels of distinct energies under an external magnetic field. The nuclear particles will randomly align parallel or anti-parallel (Fig. I.4). When nuclei with the spin number different from zero are subject to a static magnetic field, the ground states of angular momentum of spin present a degeneration survey (Zeeman Effect).

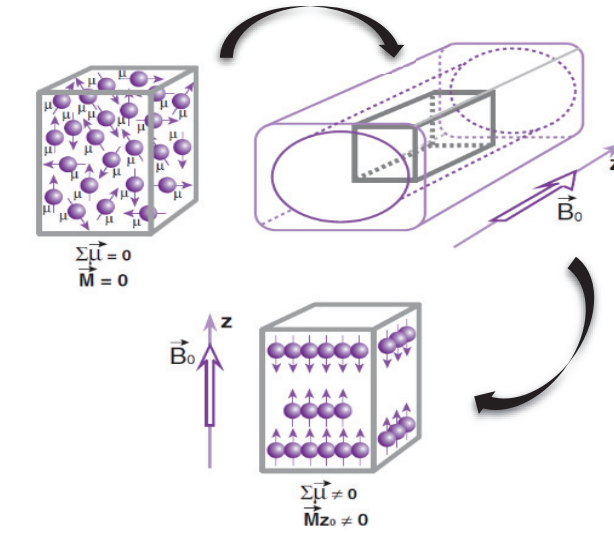


Fig. I. 4. Magnetic atomic nuclei behaviour, before and after setting it into the magnetic field

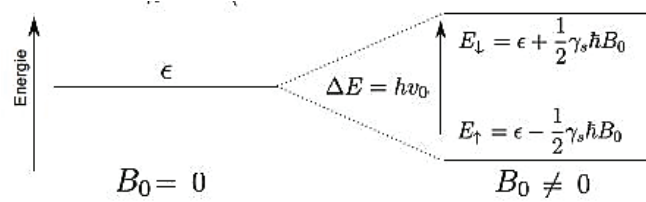


Fig. I. 5. Energy diagram describing the distribution of the nucleon quantum stats at two different energy levels, before and after setting into the static magnetic field B_0 [37]

Meanwhile, we have deduced, from Fig. I. 5:

$$\Delta E = \gamma_s \hbar B_0 \quad (I.3)$$

According to the electromagnetic principle, we know that, $\Delta E = \hbar \omega_0$;

So, we deduce:

$$\omega_0 = \gamma_s B_0 \quad (\text{I.4})$$

The equation (I.4) by a classical approach is associated with the Larmor frequency. Thus, some values of the gyromagnetic ratio for attractive atomic nuclei are given in Table I.1.

Atomic nuclei	^1H	^{13}C	^{19}F	^{31}P	^{23}Na
Spin	$\frac{1}{2}$	$\frac{1}{2}$	$\frac{1}{2}$	$\frac{1}{2}$	$\frac{3}{2}$
γ_s (MHz/T)	42.58	10.71	40.05	17.24	11.26

Table I. 1. Value of gyromagnetic ratios of specific atomic nuclei of interest

For our application, we are effectively interested in the ^1H Proton, a nucleus that is naturally about 99.98% abundant and mainly present in brain tissue. According to the Fermi distribution, applicable to a particle with a half odd integer spin [38], the spins per volume concentration n of an energetic state as a function of the probability P and the total number of spins per volume N_s is :

$$n = N_s P = \frac{1}{e^{\frac{\epsilon}{k_B T}} e^{\frac{-\gamma_s \hbar m_s B_0}{k_B T}} + 1} \quad (\text{I.5})$$

Moreover, according to Bloembergen [39], the ratio of Boltzman distributions is a good approximation of the ratio of the concentration of the two equilibrium states is:

$$\frac{n_{\downarrow}^0}{n_{\uparrow}^0} = \frac{N_s P_{\downarrow}^0}{N_s P_{\uparrow}^0} = e^{-\frac{\Delta E}{k_B T}} = e^{\frac{-\gamma_s \hbar B_0}{k_B T}} \quad (\text{I.6})$$

The ratio $\frac{-\gamma_s \hbar B_0}{k_B T} \approx 6.81 \times 10^{-6}$, if the previous ratio is $\epsilon_s \approx 0$ we can make a Tylor second-order series approximation of equation (I.6) as follows:

$$\frac{N_s P_{\downarrow}^0}{N_s P_{\uparrow}^0} \cong 1 - \frac{\gamma_s \hbar B_0}{k_B T} = 1 - \epsilon_s B_0 \quad (\text{I.7})$$

Besides, the summation of both energy state probability must be one ($P_{\downarrow}^0 + P_{\uparrow}^0 = 1$), then we might deduce:

$$\frac{1 - P_{\uparrow}^0}{P_{\downarrow}^0} \approx 1 - \epsilon_s B_0 \quad (\text{I.8})$$

With:

$$P_{\downarrow}^0 = \frac{1}{2 + \epsilon_s B_0} \quad (\text{I.9})$$

$$P_{\uparrow}^0 = \frac{1}{2 - \varepsilon_s B_0} \quad (\text{I.10})$$

Note that the difference between equation (I.9) and (I.10) is given as follows:

$$P_{\uparrow}^0 - P_{\downarrow}^0 = \frac{1}{2} \varepsilon_s B_0 \quad (\text{I.11})$$

From equation (I.11), we have defined the difference between both energetic states (level). Thus, in terms of concentration is defined in the following equation:

$$\Delta n = N_s (P_{\uparrow}^0 - P_{\downarrow}^0) = \frac{1}{2} N_s \frac{\gamma_s \hbar B_0}{k_B T} \quad (\text{I.12})$$

These few differences between both energetic states justify the source of the Magnetization per volume vector M_0 [40] [41] as the defined equation :

$$M_0 = \frac{1}{3} N_s \frac{\gamma_s^2 \hbar^2 s(s+1) B_0}{k_B T} \quad (\text{I.13})$$

The number of spins per volume unit N_s is denied by the molecular concentration C_i (*mol/kg*) the number of Avogadro N_A and the number of nuclei participating in magnetic resonance into the molecule n_{NMR} , weighted by the average percentage of the resonant isotropic P_{avg} . This percentage is representative of the abundance of the resonant isotope relative to the stable element [42].

$$N_s = n_{NMR} \times \frac{P_{avg}}{100} C_i N_A \quad (\text{I.14})$$

Through the magnetization vector, we can measure NMR signals. We can also see that M_0 is directly proportional to the intensity B_0 and the magnitude ε_s . The signal is minimal (weak); that's why the NMR experiments require strong static magnetic fields, especially when analysing small samples.

I.2.3. The Radiofrequency (RF) magnetic field

To measure the Magnetization of a sample on the B_0 axis (oz), a transversal direction generally is required to apply an RF pulse. That signal corresponds to an RF magnetic field B_1 which is applied in a perpendicular axis's direction, compared to the B_0 the magnetic field axis. Therefore, the RF pulse causes the magnetization vector to tilt from its equilibrium position to a direction predefined by the chosen NMR sequence. The pulse sequence is transmitted using a planar or volumetric NMR antenna, depending on the application.

Two types of RF pulse are frequently used to switch the magnetization into a suitable plan for NMR measurements of the signal:

- 90° – RF Pulse switches the Magnetization from its equilibrium direction to the transverse plane.
- 180° – RF Pulse shifts the Magnetization from its equilibrium position to an anti-parallel direction.

We can demonstrate by quantum mechanics theories; there is a transition of protons from a low energy level to a higher level (parallel protons are oriented in anti-parallel) when we apply an RF pulse. It occurred when the RF pulse achieved the same frequency as the *Lamor frequency* (equation (I.4)). It means that the system attends to the resonance condition $\omega_1 = \omega_0$.

Relaxation is the phenomenon that makes possible the proton analysis, so there exist two types of relaxation.

- Relaxation T_1 (longitudinal): Magnetization returns to the equilibrium position (spin-network).
- Relaxation T_2 (transversal): Magnetization returns out the ions of states in phase (spin-spin).

I.2.4. The detection of signals

The NMR signal can be detected using an RF receptor antenna after the sample \vec{B}_1 excitation. The sample (atomic nuclei) magnetization \vec{M} get precession around the static magnetic field \vec{B}_0 axis (generally oz) having an angular velocity as defined in equation (I.4).

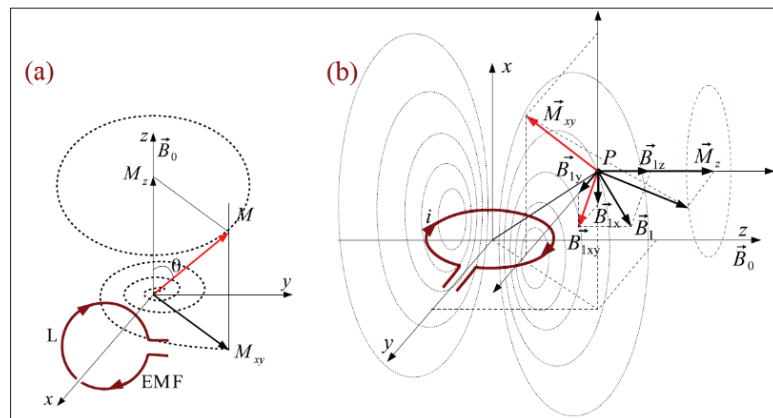


Fig. I. 6. The principle of emission and reception of FID signal. a) The rotating of magnetization \vec{M} induces a Electromotive Force (EMF) into the S loop; b) The signal at point P is proportional to the magnetic field \vec{B}_1 [43]

Figure I.6 illustrates the NMR signal Free Induction Decay (FID) principle for a coil section S [43]. The variable magnetization \vec{M} , around an axis, can produce an alternating magnetic field in the S section of a conductor coil. Assuming that the cross-sectional S of the coil through which the current i travers, the coil can generate a magnetic field \vec{B}_1 at the point P (Fig. I. 6.

a)). There is a direct interaction between the Electromagnetic Force (EMF) induced in the S section by a rotating magnetic moment element MdV in the sample volume V at point P ; meanwhile, the field \vec{B}_1 at the same point P produced by the current i in the S section [44]; consequently, EMF can be calculated as follows:

$$\delta\xi(t) = -\frac{\partial}{\partial t}(\vec{B}_1 \vec{M}(t))dv \quad (\text{I.15})$$

Where:

$\delta\xi(t)$ is the electromotive force induced into the turn S by an elementary volume dv , \vec{B}_1 is the magnetic field created in S section by the current i .

To calculate the signal induced by the whole sample, we have to integrate the equation (I.15) into the complete volume V , which correspond to the examined volume:

$$\xi(t) = -\iiint \frac{\partial}{\partial t}(\vec{B}_1 \vec{M}(t))dv \quad (\text{I.16})$$

Electromagnetic Field (EMF) signal can be calculated as the following equation (I.17), by Solving the equation (I.16), considering that i is an alternative sinusoidal signal and $\vec{M}(t)$ Magnetization.

The macroscopic magnetization \vec{M} under a static magnetic field, B_0 varies over time according to a law given by the Bloch equation:

$$\frac{\partial \vec{M}(t)}{\partial t} = \gamma_s \vec{M} \left(B_0 + \frac{\omega_0}{\gamma_s} \right) \vec{e}_z - \frac{M_z - M_0}{T_1} \vec{e}_z - \frac{M_x \vec{e}_x + M_y \vec{e}_y}{T_2} \quad (\text{I.16.1})$$

More details of the calculation of the $\xi(t)$, even how to define $\vec{M}(t)$ which corresponds to the macroscopic magnetization after the RF impulsion is applied, are given in [44] [4].

$$\xi(t) = S_0 e^{-\frac{t}{T_2^*}} \sin(\omega_0 t) \quad (\text{I.17})$$

With:

$$S_0 = \frac{B_1}{i} \omega_0 M_0 V_s \quad (\text{I.17.1})$$

\vec{e}_z , \vec{e}_x , \vec{e}_y are representing the unitary vectors for the $Oxyz$ reference plane. T_1 , T_2 are the longitudinal and transversal relaxation time. T_2^* is representing the true relaxation phenomena of T_2 , which we take into account the constant inherent inhomogeneity of the magnetic field B_0 [3].

$$\frac{1}{T_2^*} = \frac{1}{T_2} + \gamma_s \Delta B_0 \quad (\text{I.18})$$

There is an apparent decrease in FID because of the relaxation time T_2 and also to the B_0 field. The static magnetic field generally is never uniform at the microscopic scale, implying no synchronization of the elementary transverse magnetizations, which is faster than the relaxation due only to T_2 . Therefore, considering the inhomogeneity of the magnetic field B_0 , the true characteristic of relaxation time T_2 is represented by T_2^* called the true transverse relaxation time T_2 , as defined in the equation (I.17.2).

Generally, we name the NMR signal detected by an RF antenna; Free Induction Decay (FID) is a sinusoidal signal damped by an exponential signal as shown in Fig. I. 7.

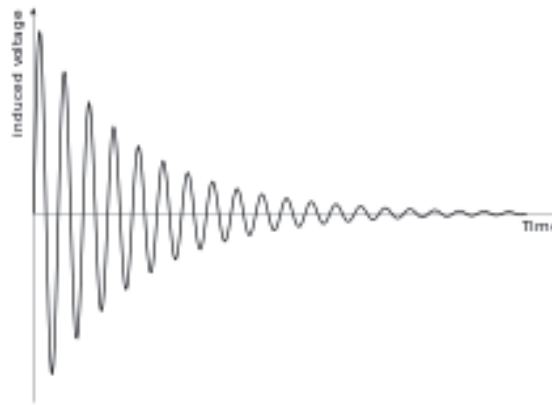


Fig. I. 7. The plot of $\zeta(t)$, detected NMR signal in the time domain, FID [43]

I.2.5. The NMR instrumentation

An MRI or MRS environment is defined by an NMR system that is composed largely of an intense static magnetic field B_0 , a variable RF magnetic field source B_1 , magnetic field gradient coils and antennas (transmitter and receiver). The functionality of the NMR instrument can be briefly described as follows: in the presence of the static magnetic field B_0 , the magnetic moments of the nuclei produce a nuclear paramagnetic polarization at equilibrium states. The application of the RF magnetic field B_1 , perpendicular to the constant magnetic field B_0 , generates a forced precession of the whole nuclei polarization around B_0 . This results in a component of the nuclear polarization, perpendicular to both the static magnetic field and the RF magnetic field B_1 , as it was recalled in the section.I.2.4 (chapter I), under standard laboratory conditions, this component can induce a measurable voltage signal (FID). This voltage is the NMR signal that the receiver antenna can then detect. This phenomenon will be followed by the progressive return of the magnetization to the equilibrium state.

Despite the technological progress of the NMR instrumentation, the main limitation of NMR technique is the sensitivity. So, several strategies to improve that sensitivity have been employed:

1. Increasing the static field B_0 , knowing that the NMR sensitivity varies as $B_0^{\frac{7}{4}}$ [3]. For Superconducting magnets with static fields starting with 4.7 T (200 MHz) up to 23.3 T (1 GHz) that are now used in "conventional" spectroscopy.
2. The improvement of the detection sensitivity by:
 - Improving the magnetic coupling between the antenna receiving the NMR signal and the sample by reducing the size of the sensor [4]. The filling factor is thus increased, and consequently, the signal to noise ratio (SNR) of the receiver increase and the antenna will optimize the measurement sensitivity.
 - Reduction of thermal noise sources by cooling the NMR detection antenna [5].
3. Reduction of the width of spectrum ray: the rapid rotation of the sample around an axis at 54.7 ° from the magnetic field direction (Magic Angle Spinning) [6] has long been used to reduce dipolar broadening in a solid environment. This technique has recently been developed for the analysis of tissue samples [7].
4. The use of capillary tubes for the analysis of very small solution quantities - devices proposed by manufacturers or suppliers of accessories. Recently it was used for a quantitative evaluation of NMR spectrometer performance [45].
5. The use of an antenna array: here, we no longer play on physical factors but on technical and instrumental elements since it is a question of superimposing the signals of each sensor [8] [9].

For our case, we focused on the approach which consists of enhancing the sensitivity of the RF receiver coil. According to Sweedler [46], reducing the antenna size, to adapt with the sample size should allow a considerable increase in insensitivity. Thus, the NMR detection idea was developed using microscopic devices and tools. This is how the notion of planar "microprobe" or "micro-coil" became popular. Its optimization has been a subject of several theses in our team. In this study, we focus mainly on the RF receiver part, particularly the microprobe. We discussed its review and sensitivity criteria in the following Section I.3.

I.3. NMR antennas and their criteria of performance

Our study mainly focuses on the planar antennas, which we will demonstrate to be suitable for analysing the small volume later in this work.

Note that the planar coil has several advantages, e.g., a high magnetic field close to the conductor wire surface, the possibility of its implantation, close to the sample (*in vivo* applications) and adapting its dimension to one of the samples, facility to microfabrication, comparing with the volumic antenna. Therefore, the planar described features represent a significant asset for NMR spectroscopy's small volume and concentrations detection.

I.3.1. Stat-of-the-art of the surface antennas

One of the first proton NMR spectroscopy studies using planar micro-antennas was carried out by Peck et al. [47]. He used a micro-coil with 4.5 spiral turns, a thickness of $2\text{ }\mu\text{m}$, an inner diameter of $97.5\text{ }\mu\text{m}$. It is a gold electroplated layer onto a GaAs (Arsenide Gallium) substrate. The antenna was suitable for NMR application, particularly in a static magnetic field of 7.05 T (300 MHz for the proton resonance frequency). Then, Stocker et al. [48] had analysed a volume of 880 pL , from which they could observe sucrose peaks. The planar micro-antenna with 3.5 turns, $60\text{ }\mu\text{m}$ inner diameter, $3\text{ }\mu\text{m}$ track thickness and also etched on a GaAs substrate, and they placed the sample above $50\text{ }\mu\text{m}$ from the micro-antenna. Their analysis of water in a 5.9 T field (250 MHz frequency) gave a Signal-to-Noise Ratio of about $SNR = 25$ per acquisition and a ray width less than 2 Hz . Therefore, by this study, they demonstrated the usefulness of planar antenna for high-resolution NMR spectroscopy experiments and how it may also be suitable for localized NMR studies [48].

The first planar micro-antenna integrated separately into a micro-fluid system for the spectroscopic study was performed by Trumbull et al. [49]. They analysed 30 nL of water sample within 5.9 T magnetic field (250 MHz), getting a proton spectrum with a SNR of 23,5 per acquisition and about 1.4 Hz for bandwidth of spectrum resolution.

Based on the planar micro-antenna developed by the team of T. L. Peck, many studies about planar micro-antenna have been published, showing the growth improving the low sensitivity of NMR measurements. Massin et al. [50] compare planar micro-antennas from different inner diameters ($2000, 1000$ and $500\text{ }\mu\text{m}$), corresponding to detection volumes of about 470 nL , 120 nL , 30 nL . They demonstrated that the sensitivity increased, reducing the planar coil diameter. Through that, they get a 1 H spectrum for $160\text{ }\mu\text{g}$ sucrose diluted in 470 nL of D_2O sample (for magnetic field of 7 T corresponding to 300 MHz for the resonance frequency).

Eroglu et al. [51] have developed a micro-antenna with an internal radius of about $750\text{ }\mu\text{m}$, 3 spiral turns, $100\text{ }\mu\text{m}$ track width, $20\text{ }\mu\text{m}$ thickness and $100\text{ }\mu\text{m}$ for the gap distance between the conductor tracks. They reached a quality factor of about 39, focusing on a comparison between theory and experience. They studied the field of views in terms of *SNR* parameters. Furthermore, they performed micro-imaging experiments on two concentric capillaries: an outer capillary with an internal diameter of 1 mm and an inner capillary with an internal diameter of $500\text{ }\mu\text{m}$ containing demineralized water and a fat, respectively. They achieved a spatial resolution of $30\text{ }\mu\text{m}$ within a static magnetic field of 11.74 T . The micro-antenna allows acquiring micro-images of living cells: Frog ovocytes and pancreatic cells isolated from rats [52].

Many authors have also studied the potential of micro-antennas for MRS analysis of nanoliter volumes [53] [54]. A first study focusing on the analysis of nano-volumes in high-resolution of MRS was presented by Olson et al. [46]. An improvement in mass sensitivity by a factor of about 140 was reported using a solenoid micro-antenna with an active volume of 5 nL (relative to a conventional antenna). These authors are the first to obtain a 1H spectrum from a sample of α -sacciform peptide cells ($\alpha - \text{BCP}$), Alysia California.

Ehrmann et al. [55] proposed the designing of a planar NMR microprobe designed for cells analysis and characterization using lipid vesicles as cell substitutes. He was able to align the sample in areas of homogeneous RF-field on the highly sensitive surface of the planar NMR microprobe using microcontact printing. So, he successfully recorded a 1H NMR spectrum of a sucrose solution confined within the lipid vesicles. They achieved a total detection volume between 1 to 2 nL from 3D Finite elements simulations.

Baxan et al. [56] proposed a planar micro-antenna with the following geometrical characteristics: Ellipsoidal, $1000 \times 500\text{ }\mu\text{m}^2$, $w = 22\text{ }\mu\text{m}$ wire width, $s = 20\text{ }\mu\text{m}$ wire spacing and thickness $t = 38\text{ }\mu\text{m}$ and 4 turns copper line. What provides an observation volume of about $0.2\text{ }\mu\text{L}$ for *In vitro* measurements by proton NMR spectroscopy. It was performed under a static field of 4.7 T with a sample containing five brain metabolites: taurine, lactate, NAA, choline and GABA. The taurine concentration was 50 mmol/kg and the metabolites remaining was 100 mmol/kg . After weighting the $\text{SNR} = 68$ by the number of acquisitions, the detection limit of this experiment, encourage the use of this micro-antenna a great as asset to measure metabolites in rodents models [57] for *in vivo* applications; however, an optimization work is still necessary.

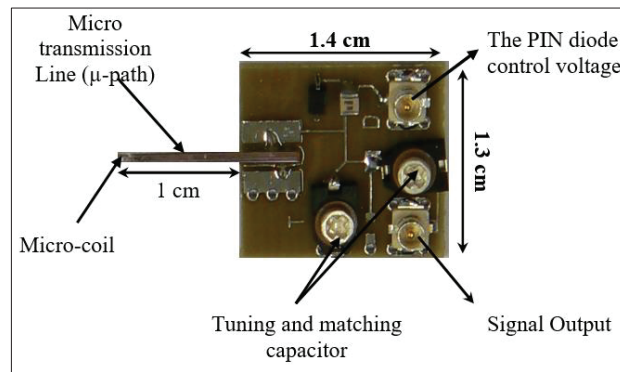


Fig. I. 8. An implantable planar micro-antenna (with ellipsoidal micro-coil): first prototype developed by our team [57]

From our team, A. Kajdo [58] reports the performance criteria of the first micro-antenna prototype proposed by Baxan et al. (Fig. I. 8). He studied its optimization for MRS *in vivo* acquisition. He also performed a biocompatibility study. Furthermore, he demonstrated that a rectangular antenna with at least a surface area of $500 \times 400 \mu m^2$ causes pressure and stress in the brain tissue, followed by relatively large scar necrosis after the implanting. Moreover, this inflammation can cause a reduction in the field of view of the micro-antenna and, therefore, may affect the NMR signal measurements. He also demonstrates that micro-coil positioning in intracerebral structures is well reproducible under stereotaxic conditions. The rat kept the micro-antenna for four months before it died [59]. He highlights that some improvements are still necessary to get a metabolic response for *in vivo* detection of small concentrations and volumes.

A new planar micro-antenna design was presented by Woytasik et al. [60]. That consist of a planar micro-coil manufactured on both sides of a flexible substrate, which allows the micro-antenna to take the form of the study object (sample). Different external diameters (3 mm, 5 mm and 15 mm) were compared with another flat antenna. They reach an *SNR* gain factor of 6 and 2 at a distance of 1 μm and 4 μm respectively inside the phantom.

A high spatial resolution antenna to study the internal structure of certain biological cells by micro imaging was developed by Weiger et al. [61]. The optimization of their equipment made it possible to attend 3 μm for isotropic resolution. A planar micro-antenna, with 20 μm for inner diameter, placed within a strong gradient, 6500 G/cm for the three directions, and a static field of 18.8 T, was used for experiments on a phantom composed of glass fibres immersed in water doped with copper sulphate ($CuSO_4$).

A portable system for molecular cell analysis was developed by Lee et al. [62]. That NMR miniaturized diagnostic system consists of a microfluidic microarray with several planar micro-coil, a printed, electronic circuit (tuning, matching, amplification) and a small magnet that

generate a magnetic field from 0.1 T to 0.5 T . The compact system allows bacteria and cancer cell profile detection. Biomarkers of the protein (α -fetoprotein) could also be identified for a sample volume of about 5 to 10 μL .

A comparative study between planar, solenoidal and Helmholtz antennas was carried out by Ehrmann et al. [63]. He noticed the variation of the quality factor Q and the electrical resistance as a function of the working frequency. A comparison in terms of the SNR , the homogeneity of the field B_1 and the width at mid-height for each antenna was performed. Continuing the comparison of micro-antennas, the 3D micro-coils (solenoidal, helmholtz) offer great sensitivity, magnetic field B_1 much more homogeneous than the planar micro-coil, but their disadvantages come from the micro-manufacturing difficulty, which can harm the electronic characteristics. For example, the Helmholtz micro-antenna manufactured on two silicon substrates lead to poor circuit quality because of the eddy currents in the semiconductor substrate [50]. The other drawback of a 3D micro-coil is: the sample must be inside the micro-antenna, which is not suitable for *in vivo* application: monitoring of the AD biomarkers variation using an animal model. What is crucial to highlight here is the homogeneity of spin excitation as a function of sample diameters of living biological cells placed on the surface of the planar micro-antenna with an inner diameter of 1 mm , two turns copper line, 15 μm for the thickness.

When comparing planar antennas with those of the solenoidal type from the literature, we can notice that planar antennas micro-manufacturing is less complicated than others (volumic antennas) presented in the literature on the small size. Planar micro-antenna can provide a good SNR and also a high spatial resolution for a very small sample volume placed in the vicinity of the antenna [64]. Finally, they can be integrated with less difficulty than solenoids into micro-analysis systems and easily used to build array antennas. On the other hand, the disadvantage is the inhomogeneity of the B_1 field the antenna compared to the volumic antennas, especially when the working frequency domain is very high i.e. a very intense magnetic field [65].

The choice among different types of micro-antennas depends strongly on the field of application, the nature of the sample to be analysed, the conditions and constraints of the work to be performed [58]. Our attention was focused on such implantable planar antennas for *in situ* or *in vivo* applications, minimally invasive, and that would allow the detection of a small amount of solutions. Our team could not yet use this original solution to detect cerebral metabolites by MRS; at least, we have demonstrated its potential for *in-vivo* applications.

Ginefri et al. [66] developed an implanted, inductively-coupled RF coil, fabricated on a flexible material, for *in vivo* rat brain MRI analysis at 7 T . The system allows acquiring the rat brain with a good resolution ($150\mu m \times 150\mu m$), reaching a visualization of a fine cerebral

structure. The implantable coil was fabricated in a PDMS substrate on both faces and reached a Q factor of 114.

Deborne et al. [67] evaluated the potential of the miniaturized implantable coil to acquire *in vivo* proton NMR spectrum in sub-microliter ROI and get metabolites information. For his study, a rat model was used, and the micro-coil was implanted in the right cortex for glioma diagnosis. The implanted micro-coil had about $450\ \mu\text{m} \times 3\ \text{mm}$ for width and length, and its detection volume was about $450\ \text{nL}$, with a sensitivity of 76. It was demonstrated that the microprobe is promising to investigate brain tumors.

My thesis aims to develop an optimized RF microprobe (microsensors) to analyse microliter volumes located within a larger sample through the MRS. The microprobe should be implanted *in situ* for a sufficient period (several weeks to several months) to monitor the concentration variation of the biomarkers through an animal model of AD. This development could lead us to an earlier diagnosis of AD. Knowing that the microprobe development has been performed by our team for years, my main role consists of proposing a new approach to optimize an implantable NMR microprobe. In the next section, we are going to describe planar antenna miniaturization, which is one of the strategies already applied by our team to increase the NMR sensitivity.

I.3.2. NMR antenna miniaturization

During the last decade, research showed the possibility of implementing NMR instrumentation at a small scale, especially with RF resonators, which can be used as NMR signal detectors. The actual NMR field trend is the analysis of very small mass and concentration samples; the main limitation is the low *SNR* representing the experiment performance.

Numerous studies using micro-antennas show the growing interest in improving the low sensitivity of NMR measurements by reducing the size of the receiver sensor for the NMR signal. Whatever some reasons are imposing this reduction in the sample volume: difficulties in producing the reagent in large quantities or miniaturization of the analysis system, it leads to questioning the design of the receiving RF coils.

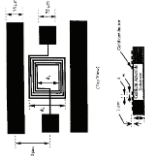
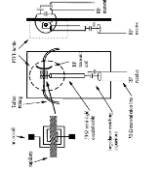
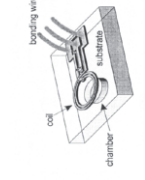

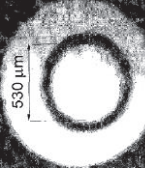
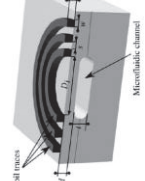
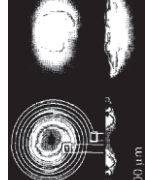
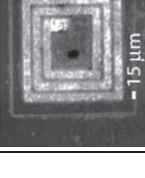
Conventional NMR instruments used for small volume analysis give a small *SNR* because of their large dimensions compared to the sample size. When the detection RF coil size matches the sample's size, the MR signal amplitude is maximized, which means that the filling factor is close to one. Therefore, an NMR micro-device specially designed for micro-samples is required to improve the *SNR* parameter and increase the sensitivity [52]. Considering the need for small quantities of tissue, examining by NMR spectroscopy or micro-imaging, it is possible to create

probes with such limitations, i.e. compatible working volume [68]. Thus, to analyze samples having volume close to the nanoliter, it is necessary to fabricate, by microelectronics technology, antennas having dimensions of several micrometers [69]. This way requires investigations essentially based on the present state-of-the-art of microelectronics, the optimization of the manufacturing process, as we are going to present in chapter IV, before the microfabrication of the final prototype of the microprobes.

On the biomedical scope, accurate quantification of metabolite variations is associated with spatial localization of small resonators (microprobe) placed directly into a well-defined region of interest (ROI) appears essential, as we will present in the next section. Before we have summarized in

several planar antenna works performed from 1994 until now (2022), studied for different teams in the whole world (Table I. 2). Furthermore, we have summarized in Table I. 3 , the works about the planar micro-antennas already performed by our team. In these tables, we recall all pertinent parameters of the microprobe, performances criteria value, fabrication methods and application. All summarized information, give an overview of works already performed on planar antenna and a basis for our project startling point.

Table I. 2. Review of all planar microprobe for NMR applications, from 1994 until now (2022)

Authors	T. L. Peck et al.	J. E. Strocker et al.	J. Dechow et al.	L. Renaud et al.	C. Massin et al.	C. Massin et al.	C. Massin et al.	G. Boero et al.	
Country-city	Chicago-USA	Chicago-USA	Wurzburg-Germany	Villeurbanne-France	Lausanne-Switzerland	Lausanne-Switzerland	Lausanne-Switzerland	Lausanne-Switzerland	
Years	[1994]	[1997]	[2000]	[2002]	[2002]	[2003]	[2003]	[2003]	
Geometry	Square	Square	Circular	Rectangular	Circular	Circular	Circular	Square	
Dimensions[μm ²]	150x150	200x200		1000x500				230x230	
wire width w [μm]	10	10		22	40	40	20	15	
Wire spacing s [μm]	3.5	10		20	30	30	10	25	
Wire thickness t [μm]	2	3	3	38	35	6	20	20	
Turn number n	4.5	3.5	1	4	3	3	5	3	
Inner diameter d [μm]	97.5	60		--	500	500	200	100	
Prototype Images									
	trip line material	Au	Au	Au	Cu	Cu	Cu	Cu	Cu
	Substrate	GaAs	GaAs	Glass and GaAs	Si	Glass	Glass	Glass	Glass
	Thickness[μm]	1000			520	--	--	--	--
Fabrication technology		Electrodeposition	Airbridge lithographic	Electrodeposition		Microfluidic channel			
Connecting solution wire	Airbridge	Airbridge	wirebonding	wire-bonding	wire-bonding	wire-bonding	wire-bonding	wire-bonding	
Magnetic field B0 [T]	7.05	5.9	11.7	2	4.7	7	11.4		
working frequency (MHz)	300	250	500			300	500	1.4GHZ	
Self frequency (GHz)	7.2 to 8.3	10.5		0.01 to 0.5			>>1		
Resistance(ohm)	5 to 25	5/ 2.7*	2	0.42		1	0.5/ 1.4*	1	
Inductance (nH)	4 to 5	5/ 2.3*		15.6		8.8	8.6*	2	
Capacitor (pF)	0.04	0.1 / 0.7*							
Q Factor (loaded)				10 *	--	--	20*		
Q Factor (unloaded)									
SNR	20	25.5*		95 *	15 / 11*	24*	74 *	18*	
Resolution				3.5*ppm	62x44	5.3*ppm	15x15μm ²	600*	
LW (Hz)	360	1.8	100	33*		9*	9*	1.4	
Sample		70%Ethanol(500-mM)	Silicone-oil	Butter (in vitro)	banna skin	sucrose	Mouse pancreatic (in vitro)		
ROI volume		880nL	60nL	0.33cm ³		30nL	30nL	(100μm) cube	
Electrical model	RLC			RLC	RLC				
NMR technique	¹ H MRS	¹ H MRS	¹ H MRS	¹ H MRS	¹ H MRI	¹ H MRS	¹ H MRI	ESR spectroscopy	
Applications	0	0		--	--	--	Imaging of biological cells	Imaging of biological cells	

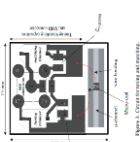
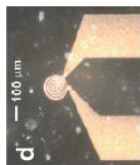
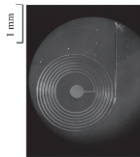
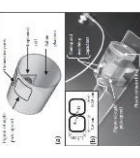
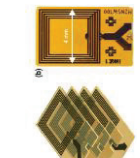
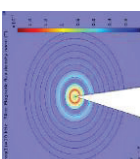

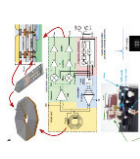
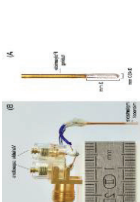

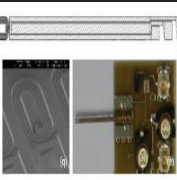
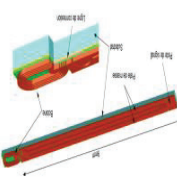
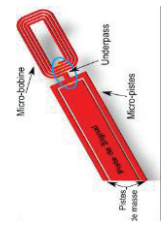
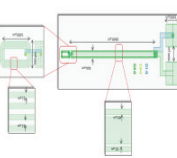
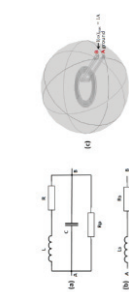
Authors	Country-city	Years	B. Sorli et al. Villeurbanne-France [2004]	M. Weiger et al. Faellanden - Switzerland [2008]	Xiaonan Li et al. Beijing - China [2009]	L. C. Ginefri et al. Paris-France [2012]	J. Watzlaw et al. Aachen-Germany [2013]	S. Krishnapriya et al. Noida- India [2017]	Xiaonan Li et al. Beijing- China [2018]	J. Handwerker et al. Stuttgart-Germany [2019]	J. Deborne et al. Bordeaux - France [2021]
Geometry			Square	Circular	Circular	Circular	Square	Circular	Circular / Square	Equilateral	Ellipsoidal
Dimensions[μm^2]			500x500	158x158	2000x2000	5400x5400	4000x4000	2200x2200	1000x1000	450x450	450x3000/700x3000
wire width w [μm]			22		20	118	100	50	80		
Wire spacing s [μm]			20			110	50	50			
Wire thickness t [μm]			46		19		25	1	19		75
Turn number n			4			7	5	5	7	24	1
Inner diameter d [μm]				20	500			100			
Prototype Images											
trip line material			Cu		Au	Cu	Au		Cu		Cu
Substrate			Si		Si	Teflon	Polymide		Glass		
Thickness[μm]			520			125	5		5		
Fabrication technology			Electroplating		Electroplating	Electrodeposition	thin-film technologies	MEMS	MEMS technology	CMOS technology	Insulated copper wire
Connecting solution wire			Micromachine channel		Microfluidic channel	Inductively coupled		no need	Wire-bonding		
Magnetic field B0 [T]			2	18.8	2	7	0.399		1.5	14.1	7
working frequency (MHz)			85.13		85	300	0.001		63.89	600	300
Self frequency (GHz)											
Resistance (ohm)					7.47			0.00075	5.532		
Inductance (nH)					298			0.5	273		
Capacitor (pF)											
Q Factor (loaded)			7*			25 *	24.3				53
Q Factor (unloaded)						114 *	30		20		55
SNR			9.45	10	21.3	185 *	4.2 / 7.0		17/ 101.1		75
Resolution				14		150x150 μm^2					
LW (Hz)			12	300	12					déc-53	5
Sample			C_2H_5OH (in vitro)	fleece of glass fibres in H2O		Rat brain	PDMS and natural rubber		4g/L CuSO4 - 200 μL		C6 Gliomas - Bearing rats
ROI volume						3.2x2x3.2cm cube			229.6 / 450.1	9.8nL	450nL / 850nL
Electrical model						RLC					COMSOL Simulations
NMR technique			1H MRS	1H MRS		1H MRI (in vivo)	1H MRS	NMR	1H MRS	1H MRS (in vivo)	1H MRS (in vitro and in vivo)
Applications						Rat brain imaging				Rat brain	Rat brain spectroscopy

Table I. 3. Summary of our team works, geometrical dimensions, electrical parameters analysis, and materials for μ manufacturing and its application

Author years	L. Renaud [2001]	N. Baxan [2008]	T. Tien [2014]	T. Josué [2014]	A. Bilel [2015]	M. Khelif [2018]	M. Khelif [2020]
Micro coil geometrical parameters							
• type of geometry	Rectangular	Ellipsoidal	Rectangular	Rectangular	Rectangular	Rectangular	Circular
• Surface dimensions [μm^2]	500x1000	500x1000	500x1000	500x1000	500x1000	500x1000	500x1000
• Wire width w [μm]	22	22	22	22	22	22	22
• Wire spacing s [μm]	20	20	20	20	20	22	10
• Wire thickness t [μm]	38	50	40	40	50	2	88.4
• Turn number n	4	4	4	4	4	4	4
• Inner diameter d [μm]							120
Image							
Micro path geometrical parameters							
• Signal μ path dimension [μm^2]		236x8720	320x9320	320x9320		320x9320	320x9320
• Gnd μ path dimension [μm^2]		110x9000	60x9500	60x9500	--	60x9500	60x9500
• Signal and ground gap [μm]		22	30	30	--	30	30
• Micro pad dimension [μm^2]		1500x1500	1500x1500	1500x1500	--	1500x1500	1500x1500
Substrate	Silicon	Glass	Glass	Silicon	Silicon	Kapton	Glass/Silicon
• Thickness [μm]	520	400	400	398	400	127	400/398
Isolator material	SiO_2			SiO_2	SiO_2	SiO_2	SiO_2
• Thickness [μm]	1			2	1		2
Adhesion material	Ti	Ti		Ti			Ti
• Thickness [μm]	0.02	0.02		0.01			0,01
Coupling technology	Capacitif	Capacitif	capacitif	Capacitif	Capacitif	Capacitif	Capacitif
Connects technology	Wire bonding	Wire bonding	Underpass vias	Underpass and vias	Underpass and vias	Underpass and vias	Underpass and vias
• Underpass dimensions		--	315x60 μm^2 , t=500nm	315x60 μm^2 , t=500nm	H=0.5 μm (Au)	568x60 μm^2 , t=1.6 μm	568x60 μm^2 , t=1.6 μm
• Vias geometrical dimensions		--	60x60 μm^2 , h=160nm	60x60 μm^2 , h=160nm	H=1.5 μm (Cu)	60x60 μm^2 , h=160nm	60x60 μm^2 , h=160nm
• Wire bonding dimensions		t=25 μm (Au)	--	--	--	--	--
• Airbridge dimensions		--	--	--	--	--	--
• Centre μ pad dimension [μm^2]		150x150			50x50		
Tuning frequency [MHz]	85.13	200	200	200	--		200
Self-resonance frequency [GHz]	0.01 to 0.5			6.67 (coil)	--		
Static magnetic field B0 [T]	2	4.7	4.7	4.7			

Electrical parameters		Measure	Calculation	Measure	Measure	Simulation	Measure	Simulation	Simulation	measure	Simulation	Measure	Simulation
Coil Resistance (ohm)	connection circuit TL (Path) antenna		0.424	1.27	2.4	0.61	4,7	0.93	0.19	--			1
			0.296					1.5			21.5		
				--	9		9	2					
					10.66	1.31	27,4	1.31			0.25		
Coil Inductance (nH)	connection circuit TL (Path) antenna		15.6	14.4	10.7	12.65	12,7	12.7	0.19	--			10
			3.8				4	--			21.5		
				--	4.7			4					
					15.34	12.6	1,099	12.6			0.25		
Q factor	Resolution (ppm)	10		14	1.81	12.1	0,05	12.1					
		3,5		2.01	3								
		33		10									
		95		68									62
Coil capacitor (pF)				1.57	0.7								
TL capacitor (pF)					5.8								
Global capacitor (pF)													
Electrical model				RLC		RLC		PI model		--	RLC		RLC
connection technology		Wire bonding		Wire bonding		Underpass vias		Underpass and vias	--	Underpass and vias		Underpass and vias	
Sample		Water and butter		cerebral metabolites									
ROI volume measurement		0.33cm^3 (ex vivo)		2.07μL (in vivo and in vitro)	2μL to 3μL	2μL to 3μL		2μL to 3μL	--	--			1nL
Magnetic field <B1>[mT]		1.34								--			--
Applications		¹ H MRS		¹ H MRS	¹ H MRS	¹ H MRS		¹ H MRS		¹ H MRS		¹ H MRS	
Implantable		yes		yes									
Technology of μprobe manufacturing		MEMS μfabrication		MEMS μFabrication	MEMS μfabrication	MEMS μfabrication	MEMS μfabrication	MEMS μfabrication	MEMS μFabrication		MEMS μFabrication		MEMS μfabrication

I.3.3. The performance criteria of the NMR antennas

The reciprocity principle [44] is usually used as a basis for optimizing the sensitivity of NMR antennas. In the following section, we will present the criteria for antenna performance, particularly defining the sensitivity of NMR antennas. We first introduce the noise, then the S_{11} parameter, finalize the Q factor and the last Signal to Noise Ratio (SNR) parameter.

I.3.3.1. Noises

Several sources of noise damage the signal's spectral domain. We are interested mainly in noise from the internal NMR system (receiver antenna). Noises sources coming from numerical acquisition, from other passives and actives electronics components we generally neglect in the first instance.

The previous section showed that the NMR signal is detected through an antenna. Thus, the NMR amplitude signal is too much weak. Hence, we have to determine the noise signal generally coming from the charges (electrons, ions) thermal agitation, the electronic circuits used in reception and the conduction behaviour of the sample.

Therefore, we can list the principal sources of noises for NMR systems:

- Noise due to the electrical resistance of the RF coil in reception.
- Noises due to capacitive (dielectric) and inductive loss on the sample.
- Noise due to electronic circuits at the acquisition chain.
- Imperfections of the Faraday cage of the NMR dispositive. It isolates no more from the disturbance in external electromagnetic fields.

Generally, the NMR system principal noise source comes from the sample. Noises come from the detection when the one induces more significant noise than the sample noise. Concretely, it happens when we adapt the NMR antenna dimension with the sample size of around $2\ \mu\text{L}$ to $3\ \mu\text{L}$ for our application case. It can be emphasized that the sample noise is neglected when decreasing the sample dimension [69]. Therefore, in our case, NMR experiment noise will come mainly from the micro-antenna [3].

A material or system with some charges (ions and electrons) does not have a perfect rest state for particle charges, even if no electric current is applied. If the temperature is not equal to zero, the system becomes a seat of thermal agitations. The Brownian motion principle can often model the random movement of charges. We can demonstrate by Langevin stochastic equation applied to a charge moving that we can explore two crucial phenomena which are connected: The fluctuation (Langevin force) and dissipation (friction force). These results stipulate that when a system gets the equilibrium state, there is no fluctuation without

dissipation [70]. Hence, it was demonstrated to fluctuate voltage magnitude and current intensity inside a conductor in a quasi-stationary regime [71]. So, the conductor voltage fluctuation depends on the resistance R and the temperature T_s as defined in the formula:

$$V_{noise} = \sqrt{4k_B R T_s \Delta f} \quad (I.19)$$

Where: k_B is the Boltzmann constant, R the resistance of the conductor, T_s represents the system's temperature and Δf the width band of the system.

I.3.3.2. S_{11} Parameter of NMR antenna

Scattering parameters or S-parameters describe the electrical behaviour of a linear electrical system. This parameter is useful for several branches of electrical engineering, including electronics, communication systems, and more particularly for MW engineering. Basically, many electrical properties of circuit components (inductor, capacitors, resistors) can be expressed using S-parameters, such as gain, return loss, voltage standing wave ratio (VSWR), reflection coefficient and amplifying stability.

Considering a two-port system (Fig. I. 9), we can represent different signals which correspond to the incident and reflected signal.

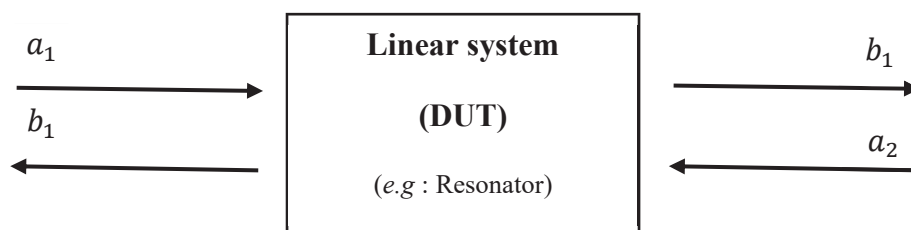


Fig. I. 9. A DUT (Device Under Test) with two ports

The relationship between the reflected and incident signal, on port 1, and 2 can be defined by the S-parameter matrix.

$$\begin{pmatrix} b_1 \\ b_2 \end{pmatrix} = \begin{bmatrix} S_{11} & S_{12} \\ S_{21} & S_{22} \end{bmatrix} \begin{pmatrix} a_1 \\ a_2 \end{pmatrix} \quad (I.20)$$

The matrix coefficient is defined as follows:

$$S_{11} = \frac{b_1}{a_1} \quad (I.20.1)$$

$$S_{21} = \frac{b_2}{a_1} \quad (I.20.2)$$

$$S_{12} = \frac{b_1}{a_2} \quad (I.20.3)$$

$$S_{22} = \frac{b_2}{a_2} \quad (\text{I.20.4})$$

The 2-port S-parameters have the following generic descriptions:

- S_{11} is the input port voltage reflection coefficient
- S_{12} is the reverse voltage gain
- S_{21} is the forward voltage gain
- S_{22} is the output port voltage reflection coefficient.

In my thesis, we work with RF antennas receivers. So, we aim to perform its behaviours simulation at reception, specifically to detect the NMR signal from a sample source. Hence, we focus on the reflection parameter (S_{11}), which represent the return loss of the signal whose the definition in dB is given in the following equation:

$$S_{11} = -20 \log \left(\frac{b_1}{a_1} \right) \quad (\text{I.23})$$

Where, a_1 represents the incident wave in the antenna system, and b_1 the reflected wave from the antenna system.

If S_{11} is zero ($S_{11} = 0$), then all wave power is reflected from the antenna system, and nothing can be converted into radiation, thus by reciprocity principle can be translated by no signal converted to an EMF for the RF receiver antennas. The receiver antenna ideally starts resonating when $S_{11} < -10 \text{ dB}$.

Since antenna resonating at a frequency ω_0 , is able to create a signal overvoltage during the resonance regime. The characteristic of a resonant circuit is its ability to strongly amplify the signal at a given frequency without amplifying it at other frequencies. The amplification is done in a range of frequencies, the smallest possible around the resonance frequency, called bandwidth $\Delta\omega$. The parameter representing the resonant circuit's performance is the quality factor, which is introduced in the following section I.3.3.3.

I.3.3.3. Q – Factor of the NMR antenna

The quality factor is a pertinent parameter that can correspond to the width at half-height of the resonance peak of the antenna, given by the measurement or simulation of the S_{11} parameter of a receiver antenna (defined in session I.3.3.2).

$$Q = \frac{\omega_0}{\Delta\omega} \quad (\text{I.24})$$

With: $\Delta\omega$ that represent the width at half-height of the resonance peak of the antenna and ω_0 is the resonance frequency of the antenna.

$$\Delta\omega = \omega_2 - \omega_1 \quad (\text{I.24.1})$$

From the energetic point of view, the Q factor of a system is also defined as follows the formula:

$$Q = 2\pi \frac{\text{Peak Magnetic Energy} - \text{Peak Electric Energy}}{\text{Energy loss in one Oscillation cycle}} \quad (\text{I.25})$$

The stocked magnetic energy is available by the inductive effect of the micro-antenna for an injected current intensity. Then the other part of the energy is dissipated by the Joule effect. It is also a standard criterion to determine the electrical circuit's performance modelling the NMR micro-antenna.

$$Q = \frac{\text{Im}\{Z\}}{\text{Re}\{Z\}} = \frac{\omega L}{R} \quad (\text{I.26})$$

Where Z corresponds to the system (resonator) impedance measured in $[\Omega]$

We need a system with the smallest bandwidth to have a very selective resonator, leading to the highest quality factor possible. It helps to ensure that the system (resonator) be more performant and selective (sensitive), avoiding noise from the measurements.

I.3.3.4. Signal Noise Ratio (SNR)

The SNR is one of the most critical factors to assess an instrument's performance in the sample measurements over a reasonable period. We can define *SNR* as the ratio between the amplitude of the free precession signal (FID amplitude) and the average quadratic value of the noise. This value is associated with the efficiency of the NMR antenna.

$$SNR = \frac{\text{signal}}{\text{noise}} \quad (\text{I.27})$$

$$SNR = \frac{\text{NMR signal Amplitude}}{\text{Average quadratique value of the noise}} \quad (\text{I.27.1})$$

Replacing the expression of the NMR signal and the noises signal in terms of voltage magnitude, we can define the *SNR* in the time domain as follows:

$$SNR_t = \frac{\frac{B_1}{i} \omega_0 M_0 V_s}{\sqrt{4k_B R T_s \Delta f}} \quad (\text{I.28})$$

Where:

ω_0 : is the resonant angular frequency, $\frac{B_1}{i}$ Corresponds the magnetic field generated by the micro-coil, M_0 is the static Magnetization, V_s is the sample volume, k_B is the Boltzmann constant, R is the antenna resistance, and Δf is the spectrum bandwidth.

The NMR experiments are generally analysed in the frequency domain (spectra). Hence, we must define the SNR formula in the frequency domain. The experimenter has easy access to the

SNR parameter in the spectral domain, usually due to the accumulation of several signal acquisitions. That means the number of acquisitions N_{acu} each other of duration T_{acq} as well as which the amplitude of the signal, we assumed the signal decreased exponentially with the time constant T_2^* . So, by Fourier Transformation (TF), we transform the SNR_t in the frequency domain equation:

$$SNR_f = SNR_t \times \frac{T_2^*}{\sqrt{2T_{acq}}} \quad (I.29)$$

When we include the acquisition number [57] the SNR_f is defined as :

$$SNR_f = SNR_t \times \frac{T_2^* \sqrt{N_{acc}}}{\sqrt{2T_{acq}}} \times \sqrt{\Delta F} \quad (I.30)$$

Where $\sqrt{\Delta F}$ is the width of the spectra [Hz]

The Q factor of the microprobe is an easily measurable parameter that can also define de RF sensitivity of the antenna, as in the given formula [72].

$$SNR = \sqrt{\frac{\mu_0 \omega_0 \eta Q}{4k_B R T_s \Delta f}} \quad (I.31)$$

$$S_{RF} \propto \sqrt{\eta Q} \quad (I.32)$$

In the optimal case of the filling factor $\eta \approx 1$, the RF probe sensitivity is quickly evaluated by the Q factor that is easy to calculate from the circuit's frequency response.

From the previous sensitivity equations, in terms of SNR we can note that the NMR sensitivity experiments also depend on the micro-probe geometrical parameters. More precisely, we can see in equation (I.28) that the SNR depends on some experimental parameters as:

ω_0 : is the resonant angular frequency, M_0 is the static Magnetization, V_s is the sample volume, k_B is the Boltzmann constant, and Δf is the spectrum bandwidth.

When we fix it, we can optimize the sensitivity by tuning the micro-antenna geometrical parameters, which are directly linked with the ratio $\frac{B_1}{i}$ and the resistance R .

So, the RF sensitivity is one of the criteria we use to optimize the NMR antenna, easily deduced as follows:

$$S_{RF} \propto SNR_t \propto \frac{\frac{B_1}{i}}{\sqrt{R}} \quad (I.33)$$

For whatever optimized microprobe, we can fix the $\frac{B_1}{i}$ and the experimental parameters. They are essential to optimize the experimental SNR and the acquisition time.

I.4. Sensitivity and Limit of detection of the NMR experiments

The investigation of mass-limited and concentration limited samples by MRS requires several performance criteria to validate the feasibility of the experiment using NMR microprobes. These criteria allow computing the approximate mass or concentration of sample needed to acquire the desired Signal to Noise Ratio (SNR) for a specific peak achieved during a particular scan time. These figures of merit are going to be explained more in detail in the following sections as the concentration and mass sensitivity (S_c and S_m), also the concentration and mass limit of detection (LOD_c and LOD_m).

I.4.1. The sensitivity of the NMR experiment

In reviews dedicated to NMR microprobe analytical investigation [73] [74], the sensitivity of a microprobe might define the performance. This indicator of sensitivity in terms of sample concentration and the amount of material (molar sensitivity), respectively as:

$$S_c = \frac{SNR_f}{[C]} \quad (I.34)$$

$$S_{mol} = \frac{SNR_f}{mol} \quad (I.35)$$

where $[C]$ is the sample concentration (mol/kg), and mol is the solute number of moles.

These sensitivity definitions were taken up by C. Massin [50], relating them to a single acquisition, thus defining them as follows:

$$S_c = \frac{SNR_f}{[C]\sqrt{N_{acc}}} \quad (I.36)$$

$$S_{mol} = \frac{SNR_f}{mol\sqrt{N_{ac}}} \quad (I.37)$$

It is also possible for the sensitivity formula in terms of acquisition time from the experiment duration. For years, the scientific community has had these sensitivity formulas to define how performant the experiment can be [75] [59].

I.4.2. Limit of Detection (LOD)

The Limit of Detection (LOD) or Lower Limit of Detection (LLD) is a concept that helps to determine the lowest amount of substance (mass or concentration) that can be detected in comparison with a measurement made in the absence of the sample within a confidence interval. These parameters were very well introduced in the thesis of N. Baxan [56]; They represent useful parameters for NMR experiments.

When we have to analyse a chemical substance, assuming that the white field does not exist or is at least constant, the LOD shall be determined from the highest peak of the SNR on the baseline. Different teams have used NMR detection limit calculations for many applications to determine the performance of micro-coils of solenoidal geometry since 1995 [46] [74] [73] [76]. It was demonstrated that the noise of the NMR spectrum increases as the root mean square value of the number of acquisitions N_{acc} while the signal remains proportional to the N_{acc} . That is also proportional to the time experiment t_{exp} . On the other hand, it is possible to standardize the detection limit $nLDO$ taking into account the number of acquisitions and the duration time of experience as follows:

$$nLDO_c = \frac{3.[C]}{SNR_f} \sqrt{N_{acc}} \quad (I.38)$$

$$nLDO_c = \frac{3.[C]}{SNR_f} \sqrt{t_{exp}} \quad (I.38.1)$$

$$nLDO_{mol} = \frac{3.mol}{SNR_f} \sqrt{N_{acc}} \quad (I.39)$$

$$nLDO_{mol} = \frac{3.mol}{SNR_f} \sqrt{t_{exp}} \quad (I.39.1)$$

The minimum of the spin number quantity that we can detect represents the micro-antenna sensitivity for catching a few spin amounts; that is defined as follows [77]:

$$N_{min} = \frac{N_s V_{sample}}{SNR} \sqrt{\Delta F} \quad (I.40)$$

Where: N_s is the number of spins per unit of volume and V_{sample} corresponds to the sample volume.

I.5. In-vivo implantation made by our team

I.5.1. Advantages of the Implanted micro-antennas

In practice, the study of cerebral metabolism in small animals can be carried out either by using a "macro-coil" or external commercial antenna such as a volumetric antenna or through an implantable micro-antenna, which is our aim work. For that, a comparative study between a commercial antenna (Rapid Biomedical 3.2cm diameter surface) and a planar micro-coil (race-track) was made by our team, the thesis of A. Kadjo [58]. A series of measurements, *in vitro* from 10 brain metabolites solution of known concentration in distilled water, allowed evaluating its performance using the photon detection limit ($LODC$) criterion.

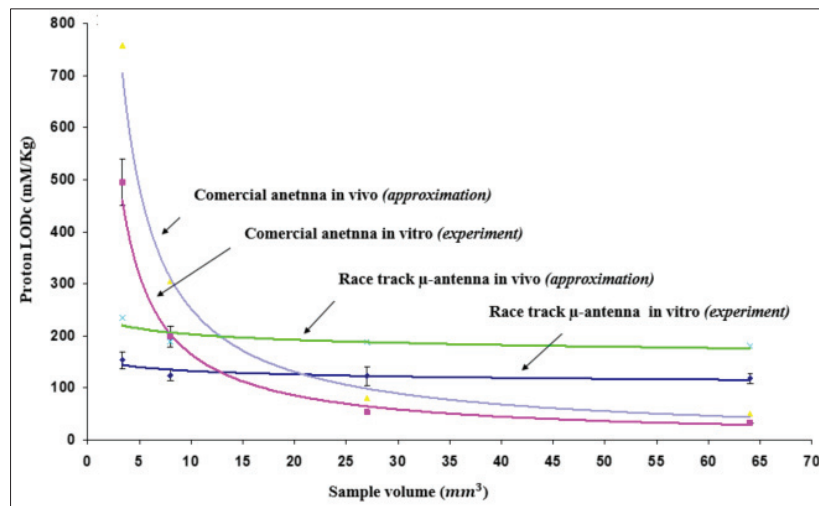


Fig. I. 10. Comparison of the LOD of a commercial antenna with the rack trace antenna [58]

In Fig. I.10, we show the comparison between the commercial antenna and the race-track antenna in terms of LOD , which has demonstrated the interest of the micro-antenna to examine small volumes (less than 10 mm^3).

The results demonstrate that the $LODC$ of the commercial antenna varies greatly depending on the volume of the examined voxel (500 mmol/kg to 4 mm^3 and 30 mmol/kg to 64 mm^3), the rack-trace $LODC$ (about 100 mmol/kg) rest quite constat for all ranges of the examined volume. Other advantages offered by the rack trace micro-coil is that we get a factor 2 for the gain instead of the commercial antenna.

Based on the outcomes Fig. I.10, the estimated *in vivo* $LODC$ of the rack – trace micro-antenna would be about 200 mmol/kg for less than 60 mm^3 volumes. Consequently, this demonstrates how useful the implantable micro-antennas should be for *in vivo* detection of metabolites by NMR [58]. Some demonstrative examples of brain metabolites spectra from volumes solution with 8 mm^3 to 64 mm^3 acquired using the micro-antenna, at 4.7 T can be seen more in detail [59].

An advantage of micro-antennas compared with the commercials macro antennas is that the magnetic losses in low conductivity samples are neglected [69] because the main source of noise is essentially from the microprobe (micro-coil + micro path and micro connection wire) resistance. This can be explained by the small volume of samples of the order of microliters, even about some nanoliters. The micro-antenna reduction dimension also favours the filling factor, allowing the microprobe sensitivity enhancement. So principal challenge rest to optimize the microprobe. All these results represent an asset for my thesis project and justify the use of a micro-antenna completely designed for our application instead of a commercial antenna.

I.5.2. Previous implantations of the Micro-coil in a rat model

Successful micro-antenna implantation was carried out by our team in the first place [56]. As shown in Fig. I.11 (a), the micro-antenna placed inside the ROI, taking into account the perpendicularity between the magnetic field B_1 , generated by the RF micro-antenna and the static magnetic field B_0 .

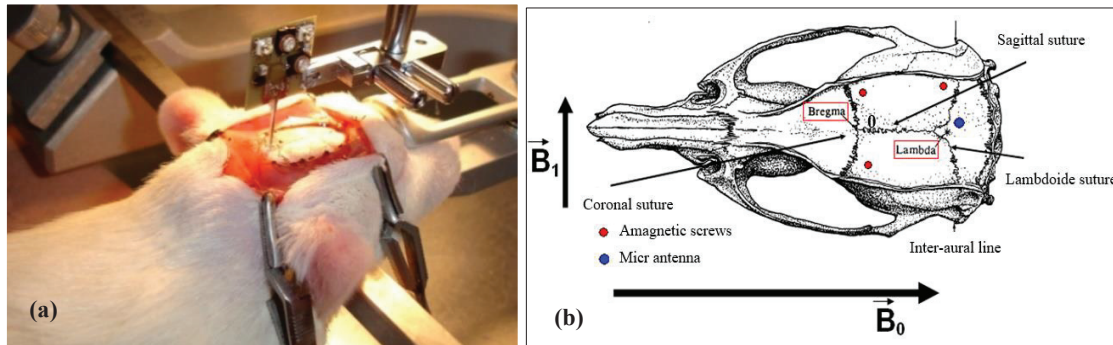


Fig. I. 11. (a) Micro-antenna implantation inside the ROI, using a stereotaxy device, (b) representing amagnetic anchoring screw and the micro-antenna site (Dorsal plans of rat skull) [56].

The experimental outcomes demonstrate that the micro-antenna is “minimally invasive” [58] [56]. The implantation was performed without significant brain lesions or postoperative complications. In the first place, the area of interest was localized by NMR imaging and correlated by histology. The measurements correspond to the coordinates of the Paxinos and Walton atlas [36]. The useful *in vivo* measured volume was about $1.86 \mu\text{L}$, corresponding to almost the *in vitro* magnitude measured ($2 \mu\text{L}$).

Fig. I. 12 shows an *in vitro* NMR spectrum of ten brain metabolites with a 50 mmol/kg concentration, which was acquired in a magnetic field of 4.7 T by the first micro-antenna prototype developed by our team.

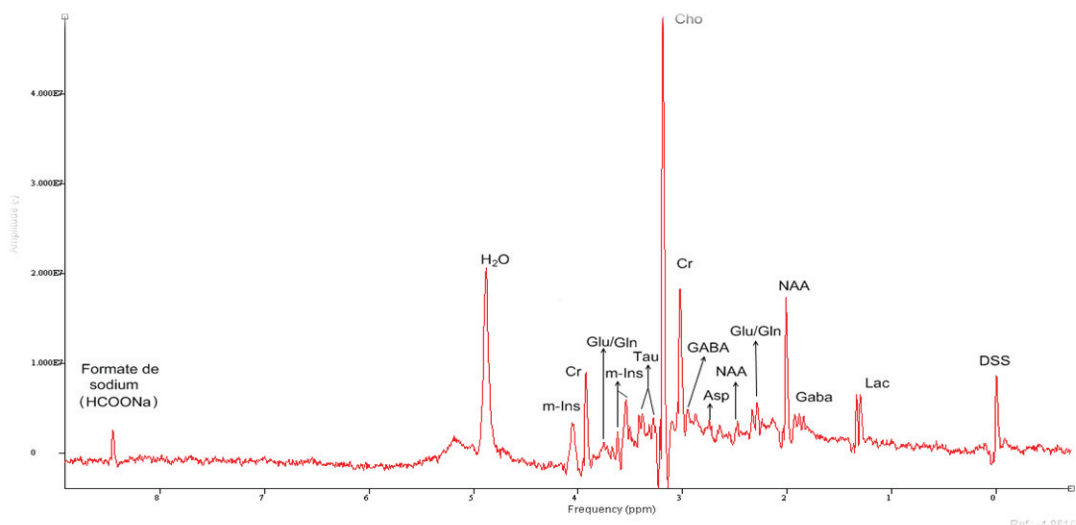


Fig. I. 12. *In vitro* NMR spectrum of 10 brain metabolites in aqueous solution using the planar micro-antenna (prototype developed by our team)

However, detecting the brain metabolites in small volume brain areas of a few meters cubic in LDT & PPT tissue presents a considerable difficulty in MRS. This difficulty is due to the low *SNR* achieved using conventional NMR sensors. Thus, in the last ten years, our research topic has focused on developing a new generation of optimal NMR sensors with a filling factor close to one ($\eta \approx 1$). They are designed to be closer as possible to the region of interest, allow to obtain the best possible *SNR*, and consequently lead to biomedical observations by NMR spectroscopy.

To address the issue of *SNR* of the micro-antenna and enhance it for our application, we first have to review the micro-antenna, last optimization work performed by our team, validate the last pertinent results and propose some enhancement on the optimization methodology proposing a new approach to model the implantable microprobe as we are going to see in the next chapter.

Conclusion

In the actual chapter, we have presented an overview of the project thesis: the introduction of Alzheimer's disease, the markers and diagnosis methods, and the present study's hypothesis for earlier detection of AD biomarkers. We also reported a brief introduction to the NMR principle and its sensitivity.

Moreover, we presented the review of our planar micro-antennas, from the conception to the *in vitro* and *in vivo* applications, highlighting their criteria of performance, the manufacturing methods and applications. We also reported in this chapter a summary of work previously done to optimize a racetrack micro-antenna and its advantage in comparison with a commercial one.

Meanwhile, according to our team previous results, we presented and validated the *in vivo* implanting pertinence for Magnetic Resonance Spectroscopy (MRS), representing a crucial starting point (hypothesis) for this project. Our team's previous works and literature propositions represent promising results for the NMR domain and have raised several questions. It demonstrated the possibility of optimising the micro-coil performance, proposing new methods/approaches for microprobe modelling and simulations. So far, the feasibility of their use *in vitro* and *in vivo* applications.

In the next chapter, we will model the microprobe antenna in terms of the magnetic field representing its sensitivity and in terms of the resistance value calculation, which represent the resistive losses of the micro-antenna.

Chapter II

Modelling of magnetic field and resistive loss of the micro antenna

Currently, many commercial software provides tools to design and simulate the performance of a 3D system (i.e, to calculate electrical parameters from the geometry and simulate the magnetic field). In the case of microprobe, the designing and performances simulation in terms of Signal to Noise Ratio (SNR) and Q factor, of such 3D system becomes too complex.

Therefore, simulation work must be performed to design and to improve the performances of the NMR probe adapted to the target application. Several studies had implemented electromagnetic simulation tools (FEMLAB, Maxwell 2D/3D, Magnetica, CST MWS, COMSOL Multiphysics, etc.) to model micro antennas, optimize their SNR parameter and consequently their performance [78] [79].

This chapter reports a new methodology of the microprobe (micro-coil + transmission line + *underpass & vias* or *airbridge*) modelling in terms of the magnetic field and resistive loss. In the first section, we reviewed the optimization work made previously by our team, and then we validated the new method, comparing our results. Magnetic field simulations were performed through CAD (Computer Aided Design), specifically for EM simulations such as CST MWS (micro-coil part) and COMSOL Multiphysics (complete microprobe). Then electrical parameters, simulations based on analytical calculations of RLC (Resistance, Inductance and Capacitance).

II.1. Review of the previous micro antennas: 1st and 2nd prototypes

Before the microprobe fabrication, there are two crucial tasks, (i) the optimization study, which helps us predict the device performance and (ii) the design of the optimal prototype according to the proposed specifications.

Before presenting the approach I chose for my work, I reviewed the previous works and prototypes - coil and transmission line with optimal dimensions, developed by our team. These prototypes were the starting point of my whole thesis.

In the second part of this chapter, I presented my own modelling work and the main results obtained.

II.1.1. The micro-coil and transmission line modelling

The Fig. II. 1 shows the 1st prototype of the Implantable NMR micro antenna fabricated by our team [56]. The micro-antenna consisted of the microprobe (i.e., micro-coil, Transmission Line (TL), and *wire-bonding*), associated with an electrical circuit fabricated on a PCB for signal matching and tuning.

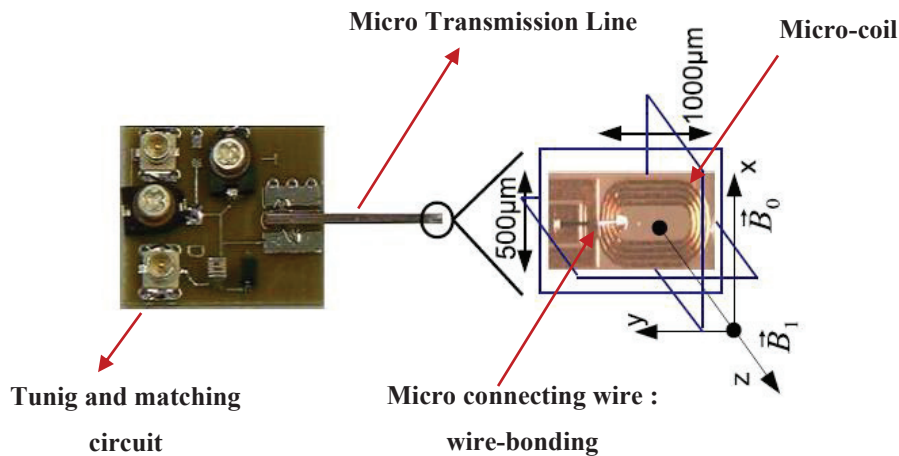


Fig. II. 1. Micro antenna prototype (the 1st fabricated by our team) [56].

The preliminary studies about its simulations were reported in the thesis of J. Rosillo Trejo [37] and T. Cong Troung [43]. They have modelled the micro antennas by an electrical circuit and calculated by a physical approach the B_1 magnetic field. In their approach, they considered only the micro-coil without the transmission line (TL), which they modelled separately. It was assumed that the sensitivity of the micro-coil (active part) could lead them to deduce the sensitivity of the microprobe, and then of the micro-antenna. Thus, they selected the best

geometry and proposed the optimal configuration for our application. Table II. 1, we have summarized the four optimized micro-coil geometries with their different dimensions and parameters. All the parameters representing the microprobe prototype must be taken into account, and be varied judiciously. Thus, we will use them to validate our own methodology which could be generalized to other types of microprobe modelling for other and other applications cases.





Configuration		Surface S [μm^2]	Turn number n	Wire width w [μm]
Rectangular		1000×500	4	22
			5	20
Ellipsoidal		1000×500	4	22
			5	20
Square		1000×1000	5	20
			6	29
Circular		1000×1000	5	20
			6	29

Table II. 1. Micro-coil layout and dimension of the optimal geometries [37]

The Transmission line (TL) of the microprobe for both prototypes correspond above, has 9 mm for the length, $500\text{ }\mu\text{m}$ for the width and a thickness of $438\text{ }\mu\text{m}$. The thickness dimension includes the copper layer ($38\text{ }\mu\text{m}$) in addition to the substrate thickness ($400\text{ }\mu\text{m}$). This TL was optimized as an RLC circuit according to the transmission lines theory. In Fig. II. 2, we can see the example of the transmission line of the 2nd prototype with two ground planes.

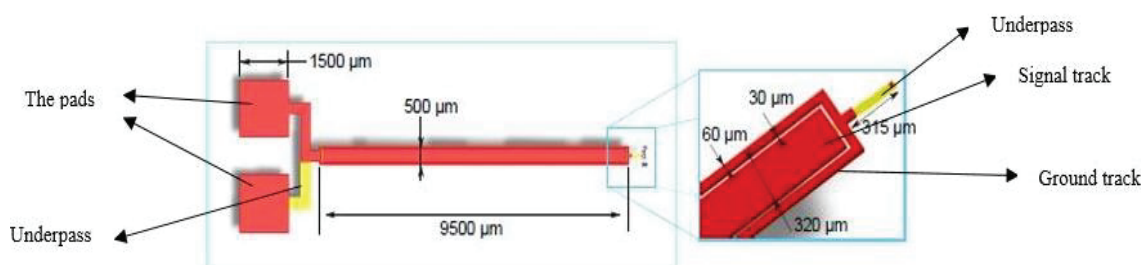


Fig. II. 2. Design and dimensions of the 2nd prototype of the micro-probe [80]

Transmission lines with two ground planes have the advantage of low attenuation and their wideband application in inhomogeneous environments [81]. For our simulation work, we keep the previous optimized layout shape for the micro-tracks, *ground /signal/ground*, with the same for the track line, and added some improvements in the new design.

II.1.2. Limitations of the previous designs

In this section, we have pointed out the limitations of previous design prototypes, highlight the parts that require to be improved.

The first point of improvement concerns the *wire-bonding*, used in the first versions of the microprobe to connect the center of the micro-coil to the TL and from the TL to the PCB. The connecting wire (*wire-bonding*) presented two major disadvantages: its delicate welding and its fragility during implantation. To solve this, our team (J. Rosillo Trejo and T. Cong Truong Thesis) have proposed a new micro-connecting wire (*underpass & vias*) and optimization of the transmission line layout as we have previously seen in the precedent section.

The *underpass & vias* solution represents an interesting solution, instead of *wire-bonding* to improve the microprobe performance. Its weak influence on the NMR signal was already reported [82]. However, according to the post-layout simulations of the prototype fabrication [37], the *underpass & vias* increases the total resistance to about 1.5Ω [37].

The impact of Vias (TSV) incorporated on a silicon substrate was also already reported in several studies for the case of high frequency. The TSV technology has been considered as a solution for 3D interconnections' problems. The main advantages of the TSV are the higher interconnection density, less parasitic effects and less power consumption [83] [84]. We do not forget that a good characterization of TSV electrical parameters and modelling of coupling effects are highly needed. However, this is not the scope of this chapter but will be discussed in detail in the chapter III. According to all these facts, the *underpass & vias* are still a good solution, so we proposed this connecting solution for the 3rd prototype of the microprobe. Nevertheless, it still requires some enhancements in the fabrication process to improve the probe performance. For the 3rd prototype fabrication, we also chose the transmission line proposed on the 2nd prototype with some upgrades. We have also proposed another micro-wire connecting solution (*air-bridge*).

II.2. The design and modelling of the microprobe.

As we previously emphasized in chapter I, our team has been working on design and optimization of implantable NMR micro-coils for many years. Several proposals were made in terms of design and of performance (Q factor, SNR). In previous modelling work, the micro transmission line (TL) and *wire-bonding* have not been taken into account to estimate resistive losses. In this section, we will present the methods used to validate the previous works done by our team.

The aim is to model the microprobe completely, predict its performance very accurately and then propose an enhancement for the next prototype fabrication. First, we need to validate our methodology with the previous results of the micro-coil simulations, assuming that the TL is the same for all geometry and will not impact the performance of the micro-coil.

To develop a microprobe prototype, we have followed the methodology summarized in Fig. II. 3. Each step represents a suitable phase to follow to design and develop an optimal prototype. So, the process is divided into two parts: First, the conception and simulation, and secondly, the experimental part, which corresponds to the optimization, characterization and validation of the microprobe fabrication.

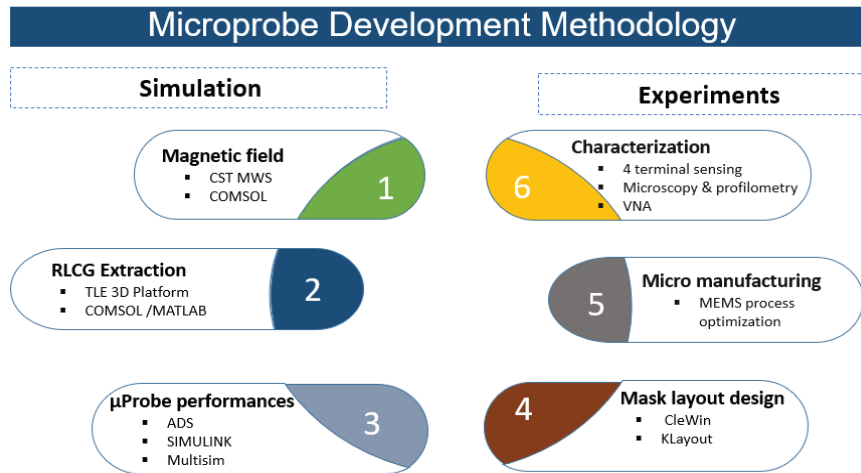


Fig. II. 3. Block diagram of our methodology to develop the new optimized microprobe prototype

This chapter mainly focuses on the conception of the microprobe and its performance simulation. We performed the simulation of the magnetic field generated by the micro-coil and the whole micro antenna, and then we calculated the RLC of the micro-coil by an analytical approach.

The magnetic field generated by the micro-coil was simulated using CST MWS (Computational System Technology Microwave Studio) for the micro-coil part, according to different geometries (given in Table I.1) and COMSOL Multiphysics to simulate the impact of the substrate to the magnetic field and then simulate the magnetic field from whole microprobe prototype.

We have also estimated the RLC (Resistance – Inductance – Capacitance) parameters of the micro-coil by an analytical approach, of which the formulas were presented in section II.2.2. This approach is widely inspired by formulas in literature and previous works done by our team (For example, the calculation of self and mutual inductance of the micro-coil). To do this, we coded a MATLAB script to calculate all parameters. We were able to validate our results with those of COMSOL Multiphysics and ADS (Advanced Design Software).

The approach to calculating the RLC parameters takes into account several physical phenomena that we will describe in the subsequent sections.

II.2.1. Simulation of the magnetic field

We have designed the four geometries as defined above, and the dimensions characteristics are detailed in the following paragraph.

Micro-coils with: the number of turns ($n = 4$), the spacing between wire turns ($s = 20 \mu m$), the wire's width ($w = 22 \mu m$), and thickness of the wire ($t = 40 \mu m$).

- Square and Circular: $1000 \times 1000 \mu m^2$
- Ellipsoidal and the rectangular: $1000 \times 500 \mu m^2$



Fig. II. 4. The four geometries of micro-coil designed in CST MWS

The comparative study of the magnetic field generated for four micro-coil geometries was performed using CST MICROWAVE Studio®, a software-based on Finite Integration Technique (FIT), where Maxwell's equations is written on a grid space both in time and frequency domain. The magnetic field analysis was set to 300 MHz working frequency domain, which corresponds to 7 T and 500 MHz for 11.4T. Notice that in our case, we have a static

approach, and the magnetic field will not depend on the frequency. We also assumed that the current through the micro-coil is unitary current intensity (i.e., $i = 1 \text{ A}$).

Fig. II. 5 shows B_z Magnetic field as a function of z – direction where we simulated the magnetic field around the micro-coil. We select the variation of the magnetic field into the perpendicular plan which represents the field of view of the micro-coil, and most precisely its sensitivity.

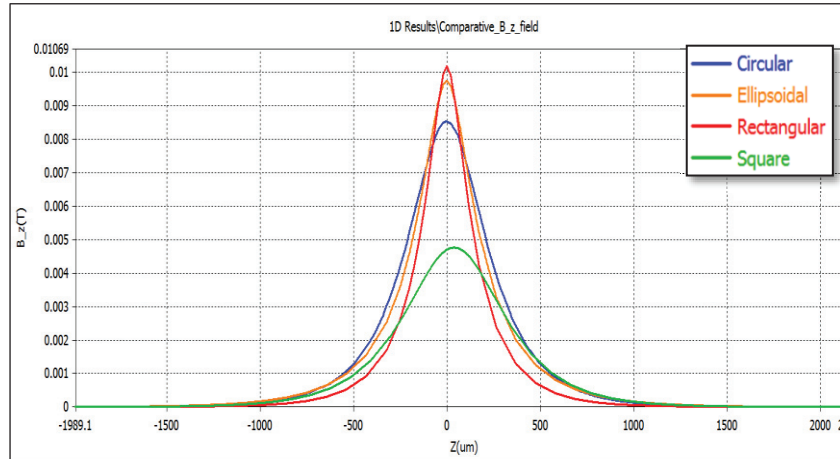


Fig. II. 5. Plot of magnetic field (B_z) variation as a function of z -direction

The rectangular micro-coil generated the highest magnetic field at the centre ($z = 0 \mu\text{m}$). Nonetheless, the magnetic field of ellipsoidal is closer to one of the rectangular (See Fig. II. 5).

Note that even if the rectangular design appears to be the most sensitive at the centre; its sensitivity decreases rapidly compared to others less sensitive in the centre (e.g., Square and circular).

II.2.2. Electrical parameters of the micro-coil (RLC)

This section focuses on the main approach and formulas used to determine the RLC parameters thanks to analytical calculations done by a developed MATLAB script.

We present an AC resistance calculation approach to determine the different micro-coils geometries resistances. That approach aims to take into account the skin and proximity effect as will be modelled into the later part of this work, with the complete microprobe through the 3D – TLE platform.

For the Inductance calculation, we used the approach previously proposed in our team which is simplest to model the analytical calculations compared to the approach proposed in the literature.

We also present the formula to model the capacitive effect in section II.3.2.4. All formulas modelling capacitive effect were extracted from the literature, and it represents the basis for the capacitive modelling of the microprobe;

The formulas we defined to estimate the RLC parameters of the micro-coil need, analytical calculation of the length of the micro-coil wire. That is why, in the section. II.2.2.1, we start by presenting the modelling of the length for the four geometries of micro-coil that are useful for the analytical estimation of RLC.

II.2.2.1. The length modelling of the four micro-coil geometries

Before describing the formulas to analytically calculate the micro-coil length, we show the micro-coil shape geometrical parameters description. To illustrate the modelling, we have three spiral turns circular and square micro-coil (Fig. II. 6) and a four spiral turn ellipsoidal geometry (Fig. II. 7).

The descriptions of all geometrical parameters of a coil are given in the Fig.II.6.

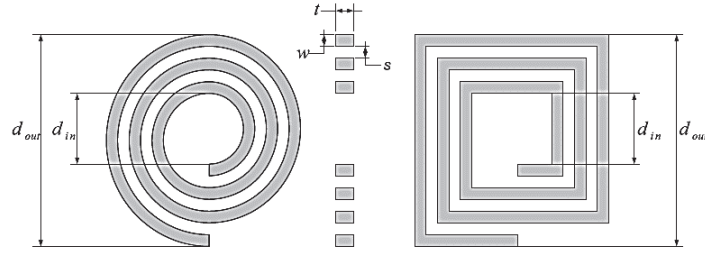


Fig. II. 6. Circular and square micro-coil shape with three spiral turns (d_{out} : outer diameter, d_{in} : inner diameters, w : width of wireline, t : the thickness of wire and s : separation distance between two wires) [43]

II.2.2.1.1. Rectangular and square micro-coil shape

The length of a planar spiral rectangular is calculated analytically through the equation (.II.1) defined by recurrence. Then, to determine the square micro-coil length, we assume that $d_{out} = d'_{out}$.

$$l_{avg-n} = l_{avg-(n-1)} + 2[(d_{out} + d'_{out}) - 4(n-1)(w + s)] \quad (II.1)$$

With:

$$l_{avg-1} = 2(d_{out} + d'_{out}) - (w + s) \quad (II.2)$$

Where: d_{out} and d'_{out} are the outer diameter of two sides of a rectangular spiral, and n corresponds to the number of turns.

II.2.2.1.2. Circular micro-coil shape Rectangular and square micro-coil shape

We model the planar circular coil like a spiral Archimedes, calculations based on a website: <https://inmath.com>. One was adapted for our case as the equation follows:

$$r = \left(\frac{d_{in}}{2} + w \right) + \gamma\theta \quad (II.3)$$

With:

$$s + w = 2\pi\gamma \text{ and } d_{in} = d_{out} - w(2n + 1) - s(2n - 1) \quad (II.4)$$

$$l_{avg-n} = \int_0^{2\pi n} \sqrt{r^2 + \left(\frac{dr}{d\theta} \right)^2} d\theta \quad (II.5)$$

Where n is the number of spires and r represents the polar coordinate of the circular spiral.

II.2.2.1.3. Ellipsoidal micro-coil shape

We assume the ellipsoidal planar micro-coil is a composition of a half circle on each extreme side with a length size corresponding to the outer circle diameter.

$$l_{avg-n} = 2nd_{out} + \int_0^{2\pi n} \sqrt{r^2 + \left(\frac{dr}{d\theta} \right)^2} d\theta \quad (II.6)$$

The analytical modelling seems to agree with direct measurements. It can be useful to calculate the ellipsoidal planar coil's resistance, inductor, and capacitance like the previously related shape.

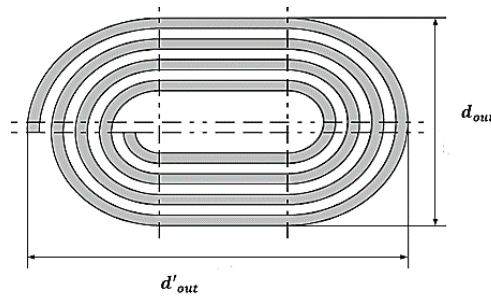


Fig. II. 7. Ellipsoidal micro-coil shape with four spiral turns [43]

II.2.2.2. The resistance of rectangular conductor

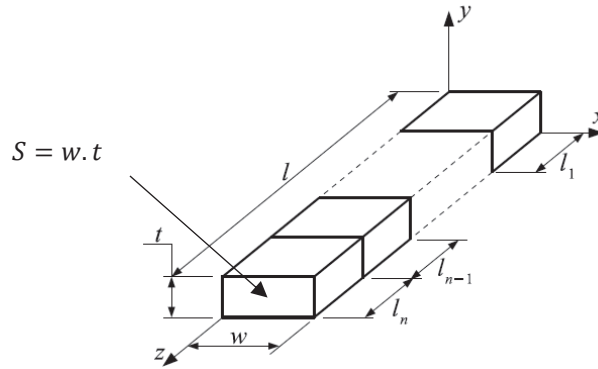


Fig. II. 8. Conductor wire, with rectangular surface cross-section [43]

In the low-frequency domain (DC), the resistance from a rectilinear conductor wire, with rectangular surface cross-section (Fig. II. 8) is calculated by Ohm's law:

$$R_{DC} = \rho \frac{l}{S} \quad (II.7)$$

Where:

ρ : is the conductor electrical resistivity [Ωm]

l : is the length of conductor wire [m]

S : is the rectangular surface cross-section [m^2]

In this approach, the current passes through all conductor surface cross-sections. We consider that the current density is uniform across the entire surface S , whereas it happens differently.

II.2.2.3. Skin effect and proximity effect approach

When we inject an alternating current through a metallic wire, we create an alternating magnetic field having flux lines concentric with the wire axis. The magnetic field generated induces eddy currents throughout its wire as well as inside another nearby conductor. Its phenomena (skin effect) contribute to increasing the alternative resistance on the conductor wire. The following equation defines the skin effect thickness δ [m] in a conductor:

$$\delta = \sqrt{\frac{\rho}{\pi \mu f}} \quad (II.8)$$

With:

$$\rho = \frac{1}{\sigma} \quad (II.9)$$

Where:

μ : Magnetic permeability of conductor wire [Hm^{-1}]

f : Frequency domain of the alternating current [Hz]

σ : is the electrical conductivity of the conductor wire [Sm^{-1}]

The skin effect formula demonstrates the increase in the conductor wire resistance at the high-frequency domain qualitatively. The threshold frequency can be determined by the equation (II.10). This formula allows determining the frequency from which the skin effect appears for a conductor wire radius.

$$f_{\delta} = \frac{\rho}{\pi\mu r^2} \quad (II.10)$$

The proximity effect also appears when we place a fed wire nearby another one (complicated phenomena to model analytically) [85]. Hence, we neglected its influence, even though it was shown that it is essential to estimate microprobe electrical losses [86]. The proximity effect modelling is so complex to calculate analytically [43].

II.2.2.4. Skin effect for a micro-conductor

Let's consider a micro-wire fabricated by copper electro-plating ($\sigma = 5.96 \times 10^7 Sm^{-1}$, $\mu_r = 1$ and $\mu_0 = 4\pi \times 10^{-7} Hm^{-1}$) we want to determine whether the skin effect might be taken into account for a specific conductor radius. We have to compare the skin thickness given in equation II.8 against the wire conductor thickness.

To illustrate our example, we studied the optimized geometrical parameters of the micro-coil from previous thesis work carried out by our team (i.e., micro-coil with $t = 40 \mu m$ and $w = 20 \mu m$), which correspond to an average radius $r = 28.284 \mu m$. So, we can deduce the threshold frequency, $f_{\delta} = 5.3127 MHz$, keeping in mind that our frequency domain is $300 MHz$ or $500 MHz$.

Through the equations (II.8), we can calculate the skin effect thickness for $3.764 \mu m$ and $2.915 \mu m$ wire radius. Therefore, the skin effect must be taken into account to determine the accurate microprobe resistance for both working frequency cases, knowing that the working frequency domain defined for our application is higher compared to the threshold frequency previously determined for the geometry of the micro-coil ($f_{\delta} = 5.3127 MHz$). Thanks to the same process, we can easily calculate the threshold frequency for the *underpass* & *via*. For its

diameter $60 \mu m$ and thickness $t = 150 nm$, we have a threshold frequency $f_\delta = 1.42 GHz$, which is also higher than our frequency domain. This allows us to conclude that we must include the skin effect calculation to estimate accurately the resistive losses from the NMR microprobe.

II.2.2.5. Resistance modelling with skin and proximity effect

We defined the AC resistance, the addition of DC resistance plus skin and proximity effect resistances. That definition includes the frequency impact, knowing that the skin and proximity effect appears when working at the high-frequency domain or simply when the threshold condition is verified. We previously demonstrated in section II.2.2.4 that we must consider the skin and proximity.

$$R_{AC} \approx R_{DC} + R_\delta + R_{proximity} \quad (II.11)$$

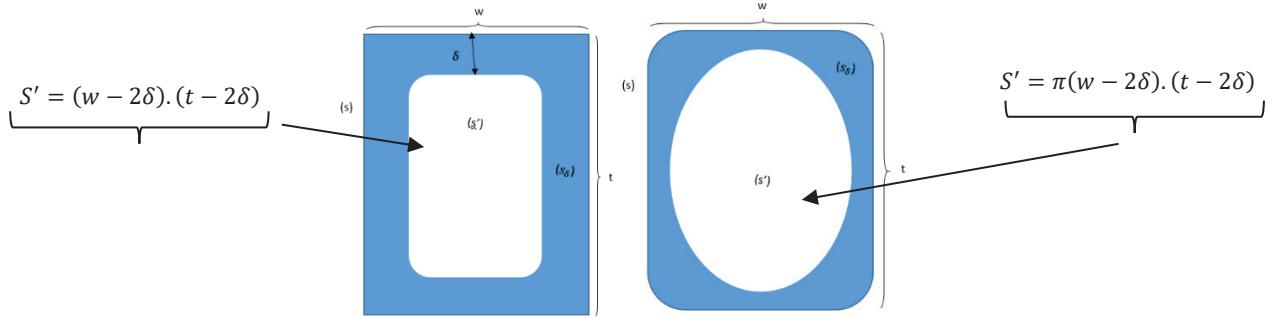


Fig. II. 9. Skin effect phenomena illustration in the case of a rectangular (a) and ellipsoidal (b) conductor surface section. The blue area represents the surface cross-section region where the current is going to pass-through

$$S_\delta = S - S' \quad (II.12)$$

Fig. II. 9 represent the skin effect for a rectangular and ellipsoidal surface; from that, we can deduce the skin surface that allows determining each equation as follows:

$$S_\delta = 2\delta(t + w - 2\delta) \quad (II.13)$$

$$S_\delta = \pi\delta(t + w - 2\delta) \quad (II.14)$$

The two cases model the skin effect phenomena. Fig. 9 (a) represents the ideal case for a wire with a rectangular surface section, where the rectangular corners lack any fabrications residues or some shape defaults, whereas that is more realistic for a conductor wire with an almost ellipsoidal surface cross-section (b) because we consider the microfabrication defaults

and neglected the proximity effect. From all previous considerations, we can calculate AC resistance using the following equation:

$$R_{AC} = \rho \frac{2l_{avg}}{\pi\delta(t+w-2\delta)} \quad (II.15)$$

With:

$$R_{\delta} = \left(\frac{2wt - \pi\delta(t+w-2\delta)}{\pi\delta wt(t+w-2\delta)} \right) \rho \cdot l_{avg} \quad (II.16)$$

Where: l_{avg} represents the conductor wire length. The formula corresponding to different micro-coil geometry is given in section II.2.2.1.

II.2.2.6. The self and mutual inductance

The analytical calculation of the inductance of a conductor has been reported in numerous articles but, these formulas are only applicable for long conductors or conductors of specific cross-sections [87] [88] [89] [90]. Based on Neumann's formulations work, several other teams have proposed different formulas to determine the self-inductor and mutual inductor for the recline rectangular cross-section conductor [87]. Nonetheless, that approach is still complex for the conductor inductance calculation.

In radio-frequency (RF) microsystems, the sizing study to determine the inductance of the system is necessary because the performance is strongly influenced by high resonance self-frequency.

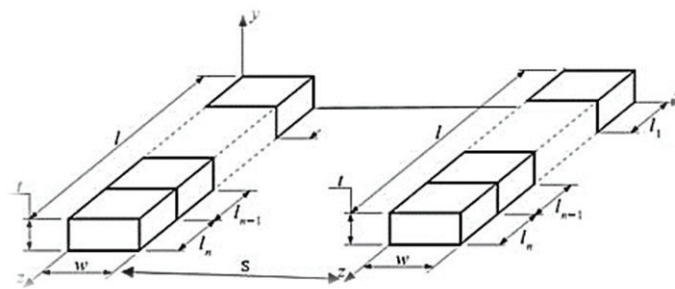


Fig. II. 10. Coplanar line structure for two close wires with the rectangular surface [43]

Practically, the geometry of our microprobe is quite complex; the discretization (segmentation) of the conductor into many small straight elements is decisive for calculating the inductance. However, given the various existing formulas, the theoretical analysis of the inductance of a coil with a rectangular cross-section remains challenging and often inaccurate.

The method to calculate a conductor's inductance was demonstrated in the thesis of T. Cong Troung [43]. His approach considers the interaction between self-inductance and mutual inductance for several geometries and conductor shapes.

The calculation of conductors' self-inductance and mutual inductance with a rectangular cross-section is identical to a thin strip-line. However, the discretization of the conductor into many filaments will be performed in both directions of the conductor cross-section [91] [89].

The self-inductance from a conducting wire with a rectangular cross-section surface can be calculated through the following formula [43]:

$$L_{\text{self}} = \frac{\mu \cdot l_{\text{avg}}}{2\pi} \left[\ln \left(\frac{2l_{\text{avg}}}{w+t} \right) + \frac{1}{2} \right] \quad (\text{II.17})$$

Following some enhancement on the previous formula of the self and mutual inductance, the planar conductor is calculated depending on analytical expressions [89]:

$$L_{\text{self}} = \frac{\mu \cdot l_{\text{avg}}}{2\pi} \left[\ln \left(\frac{2l_{\text{avg}}}{w+t} \right) + \frac{1}{2} + \frac{0.447(w+t)}{2l_{\text{avg}}} \right] \quad (\text{II.18})$$

$$M_{12} = M_{21} = M = \frac{\mu \cdot l_{\text{avg}}}{2\pi} \left[\ln \left(\frac{2l_{\text{avg}}}{s} \right) - 1 + \frac{s}{l_{\text{avg}}} \right] \quad (\text{II.19})$$

Where $\mu = \mu_r \mu_0$ with $\mu_0 = 4\pi \times 10^{-7} \text{ H/m}$

II.2.2.7. The capacitor of the microprobe model

A capacitor is the capacity of a device to store charges, depending on geometrical parameters. Generally, it is defined by the following equation:

$$C_s = \epsilon \frac{l_{\text{avg}} \cdot t}{s} \quad (\text{II.20})$$

These formulas represent the capacitive coupling of the micro-device according to different parts. We will see more in detail in the following sections; There are several parasitic capacities from the microprobe due to the coupling between the loops and the one with the substrate and oxide layer, in the case of the silicon substrate.

We have an interline coupling capacitance C_{inter} , its value is calculated according to the equation defined by Nurmi Osborn [92]. From the concerned lines, surfaces and fringe capacities (capacities between the copier layer and the substrate: C_f and C_f'). This capacity is

taken at the line extremities as well as the C_p . The coupling capacity between the ground plan and the concerned line surface can be referred to in the literature as line self-capacity.

$$C_{\text{inter}} = C_f - C'_f + \frac{\varepsilon \cdot l_{\text{avg}}}{100} \left(3 \frac{w}{t_{\text{oxid}}} + 83 \frac{t}{t_{\text{oxid}}} - 7 \left(\frac{t}{t_{\text{oxid}}} \right)^{0.222} \right) \left(\frac{t_{\text{oxid}}}{s} \right)^{1.24} \quad (\text{II.14})$$

With:

$$C_f = \varepsilon l_{\text{avg}} \left(\frac{0.075(w)}{t_{\text{oxid}}} + 1.4 \left(\frac{t}{t_{\text{oxid}}} \right)^{0.222} \right) \quad (\text{II.15})$$

$$C'_f = \frac{C_f}{1 + \frac{t_{\text{oxid}}}{s}} \quad (\text{II.16})$$

$$C_p = \varepsilon \frac{l_{\text{avg}} \cdot w}{t_{\text{oxid}}} \quad (\text{II.17})$$

Where $\varepsilon = \varepsilon_r \varepsilon_0$ with $\varepsilon_0 = 8,85 \times 10^{-12} \text{ F/m}$

II.2.3. Summary of electrical and magnetic parameters of the micro-coils

To validate our studies, we have modelled four micro-coils, simulated its magnetic field and then calculated analytically its RLC (resistance R , inductance L , capacitance C) parameters using a MATLAB script that we developed.

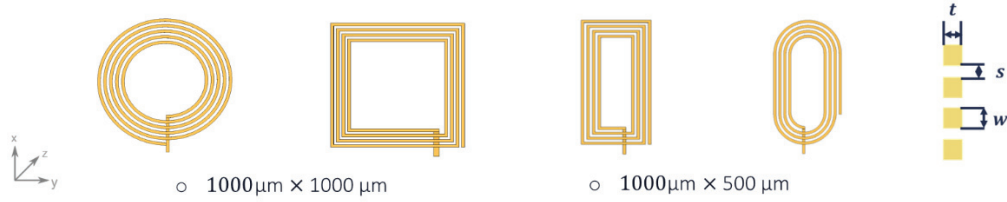


Fig. II. 11. The four modelled geometries: $n = 4, t = 40 \mu m, w = 22 \mu m, s = 20 \mu m$

In Table II. 2, we summarized the parameters of planar simulated micro-coils (Fig.II.11)

Geometry	$\frac{B_1}{i}$ [mT/A]	R [Ω]	L [nH]	C [pF]	Q	SNR [$\frac{mT}{A\sqrt{\Omega}}$]
Rectangular	10.10	0.518	12.468	0.176	45.347	14.033
Ellipsoidal	9.80	0.453	10.683	0.154	44.429	14.561
Square	4.70	0.726	18.428	0.247	47.821	5.516
Circular	8.20	0.572	13.995	0.194	46.095	10.842

Table II. 2. Summary of electrical and magnetic parameters from each micro-coil geometry at **300 MHz**

The Q factor and the sensitivity in terms of the SNR were deduced by the formulas as defined in chapter I, Q factor (equation (I.3.3.3)) and SNR parameters (equation (I.3.3.4)).

It is relevant to mention that the magnetic field B_z value was extracted in Fig. II. 5 (Magnetic field varying according to perpendicular direction). B_z value on the table corresponds to the magnetic field yield at the micro-coil centre (i.e., B_z value for $z = 0$).

We can confirm that the rectangular micro-coil is the best geometry due to its optimal sensitivity (greater magnetic field at micro-coil centre) and good quality factor (Table. II.2). We also observed from these results that the rectangular and the optimized ellipsoidal shapes, with the same characteristics (i.e., w, s, t , and outer diameter, see section.II.2.1 and Fig.II.6) have a very little difference in the SNR value (Table II.2). Hence, we use the rectangular micro-coil to model the complete microprobe through the 3D electrical circuit proposed in chapter III.

II.2.4. The impact of the geometrical parameters

After we validated the methodology for magnetic field simulation and the resistive losses estimation, we simulated the impact of the dimensions of the micro-coil on its performances.

First of all, we selected the rectangular geometry; to balance the micro-coil parameters, we fixed its thickness to $t = 40 \mu m$, the value of turn number to $n = 4$. For the following simulation, we adjust the w, s and external diameter (dimension).

In Fig. II. 12, we showed the B_z fields variations generated by different dimensions of rectangular micro-coils.

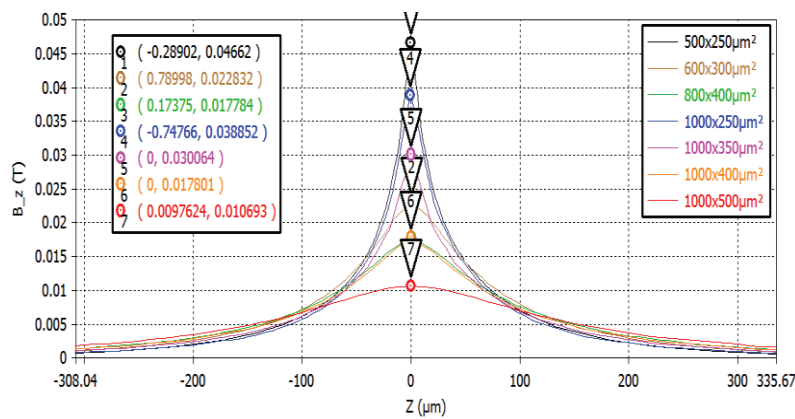


Fig. II. 12. Variation of the magnetic field as a function of the z -direction for different dimensions of rectangular micro-coil

In the following Table II. 3, we summarized the magnetic ($B_z(z = 0)$) and electrical parameters (RLC) and its deduced performance parameters (Q and SNR) for each dimension of

a rectangular micro-coil with $n = 4$, $t = 40 \mu m$. Where w is the width of the conductor, t is the thickness of the conductor, s is the distance between the turns, n the number of spiral turns, R is the resistance of the micro-coil, L is the inductance, Q is the quality factor and B_z is the z component of the field generated by the micro-coil at its centre.

Dimensions [μm^2]	w [μm]	s [μm]	R [Ω]	L [nH]	C [pF]	Q	B_z [mT/A]	SNR [$\frac{mT}{A\sqrt{\Omega}}$]
1000×500	22	20	0.518	12.468	0.185	45.319	10.68	14.839
1000×400	22	20	0.476	11.312	0.170	44.476	17.80	25.826
1000×350	18	18	0.508	11.28	0.155	41.55	18.96	26.601
1000×350	12	20	0.589	11.76	0.163	37.38	29.80	38.829
1000×250	12	20	0.538	10.59	0.149	36.902	38.72	52.789
800×400	22	20	0.393	9.042	0.133	43.189	17.84	28.458
600×300	12	20	0.359	6.620	0.100	34.74	22.91	38.236
500×250	12	20	0.283	4.998	0.078	33.273	47.02	88.387

Table II. 3. The electrical and magnetic parameters of each rectangular micro-coil at **300 MHz**, for different dimensions

The same work was performed for several dimensions of square micro-coil; the results for the magnetic field value on the centre of the micro-coil are shown in Fig. II. 13. and electrical parameters ($RLCQ$) and SNR parameters are summarized in Table II. 4.

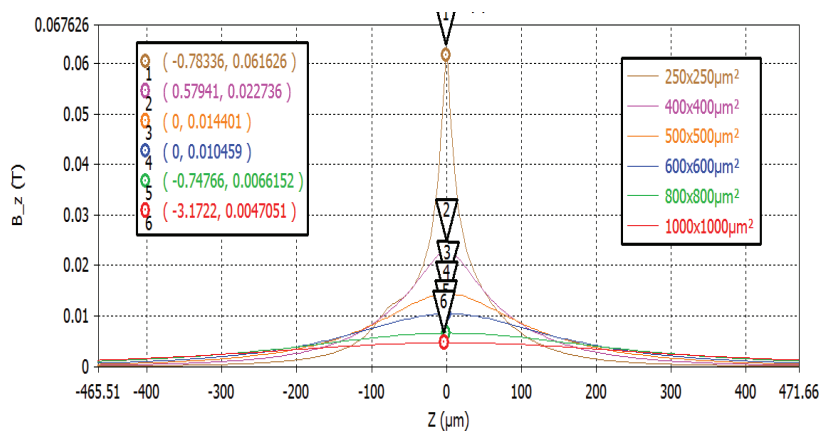


Fig. II. 13. B_z variation as a function of the z -direction, for different dimensions of the square micro-coil

Dimensions [μm^2]	w [μm]	s [μm]	B _z [mT/A]	L [nH]	R [Ω]	C [pF]	Q	SNR [$\frac{mT}{A\sqrt{\Omega}}$]
1000× 1000	22	20	4.78	18.428	0.726	0.246	47.82	5.516
800× 800	22	20	6.61	13.638	0.559	0.190	45.96	8.840
600× 600	22	20	10.45	9.040	0.392	0.133	43.44	16.73
500× 500	22	20	14.40	6.684	0.309	0.105	40.44	25.90
400× 400	22	20	22.73	4.725	0.226	0.076	39.39	47.75
250× 250	13	20	61.62	2.382	0.148	0.042	30.32	160.17
250× 250	12	12	67.22	2.930	0.182	0.083	30.33	157.67
300× 300	15	15	27.85	3.527	0.199	0.075	33.24	62.430
350× 350	18	15	23.12	4.552	0.247	0.097	34.72	46.520

Table II. 4. The electrical and magnetic parameters of each square micro-coil at **300 MHz**, for different dimensions

The smallest dimension generates the most intense field in the centre of the micro-coil geometry section, $250 \times 250 \mu m^2$ for the square geometry (Fig. II. 13) and $500 \times 250 \mu m^2$ for the rectangular (Fig. II. 12).

II.2.5. Design limitation of the smaller micro-coils

When we reduce the dimension of the micro-coils, it is essential to define the minimum outer diameter, that can be reached for the micro-coil layout design and its manufacturing. We consider the geometrical parameters such as n , w , s , p (width of the central track); the external diameters will have a threshold for the respective geometrical parameters mentioned above.

In this section, we will define the limit of design of a micro-coil, considering the fabrication constraints. It requires considering the minimal distance between microwires and the space necessary to the centre pad of the micro-coil.

The centre track links the micro-coil part with the connector track (Transmission line) through the *underpass & vias* connecting wire solution, *air bridge* or *wire-bonding* when we consider the central micro-track having the corresponding dimension ($60 \times 60 \mu m^2$) defined previously by our team in the context of the 1st prototype fabrication (pad for *wire-bonding* connecting solution). In our case, we can achieve a minimum dimension of $40 \times 40 \mu m^2$,

knowing that the smallest *wire-bonding* diameters can have 15 to 25 μm , for an aluminium bond wire [93], usually ranging from 18 μm to 33 μm in diameter for a gold wire [94]).

Through the following formula, we can define the threshold outer diameter of the micro-coil:

$$D_{out_limit} = 2n \times [w + s] + p \quad (II.24)$$

Where: n is the number of turns and s the width of the conductor and the distance between turns of the spires, p the width of the central track, w is the micro-coil wire width.

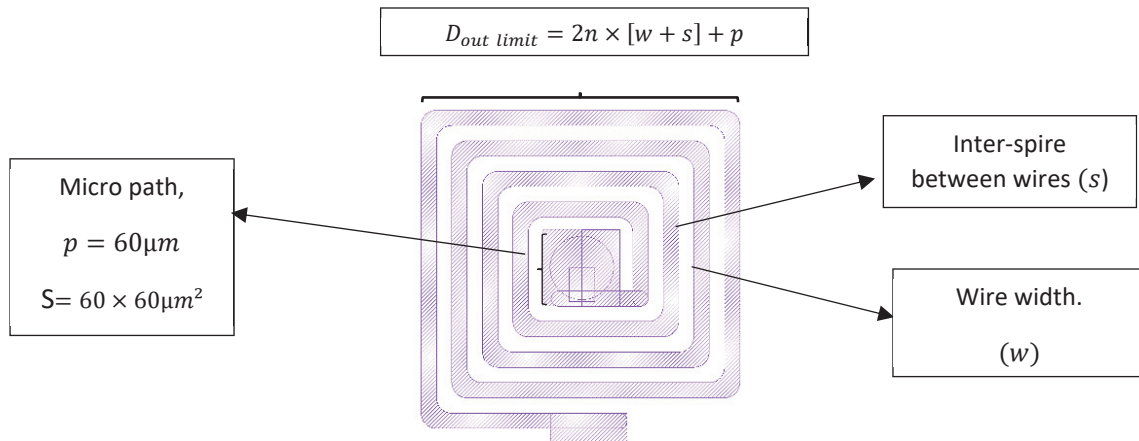


Fig. II. 14. Representation of the limiting external diameter as a function of the geometric parameters of the μ coil

To better illustrate our approach to define the threshold dimension of a micro-coil, let's take a micro-coil, with the following geometrical parameters: the number of turns ($n = 4$), conductor width ($w = 22\ \mu m$), conductor thickness ($t = 40\ \mu m$), inter-turn distance ($s = 20\ \mu m$) and width of the center micro-path ($p = 60\ \mu m$). The value of the threshold diameter can be evaluated at about $D_{out-limit} = 400\ \mu m$. This implies that the micro-coil must have a minimum surface of $400 \times 400\ \mu m^2$. Reducing the size of the surface of the micro-coil to increase its field strength means to vary the parameters n, w, s or p , which could modify the value of the resistance.

Since the number of turns has already been optimized to $n = 4$, we proposed to keep the number of spires turns n and the dimension of the track as optimal for the issue of its manufacture. Therefore, we obtained suitable s and w for the manufacturing of micro-coils smaller than $400 \times 400\ \mu m^2$.

For micro-coils dimensions of $500 \times 250 \mu m^2$, $600 \times 300 \mu m^2$, $1000 \times 250 \mu m^2$, we proposed the value of the following size for the w, s parameters suitable for our limited manufacturing feasibility.

n	w [μm]	s [μm]	$D_{out-limite}$ [μm]
4	12	12	250
4	15	15	300
4	18	18	350

Table II. 5. Geometric parameters with the limiting diameter for the feasibility

Here, we keep as limit dimensions $400 \times 400 \mu m^2$ being the optimal one, but we propose also to manufacture a square of $250 \times 250 \mu m^2$ with the parameters s and w predefined in Table II. 5. In this way, we are going to confirm it feasibility for prototype microfabrication with wire-bonding connecting solution.

<i>Dimensions</i> [μm^2]	<i>Geometry</i>	w [μm]	S [μm]	R [Ω]	L [ηH]	B_z [mT]	Q	SNR [$\frac{mT}{A\sqrt{\Omega}}$]
1000 \times 500	Rectangular	22	20	0.518	12.468	10.68	45.319	14.839
1000 \times 400	Rectangular	22	20	0.476	11.312	17.80	44.476	25.823
500 \times 500	Square	22	20	0.309	6.684	14.40	40.44	33.94
400 \times 400	Square	22	20	0.226	4.725	22.73	39.39	63.04
250 \times 250	12	12	67.22	2.930	0.182	0.083	30.33	157.67

Table II. 6. Geometrical configurations to be manufactured, $n = 4$ and $t = 40 \mu m$.

According to our results presented in the Table II. 6, we can notice that the square geometries ($500 \times 500 \mu m^2$) present the highest SNR ratio than the rectangular ($1000 \times 500 \mu m^2$). Therefore, it would be wise to say that the best configuration of micro-coil is the square geometry for the dimensions given in Table II. 6.

II.3. Simulation of the magnetic field generated by the microprobe using COMSOL Multiphysics.

COMSOL Multiphysics is a software-based on Finite Element Methods (FEM). It is one of the best-known commercial software that is used for the analysis of characteristics of mechanical, electrical and magnetic systems; It is also dedicated to studying the heating transfer of various 3D systems. Mainly for our microprobe modelling study, we used several modules such as RF Module, AC/DC Module, Optimization Module, live Link for MATLAB Module, CAD import Module and Live Link for SOLIDWORKS.

As previously mentioned, we use this software to simulate the magnetic field generated by a 3D model of the microprobe. So, we briefly introduced the main electromagnetics principle, particularly Maxwell's equations which is a fundamental base of the software RF module to calculate the magnetic field in a 3D system through the Finite Element Method (FEM).

II.3.1. Electromagnetic principle of the approach

To build a micro-coil model and simulate its electromagnetic behaviour as an RF receiver in MRI, we need to deal with a set of equations named after Maxwell equations (see appendix A.1) and solve them accurately to better approach the model to the actual system. In electromagnetism, modelling is naturally complicated, especially in a three-dimensional representation, vector character of the manipulated magnitudes and the relative complexity of the associated mathematical equations. Above all, the modelling strategy is rarely apparent, given the diversity of the different possible formulations (*e.g.*, the possibility of using Maxwell's equations directly or of utilizing the propagation equations, of constructing an equivalent problem or not, of working in the harmonic regime or not, of choosing one coordinate system or another). For our case, we used the linear solver and a physics-controlled mesh. We carried out a stationary and frequency domain study (quasi-stationary approach).

II.3.2. Simulation of substrate impact to the magnetic field

The microprobe prototype is fabricated on a silicon or glass substrate. On the previous approach modelled in section II.2.1.1, we modelled the copper micro-coil, and the substrate part was neglected. In this section, we first design the complete micro-coil, which is the design of a micro-coil in a substrate. Then, we simulate the magnetic field generated in the case of

different substrates (Glass, Silicon, PEEK, PDMS, Quartz); at the end, we will perform a simulation showing the impact of the frequency.

The table II.7 list the physical properties of substrate used for our simulations [95] [96]. Where σ is the electrical conductivity, λ is the thermal conductivity, ϵ_r and μ_r are the relative permeability and permittivity, C_p is the heat capacity by mass and ρ is mass density of the material.

Martials	σ (S/m)	ϵ_r	μ_r	λ (W/mK)	C_p ($J/Kg.K$)	ρ (kg/m^3)	Thickness (μm)
Copper	5.99×10^7	1	1	400	385	8700	40
Glass	10^{-12}	3.9	0.549	1.4	730	2210	400
Silicon	2.5×10^{-4}	11.7	0.983	130	700	2329	400
PEEK	5×10^{-12}	2.2	1	1.3	1750	1200	400
PDMS	2.5×10^{-14}	2.7	1	0.16	1460	970	400
Quartz	1.3×10^{-18}	3.8	1	3	820	2600	400
Diox. of silicon	10^{-15}	3.9	0.549	1.3	1000	2770	2
Air	4×10^{-15}	1	1	0.026	1006	1.177	--

Table II. 7. The physical properties of the substrate material used for our simulations, at room temperature.

We begin by modelling the rectangular micro-coil (the best geometry), including the substrate part and then inserting it inside a system (airbox) to propagate the magnetic field. This model was conceived using COMSOL Multiphysics, more precisely the RF module. We needed to ensure that the electromagnetics simulations are reliable and robust.

The airbox volume was $4cm \times 2mm \times 8mm$, hight of the box correspond to at least 10 time as recommended, and then we applied as limited condition of the system, the infinite coordinate to avoid the reflexion or absorption of the magnetic fields generated by the micro-coil

Fig. II. 15. a) where the micro-coil on substrate support is modelled, the red line help to define the direction in which the magnetic field will evaluate (field of the view of the micro antenna). In Fig. II. 15.b), we plot different plans in which the magnetic field is propagated.

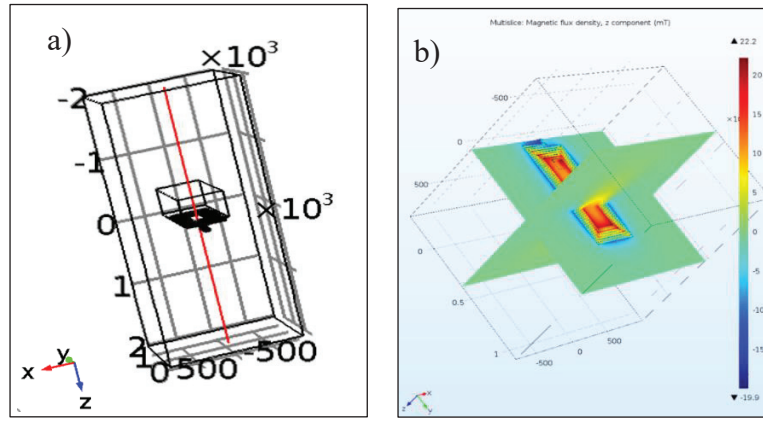


Fig. II. 15. a) The micro-coil modelled on the substrate inside a rectangular system. b) 3D view of the magnetic field variation on the parallel and perpendicular plan against micro-coil

Fig. II. 16 shows the field line propagated on the parallel micro-coil plan. It can be highlighted in the figure the magnetic field line symmetry, according to both perpendicular plans. The field line is more concentrated on the coil centre and at the conductor vicinity.

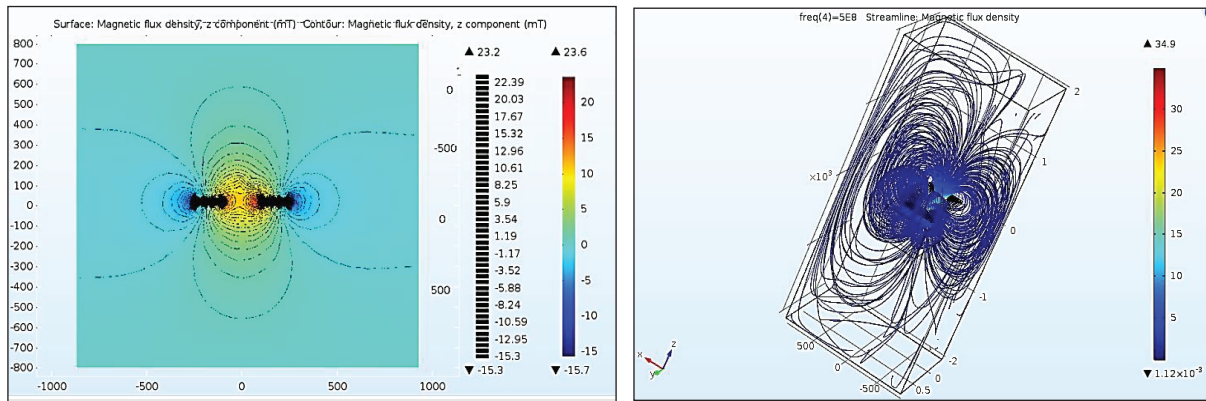


Fig. II. 16. Lines of the magnetic field generated by the micro-coil: 2D view (a) situated at $z = 600 \mu m$ and 3D view (b)

From plotted data in the Fig. II. 16, we could extract the 1D plot of the magnetic field to analyse how the z-component of the magnetic field change as a function of the perpendicular direction at several working frequencies.

For our study, it is pertinent to see how the frequency and substrate can impact the magnetic field generated by the micro-coil, a simulation of the micro-coil designed on a silicon substrate. We plotted the magnetic field varies with the perpendicular direction (*z-direction*). Thus, in Fig. II. 17, we show the results of the frequency impact in a frequency range of *200 MHz to 900 MHz*.

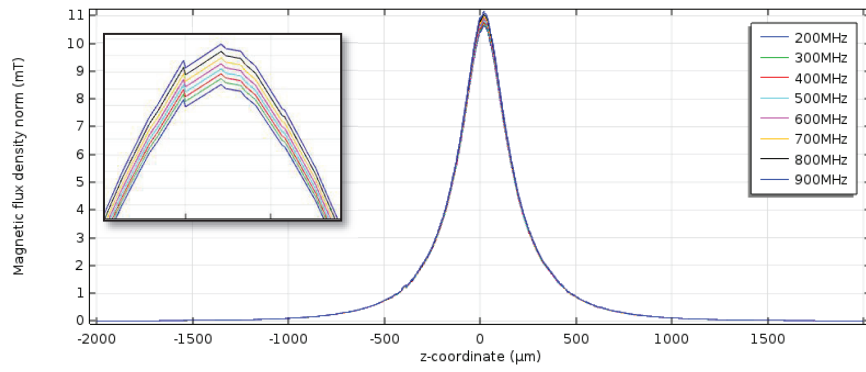


Fig. II. 17. Profile of the z magnetic field component from several working frequencies.

In Fig. II. 18, we have shown the impact of the substrate. For this, we fixed the frequency simulation (300 MHz); Then we plotted the magnetic field for fives substrates (Glass, Silicon, PEEK, PDMS, Quartz).

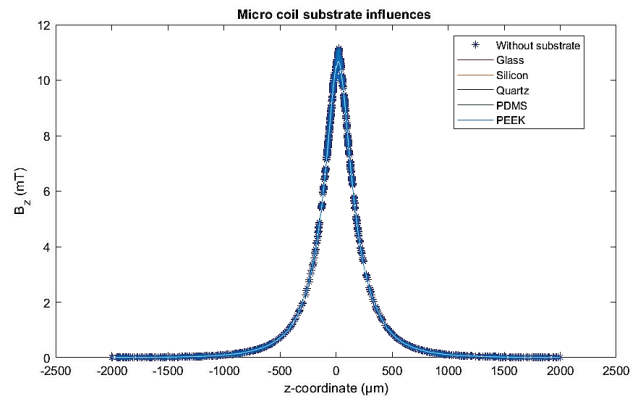


Fig. II. 18. Magnetic field z component as a function of the z-direction for substrates types

We studied how the magnetic field varies in the z-direction (perpendicular direction) and the plane containing the microprobe. Here, we have only the micro-coil (active part) of the microprobe designed on a substrate. We change the properties of the materials which correspond to each type of substrate for our study. We noted that the magnetic field did not significantly change when we changed the substrate type (Fig.II.18). As well as, the magnetic field did not considerably change when we varied the frequency from the range of 200 MHz to 900 MHz (Fig.II.17)

II.3.3. The magnetic field generated by the complete microprobe prototype

The microprobe 3D model simulated on COMSOL Multiphysics we conceived through SOLIDWORKS, and then we imported to the COMSOL workflow thanks to the COMSOL module (Live Link SOLIDWORKS and CAD module). We import the 3D model builder CAD (Computer Aided Design) file. The model designed is shown in Fig. II. 19 is the optimized

shape of the microprobe (prototype 3), which was designed based on the previous prototype fabricated by our team. This form represents an enhancement compared with the earlier versions (1st and 2nd prototypes). Here, we change the *wire-bonding* and *underpass & vias* to a new method (*air-bridge*). The next chapter will report its modelling and performance study in terms of electrical parameters.

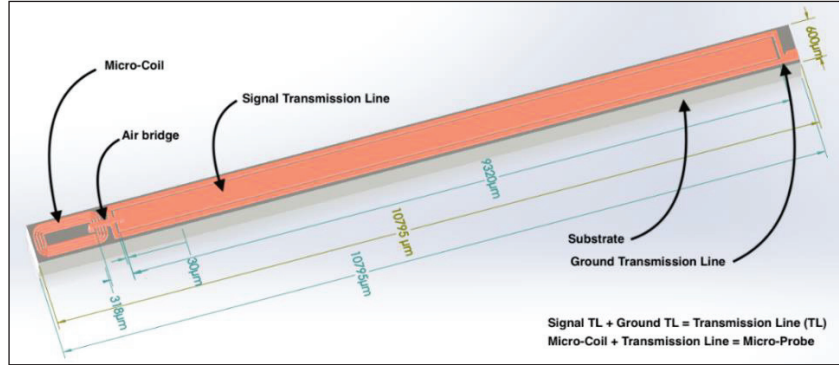


Fig. II. 19. The 3D layout of the proposed microprobe: new prototype (Coil Needle) with rectangular coil

The microprobe layout design shown in Fig. II. 19 includes different parts such as:

- A micro-coil (active part).
- A micro-Transmission Line (micro-path) to reach the region of interest (ROI), at a depth of 9 mm inside the animal brain.
- A micro-wire connecting part (*Airbridge* or *Wire-bonding* or *underpass & vias*), ensuring the connection of the centre of the micro-coil to the signal Transmission line (on the centre track).

The implantable microprobe consists of a copper layer deposited onto a wafer (Glass or silicon substrate). The copper is either directly deposited at a glass substrate or a Silicon dioxide layer for the silicon substrate. For this simulation, we have used the rectangular micro-coil as active part with thickness $t = 40 \mu m$, inter-spiral gap $s = 20 \mu m$, the wire width $w = 22 \mu m$, with $1000 \times 500 \mu m^2$ surface section occupied.

Our complete simulated system is represented by the microprobe inside a spherical volume of 0.6 cm in diameter, centred on the surface of the active part of the microprobe (rectangular micro-coil).

Fig. II. 20 shows the magnetic field lines generated around the micro-coil and the micro-transmission line. We note that the magnetic field is higher at the centre of the micro-coil. Nonetheless, the micro-transmission line also irradiates a magnetic field that is not negligible.

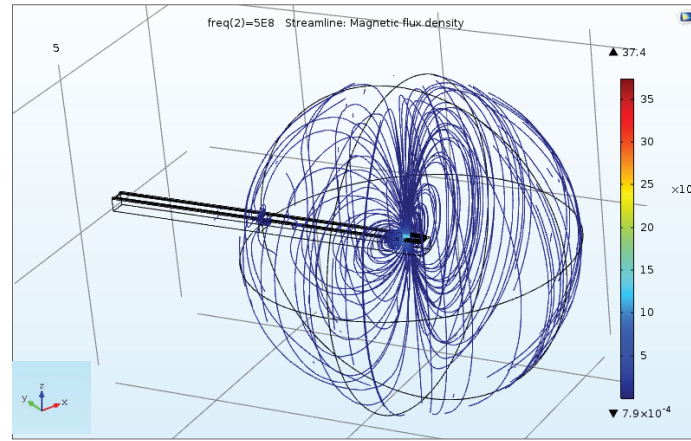
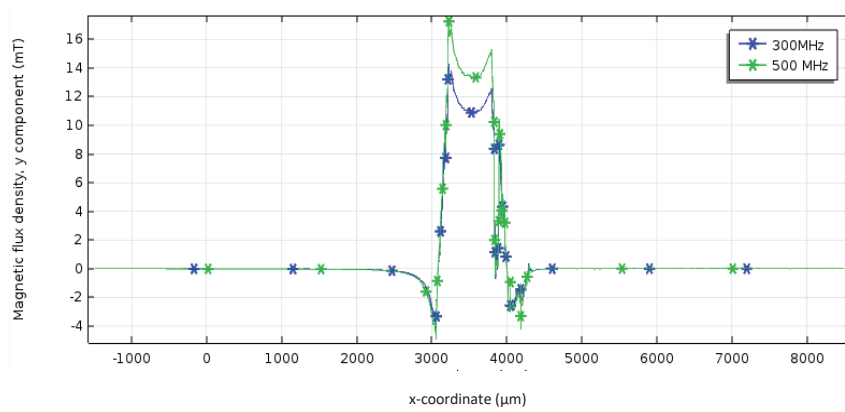


Fig. II. 20. 3D view of the microprobe magnetic field lines

Even if microprobe transmission line also generates a magnetic field, it does not impact the magnitude of the magnetic field generated by the micro-coil (active part).

The objective of the above simulation (Fig.II.20) was to study how the component (B_z) of the field generated by the microprobe varies along its perpendicular direction (Oz axis) and its variation in the microprobe direction, according to the z -direction (Oz). Thus, a 1D plot of the magnetic field z -component is shown in the Fig. II. 21 and Fig. II. 22, for two frequency cases and only on the silicon substrate. This helps us quantify and compare the intensity of the magnetic field generated by the micro-coil against the transmission line.

Fig. II. 21. Magnetic field z component as a function of microprobe parallel direction (Ox)

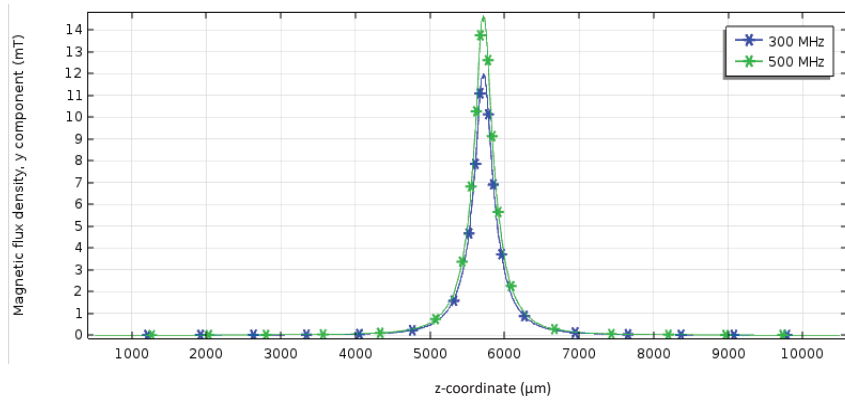


Fig. II. 22. Magnetic field z component as a function of microprobe perpendicular direction (Oz).

Fig. II. 22 shows that the magnetic field generated by the microprobe at 300 MHz is lower than at 500 MHz in the centre ($z = 5850 \mu m$). That simulation was performed for a design of the microprobe on the silicon substrate.

Table II. 8 shows the magnetic field on the centre of the micro-coil for two frequency cases.

Working frequency	300 MHz	500 MHz
Micro-coil MF : B_z ($z = 0 \mu m$) [mT]	10.62	10.75
Microprobe MF : B_z ($z = 5850 \mu m$) [mT]	12.01	14.90

Table II. 8. Magnetic field z component as a function of microprobe perpendicular direction (Oz)

We compared the magnetic field generated by the simplest model (micro-coil) and the complete one (microprobe). The results show a magnetic field changing when we change the model, as well as the working frequency.

Conclusion

In this chapter, we reported a new methodology to model the implantable NRM microprobe in terms of the magnetic field and resistive loss. In section II.1.1, we reviewed the optimization work made previously by our team, and we confirmed that from four geometries (square, circular, rectangular and ellipsoidal), the rectangular one is the best regarding its higher magnetic field at its centre ($B_1(z = 0) = 10.1 \text{ mT}$). Even if its magnetic field variation decreases faster than the one from the other geometry (Fig. II. 5).

We also extrapolated the conception and 3D modelling of the complete microprobe, thanks to COMSOL Multiphysics, simulating the magnetic field in the case of 300 MHz and 500 MHz working frequency. We noted that the magnetic field changes according to the model, and a significant magnetic field change from the coil part is indicated when we change the working frequency. Moreover, we simulate the impact of the substrate to the magnetic field on the simple design of the micro antenna since one of the complete models rests complex to perform due to the long computational time.

Our simulations lead to the prediction and validation of an optimal prototype design and validating using commercial software and analytical calculation to estimate the losses. As mentioned, the simulation task takes considerable time, and it is pretty challenging to deduce the impact of each part that constitutes the microprobe device. Work will be done, intending to enhance our methodology and get a complete scientific explanation of the results from our simulations work. Using this methodology, we proposed an electrical circuit that models the complete Microprobe (micro-coil, connecting micro-wire and TL) in chapter III.

Chapter III

3D – Electrical model of the Microprobes and prediction of their performances criteria (Q – factor and SNR)

One of the NMR technique's main challenges is to improve the sensitivity in terms of Signal to Noise Ratio (SNR) and spectral resolution to detect weak metabolites concentration in a small region of interest ($\text{ROI} \sim 2 \mu\text{L} - 3 \mu\text{L}$). An approach that increases sensitivity consists in miniaturizing of the NMR receiver. Thus, the RF coil size will be adapted to the sample dimension that minimizes its equivalent resistance R_s , enhances the magnetic field B_1 , and increases the SNR. Another way is to improve its performance by optimizing the microfabrication process [57] [63].

However, microfabrication processes involve long and costly steps. Simulation might be a way to shorten this time and save enough effort for experimentation. Simulations can also provide significant data trends, a comparison between prototypes and process options. So, we developed a platform called 3D Transmission Line Extractor (3D-TLE), in collaboration with INL (Institut des Nanotechnology de Lyon). This tool was used to design planar NMR micro antennas and calculate their equivalent RLC parameters analytically.

In this chapter, we also presented the AI approach, based on the Artificial Neuronal Network (ANN) model to demonstrate the possibility of predicting the microprobe performance criteria (Q factor and Resistance) from its geometrical dimensions, electrical properties of the used substrate, and its working frequency. Our ANN model was trained and tested through the dataset generated by simulations (6621 observations).

III.1. 3D – TLE (Transmission Line Extractor)

3D-TLE is a platform created in MATLAB GUI (Graphical User Interface) which can generate the *netlist* of a given structure. 3D TLE can automatically extract impedances of arbitrary shapes and materials. This extractor is 100% compatible with SPICE (Simulation Program with Integrated Circuit Emphasis) core simulator, like ADS (Advanced design system).

Our in-lab-made software (3D-TLE) is based on the parasitic effects, and we can see in Fig. III. 1 the graphical user interface of the platform.

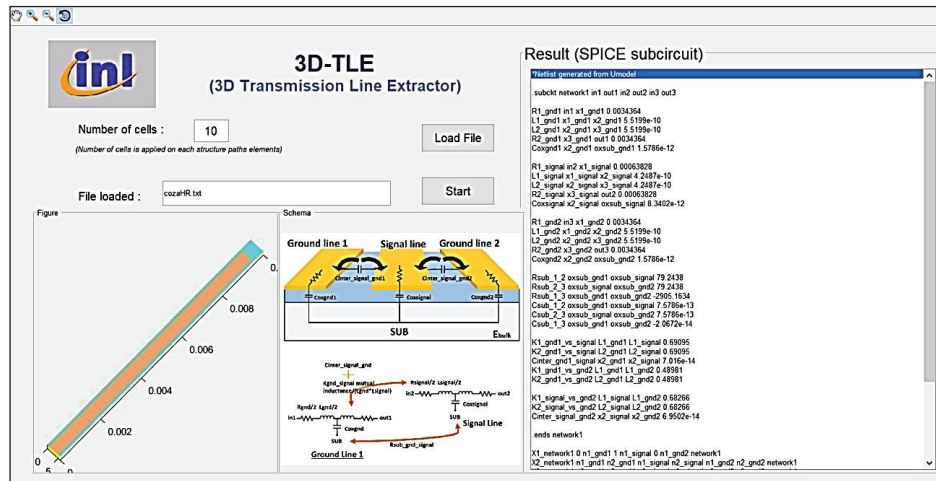


Fig. III. 1. User Interface of 3D-TLE (Transmission Line Extractor)

This extractor is based on the closed-form expressions of the RLCG (Resistance, Inductance, Capacitance, Conductance) compact models that were built from the Transmission Line Method and 3D full-wave electromagnetic analyses [97].

The RLCG network is modelled with passive components, resistances and inductances to model the signal propagation and capacitance or conductance to model the parallel elements or the interconnect environment. The proximity (or track coupling) and skin effects are also taken into account in the compact model description [98] [99].

III.1.1. The principle of 3D -TLE

Fig. III. 2 shows the specific syntax and statements for generating the 3D structure design and views. The simulations are performed in two main steps: first, the creation of a *.txt* file with the system information and then a *netlist* with results of the simulation are generated.

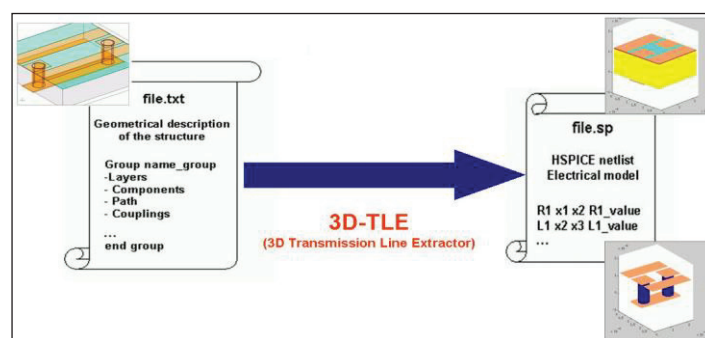


Fig. III. 2. 3D-TLE extraction tool environment [100]

The data saved in a `.txt` file contain the geometrical parameters and technical description (material electrical properties and structure coupling). It also allows the design of the 3D structure of the modelled device (microprobe).

As mentioned above, all parameters are defined in a `.txt` file (For more detail, see appendix A.3 and 4). The file is composed of four classes, namely:

- **Layers:** represents the basic information about the layers;
- **Components:** defines every single component;
- **Paths:** represent the interconnections between components;
- **Couplings:** defines the coupling relationship between components;

After running the platform, the *netlist* of a 3D structure that corresponds to its equivalent RLCG circuit can be exportable under any CAD (Computer Aided Design) software; for our case, we used ADS® (Advanced Design System) through S-parameters simulation and Q factor.

The previously presented syntax (Fig.III.2) represents the base to build a 3D model of the devices and extract their electrical parameters. Among structures that compose a 3D device, we can list Underpass, Vias or TSV (Through Silicon Vias), metallic strip lines on a substrate, substrates, oxides layer, etc.

For the following study, we will present how to model the *underpass & vias* part, the approach to model the losses on the substrate in the case of high frequency, which are the most complicated parts to consider when we design the complete electrical model of the microprobe.

III.1.2. The model of Underpass & Vias (TSV - Through Silicon Vias)

3D interconnecting requires the consideration of the global electrical model to evaluate complete system performance correctly.

The TSV can be defined as a metal conic structure surrounded by an oxide layer and filled by anti-corrosion (Fig. III. 3).

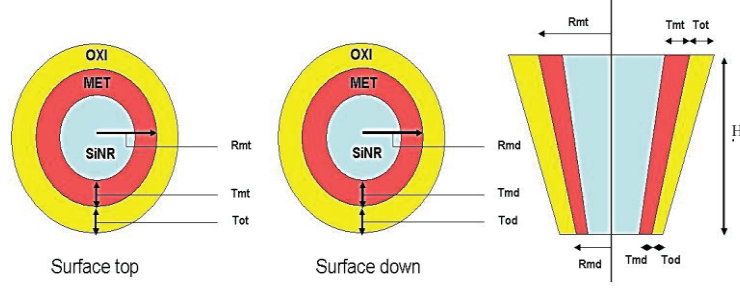


Fig. III. 3. 3D Compact model of the TSV as defined in 3D-TLE [96]

As shown in the Fig. III. 4, the TSV electrical model consists of serial elements (partial Resistance and Self-Inductance) representing the signal propagation and also parallel elements modelling the TSV environment coupling. In particular, when these elements are fed by a current, its vertical current path goes through the oxide layer and reaches the ground lines. Only the inductive coupling between TSV is considered for the Low Frequencies.

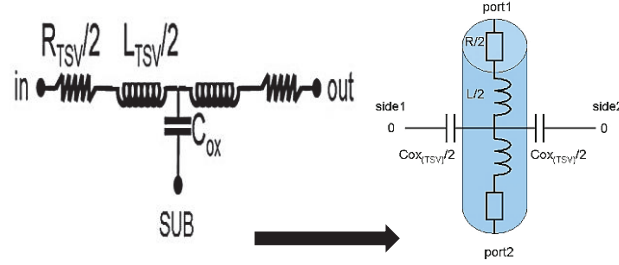


Fig. III. 4. The electrical model of the TSV orientation according to its I (1) /O (2) ports [99] [98]

$$R_{TSV} = \frac{H}{\pi \sigma} \frac{1}{2(R_{met_top} T_{met_down} - R_{met_down} T_{met_top})} * \ln \left(\frac{T_{met_down}}{2R_{met_down} - T_{met_down}} \frac{2R_{met_top} - T_{met_top}}{T_{met_top}} \right) \quad (III.1)$$

$$C_{OX-TSV} = \frac{\epsilon_0 * \epsilon_r * 2\pi * H}{T_{oxi_top} - T_{oxi_down}} \left[R_{oxi} + \frac{R_{oxi_top} T_{oxi_down} - R_{oxi_down} T_{oxi_top}}{T_{oxi_top} - T_{oxi_down}} * \ln \left(\frac{T_{oxi_down}}{T_{oxi_top}} \right) \right] \quad (III.2)$$

With:

$$R_{oxi} = (R_{oxi_top} - R_{oxi_down}) \quad (III.3)$$

$$R_{oxi_top} = R_{met_top} + T_{oxi_top} \quad (III.4)$$

$$R_{oxi_down} = R_{met_down} + T_{oxi_down} \quad (III.5)$$

Self and mutual inductances for cylindrical conductors are considered, and we have defined them as the following (III.6 and III.7) equations.

$$L_{TSV} = \mu \frac{H}{2\pi} \left(\sinh^{-1} \left(\frac{H}{D/2} \right) + \frac{D/2}{H} - \sqrt{\left(\frac{D/2}{H} \right)^2 + 1} + \frac{1}{4} \right) \quad (III.6)$$

$$M_{TSV} = \mu \frac{H}{2\pi} \left(\sinh^{-1} \left(\frac{H}{l_{und}} \right) + \frac{l_{und}}{H} - \sqrt{\left(\frac{l_{und}}{H} \right)^2 + 1} \right) \quad (III.7)$$

In our case, *underpass & vias* altogether were modelled as a *U* structure, where both TSV (vias) are connected toward a signal Transmission Line, which can be easily modelled rectangular micro-transmission Line.

Series elements (partial inductances and resistors) model the signal propagation through the TSV or transmission Line connector. Parallel components are used to describe the interactions between the TSV and its environment, for example, the substrate or another compound close to the TSV in a high-frequency case. The currents propagate vertically from the oxide layer to the ground lines. A resistor models this path in parallel with a capacitance plus the capacitance of the thin oxide layer (SiO_2) separating the TSV from the substrate [98]. Finally, to estimate all the interactions, it is required to extract the substrate losses in terms de resistance and capacitance value to quantify its contribution to the electrical loss of our NMR implantable device.

III.1.3. Substrate losses in the high-frequency domain

In our working frequency domain (200 MHz to 900 MHz), the effects of the substrate must be added to the electrical circuit to model our device. Generally, we can represent the substrate as an *RLCG* network to estimate the system's loss more accurately. The modelling becomes quickly complex when the coupling effects are considered between all the components of the system (TSV, underpass, signal and ground transmission line, micro-coil and oxides layer in the case of the silicon substrate). In addition, the substrate can be anisotropic with different doping values, i.e., different resistivity and permittivity throughout a specific volume. The substrate is therefore modelled as a stack of parallel heterogeneous dielectric layers because of the doping [100].

In this perspective, an extraction method was proposed relying on the Transmission Line method applied to a multi-layered substrate and the Green electrostatic functions [101] [102]. The method is incorporated in 3D-TLE platform, and we used it for our global modelling of the microprobe system [105]. As in the case of the microprobe model, a current is applied on a contact pad located on the top or inside the substrate. A voltage is then measured at the level of another contact, enabling to deduce impedance matrix $[Z_T]$ whose dimensions correspond to

the number of contacts. Resistance generally models the substrate coupling between two elements in parallel with a capacitance [99].

The approach was already integrated into 3D - TLE to model the compound of the microprobe, such as: *underpass & vias* and the transmission line (TL) of the microprobe embedded on the substrate. Note that TL corresponds to a copper layer embedded on a substrate surface. The transmission line was designed as a coplanar waveguide at the top of a high resistive substrate with a SiO_2 layer. The coplanar lines (TL) were previously reviewed in chapter II. It can be assimilated into three lines (*ground – signal -ground*), and the vias with substrate coupling have been modelled.

III.2. The electrical circuit of the implantable NMR microprobe

We proposed an equivalent 3D electric circuit that models the microprobe on a glass and a silicon substrate, respectively. To start, we presented a brief review of the electrical circuits (Previous electrical models) to study the NMR receiver performance in terms of electrical losses. Then an analytical study is done on the impedance circuit's equations allowing us to calculate the performance parameters like S_{11} parameters and deduce the Q factor.

This Section presents advancements in 3D-TLE development and illustrates its efficiency and accuracy in our application case: Transmission Line (TL) modelling of an implantable NMR microprobe and the *underpass & vias* within a substrate.

III.2.1. The RLC electrical circuit and PI model

The simplest representation of an NMR microprobe or any passive RF receiver is an RLC circuit resonating at the *Lamor frequency* of the sample being studied. This representation is only valid as long as the wavelengths involved are much greater than the length of the microprobe conductor. Otherwise, the propagation phenomena are no longer negligible. Therefore, more complex models must be considered to represent the different parts of the RF receiver correctly with an equivalent circuit and to take into account the effective addition of extra components that induce non-negligible capacitive and inductive effects (Substrate, *underpass & vias*, micro-transmission line and oxide layer in the case of silicon substrate).

For the RLC circuit, the capacitor can be placed in series or parallel with the Resistance and inductor giving resonant circuits. Some proprieties of the RLC parallel and series model of our planar micro-coil was studied by simulation in the thesis of J. Trejo Rosillo [37].

The RLC electrical circuit in Fig. III. 5 models a planar micro-coil fabricated on a glass substrate; this model does not take into account the loss on the substrate. The RLC circuit characteristics correspond to a passband filter. It describes the resonance behaviour of an NMR coil widely at reception.

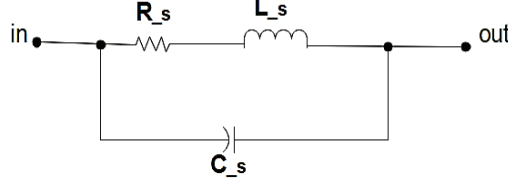


Fig. III. 5. Electrical circuit that models the micro-coil (RLC model)

Based on the RLC micro-coil electrical circuit, we can show that the Z_s impedance is calculated by the formula:

$$Z_s = \frac{R_s + j\omega L_s}{1 + j\omega R_s C_s - \omega^2 C_s L_s} \quad (\text{III.8})$$

We can deduce the previous impedance formula as follows:

$$Z_s = \frac{R_s}{(1 - \omega^2 C_s L_s)^2 + \omega^2 R_s^2 C_s^2} + j\omega \frac{(L_s - R_s^2 C_s - \omega^2 C_s L_s^2)}{(1 - \omega^2 C_s L_s)^2 + \omega^2 R_s^2 C_s^2} \quad (\text{III.8.1})$$

When the system resonates, the frequency of the system is defined ω_0 :

$$\omega_0 = \frac{1}{\sqrt{C_s L_s}} \quad (\text{III.9})$$

We can deduce the quality factor of the RLC circuit as follows when the receiver achieves the resonance condition.

$$Q_{\text{RLC}} = \frac{L_s \omega_0}{R_s} \cong \frac{\text{Im}\{Z_s\}}{\text{Re}\{Z_s\}} \quad (\text{III.10})$$

With: R_s the micro-coil resistor, L_s self-inductor and C_s is the capacitor from the close wires coupling.

When the micro-coil is fabricated on the silicon substrate, the receiver can be modelled by PI model [103] [104]. This model (Fig.III.6) considers the main physical phenomena, particularly the substrate effect, because, in the case of the silicon substrate, there is a high resistive loss while flowing a current throughout the micro-coil.

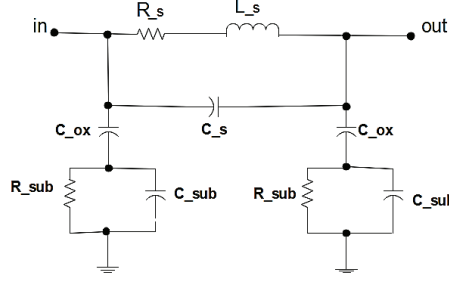


Fig. III. 6. The electrical circuit that models the micro-coil on the silicon substrate (PI Model)

When we apply a voltage to a conductor wire, it generates an electrical field throughout the micro-coil wire that allows the charges (electrons) motion along the conductor. During that, the resistive loss phenomenon appears. The most important phenomenon to consider here is magnetic induction. The current applied at the micro-coil terminal can generate a magnetic field. This phenomenon is modeled by resistor R_s in Serie configuration with an inductor L_s [108]. So, the planar coil can generate a second electric field because of the electric potential between two closes wires. This electric field generates a capacitive coupling between the different turns of the micro-coil (micro-coil closed wires), which is modelled by a parallel capacitor C_s . The resistive losses and capacitive coupling from the substrate are due to a second electric field between the coil, the dielectric layer (Si_2O) and the substrate. That is why the electrical losses on the substrate as well as on the oxide layer were modelled by a capacitor C_{ox} in serie configuration with $R_{subst} // C_{subst}$.

To study the performance of the electrical circuit, in terms of the analytical calculation of Q factor parameter, Resistance and Inductance, we can transform the PI model into a simple block diagram to calculate impedance and then deduce other parameters as Q factor, Resistance and Inductance [106]. The block diagram is composed of the RLC impedance in parallel with an oxide & substrate impedance (Fig. III. 7). It simplifies the calculation considerably.

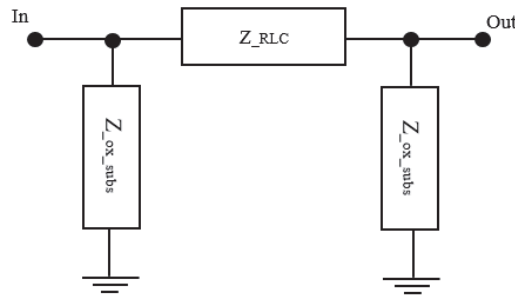


Fig. III. 7. Model PI block diagram

The equivalent impedance, from the PI model diagram, can be analytically determined [106] :

$$Z_{PI} = \frac{2Z_s \cdot Z_{ox-subst}}{Z_s + 2 \cdot Z_{ox-subst}} \quad (III.11)$$

With:

$$Z_{ox-subst} = \frac{1}{j\omega C_{ox}} + \frac{R_{sub}}{1+j\omega R_{sub}C_{sub}} \quad (III.12)$$

From the Z_{in_out} equation, we can calculate the Q factor analytically as follows:

$$Q_{PI} = \frac{I_m\{Z_{PI}\}}{Re\{Z_{PI}\}} \quad (III.13)$$

From the literature, it was already demonstrated that the Q factor of the PI model could be calculated by the equation [107]:

$$Q_{PI} = \frac{L_s \omega_0}{R_s} \times \underbrace{\frac{R_p}{R_p + \left[\left(\frac{\omega_0 L_s}{R_s} \right)^2 + 1 \right] R_s}}_{\text{Loss from the substrate}} \times \underbrace{\left[1 - \frac{R_s^2 (C_s + C_p)}{L_s} - \omega^2 L_s (C_s + C_p) \right]}_{\text{The self-resonance of the model}} \quad (III.14)$$

With:

$$R_p = \frac{1}{\omega^2 C_{ox}^2 R_{sub}} + \frac{R_{sub} (C_{ox} + C_{sub})^2}{C_{ox}^2} \quad (III.15)$$

$$C_p = C_{ox} \times \frac{1 + \omega^2 (C_{ox} + C_{sub}) C_{sub} R_{sub}^2}{1 + \omega^2 (C_{ox} + C_{sub})^2 R_{sub}^2} \quad (III.16)$$

The equation given by Yue and Wong [107] illustrates the complexity of the electrical circuit to model the micro-coil in a silicon substrate. In equation (III.14), we can see that the quality factor also depends on the substrate losses and the self-resonance of the model.

Note that the previous models (RLC and PI) represent the electrical circuit of micro-coil, considering all physical phenomena but still needing some enhancement to model the NMR implantable microprobe. In this perspective, we proposed in Section III.2.2 a complete model that includes all parts of the microprobe that considers all the capacitive and inductive coupling and the losses from the substrate part. Note that we define here as microprobe, the composition of the micro-coil, in addition to the micro transmission line (micro-path) and a connecting wire (*underpass & vias, wire-bonding or air-bridge*).

III.2.2. Our proposed microprobe electrical circuit

In Fig. III. 8, we show the complete electrical circuit that models the microprobe on glass.

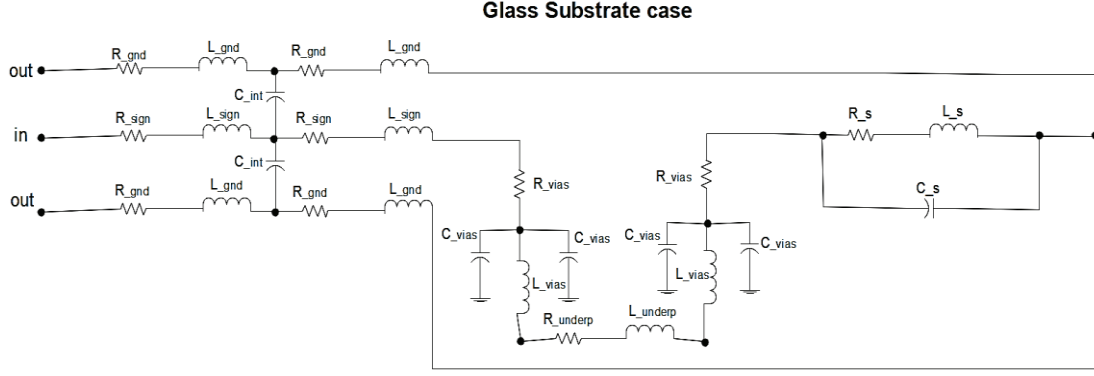


Fig. III. 8. The electrical circuit modelling the microprobe on a glass substrate (complete model)

As we know, conductor wires can be modelled by a series association of a Resistance with an inductor and two close wires by a capacitive effect.

Note that the Q factor of our complete model was deduced by calculating the complete impedance of the electrical circuit. The impedance expression can ever be written as a composition of a real impedance part and an imaginary part.

From the complete electrical circuit of the microprobe on the glass substrate, we determined the Q-factor analytically as detailed in the following formulas:

In the first place, we define: $Z_i = R_i + j\omega L_i$ with the notation: $i \in \{sign, gnd, und, vias\}$.

$$Z_{\mu coil-TL-und\&vias} = \frac{Z_{\mu coil_und_vias}}{2j\omega C_{int}Z_{\mu coil_und_vias}+1} + Z_{sign} + \frac{Z_{gnd}}{2} \quad (III.17)$$

$$Z_{\mu coil_und_vias} = Z_{sign} + \frac{Z_{gnd}}{2} + Z_{und\&vias} + Z_s \quad (III.18)$$

$$Z_{und\&vias} = 2 \cdot R_{vias} + \frac{Z_{und}+2j\omega L_{vias}}{1+j\omega C_{vias} (2j\omega L_{vias}+Z_{und})} \quad (III.19)$$

The Q factor is given by the equations following:

$$Q_{\mu coilTL_und_vias} = \frac{\text{Im}\{Z_{\mu coilTL_und_vias}\}}{\text{Re}\{Z_{\mu coilTL_und_vias}\}} \quad (III.20)$$

Where:

$$R_{\mu coilTL_und_vias} = \text{Re}\{Z_{\mu coilTL_und_vias}\} \quad (III.21)$$

$$L_{\mu coilTL_und_vias} = \frac{\text{Im}\{Z_{\mu coilTL_und_vias}\}}{\omega} \quad (III.22)$$

Our analytical calculations were done, associating the complete electrical circuit with a block diagram (Fig. III. 9) representing different main parts of the microprobe. Therefore, the block

diagram simplifies how to handle the calculation of the model impedance and to deduce the Resistance, Inductance and Q-Factor (RLQ) parameters of the system (complete microprobe). Following the same procedure, we could carry out the analytical calculations of the equivalent impedance of the microprobe model on the silicon substrate.

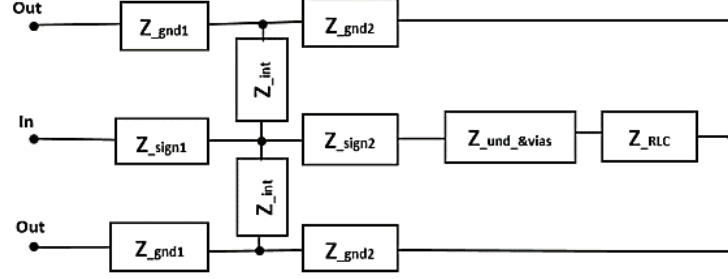


Fig. III. 9. Block diagram of the electrical circuit of microprobe on a glass substrate

Fig. III. 10 shows the complete electrical circuit to model the microprobe on a silicon substrate. This model is more complex compared with the microprobe model on the glass substrate (Fig.III.8) due to the consideration of the resistive loss on the substrate, induced by the micro-coil, transmission line, in addition to the *underpass & vias*.

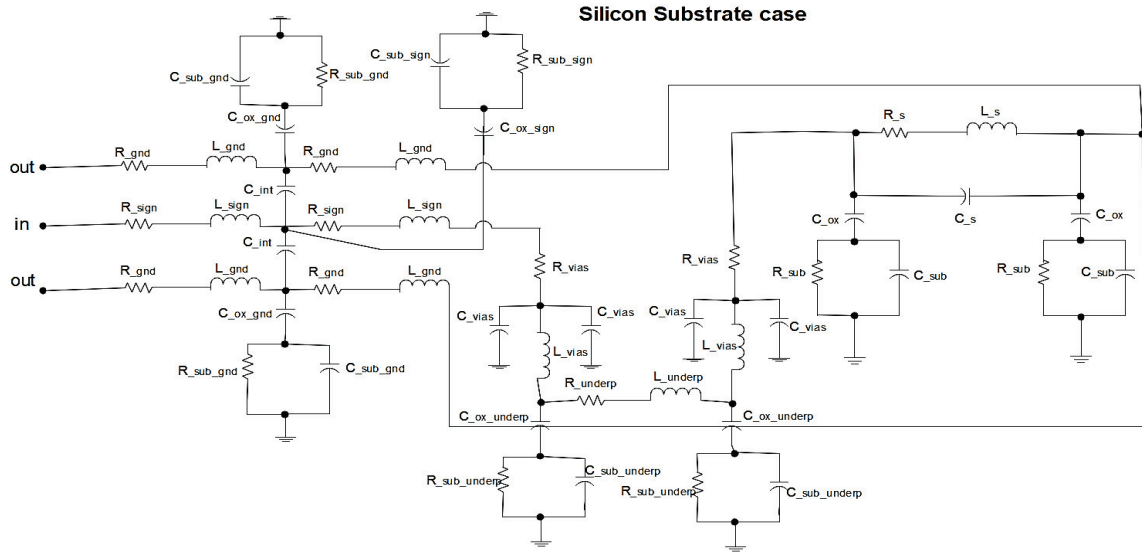


Fig. III. 10. The electrical circuit modelling the microprobe on a silicon substrate (complete model)

$$Z_{\mu\text{coil-TL-und\&vias}} = \frac{Z_{\mu\text{coil_und_vias}} \times Z_{\text{TL-subs}}}{Z_{\mu\text{coil_und_vias}} + Z_{\text{TL-subs}}} + Z_{\text{sign}} + \frac{Z_{\text{gnd}}}{2} \quad (\text{III.23})$$

with:

$$Z_{\text{TL-subs}} = Z_{\text{ox-subs-TL}} // Z_{\text{int}} = \frac{Z_{\text{ox-subs-TL}} \times Z_{\text{int}}}{2Z_{\text{ox-subs-TL}} + Z_{\text{int}}} \quad (\text{III.24})$$

$$Z_{\mu\text{coil_und_vias}} = Z_{\text{sign}} + \frac{Z_{\text{gnd}}}{2} + Z_{\text{und\&vias}} + Z_{\text{PI}} \quad (\text{III.25})$$

$$Z_{\text{und\&vias}} = 2 \cdot R_{\text{vias}} + \frac{Z_{\text{und-subst}} + 2j\omega L_{\text{vias}}}{1 + j\omega C_{\text{vias}} (2j\omega L_{\text{vias}} + Z_{\text{und-subst}})} \quad (\text{III.26})$$

$$Z_{\text{und-subst}} = \frac{Z_{\text{und}} \times Z_{\text{ox-subst_und}}}{Z_{\text{und}} + Z_{\text{ox-subst_und}}} \quad (\text{III.27})$$

$$Z_{\text{ox-subst_und}} = \frac{1}{j\omega C_{\text{ox_und}}} + \frac{R_{\text{sub-und}}}{1 + j\omega R_{\text{sub_und}} C_{\text{sub_und}}} \quad (\text{III.28})$$

$$Z_{\text{ox-subst-TL}} = [Z_{\text{ox-TL}} + (\frac{2R_{\text{sub-gnd}}}{1 + j\omega R_{\text{sub-gnd}} C_{\text{sub-gnd}}} + \frac{R_{\text{sub-sign}}}{1 + j\omega R_{\text{sub-sign}} C_{\text{sub-sign}}})] \quad (\text{III.29})$$

With:

$$Z_{\text{ox-TL}} = \frac{1}{j\omega} \left(\frac{2}{C_{\text{ox-gnd}}} + \frac{1}{C_{\text{ox-sign}}} \right) \quad (\text{III.30})$$

The Q factor is defined as the equations following:

$$Q_{\mu\text{coilTL_und_vias}} = \frac{\text{Im}\{Z_{\mu\text{coil-TL_und_vias}}\}}{\text{Re}\{Z_{\mu\text{coil-TL_und_vias}}\}} \quad (\text{III.31})$$

Where:

$$R_{\mu\text{coilTL_und_vias}} = \text{Re}\{Z_{\mu\text{coil-TL_und_vias}}\} \quad (\text{III.32})$$

$$L_{\mu\text{coilTL_und_vias}} = \frac{\{Z_{\mu\text{coilTL_und_vias}}\}}{\omega} \quad (\text{III.33})$$

Note that all these analytical formulas are too complex to evaluate the value of each parameter manually, so a MATLAB script was developed to calculate the value of each parameter (R , L and Q factor) from the proposed electrical model. The analytical value from the MATLAB was compared and validated with the simulations done by ADS software.

III.2.3. The electrical parameters (RLC) of the microprobe extracted by 3D-TLE

The electric parameters (RLC) were extracted from each part of the microprobe at an operating frequency of 300 *MHz* through the 3D-TLE platform. (See Fig.II.2 for the complete design of the microprobe with a rectangular micro-coil and an *underpass & vias* connecting wire solution).

Table III. 1 summarizes the extracted value of different parts of the microprobe. The parameter l represent the length of each part of the microprobe. The micro-coil length is calculated using the analytical formula in section II.2.2.1.

Description		Dimensions (μm)				C_{int} (pF)	L_{self} (nH)	R (Ω)	C_{ox} (pF)	C_{sub} (pF)	R_{sub} ($\text{M}\Omega$)
		l	t	w	s						
μPath	sign	9320	40	320	30	0.109	8.289	0.075	1.2867	0.789	0.0133
	gnd	9500	40	60	30	0.109	10.91	0.291	0.2459	0.150	0.0698
Underpass		315	0.5	60		-	0.207	0.2097	0.1630	5.01e-3	2.105
Vias		1.5	60	60			7.498e-6	3.784e-5	0.03e-4	7.03e-4	0.0062
Vias		0.16	60	60			8.533e-8	4.037e-6	0.03e-4	7.03e-4	0.0062
μcoil		9942.0	40	22	20	0.175	12.468	0.518	0.0943	0.02894	0.364

Table III. 1. The electrical parameters (RLC) from different parts and according to their dimensions.

With the proposed equivalent electrical circuit of the complete microprobe, we could simulate the performance of the electric model in terms S_{11} parameters and deduce the Q factor, using ADS. We also used the analytical formulas defined in the Section III.3.1 and section III.3.2 to deduce the RLQ value of the microprobe more quickly.

The S_{11} parameter criteria were already defined in chapter I (For more details, see section I.3.3.2). Note that from a S_{11} plot, we can deduce the Q factor of the resonator (Microprobe). Because of that, we were able to add a circuit for the tuning and impedance matching of microprobe in ADS software to achieve the required resonance frequency for our application to accurately measure the Q factor.

In our case, ADS software provides variable capacitors that we combine in serial and parallel associated with the microprobe. We variated their value until the resonance peak was placed at the frequency of 300 *MHz*.

Measuring the Q factor of the model and then comparing it with the previous value from our team, we evaluated the contribution of each part of the microprobe. This process is necessary to validate the proposed electrical models for the microprobe on the glass and silicon

substrate. When all this is validated, we compared the RLQ value of the model (an electrical circuit) with one of the analytical formulas. In this way, we could generalize the process for other geometries and dimensions.

In Section III.2.4, we will present the results from the simulations of the frequency response of S_{11} parameters of different models in the glass and silicon substrate previously introduced (RLC, PI and complete model).

Then in Section III.2.5 we show the variation of the Resistance and inductance of the models according to the frequency.

III.2.4. Results of the Q factor and S_{11} parameters of the simulation of models

Figure. III.11 shows the S_{11} parameter results of the electrical circuit such as RLC, PI model $\mu probe$ & $\mu path$ and complete model. We denoted here by $\mu probe$ & $\mu path$ the completed model with the *underpass* & *vias* replaced by a short-circuit.

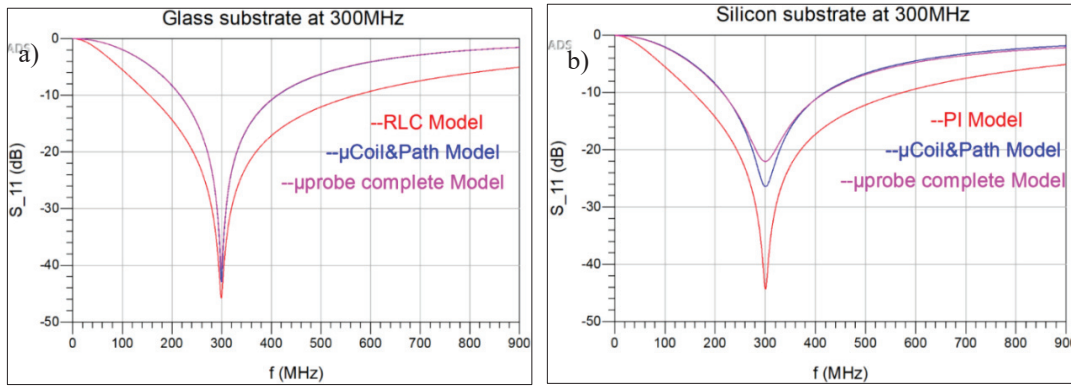


Fig. III. 11. S_{11} parameters of the microprobe electrical model from the silicon substrate (a) and the glass (b)

As already said, before simulating the full electrical model of the microprobe on the glass and silicon substrate, we proposed an intermediate model called $\mu coil$ & $path$ (i.e, micro-coil plus micro-transmission), which only includes the contribution of the micro-coil part and the one of the micro-Transmission Lines (TL). This model has been helpful to deduce the contribution of the *underpass* & *vias* in the overall resistive loss of the microprobe.

In Fig. III. 11b) we can note a high variation of the resonance peak of the electrical model of the microprobe without the *underpass* & *vias*, compared to the complete model, specifically to the one of the silicon substrates. In addition, we can see in Fig. III. 11 a) & b) that when the model gets more complex, the peak of the resonance curve starts to decrease. This can be explained by the energy losses of the *underpass* & *vias* on the substrate.

Fig. III. 12 shows the plot of the complete model of the microprobe on a glass and silicon substrate. We notice that the resonance from the glass substrate has a narrowband and an S_{11} value about -40.6 dB , while for the silicon is about -20 dB , both smaller than -10 dB .

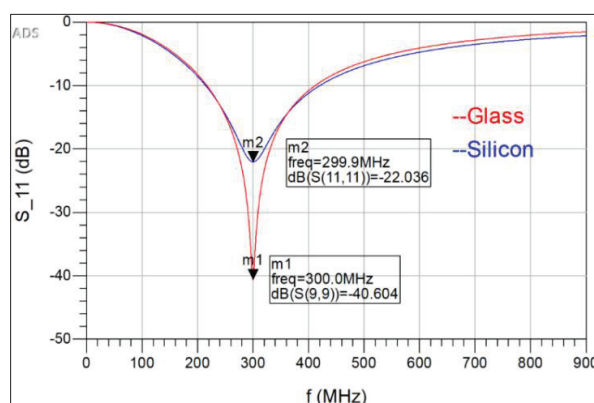


Fig. III. 12. S_{11} parameters of the complete model of microprobe on a silicon and glass substrate

Note that, the minimum value of S_{11} parameter of all studied models are still smaller than -10 dB (Fig. III. 11 and Fig. III. 12). This means there is no signal reflection after a good impedance matching and tuning of the all-microprobe electrical models.

Fig. III. 13 shows the variation of the Q-factor simulated for the complete electrical model of the microprobe on glass and silicon substrate.

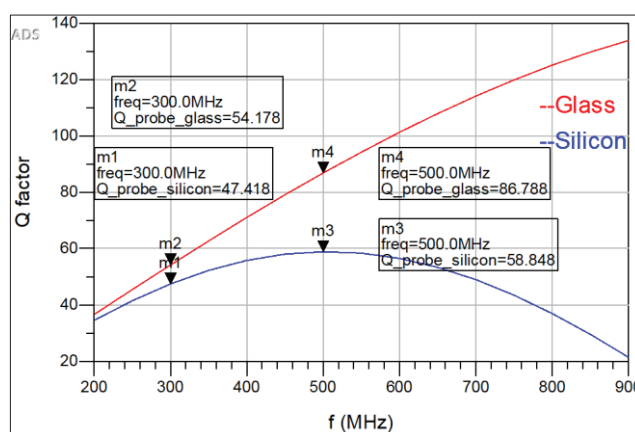


Fig. III. 13. Q-factor variation of both complete electrical models of NMR micro-probe

Note that the value of the Q factor from the microprobe model on the silicon substrate stop increasing when it reaches the frequency of 500 MHz .

III.2.5. Results of the microprobe modelled on glass and silicon substrate (RLQ)

Fig. III. 14 shows the variation of the resistive and inductance from each model representing the microprobe on glass and silicon substrate. We have plotted in the same graph

the different models to evaluate the impact of each part on the global Resistance of the microprobe and the Inductance.

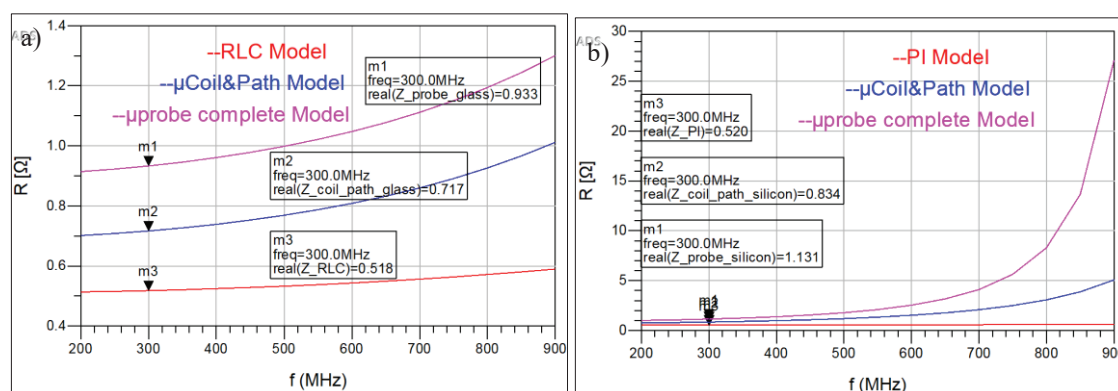


Fig. III. 14. Resistances variation from electrical models of microprobe on a glass substrate a) and silicon b)

Note that the resistance and inductance increase with the frequency, even if the Resistance of the silicon models increase very quickly from the frequency value close to 500 MHz. Fig. III. 14 a) and Fig. III. 14 b) show the different values of the Resistance at the resonance frequency, which corresponds to 300 MHz.

In Fig. III. 15, we have the Resistance variation with the frequency a) and the one of inductance b) for the complete electrical circuit of the microprobe modelled on glass and the silicon substrate. Again, the resistance and inductance increase as a function of the frequency. In Fig. III. 15, we have also highlighted their values in 300 MHz and 500 MHz.

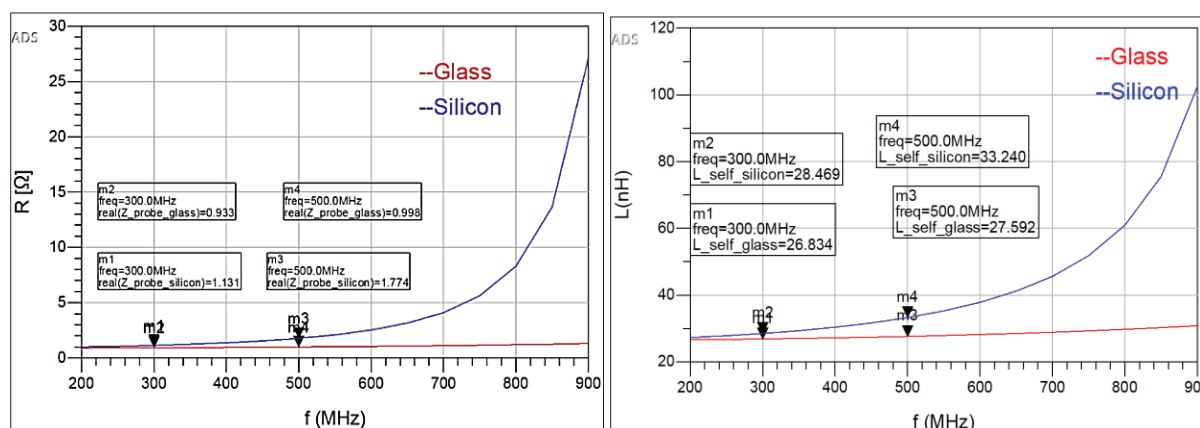


Fig. III. 15. The variation of Resistance a) and Inductance from complete electrical models of microprobe on a glass substrate and silicon

We have summarized in Table III.2 the results from ADS simulations to illustrate the impact of each part of the microprobe on glass and silicon substrate cases, specifically their performance at 300 MHz and 500 MHz of (Resistance R , self-inductance L and Quality factor Q of each electrical circuit model). Then we compared the results with the analytical results.

Working frequency		300 MHz						500 MHz					
Electrical parameters		R [Ω]		L_{self} [nH]		Q		R [Ω]		L_{self} [nH]		Q	
Model Type		Calc.	ADS	Calc.	ADS	Calc.	ADS	Calc.	ADS	Calc.	ADS	Calc.	ADS
Micro-coil	RLC	0.53	0.53	12.56	12.57	45.02	44.85	0.68	0.53	12.74	12.79	59.10	75.14
	PI	0.53	0.53	12.59	12.57	44.78	44.85	0.69	0.54	12.82	12.79	58.32	74.57
Micro-coil & micro-path	Glass	0.77	0.77	25.77	26.61	65.43	65.45	1.03	0.77	27.37	27.37	83.22	111.77
	Silicon	0.78	0.89	26.71	27.63	65.02	58.59	1.10	0.84	27.49	30.42	81.96	80.96
Complete model	Glass	0.98	0.95	25.98	26.83	51.43	53.50	1.26	1.01	27.59	27.59	68.63	86.99
	Silicon	0.94	1.10	27.99	28.01	51.20	47.89	1.30	1.77	27.72	33.24	67.83	58.85

Table III. 2. The RLQ parameters from different models of microprobe, performed at **300 MHz**, although **500 MHz**

Based on the ADS results of the RLQ parameters summarized in Table III. 2, we normalized the highest value of each parameter (RLQ) to 100%, and we performed a statistical study. We applied uniform normalization in the range of 0 to 1. The impact of each component of the micro-probe (micro-coil, TL, *underpass* & *vias*, and the substrate) in the variation of R , L and Q -factor parameters were detected through a good understanding of the global electrical diagram.

In Fig. III. 16, we show the normalized value of RLQ parameters of different electrical models for the glass and silicon substrate at 300 MHz.

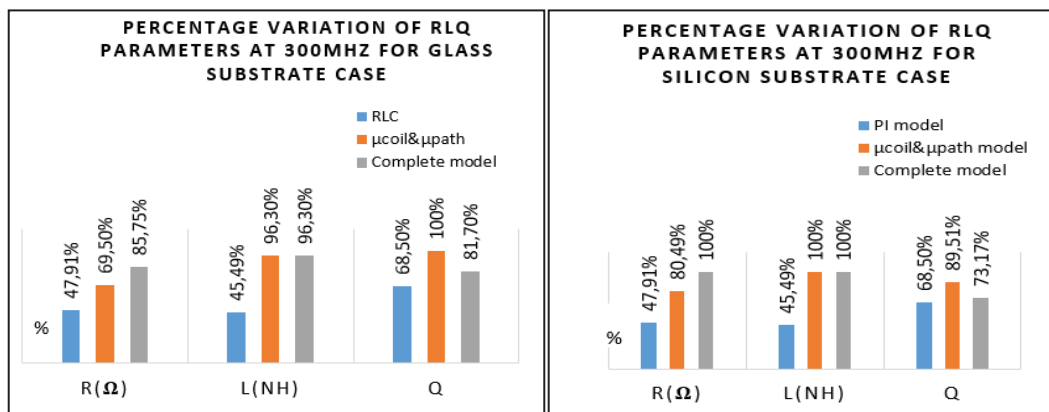


Fig. III. 16. The statistical study of RLQ parameters, comparing different models of microprobe modelled on a glass and silicon substrate, for **300 MHz**

In Fig. III. 16, we noticed two points: First, the transmission line contributes to the increase of the Q-factor on two substrate cases (32 % for a glass and 21 % for the silicon substrate). Secondly, *underpass & vias* decreases the value of the Q factor (18 % in the glass and 19 % for the silicon substrate).

When we add the TL to the model to complete it, we should increase its global Resistance. But note that even it happens, the Inductance increase of almost 53 % is still proportionally higher than Resistance increasing (27 %). This explains the increase of the Q factor even when we add the TL. Then, when we add the *underpass & vias*, we note that the Resistance increases considerably (16 % on glass substrate and 20 % on silicon substrate) and the Inductance not so much (less than 1 % for both substrates cases).

The same analyse was performed in the case of 500 MHz. In the Fig. III. 17, we showed the percentage variation of each model, for both case of substrates (glass and silicon)

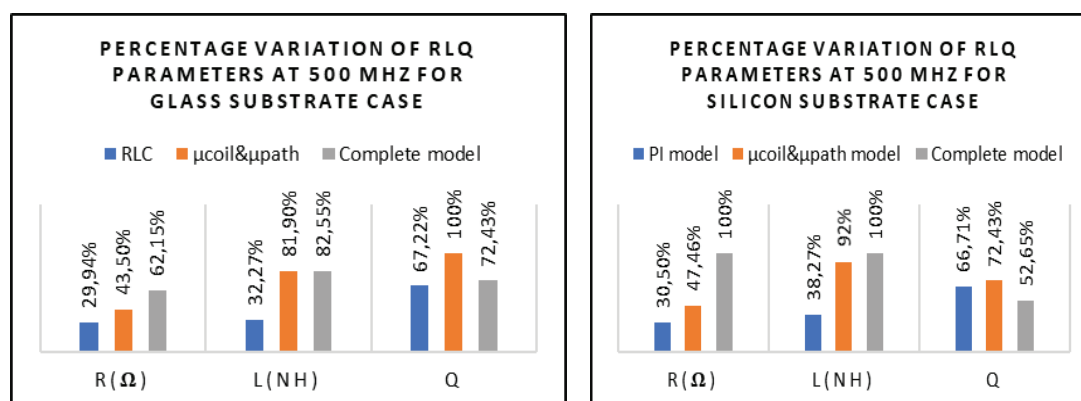


Fig. III. 17. The statistical study of RLQ parameters, comparing different models of microprobe modelled on a glass and silicon substrate, for **500 MHz**

Note that the percentage variation for the case of 500 MHz, in both substrates is quite similar to the one of 300 MHz. The difference is about the percentage intensity due to the frequency that is much higher than 300 MHz.

Fig. III. 18 shows the variation of Q-factor of the complete electrical circuit on glass and silicon substrate and two operating frequencies (300 MHz and 500 MHz).

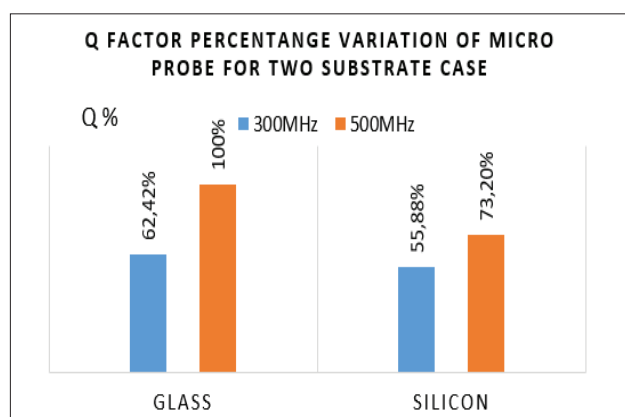


Fig. III. 18. A statistical study of Q-factor variation from microprobe operating at **300MHz** and **500MHz** for both substrate cases

In Fig. III. 18, we can highlight two points: Firstly, the quality factor increases by 38% when we move the frequency from 300 MHz to 500 MHz, in the glass substrate and secondly, the Q factor growth is 18 % in the silicon substrate.

Therefore, we can now conclude that each part of the microprobe (micro-coil, TL, *underpass* & *vias*) and the substrate make an influence on the variation of Resistance, self -Inductance and Q-factor parameter. The influence is mostly understood through the several models we described in the previous sections (Section III.2.1 and Section III.2.2), more particularly thanks to our original model representation of the electrical circuit from the complete microprobe. The TL contributed to the increase of the Q-factor, while the *underpass* & *vias* can deteriorate the Q-factor of the microprobe when it is not optimized.

At 300 MHz, the fabrication changes of microprobe substrate from glass to silicon provided an impact on the performance of the Q-factor (decreasing by 7 %). At 500 MHz, the Q-factor of the microprobe degraded by 27 % if used with silicon substrate instead of the glass substrate. Thus, the best working frequency for our application could be 500 MHz, a microprobe on a glass substrate. We were sure that we could optimize considerable resistive loss due to the *underpass* & *vias* embedded on a silicon substrate or simply change the connecting wire type to *wire-bonding*, *airbridge*, which require an adaptation on the manufacturing process microprobe prototype.

From the results of our simulations, we could affirm that the prediction of the performance parameters of the microprobe with an optimized *underpass* & *vias* with a thickness ($t_{und} = 10 \mu m$ instead of $0.5 \mu m$), is much better, as we can summarize in the Table. III.3. The complete model on a glass substrate corresponds to a microprobe with an *airbridge* connecting wire ($t_{airbridge} = 10 \mu m$).

Working frequency		300 MHz						500 MHz					
Electrical parameters		R [Ω]		L _{self} [nH]		Q		R [Ω]		L _{self} [nH]		Q	
Model Type		Calc.	Sim.	Calc.	Sim.	Calc.	Sim.	Calc.	Sim.	Calc.	Sim.	Calc.	Sim.
Complete model	Glass	0.77	0.73	26.80	26.80	65.87	69.10	1.03	0.79	27.57	27.55	86.76	110.20
	Silicon	0.78	0.91	26.88	28.01	65.31	59.06	1.06	1.48	27.77	33.24	81.97	70.69

Table III. 3. The **RLQ** electrical parameters from the best model of micro-probe, all of them tuned at **300 MHz** and **500 MHz**

Note that, the model of an *airbridge* is equivalent to the *underpass & vias* if we assume that there is no substrate loss for the connecting wire.

Optimizing the transmission line, *underpass & vias* part associated with different geometries required several simulations and different cases with our validated model. Thanks to our MATLAB *script*, we automatically generated data from the simulation of four geometries, different dimensions of the micro-coil, *underpass & vias* dimensions, and two substrate types in the frequency range of 200 MHz to 900 MHz (more details about the procedure, see the appendix, A.6).

III.3. Prediction of the microprobe performances: Artificial Intelligence approach

III.3.1. Introduction

Artificial intelligence (AI), one of the developments in computer technology, has been widely used in several fields of applications, particularly in IMR for image processing and analysis [108], brain image segmentation [109], image classification and segmentation of the human brain for AD diagnostics [110], spectra reconstruction from under-sampled data [114], very fast reconstruction of NMR spectra from limited experimental data [112]

For more than one decade, AI has been improving its development in many application domains. Very recently, AI technology has been used to solve complex problems such as antenna parameters extractions, structural design and data interpretation for radar and Multiple Input and Multiple Output (MIMO) systems [113] [114]. Artificial Neural Networks (ANN) is one of the AI branches beneficial for solving problems of modelling where the relationship between system inputs and outputs are relatively too complex. The advantages of the Artificial Neural Network (ANN) to model system are: reduce computational complexity and time. Moreover, decrease some cost compared to traditional computational modelling and leads to highly accurate data set analysis [115]. These facts represent a great asset to perform the design and optimization of our microprobe structure.

In the following section III.3.2, we have briefly recalled the principle of the classical methodology for optimal microprobe design. Then in section III.3.3 and section III.3.4, we have presented a new approach and some basic AI concepts that were useful for this work.

III.3.2. Traditional simulation method for microprobe model

Experiments in real life are often limited, either by the execution time, financial cost, or simply by the impossibility of performing them. For example, observing and analyzing deformation mechanisms of tissue *in vivo* at the nanoscopic scale is still tricky, even impossible in many cases, mainly due to the limitations of microscopy techniques. Computer simulations can overcome these constraints either by replacing observations and analyses that are difficult to measure. Simulation can also be complementary, completing experiments that have already been made. Furthermore, numerical simulations can also reveal previously unsuspected mechanisms, or still largely misunderstood, in many disciplinary fields.

In our case, we have been carried out a simulation of an implantable microprobe designed for *in vivo* applications. Usually, microprobe manufacturing is time-consuming and expensive. So, simulation makes possible the examination of different scenarios without experimentations and then select the main parameters for the required performances. It can also provide meaningful data trends and guide the manufacturing process. Until now, our team has applied a classical methodology for microprobe design simulation and performance study [37] [43]. The used optimization processes of microprobe design are reminded on a block diagram (Fig. III. 19.) of the developed homemade simulation software by T. Cong Truong (Thesis work, 2014) [43].

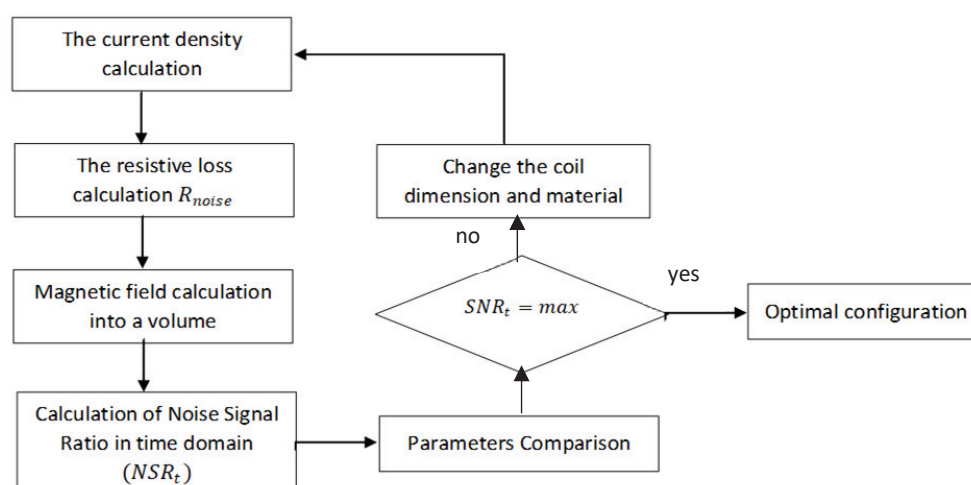


Fig. III. 19. Block diagrams of the classic simulation methodology for microprobe parameters optimization [43]

We need an approach that can generalize the design and optimization of multi-parameters systems. Thus, in the Fig. III. 20, we shows the principles of classical methods (a), comparing to an AI approach (b). Using the classical method, usually we might know the model that will be used to simulate the performance of the system. In the Machine Learning approach, we do not need to know the model, we can train an AI model (black-box) directly with the expected input and output, and then we can predict the required performances according to the characteristics of the system.

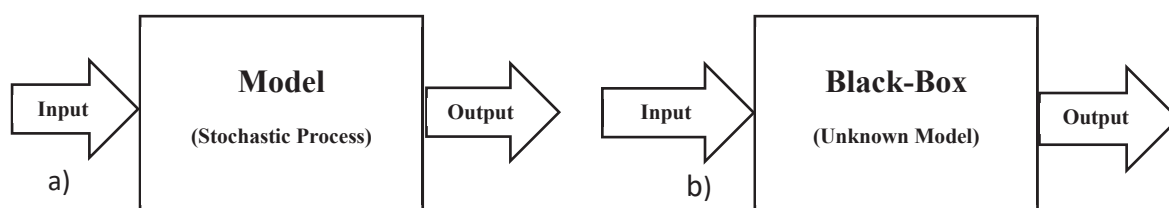


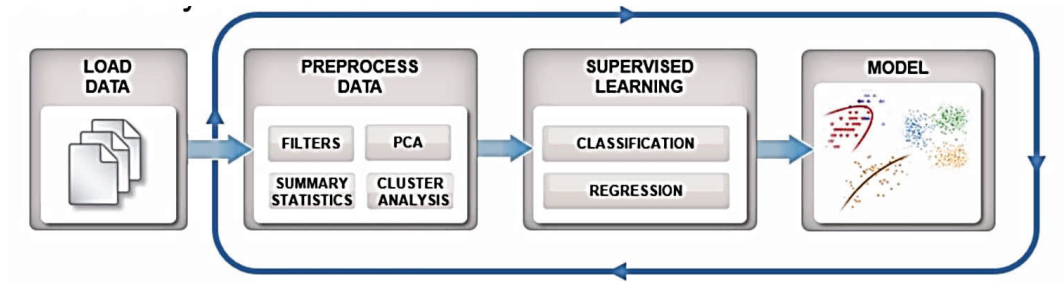
Fig. III. 20. (a) Traditional method vs (b) Machine Learning approach

III.3.3. Machine Learning Approach

Machine Learning (ML) is a part of AI that allows the software to achieve some tasks as a prediction of parameters without being explicitly programmed to perform so. ML algorithms use computational methods to learn information directly from data. The algorithms adapt and become more powerful as the number of samples available for learning increases.

The following figure (Fig. III. 21) presents the main steps of an ML workflow.

- Train: iterate till the best model is found



- Predict: integrate trained model in to applications

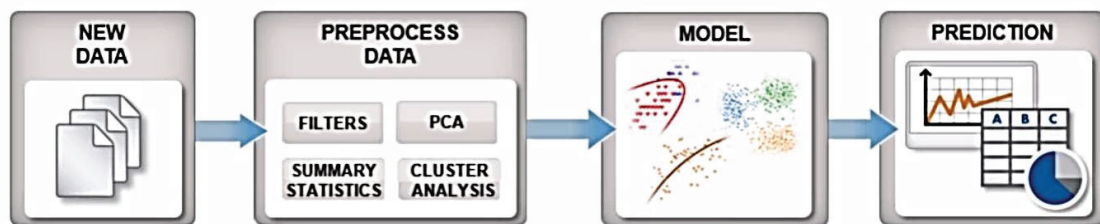


Fig. III. 21. Machine Learning Workflow [116]

ML algorithms can be divided in two categories of learning techniques (Fig. III. 22): supervised learning, which involves training a model on known input and output data to predict future outcomes, and unsupervised learning, which identifies hidden patterns or intrinsic structures in the input data. Unsupervised learning algorithms experience a dataset containing many features then learn useful properties of the structure of this dataset.

A supervised ML algorithm experience a dataset containing features, but each example is also associated with a label or target. This requires training the model with a known set of input data (Predictors, conventionally designated X) and known responses (output or target, conventionally designated Y or O). Supervised learning can be used since the data you must predict has outcomes that are very well known.

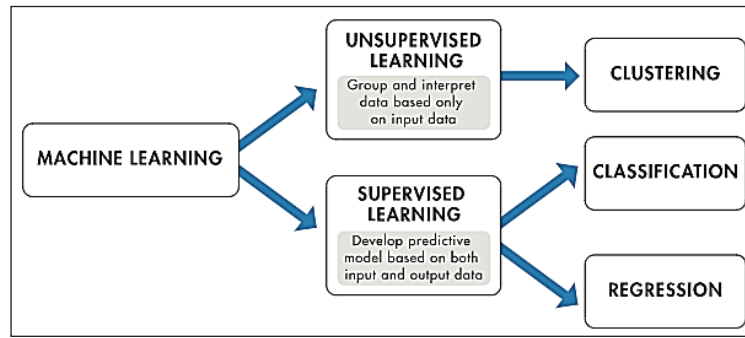


Fig. III. 22. Two categories of machine learning techniques: Supervised and unsupervised learning [117]

Supervised learning develops predictive models using classification and regression techniques. Common regression algorithms include linear model, nonlinear model, regularization, stepwise regression, decision tree boosting/bagging, neural networks, and adaptive neural learning.

Regression methods of ML are used to predict the continuous values of a magnitude using an experience of the dataset. The dataset is characterized by two types of variables: dependents (Y in my thesis designated by O) and independent variables (X).

Independent variables can be related to the cause of the states or the feature of the system to predict the evolution (Predictors). The dependent variable can be seen as the state or target, as the final goal of the study or trying to predict (Target). Certainly, for our dataset, the simulation results are well-known, which correspond to the performance of the microprobe in terms of the Q factor and Resistance, as well as the system predictor, which are the geometrical parameters, substrate electrical properties, frequency domain.

To manage our datasets, we developed our predictive model using the Artificial Neural Network (ANN), a computer system inspired by the biological neural network, as we will see later in the following section.

III.3.3.1. Deep Learning (DL) architecture

DL is a specific kind of Machine Learning branch that corresponds to an AI able to assimilate new knowledge through a Network of Artificial Neurons. The motivation behind using a Neural Network (NN) model is to organise them in several layers and different shapes. A standard neural network consists of many simple, connected neurons, each producing a sequence of real-valued activations. Input neurons are activated through sensors perceiving the environment, and other neurons are activated through weighted connections from previously active neurons.

Some neurons may influence the environment by triggering actions [121]. Learning (training) is about finding weights that make the NN show the desired behaviour of the model.

The training of different architectures is very well understood by mathematical models [122] [120]. For our study, we trained the AI model based on the family of feedforward Neural Networks via the Back Propagation technique, which we will describe its principle in section (III.3.3.6).

III.3.3.2. The principle of an Artificial Neuron

The human brain is very efficient for solving tasks such as object recognition by the human eye or object segmentation in images [124]. This reason has motivated the research community to understand the human brain by proposing models representing its behaviours since 1943 [125] [123]. The basic computational unit of the brain is a neuron. Approximately 86 billion neurons are inside the human nervous system. The neurons are connected with approximately 10^{14} synapses. A neuron receives input signals from its dendrites and produces an output signal along its axon. The axon connects to the dendrites of other neurons. Fig. III. 23 a) shows images of a human neuron.

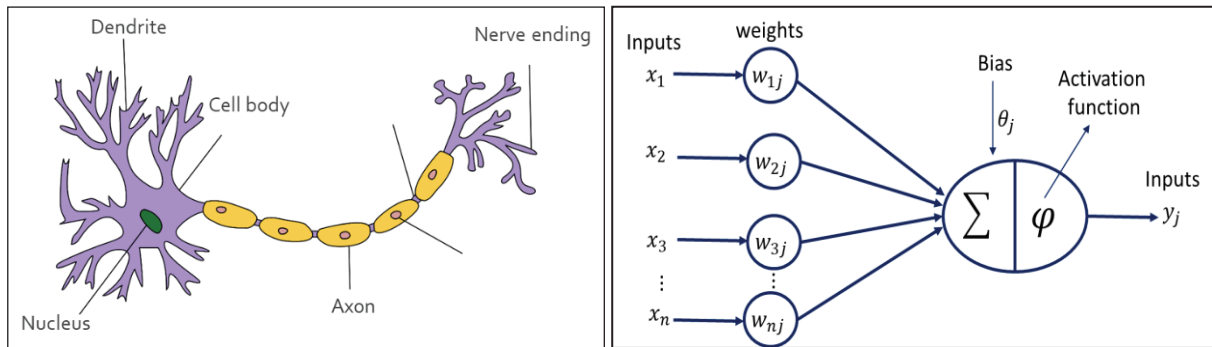


Fig. III. 23. Human neuron (a) versus a standard mathematical model of a neuron (b) [127] [125]

In the standard mathematical model of a neuron (Fig. III. 23b), the signal x_1 travels along the axon of a neuron and interact multiplicatively with the dendrite of the current neuron based on the synaptic strength of the dendrite w_1 (*weights*). The dendrites carry different signals to the current neuron body where they are summated, as well as a *bias* coefficient θ_j for each neuron. *Bias* coefficient and the *weights* represent the learnable parameters of a Neuron [129].

In the following equation, we defined the mathematical model of an artificial neuron (perceptron) without activation function (net_j):

$$net_j = \sum_{i=1}^n w_{ij}x_i + \theta_j \quad (\text{III.35})$$

The previous regression model can be represented in the matrix form as the following equation:

$$net_j = W_j^T X + \theta_j \quad (III.35)$$

The goal here is to build a system that can take a vector $X \in R^n$ as input and predict the value of a scalar $net_j \in R$ as an output before we apply the activation function. Where $W_j^T \in R^n$ is the vector of the parameters.

The output o_j of the neuron is defined as the following equation (III.36). The activation function, we denoted by φ which allow the evaluation and transformation of the linear output of the neuron:

$$o_j = \varphi(net_j) \rightarrow o_j = \varphi(W_j^T X + \theta_j) \quad (III.36)$$

The activation functions add non-linearity to the output, which enables Neural Network (NN) to solve nonlinear problems. The standard activation functions φ include *Linear*, *sigmoid*, *Tanh*, and *ReLU*, but many others also exist [127] [128]. These are the most currently used for regression and classification problems.

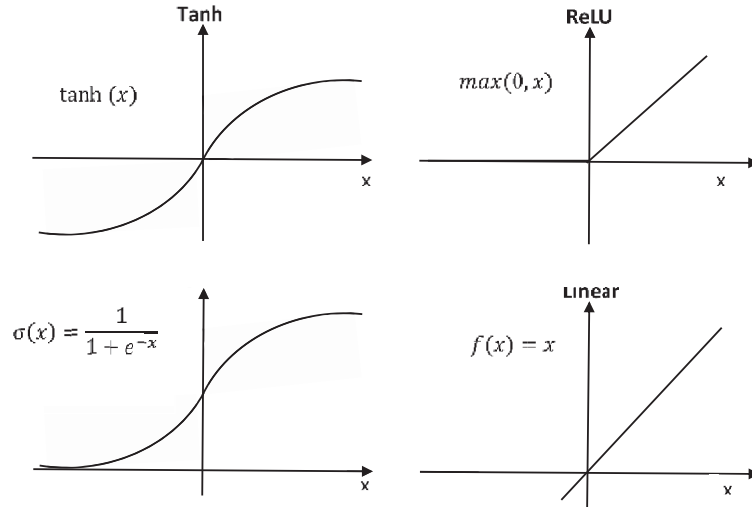


Fig. III. 24. Representation of the standard activation functions

One of the most frequent used activation functions is the sigmoid. This function is also used to model a logistic regression algorithm which is often associated with the single perceptron. Logistic regression is also used to illustrate the idea behind a simple neuron network approach. Thus, in the next section, we will introduce the loss functions, more precisely, the log loss function that is commonly used for classification problems and associated with a logistic

regression algorithm [129]. Note that, logistic regression we used here to illustrate the different steps used for a standard neuron network which are at the base of several neuronal network architectures;

III.3.3.3. The loss function and descendent gradient of a Logistic regression

The loss or cost function is a function that allows evaluating the error made by an AI model. If the model prediction is completely wrong, the loss function will be the highest value, and if not, the loss function is a lower value. So that, give information about how well the model is learning from the dataset.

The cost function is defined as follows:

$$\text{Log Loss} = L = -\frac{1}{m} \sum_{k=1}^m o_j^{(k)} \log \hat{o}_j^{(k)} + (1 - o_j^{(k)}) \log(1 - \hat{o}_j^{(k)}) \quad (\text{III.37})$$

Where:

- m represents the number of observations
- \hat{o}_j : is the model ouput (predicted value)
- o_j : the true value of the output.

The challenge of this approach is to find how to minimize the log loss function, which means minimizing the error of the AI model to train from the dataset. For this, one of the most used methods is the gradient descendent.

Gradient descend is a first-order iterative algorithm for the optimization of most of ML methods. For example, in deep learning is used to find a local minimum of the loss function, which is a differentiable function.

The formula used for the gradient descendent algorithm is the following equation:

$$W_{j+1} = W_j - \alpha \frac{\partial L}{\partial W_j} \quad (\text{III.38})$$

With:

W_{j+1} and W_j : the parameters to optimize at time $j+1$ and j

α : The learning step (always $\alpha > 0$)

$\frac{\partial L}{\partial W_j}$: is the gradient of the loss function in time j

- If $\frac{\partial L}{\partial W_j} < 0$ we have a growing up the gradient. Which means $W_{j+1} > W_j$

- If $\frac{\partial L}{\partial W_j} > 0$ we have a descendent gradient. Which means $W_{j+1} < W_j$

The idea is to make repeated steps in the opposite direction to the gradient of the loss function at the current point. The second condition has to be repeated several times until we find the minimum of the log loss function.

We can easily demonstrate that, for a logistic regression the $\frac{\partial L}{\partial W_{ij}}$ and $\frac{\partial L}{\partial b}$ are calculated by the following formula:

$$\frac{\partial L}{\partial W_{ij}} = \frac{1}{m} \sum_{k=1}^m x_i (o_j^{(k)} - \hat{o}_j^{(k)}) \quad (\text{III.39})$$

And:

$$\frac{\partial L}{\partial b} = \frac{1}{m} \sum_{k=1}^m (o_j^{(k)} - \hat{o}_j^{(k)}) \quad (\text{III.40})$$

Equations (III.39) and (III.40) can easily be implemented with the aim of the weight and bias of the neuronal are adjusted on presentation of each sample containing the information about the data tendency. Note that the cost function of the logistic regression is a continuous and differentiable function with a local minimum, as we can determine using the previously shown equation. But for the more complicated case, where an analytical function does not define the gradient, other more complex gradients algorithms can help find an approach suitable for the application case [130].

III.3.3.4. Vectorization of the mathematical model of a neuron

In computer programming, vectorization consists of transforming data in the form of vectors, matrices or N-dimensional arrays in order to perform mathematical operations on the dataset in the simplest and fastest way. Vectorization is a valuable technique in ML and DL because we deal with a huge amount of data in these domains of AI.

The vectorization technique reduces the computation time of the model by avoiding computing the data one by one. In contrast, in the neural network, the same computation must be done several times for different data. So, it is more practical to vectorize the data to process all data at once and help to avoid a consuming time for computation.

Therefore, to illustrate the technique in the following section, we will vectorize the equation of the artificial neuron model for logistic regression that is the algorithm previously described in section III.3.3.3.

- a) The ANN model trained for several observations can be defined as follows:

$$net^{(m)}_j = \sum_{i=1}^n w_{ij} x_i^{(m)} + \theta_j \quad (\text{III.41})$$

Where we define m as the number of the dataset (observations), n is the number of neuron inputs (predictors), e.g., in our case, we have $n = 6621$ observations, and $n = 12$ predictors.

$$X = \begin{bmatrix} x_1^{(1)} & x_2^{(1)} & \cdots & x_n^{(1)} \\ x_1^{(2)} & x_2^{(2)} & \cdots & x_n^{(2)} \\ x_1^{(3)} & x_2^{(3)} & \cdots & x_n^{(3)} \\ \vdots & \vdots & \ddots & \vdots \\ x_1^{(m)} & x_2^{(m)} & \cdots & x_n^{(m)} \end{bmatrix} \in R^{m \times n} \quad (\text{III.42})$$

And:

$$O_j = \begin{bmatrix} o_j^{(1)} \\ o_j^{(2)} \\ o_j^{(3)} \\ \vdots \\ o_j^{(m)} \end{bmatrix} \in R^{m \times 1} \rightarrow Net_j = \begin{bmatrix} net_j^{(1)} \\ net_j^{(2)} \\ net_j^{(3)} \\ \vdots \\ net_j^{(m)} \end{bmatrix} \in R^{m \times 1} \quad (\text{III.43})$$

Thus:

$$Net_j = \begin{bmatrix} net_j^{(1)} \\ net_j^{(2)} \\ net_j^{(3)} \\ \vdots \\ net_j^{(m)} \end{bmatrix} = \begin{bmatrix} x_1^{(1)} & x_2^{(1)} & \cdots & x_n^{(1)} \\ x_1^{(2)} & x_2^{(2)} & \cdots & x_n^{(2)} \\ x_1^{(3)} & x_2^{(3)} & \cdots & x_n^{(3)} \\ \vdots & \vdots & \ddots & \vdots \\ x_1^{(m)} & x_2^{(m)} & \cdots & x_n^{(m)} \end{bmatrix} \times \begin{pmatrix} w_{1j} \\ w_{2j} \\ w_{3j} \\ w_{4j} \\ \vdots \\ w_{n-1j} \\ w_{nj} \end{pmatrix} + \begin{bmatrix} \theta_j \\ \theta_j \\ \theta_j \\ \vdots \\ \theta_j \end{bmatrix} \quad (\text{III.44})$$

With:

$$W_j = \begin{pmatrix} w_{1j} \\ w_{2j} \\ w_{3j} \\ w_{4j} \\ \vdots \\ w_{n-1j} \\ w_{nj} \end{pmatrix} \in R^{n \times 1} \quad \text{and} \quad \theta_j = \begin{bmatrix} \theta_j \\ \theta_j \\ \theta_j \\ \vdots \\ \theta_j \end{bmatrix} \in R^{m \times 1} \quad (\text{III.45})$$

Therefore, we can define the net model for m observation in matrix form as the equations:

$$Net_j = X \times W_j + \theta_j \quad (\text{III.46})$$

$$O_j = \varphi(Net_j) \rightarrow O_j = \varphi(X \times W_j + \theta_j) \quad (\text{III.47})$$

b) We can demonstrate that vectorization of the log loss function is given by the formula:

$$L = -\frac{1}{m} \sum_{k=1}^m \hat{o}_j^{(k)} \log O_j + (1 - \hat{o}_j^{(k)}) \log(1 - O_j) \quad (\text{III.48})$$

c) The vectorization of the descendent gradient we can define as:

$$\begin{bmatrix} w_{1j} \\ w_{2j} \\ w_{3j} \\ w_{4j} \\ \vdots \\ w_{n-1j} \\ w_{nj} \end{bmatrix} = \begin{bmatrix} w_{1j} \\ w_{2j} \\ w_{3j} \\ w_{4j} \\ \vdots \\ w_{n-1j} \\ w_{nj} \end{bmatrix} - \alpha \underbrace{\begin{bmatrix} \frac{\partial L}{\partial w_{1j}} \\ \frac{\partial L}{\partial w_{2j}} \\ \vdots \\ \frac{\partial L}{\partial w_{nj}} \end{bmatrix}}_{\text{The Jacobian without bias}} \quad (\text{III.49})$$

We deduce the vectorization of the descendent gradient as defined:

$$W_{j+1} = W_j - \alpha \frac{\partial L}{\partial W_j} \quad (\text{III.50})$$

Note that the matrix notation does not consider the j index; moreover, it looks like the previous formula without vectorization and the bias coefficient calculation. When we replace the equation (III.39) in the Jacobian, we can deduce the following formula for the gradient vectorization:

$$\underbrace{\frac{\partial L}{\partial W_j}}_{(n,1)} = \begin{bmatrix} \frac{\partial L}{\partial w_{1j}} \\ \frac{\partial L}{\partial w_{2j}} \\ \vdots \\ \frac{\partial L}{\partial w_{nj}} \end{bmatrix} = \begin{bmatrix} \frac{1}{m} \sum_{k=1}^m x_1^{(k)} (o_j^{(k)} - \hat{o}_j^{(k)}) \\ \vdots \\ \frac{1}{m} \sum_{k=1}^m x_n^{(k)} (o_j^{(k)} - \hat{o}_j^{(k)}) \end{bmatrix} \quad (\text{III.51})$$

$$\frac{\partial L}{\partial W_j} = \frac{1}{m} \underbrace{\begin{bmatrix} x_1^{(1)}(o_j^{(1)} - \hat{o}_j^{(1)}) + \dots + x_1^{(m)}(o_j^{(m)} - \hat{o}_j^{(m)}) \\ \vdots \\ x_n^{(1)}(o_j^{(1)} - \hat{o}_j^{(1)}) + \dots + x_n^{(m)}(o_j^{(m)} - \hat{o}_j^{(m)}) \end{bmatrix}}_{\frac{1}{m} X^T \times (O_j - \hat{O}_j)} \quad (\text{III.52})$$

So, we can deduce the gradient matrix of the weights parameters as:

$$\frac{\partial L}{\partial W_j} = \frac{1}{m} X^T \times (O_j - \hat{O}_j) \quad (\text{III.53})$$

Following the same procedure as in the equation (III.51), we can deduce the gradient for the bias as follows:

$$\frac{\partial L}{\partial \theta_j} = \frac{1}{m} \times (O_j - \hat{O}_j) \quad (\text{III.54})$$

So, the general formulation of the vectorization of the model, the loss function and descendent gradient avoid the utilization of several loop “*for*” during the model coding for computation of the model. We can also generalize the calculation of the amount of the dataset and variable (predictor). The only parameter we will have to update is the size of the matrix according to the case. All these concepts are already embedded in the MATLAB GUI application for Deep learning, more precisely Neural Network Toolbox; we performed the optimization of the parameters and hyperparameters, as well as the data pre-processing before the model training.

In the next section, we will present the generalization of the artificial neuron for several neurons and layers, which is the base for the architecture chosen for the training of our model.

III.3.3.5. The principle of an Artificial Neuronal Network

An Artificial Neural Network (ANN) is defined as a group of neurons that are connected in an acyclic graph. Instead of using unstructured groups of connected neurons, they are organized into layers. This way, the outputs of some neurons become inputs to other neurons. Each Artificial Neuron has a processing node (body) represented by circles, as well as connections from (dendrites) and connections (axons) to other neurons, which are defined as arrows in Fig. III. 25.

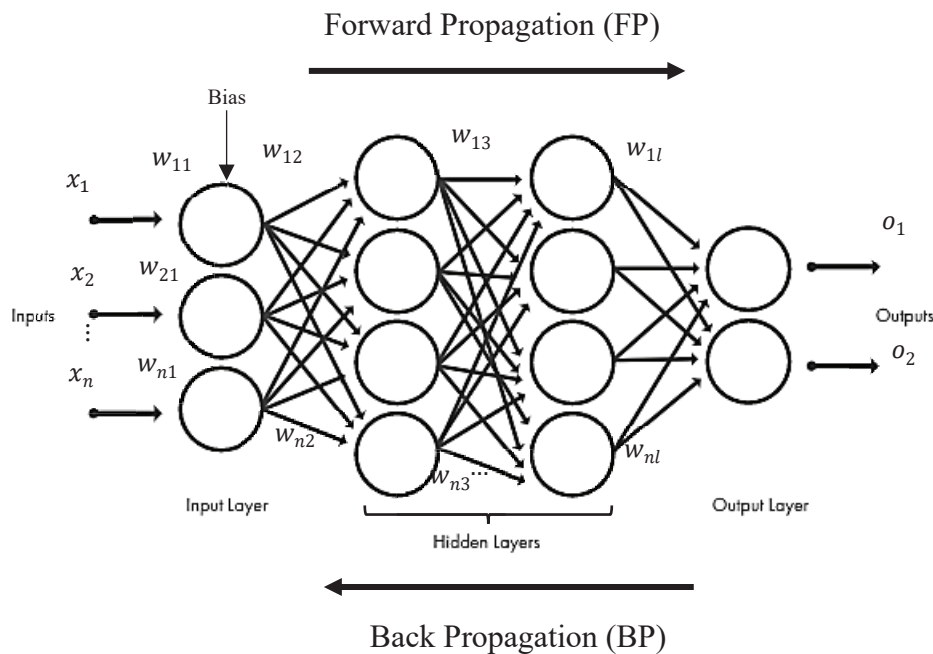


Fig. III. 25. Artificial Neural networks are organized in layers consisting of a set of interconnected nodes

For our example, we have in Fig. III. 25 a network architecture with an input layer of n neurons, with an output layer with two neurons, and a network with a hidden layer of $l - 2$,

where each hidden layer has $n^\#(l) = n$, with $l \in \mathbb{N}$ and $n \in \mathbb{N}^*$. The input values ($\{x_i\}, i \in \mathbb{N}^*$) is noted as layer $l = 0$, even if generally that is not counted as a layer on the network architecture.

Most Deep Learning Methods (DLM) use neural network architectures, so deep learning models are often referred to deep neural networks. The term deep usually refers to the number of hidden layers in the neural network (e.g., shallow architecture is a network with a single hidden layer [131]). Conventional neural networks have almost 2-3 hidden layers, while deep networks can have up to 150. One of the significant advantages of deep learning networks is their ability to improve the model when your data volume increases.

III.3.3.6. Feed Forward propagation and Backpropagation

In Fig. III. 25, we can see that Feedforward Propagation is the way to move the data computation from the input layer to the output layer in the neural network. In contrast, the opposite process is backpropagation, which is the method used to optimize the weights and bias parameters reaching the minimum of the loss function. A standard backpropagation is a gradient descent algorithm. The term backpropagation refers to how the gradient is computed for nonlinear multilayer networks.

Feedforward networks are of extreme importance to machine learning practitioners. They represent the basis of many important commercial AI applications [132].

Specifically, we will introduce a feedforward computation for the network shown in Fig. III. 25. For an illustration of this model. This feedforward network has an activation function for all layers that is computed by a function $\varphi^{[l]}(Net^{[l]})$. The values of these hidden units are then used as the input for a second layer, and so on, until the last layer, which corresponds to the output of the network architecture.

$$l = 1 \quad \begin{cases} Net^{[1]} = W^{[1]}X + \theta^{[1]} \\ O^{[1]} = \varphi^{[1]}(Net^{[1]}) \end{cases} \quad (III.55)$$

$$l = 2 \quad \begin{cases} Net^{[2]} = W^{[2]}O^{[1]} + \theta^{[2]} \\ O^{[2]} = \varphi^{[2]}(Net^{[2]}) \end{cases} \quad (III.56)$$

$$\vdots$$

$$l = l \quad \begin{cases} Net^{[l]} = W^{[l]}O^{[l-1]} + \theta^{[l]} \\ O^{[l]} = \varphi^{[l]}(Net^{[l]}) \end{cases} \quad (III.57)$$

With:

$$X = O^{[0]}$$

$$W = [W^{[1]} \ W^{[2]} \ \dots \ W^{[l]}] \quad (\text{III.58})$$

$$W = \begin{bmatrix} w_{11} & \cdots & w_{l1} \\ \vdots & \ddots & \vdots \\ w_{n1} & \cdots & w_{nl} \end{bmatrix} \in R^{n \times l} \quad (\text{III.59})$$

Basically, each neuron of the input layer distributes its value to all the neurons in the middle layer. Along with each connection between input and middle neurons, there is a connection *weight* W_{ij} so that the middle neuron receives the product of the value from the input neuron and the connection weight; thus, neurons in the middle layer take the sum of its weighted inputs and then applies a nonlinear function (activation function) to the sum. The result of the function then becomes the output for the entire architecture [136]. All this process represents the first Feedforward propagation of the network computation before evaluating the training performance (by backpropagation).

Theoretically, PB provided with a simple layer of hidden units is sufficient to map any mathematical problem. If provided with an appropriate number of hidden units (neurons), they will also be able to minimize the error of nonlinear functions of high complexity [134].

Back-propagation refers only to the method for computing the gradient, while another algorithm, such as stochastic gradient descent, is used to learn using this gradient. Furthermore, back-propagation is often misunderstood as being specific to multilayer neural networks, but in principle, it can compute derivatives of any function (for some functions, the correct response is to report that the derivative of the function is undefined) [130]. Specifically, we will describe how to compute the gradient for our neural architecture with an arbitrary loss function.

For a regression model, the cost function is defined as the mean square error of the true value of the system output and the prediction from the feedforward propagation process.

$$C = (O_j^{[l]} - o_j)^2 \quad (\text{III.60})$$

The aim is to minimize the cost function; thus, the gradient of the cost function is defined according to the matrices of weights and bias parameters using the chain rule.

$$\frac{\partial C}{\partial w_{ij}^{[l]}} = \frac{\partial C}{\partial o_j^{[l]}} \frac{\partial o_j^{[l]}}{\partial \text{Net}_j^{[l]}} \frac{\partial \text{Net}_j^{[l]}}{\partial w_{ij}^{[l]}} = O_j^{[l-1]} \phi'^{[l]}(\text{Net}_j^{[l]}) \frac{\partial C}{\partial o_j^{[l]}} \quad (\text{III.61})$$

$$\frac{\partial C}{\partial w_{ij}^{[l]}} = 2(O_j^{[l]} - o_j)O_j^{[l-1]}\varphi'^{[l]}(Net_j^{[l]}) \quad (III.62)$$

$$\frac{\partial C}{\partial \theta_j} = 2(O_j^{[l]} - o_j)\varphi'^{[l]}(Net_j^{[l]}) \quad (III.63)$$

The following formula gives the overage of the cost function for all training:

$$\langle \frac{\partial C}{\partial w_{ij}^{[l]}} \rangle = \sum_{k=1}^m \frac{\partial C_k}{\partial w_{ij}^{[l]}} \quad (III.63)$$

$$\langle \frac{\partial C}{\partial w_{ij}^{[l]}} \rangle = \sum_{k=1}^m 2(O_j^{[l](k)} - o_j^{(k)})O_j^{[l-1](k)}\varphi'^{[l]}(Net_j^{[l](k)}) \quad (III.64)$$

With:

$$Net_j^{[l]} = W_{1j}^{[l]} O_1^{[l-1]} + W_{2j}^{[l]} O_2^{[l-1]} + \dots + W_{ij}^{[l]} O_j^{[l-1]} \quad (III.65)$$

$$O_j^{[l]} = \varphi^{[l]}(Net_j^{[l]}) \quad (III.66)$$

The most effective modern optimization algorithms are based on gradient descent, but many useful loss functions have no useful derivatives (the derivative is either zero or undefined everywhere). These two problems mean that we rarely use empirical risk minimisation in the context of deep learning. Instead, we must use a slightly different approach, in which the quantity that we actually optimize is even more different from the quantity that we truly want to optimize. For our approach, we used a GUI from MATLAB Toolbox that takes into account all these details and provides different types of training functions and algorithms for optimization of the model dataset training.

III.3.4. The evaluation metrics of a trained model

One way to evaluate the performance in terms of the model's accuracy to predict the data correctly is when we test with new data. For the regression problem, a quantitative way is using some statistical metrics that we will describe in the following sections. We defined as the amount of test data K .

III.3.4.1. Mean Absolute Error (MAE)

MAE is the simplest method to calculate the error function for a regression problem. It is calculated as the absolute difference between the true and prediction values.

$$MAE = \frac{1}{K} \sum_{k=1}^K \left| \underbrace{O_j^{(k)}}_{\text{Predicted value}} - \underbrace{\hat{O}_j^{(k)}}_{\text{True value}} \right| \quad (III.67)$$

Due to the simplicity of the method, it takes less computation time compared with the other methods. This method emphasizes that all errors are weighted equally on the same scale.

III.3.4.2. Mean Absolute Percentage Error (MAPE)

MAPE is quite similar to MAE, while MAPE is the calculated error in percentage.

$$MAPE = \frac{1}{K} \sum_{k=1}^K \left| \frac{o_j^{(k)} - \hat{o}_j^{(k)}}{o_j^{(k)}} \right| \times 100\% \quad (\text{III.68})$$

Note that we have the actual value of the observation in the denominator, which can not be equal to zero. The advantage of this metric is that the error is normalized on a common scale, according to the amount of dataset.

III.3.4.3. Mean Square Error (MSE)

MSE, as its name suggests, is the average of the squared difference between predicted and actual values.

In MSE metric, we calculate the square of our error, and then we take its mean. This is a quadratic scoring method, which means that the penalty is not proportional to the error like in MAE metric but to the square of the error. It gives relatively higher weight (penalty) to large errors or outliers while smoothening the gradient for smaller errors.

$$MSE = \frac{1}{K} \sum_{k=1}^K \left(o_j^{(k)} - \hat{o}_j^{(k)} \right)^2 \quad (\text{III.69})$$

III.3.4.4. Root Mean Square Error (RMSE)

RMSE is just the square root of MSE, which means it is again a linear scoring method but still better than MAE as it gives comparatively more weightage to larger errors.

$$RMSE = \sqrt{\frac{1}{K} \sum_{k=1}^K \left(o_j^{(k)} - \hat{o}_j^{(k)} \right)^2} \quad (\text{III.70})$$

The advantages of this metric are that we obtain extreme losses for a larger value. It is more sensitive to the outlier than the MAE. The error value from the calculation has the same magnitude scale as the predicted magnitude, while the MSE does not have.

III.3.4.5. Relative Absolute Error (RAE)

RAE is also known as the residual sum of a square, where we take the total absolute error and normalize it by dividing by the total absolute error of the simple predictor.

$$RAE = \frac{\sum_{k=1}^K |O_j^{(k)} - \widehat{O}_j^{(k)}|}{\sum_{k=1}^K |O_j^{(k)} - \overline{O}_j^{(k)}|} \quad (III.71)$$

III.3.4.6. Relative Squared Error (RSE)

RSE is very similar to RAE, and it is widely adopted by the data science community to calculate the R square metric.

$$RSE = \frac{\sum_{k=1}^K (O_j^{(k)} - \widehat{O}_j^{(k)})^2}{\sum_{k=1}^K (O_j^{(k)} - \overline{O}_j^{(k)})^2} \quad (III.72)$$

And:

$$R^2 = 1 - RSE \quad (III.73)$$

R square is not an error percentage but is a popular metric for the accuracy of the model. It represents how close the data values are to the fitted regression line. The higher is R^2 , better the model fits our data. Each of these metrics can be used to quantify the model prediction using the test dataset.

To sum up, MAE is the easiest of the metrics to understand since it is just the average error, while the MSE metric is more popular than MAE because the focus is geared more towards large errors. This is due to the squared term exponentially increasing larger errors in comparison to smaller ones. RMSE is one of the most popular evaluation metrics because root mean squared error is interpretable in the same units as the response vector or $O_j^{(l)}$ units, making it easy to relate its information.

III.3.5. Model training for the prediction of the micropore performance

In this section, we will present the methodology we used to train the model for micropore performance prediction. In addition, we explored Deep Learning Tool from the Matlab GUI APP.

The methodology of our approach consists of several steps (Fig. III. 26):

- Generating data from the micropore performance simulations
- Data pre-processing to study the distribution, select the optimal parameters and clean the data if necessary.
- Train the AI model, selecting the optimal parameters and hyperparameters to reach a good accuracy for the data generalization

- Test the model with new data and evaluate the accuracy of the model

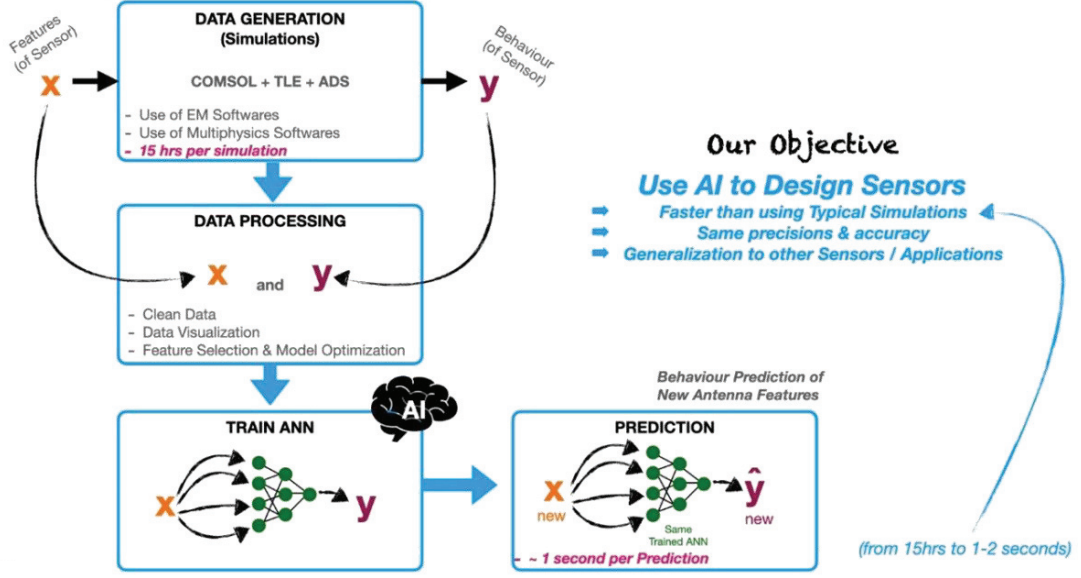


Fig. III. 26. Schematic procedure of the AI approach to predict the microprobe performances

III.3.5.1. The assumption of the ANN model to the generated data

An ANN model requires a large dataset corresponding to inputs and their target (outputs). In the dataset for our study, we can note the predictors and the targets as follows:

- **Predictors (X):** $[D_{out} \ D'_{out} \ w \ t \ s \ n \ w_{und} \ t_{und} \ h_{vias} \ w_{sign} \ w_{gnd} \ \rho \ \varepsilon \ f]$; Parameters that represent input feature used to feed the model during training and prediction testing.
- **Target (Y):** $[R_{probe} \ Q_{probe}]$; They are the output of the data, which was used for the model learning process.

For our study, we assumed that our system could be defined as a 4D (dimension) problem, as shown in Fig. III. 27. The dimensions correspond to the microprobe performance (Q -factor and Resistance), geometric parameters of the system, the electrical properties of the materials, and the fourth dimension correspond to the working frequency.

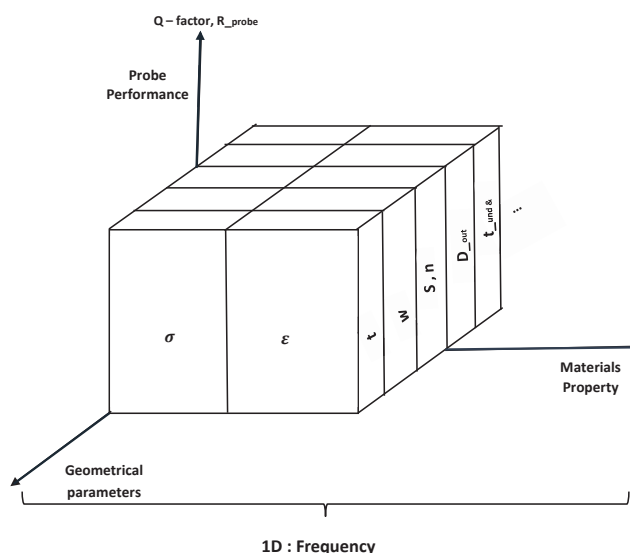


Fig. III. 27. The tensor model of our multiparameter system

To illustrate the 4th dimension, we used the tensors analogy. We see in Fig. III. 28, several representations for dimensions of a tensor. The 4th dimension can be generated by replicating several times the 3D case. For our case, the 3D tensor corresponds to [Performance (Geometrical parameters) (Material properties)] repeated for each frequency case which represents the 4th dimension.

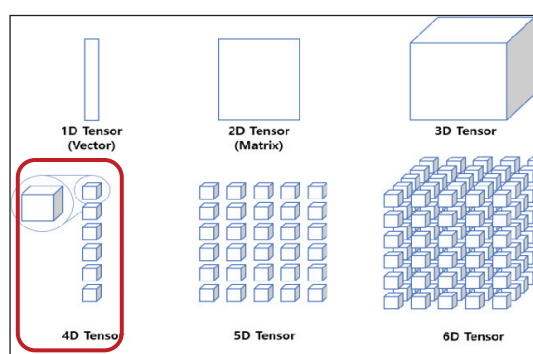


Fig. III. 28. The analogy of tensors dimensions [138]

The tensor analogy matches very well with the representation of the parameters defining our system (Microprobe designing features and performances parameters). All these assumptions were required for the microprobe performance prediction. Note that the SNR parameter (defined in chapter I, section (I.3.3.4)) is a function of the targets parameters of the system (Q factor and Resistance). Therefore, we trained an ANN model to predict all these parameters, which represent the target of the system.

Our dataset used to train the model was generated from numerical simulation of the microprobe Resistance and Q factor using the 3D-TLE (Transmission Line Extractor) platform, associated

with ADS software (Advanced Design System). Fig. III. 29 shows the schematic block of the main step to simulate the microprobe e performance.

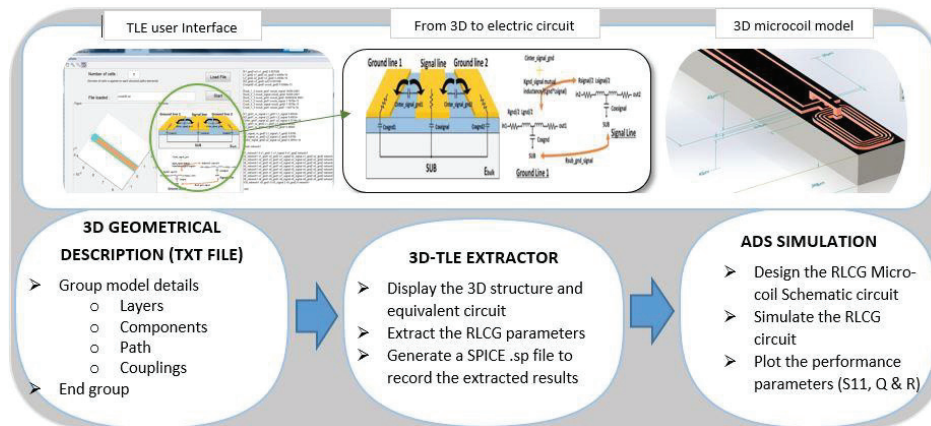


Fig. III. 29. Block diagrams of the simulation methodology: TLE user interface and 3D design of the microprobe with its dimensions

The principle consists in creating a *.txt* file with all geometrical parameters of the system, material properties and the coupling among different system parts. Then, a spice file is generated with all electrical parameters, where the performance in terms of Q factor and the resistance value were simulated through ADS. Four micro-coil geometries (rectangular, ellipsoidal, square and circular) were simulated, two types of substrates (glass and silicon) in the working frequency range of 200 MHz to 900 MHz. For each geometry, we have several coil width and length sizes (corresponding to the outside diameters of the micro-coils) with the value of 500 μm to 1000 μm , as well as all other geometrical parameters from the microprobe shape that we are going to see in the latter part of this section. With our method, we were able to generate 6528 observations (For more details, see Section III.4.3).

III.3.5.2. The pre-processing of our generated dataset

After the data generating, we performed the data pre-processing to better understand the distribution of our data and train our model with the best-selected dataset. In the following section, we presented the results of the histogram plotting (Fig. III. 30), boxplot (Fig. III. 31) and correlation plot between the targets (Fig. III. 32 and Fig. III. 33). We performed the histogram and box plot for the statistical distribution of the data and the scatter plot for the correlation between the targets. That reveals how the targets are linearly connected.

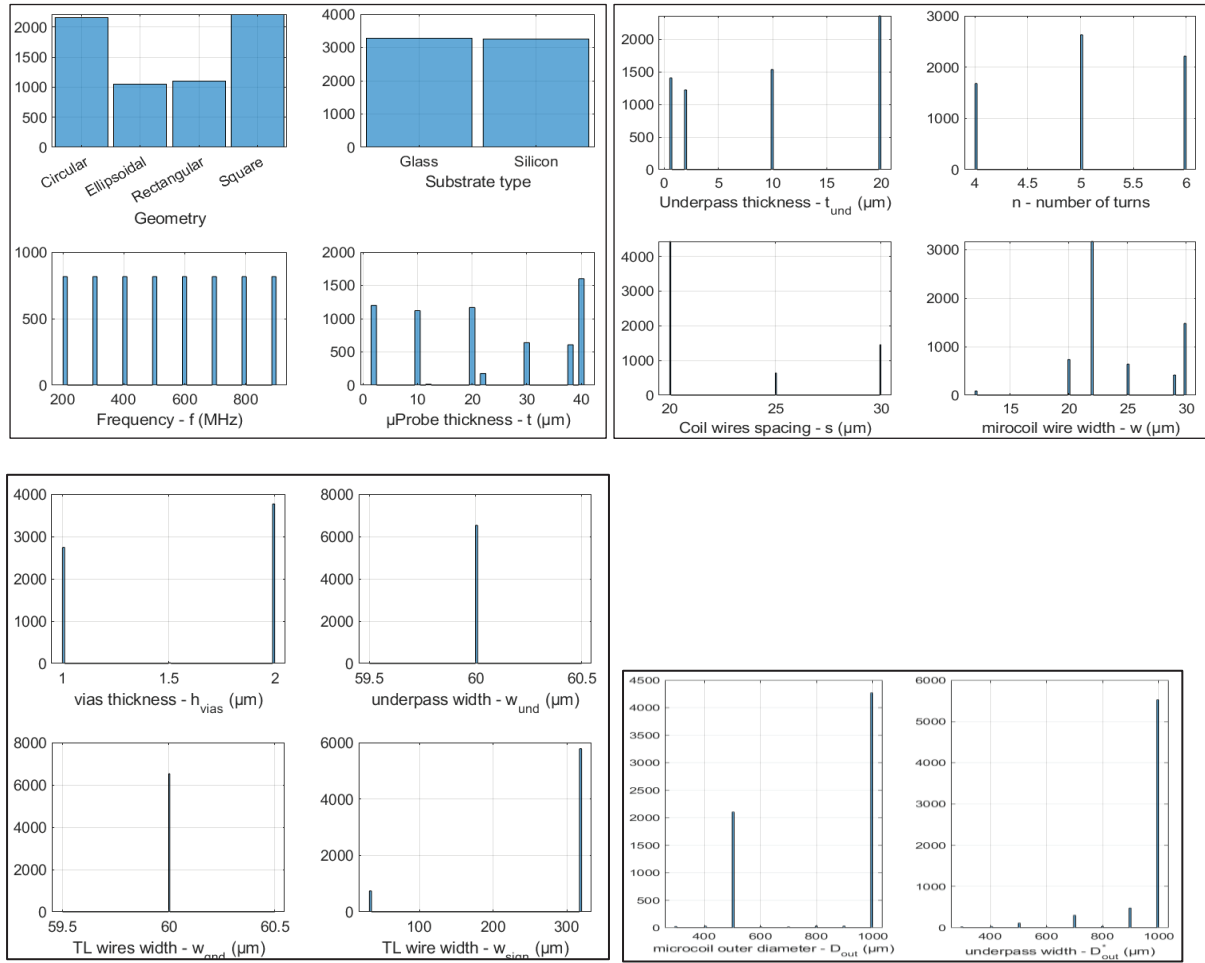


Fig. III. 30. The histogram of the dataset predictors

Note that we have two features of the system uniformly distributed (frequency and substrate type) and two parameters that do not change (TL width part *gnd* and underpass width).

Those uniformly distributed features represent good predictors whose we train with the AI model, and those that do not variate should not impact the learning process of the model, so we did not select them as the model predictors.

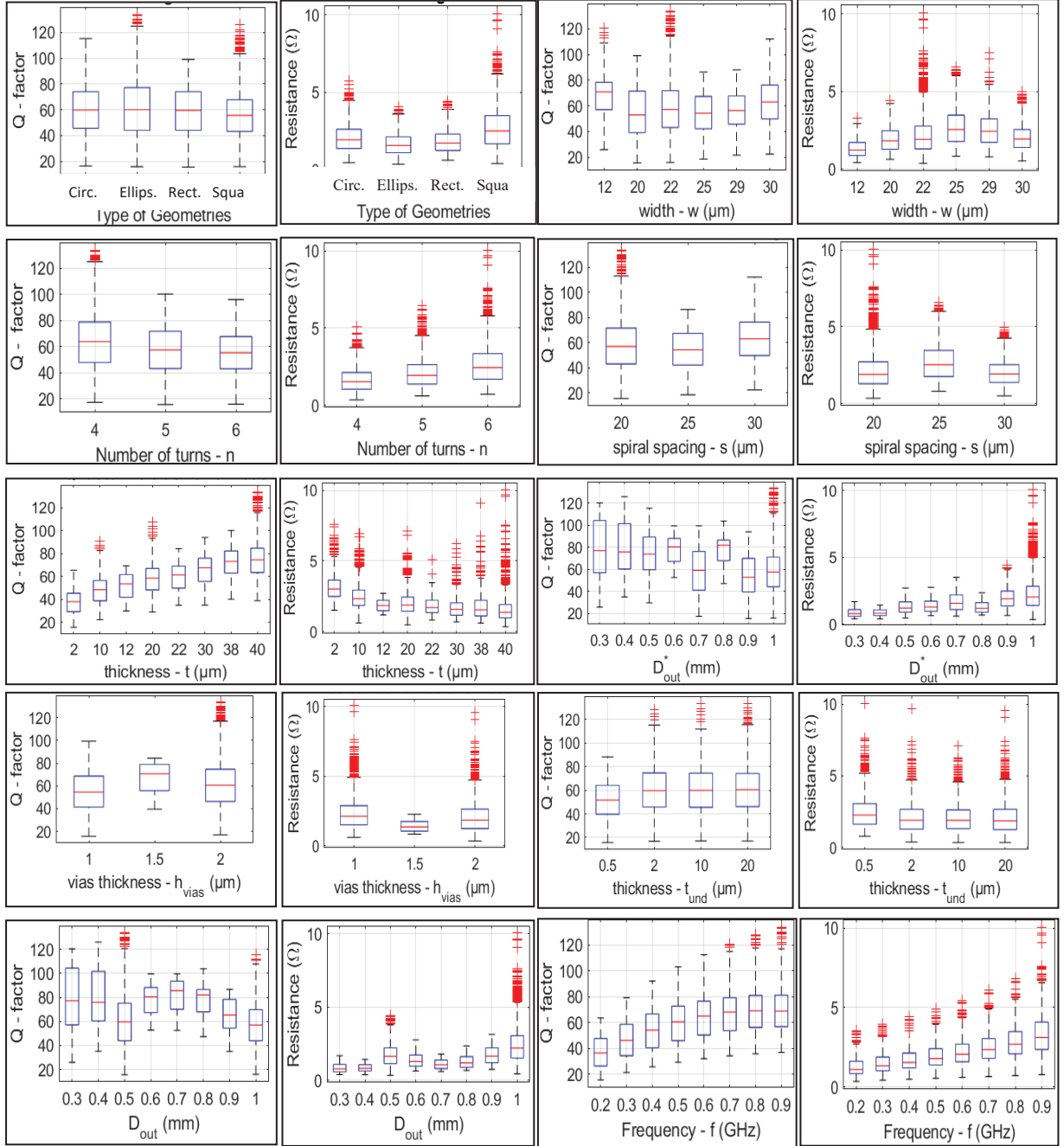


Fig. III. 31. The boxplot of 10/12 predictor with the targets (Resistance and Q factor of microprobe)

In the boxplot from Fig. III. 31, we can highlight three points: Firstly, the outlier of the Q factor target represents the most pertinent value of the microprobe performance. Secondly, there are more outliers on the resistance target than the Q factor, and finally, such behaviours occur for all predictors parameters.

Fig. III. 32 and Fig. III. 33 show that the Q factor and the Resistance have a poor correlation coefficient even though microprobe Resistance is much smaller than the micro-coil Resistance.

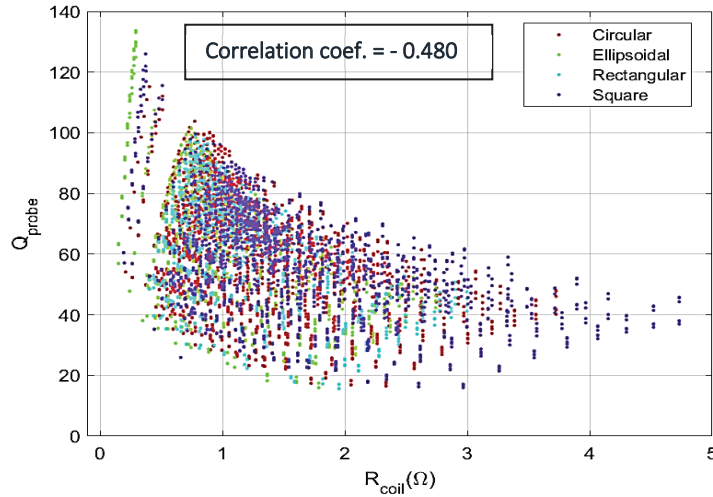


Fig. III. 32. The plot of the targets (Q – factor and micro-coil Resistance): four types of geometry

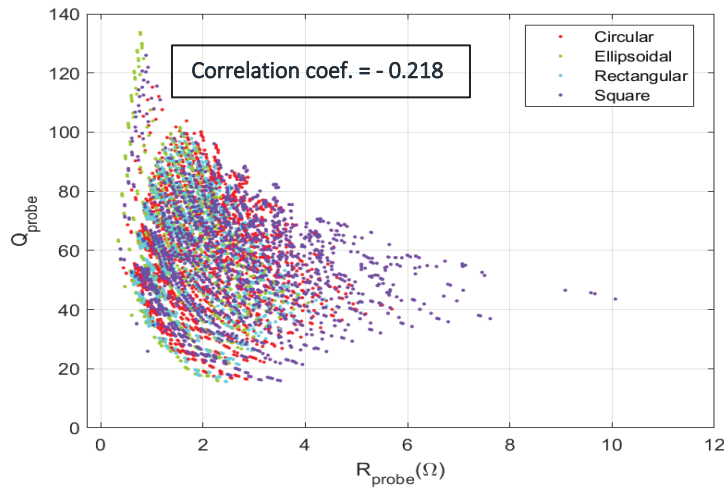


Fig. III. 33. The plot of the targets (Q – factor and Microprobe Resistance): four types of geometry

Note that, in the plot of the Q factor and the resistance parameters for the four geometries, there is a poor correlation between them, knowing the correlation coefficients are below 0.7.

For our model training, we used data augmentation instead of dropout methods. This is the more adapted technique for our case. As we are going to see, we used a simple Neuronal architecture. So, there was more need to increase the amount of our data than deal with the neuronal architecture (see appendix A.8, for more details about data regularization methods).

III.3.5.3. The architecture used for our model training

For the Artificial Neuronal Network (ANN), there is a MATLAB Toolbox, for Deep Learning (DL) applications called *nnstart*. It is a Graphical User Interface (GUI), where the model parameters were pre-defined, and we could generate a MATLAB script to customize the parameters and hyperparameters of our ANN model for training.

To find the best model training, we need to define which shape of the model we should use, select the best feature, know what features are important, and tune several parameters to find the optimal parameters. We needed to iterate many times to find the best fit for our data.

In Fig. III. 34, we show the ANN shallow architecture, which is the architecture that we chose for our study. Shallow is a neural network that provides only a single hidden layer. We provided an architecture with 14 neurons in the input layer (corresponding to the number of data predictors) and two neurons in the output layer (corresponding to the data targets). The number of neurons for the hidden layer will be optimized by a script, which calculates the optimal number of neurons according to the RMSE criterion.

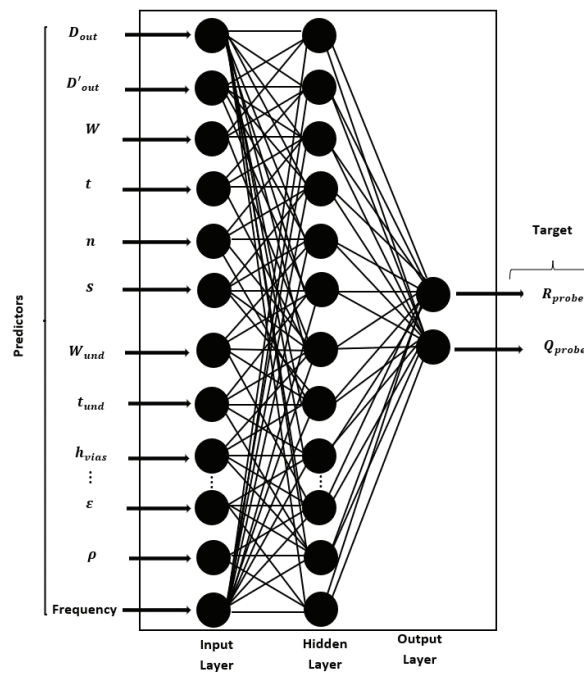


Fig. III. 34. ANN architecture for Microprobe dataset training model

Generally, we want a model that captures the data trend without fitting the noise in the data. Therefore, when the model fits the noise, we call it overfitting. So, using validation data during the training process helps prevent overfitting. For validation data, there are two approaches: cross-validation and holdout validation methods. In our work, we have chosen the holdout method.

To evaluate the quality of the chosen model, it was important to divide our data (data sets). We distributed it randomly as follows: 70 % of our data were used for training, 15 % for validation and 15 % for testing. So, when we find the best model options, we trained the model using the

combined training and validation data. Once we get the final model, we have applied the new observations; That is why, it was crucial to provide the test data.

III.3.5.4. The testing of Backpropagation algorithms and activation function

Generally, each backpropagation training section starts with different initial values for the weights and bias coefficient parameters of each ANN unit neuron. We can also fix the random divisions of the dataset for training and validation or, therefore, randomly divide data for different values of training, validation, and test for each trial. We can choose different activations functions. These additional conditions can lead to very different solutions for the same problem.

One of the most important parameters to define is the type of training algorithms to optimize the cost function. It is very difficult to know which training algorithm will be optimal and fastest for a given problem. It depends on many factors, including the complexity of the problem, the number of data points in the training set, the number of *weights* and *biases* in the network, the error goal, and whether the network was being used for pattern recognition (discriminant analysis) or function approximation (regression). This section compares the various training algorithms applied to our dataset.

We performed the trial training for several cases of the optimal number of neurons (I) for the hidden layer; we chose the min and max value for the RMSE metric that we denoted by the best model and poorest model among several trials of the optimal (I model) training and validation. We tested the best and poorest model with new data, and we plotted the prediction of the Q factor and resistance R , compared to the true value. Thus, we performed our test using different backpropagations algorithms for the training of the ANN model such as:

- *Trainlm* : Levenberg-Marquardt backpropagation
- *Trainbr* : Bayesian Regularization Backpropagation
- *Trainscg* : Scaled Conjugate Gradient backpropagation
- *Trainoss* : One Step Secant backpropagation
- *Traingdx* : Variable Learning Rate Backpropagation/Gradient descent with momentum and adaptative learning rate backpropagation
- *Trainrp* : Resilient Backpropagation
- *Traingdm* : Gradient Descent with Momentum backpropagation

We also tested two cases of activation function of the output layer (linear function and *ReLU* function), knowing that we used as activation function in the hidden layer the hyperbolic tangent (*tanh*).

Training parameters: *epoch* = 2000, *plot interval* = 53 *epoch* (see appendix, A.9, for more details about epoch), variation of number of neurons for the hidden layer (1 to 1000), number of trial training for parameters optimization 500 trials.

The following table list the results of algorithms that were tested for our problem with the model performance obtained for training, validation and test of the models.

Train algorithm	NN	RMSE optimal	RMSE train	RMSE validation	RMSE test	RMSE min	RMSE max	RMSE mean	Comput. time
Lm (Linear)	12:125:2	0.7379	0.8354	0.8995	0.8665	0.7379	2.8207	1.3247	8 h 30 min
Lm (ReLU)	12:505:2	16.967	1.426	1.848	1.923	16.968	18.820	17.922	0h 30 min
Scg (Linear)	12:125:2	0.7379	0.8354	0.8995	0.8665	0.7379	2.8207	1.432	7 h 30 min
Scg (ReLU)	12:505:2	16.968	1.427	1.848	1.923	16.968	18.820	17.922	1h 30 min
Gdm(Linear)	12:4:2	23.102	56.0913	56.6369	56.513	13.893	115.42	44.501	0h 10 min
Gdm (ReLU)	12:163:2	17.142	298.669	292.927	288.537	17.078	1.02e6	2.99e3	0h 20 min
Oss (Linear)	12:3:2	1.0840	3.0711	3.072	3.315	1.0477	4.795	2.2547	5h 30 min
Oss (ReLU)	12:505:2	16.819	3.7624	4.599	4.593	16.819	224.614	19.612	2h 00 min
Rp (Linear)	12:8:2	1.173	1.704	1.639	1.756	0.908	3.349	1.688	5h 30 min
Rp (ReLU)	12:505:2	16.819	4.199	5.1489	5.395	16.819	26.915	17.986	0h 15 min
Br (Linear)	12:4:2	23.102	56.187	NaN	56.5935	13.893	115.42	44.5010	0h 5 min
Br (ReLU)	12:202:2	17.874	317.25	NaN	310.86	17.546	606.45	171.91	0h 5 min
Gdx (Linear)	12 : 7 : 2	3.717	4.479	4.723	4.861	3.229	79.006	5.211	1h 30 min
Gdx (ReLU)	12 : 717 : 2	17.0718	40.3672	42.3451	41.019	17.059	974.244	28.944	0h 30 min

Table III. 4. List of the algorithms and models performance obtained during the testing of algorithms

There are several algorithm characteristics that can be deduced from the table of experiments described (Table III. 4). In general, on function approximation problems, for networks that contain down to a few twenty weights in the input layer, as our case, 12 *weights*, the Levenberg-Marquardt (LM) algorithm had the latest convergence (8 h 30 min for computation). With *trainlm* we obtained the lower RMSE than any of the other algorithms tested ($RMSE = 0.7379$, for a linear activation function). However, as the activation function of the *trainlm* change to ReLu, the advantage of *trainlm* decreased ($RMSE = 16.967$), we could confirm that the *trainoss*, *trainrp* and *traingdx* have shown lower *RMSE* with a linear

activation function ($RMSE_{oss} = 1.084, RMSE_{rp} = 1.173$ and $RMSE_{gdx} = 3.717$). The memory requirements of *trainlm* are larger than the other algorithms tested.

The *trainrp* function is the fastest algorithm (5 minutes for computation time). However, it did not perform well on function approximation problems. The memory requirements for this algorithm are relatively small in comparison to the other algorithms considered.

The conjugate gradient algorithms, in particular *trainscg*, seems to perform well over a wide variety of problems, particularly for our case, which seems to be similar to the *trainlm*. The SCG algorithm is almost as fast as the LM algorithm on function approximation problems. The conjugate gradient algorithms have relatively modest memory requirements. Furthermore, the SCG performance seems to be similar to the LM algorithms performance.

Now, we have the performance of the model to generalize the prediction of our data. Thus, we used completely new data to predict the Resistance and Q factor of the microprobe. In Fig. III. 35 (optimal model testing) and Fig. III. 36 (the best and poorest model testing), we can see the plot of the prediction and true value. For this, we performed a test of 25 observations corresponding to the Resistance and Q factor from a rectangular geometry on a glass and silicon substrate with $w = 24\mu m$ (micro-coil width completely outside the previous splitted dataset, as well as a square geometry on a glass substrat with $w = 34\mu m$ both one from 200MHz to 900MHz (See appendix A11, for more details).

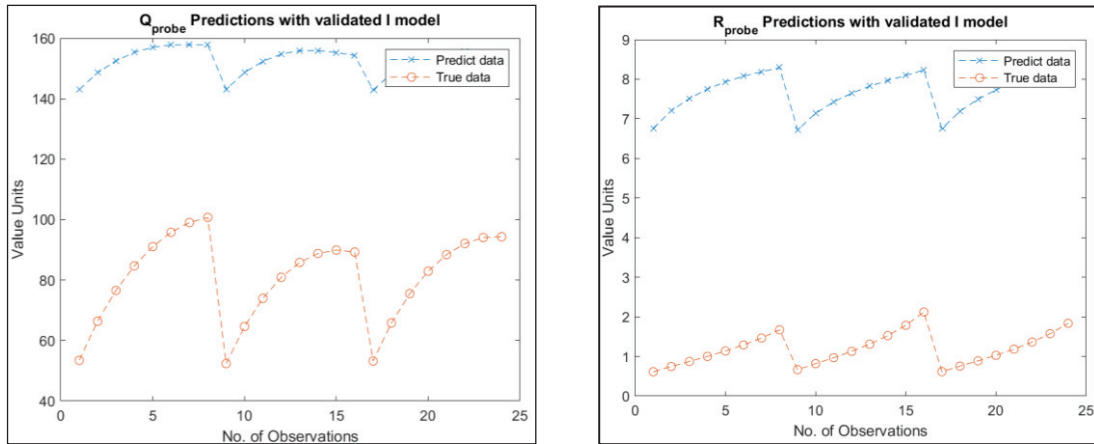


Fig. III. 35. The microprobe Q factor and Resistance R prediction, using the optimal number of neurons according to the evaluation of RMS from training, validation and testing

What we called by the optimal model (*I model*) corresponds to the optimal model, among the trial training and testing to choose the optimal number of neurons for the hidden layer (Test of neuron number from 1 to 1000, step of 1). And the *best* and *poorest* models correspond to the

min and *max* performance of the optimal model (optimal number of neurons for the hidden layer), but for different calibrations of ANN parameters (e.g., Weights and bias) for 500 trials.

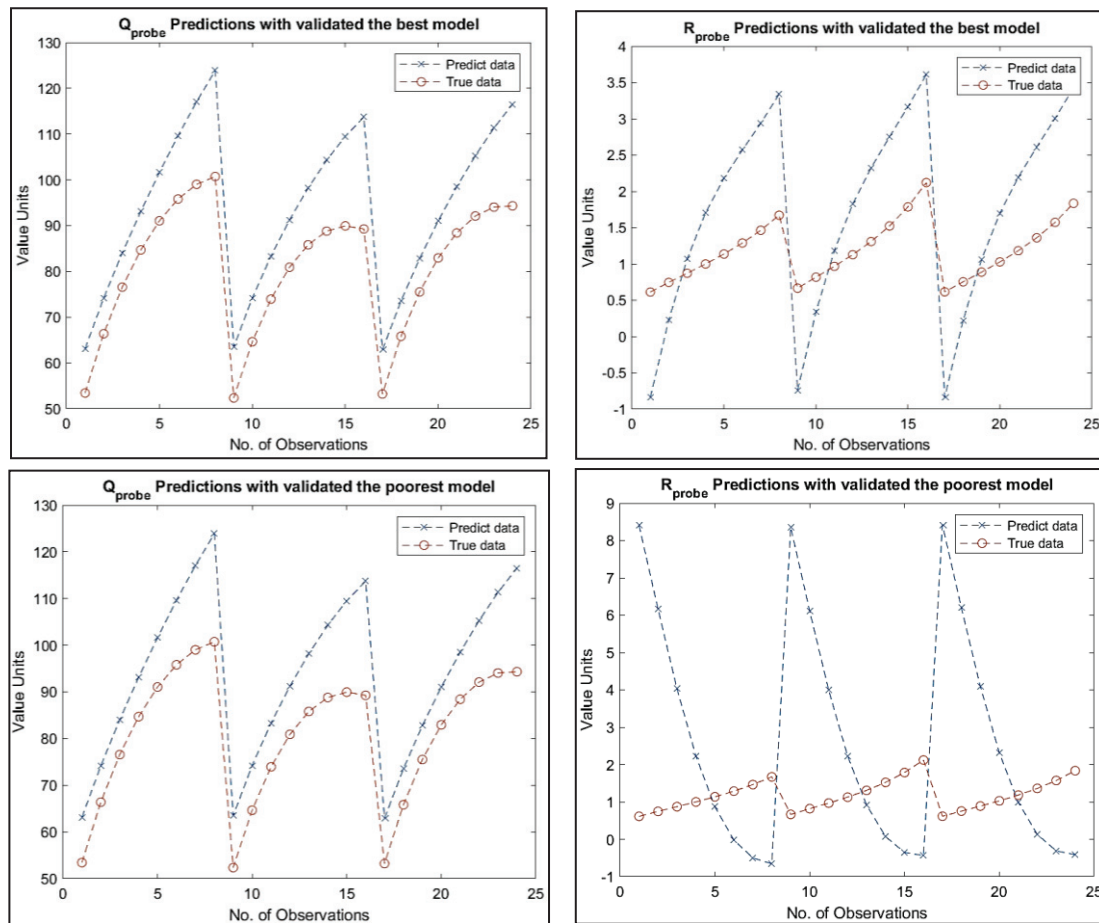


Fig. III. 36. The microprobe Q factor and Resistance R prediction, using the min and max RMSE of the testing model according to the trial of training with different weights and bias parameters

Note that the models (*I model* and *the best*) seem to predict the Resistance and Q factor tendency for completely new data while the poorest do not predict at least the tendency.

To sum up, we selected the *trainlm* and *trainscg* as the best algorithms. Furthermore, we are going to use them to study more in detail the model training performance and test the new data. We use as the activation function hyperbolic tangent (*tanh*) for the hidden layer and a Linear function for the Out-put layer. For the performance, we used the MSE metric (Fig. III. 37).

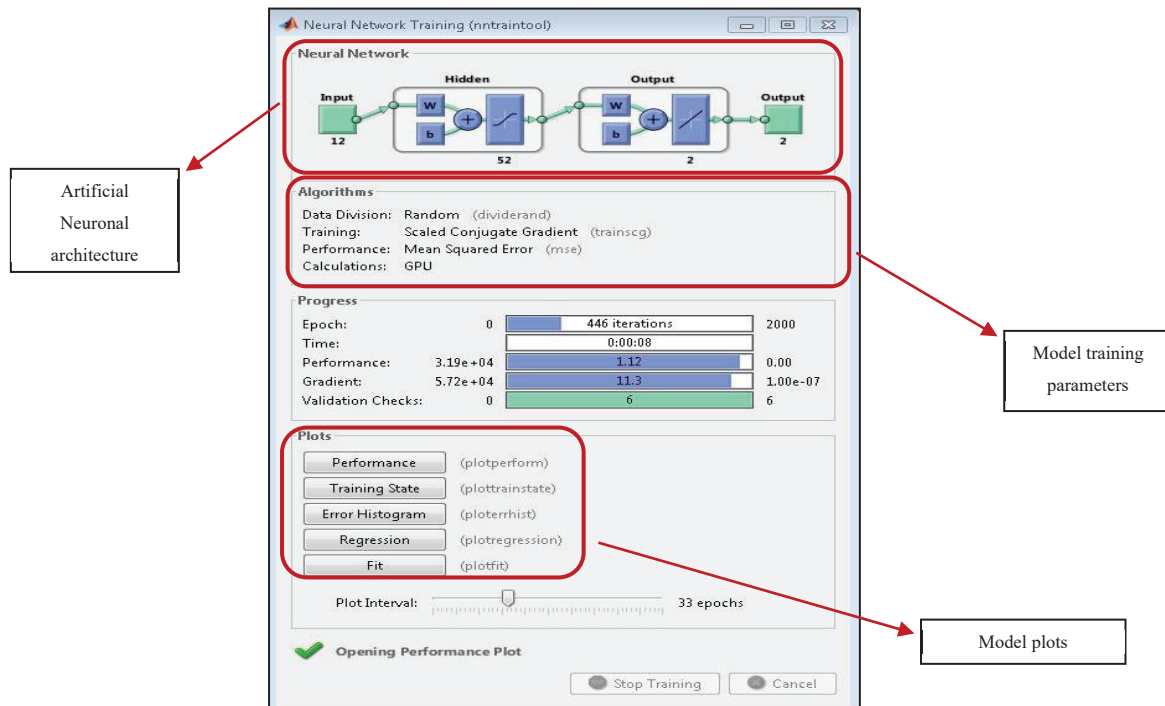


Fig. III. 37. ANN architecture for Microprobe dataset training model

III.3.5.5. The results of the optimization of model parameters of LM algorithms

Using the custom-made script to automatically test the different quantity of neurons for the hidden layer. That script allows choosing the optimal number of hidden layer neurons in terms of RMSE (Root mean square error) according to the test dataset performance as shown in Fig. III. 38. We tested the number of neurons for the hidden layer from 1 to 1000.

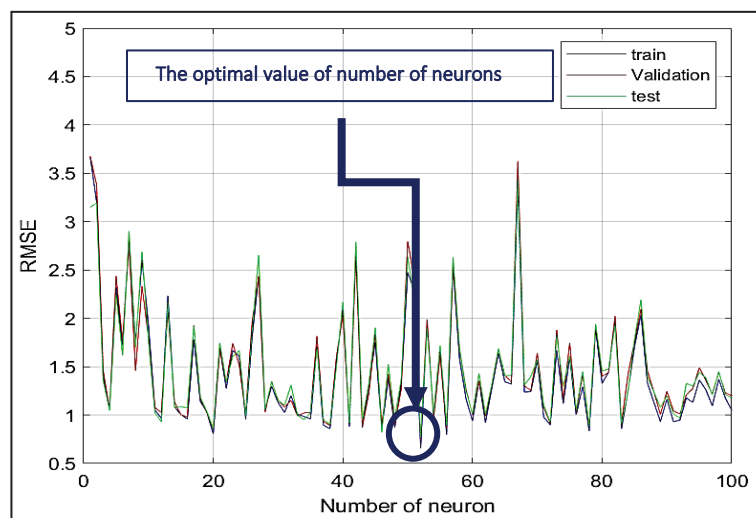


Fig. III. 38. The RMSE variation in terms of the number of neurons in the hidden layer

One of the major aspects of training an ANN model is avoiding overfitting. That is a concept in data sciences, which occurs when the model fits exactly against its training data, memorizing

the noises and fits too closely during the model training that it is not able to generalize. So, the model has great performance for training but the poorest performance for the test. This happens because the model is trying too hard to capture the noise in the training dataset. By noise, we mean the data points that do not represent the true properties of your data (tendency) but random position. Learning such data points makes the model more flexible, at the risk of overfitting.

The training performance of our ANN model can be seen in Fig. III. 39, more particularly in Fig. III. 39 a) our model does not present a training overfitting (The training performance seems to be close to the validation and test performance as well as both reach the best value RMSE value together). Fig.III.39 b) shows the histogram of the error from training, validation and testing. There is most part of the error close to the mean error which is the smallest error value; in addition, the validation error is similarly distributed as the test error.

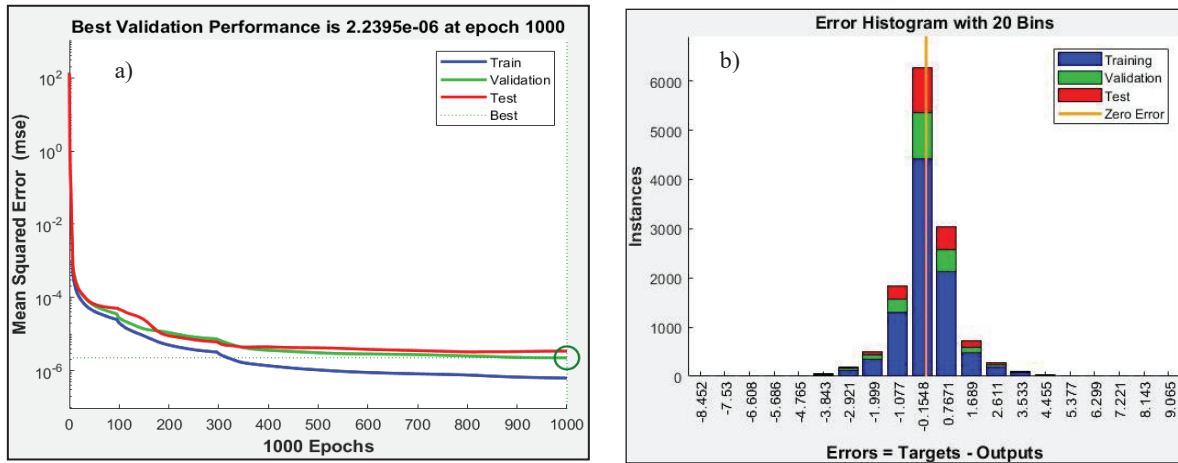


Fig. III. 39. (a) The performance variation as a function of epoch (train, validation and test) (b) The error histogram for the R_{probe} training model

The following figure shows that the target data fit very well with the prediction by regression of performance close to one ($\langle R \rangle = 0.99961$) for testing, validation, and training. We can also note that the data fit well the model; furthermore, the model fits the true data tendency.

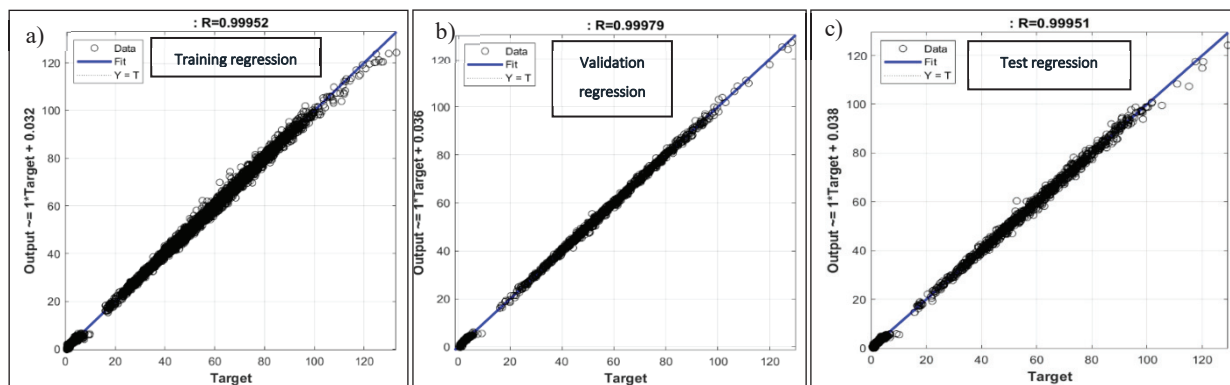


Fig. III. 40. A plot of the regression of the (a) Training dataset, (b) the validation and (c) Test dataset

Fig. III. 41 shows the plot of the Microprobe Q-factor and Resistance R prediction using the ANN model. We can note that the prediction and true data value are in good concordance, which means that we can accurately predict the microprobe's Q factor based on its geometrical parameters, working frequency, and materials properties. Even if the prediction of the Resistance still needs some enhancement.

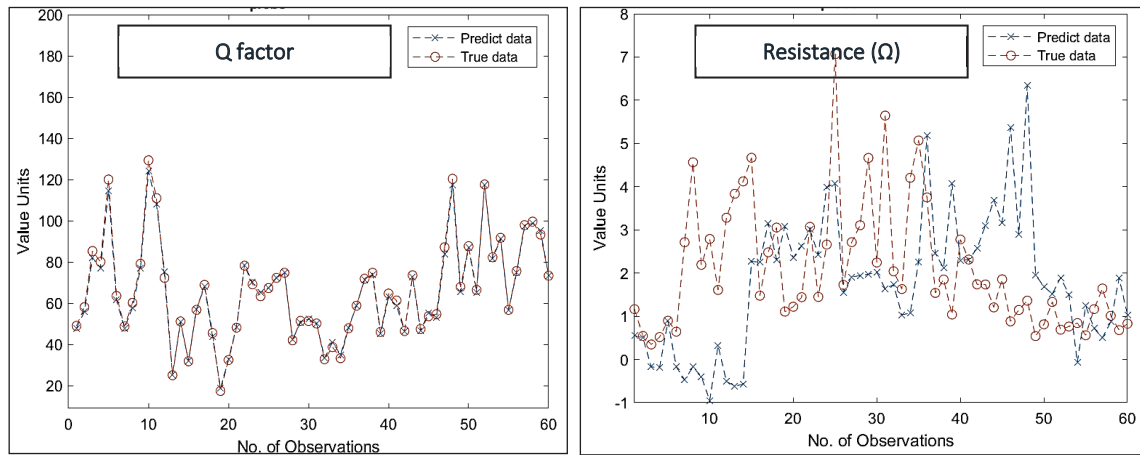


Fig. III. 41. The prediction and the true value of the Q factor and Resistance of the microprobe

Each network starts from different initial weights and bias coefficients and with a different division of training, validation, and test sets. So, we train several times (500 trials) to get the optimal value of bias and weights for the optimal number of neurons for the hidden layer. In the next Figures, we can see the results of the enhancement of generalization for the R_{probe} and the Q factor prediction.

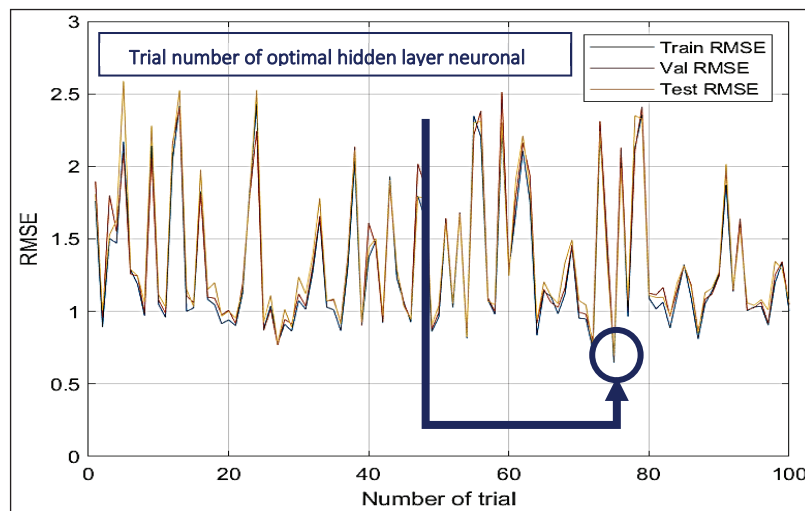


Fig. III. 42. RMSE performance of the optimal trial

Fig. III. 42 shows the fluctuation of RMSE performance of the model trials. We can see that we have a different value for the optimal neuron number from the hidden layer when we train the

model several times. That helps us choose the best one of the optimal models as we will show the performance prediction for the first optimization and then the poorest model.

We can note in the Fig. III. 43 that the Q factor prediction matches very well with the true value of the data.

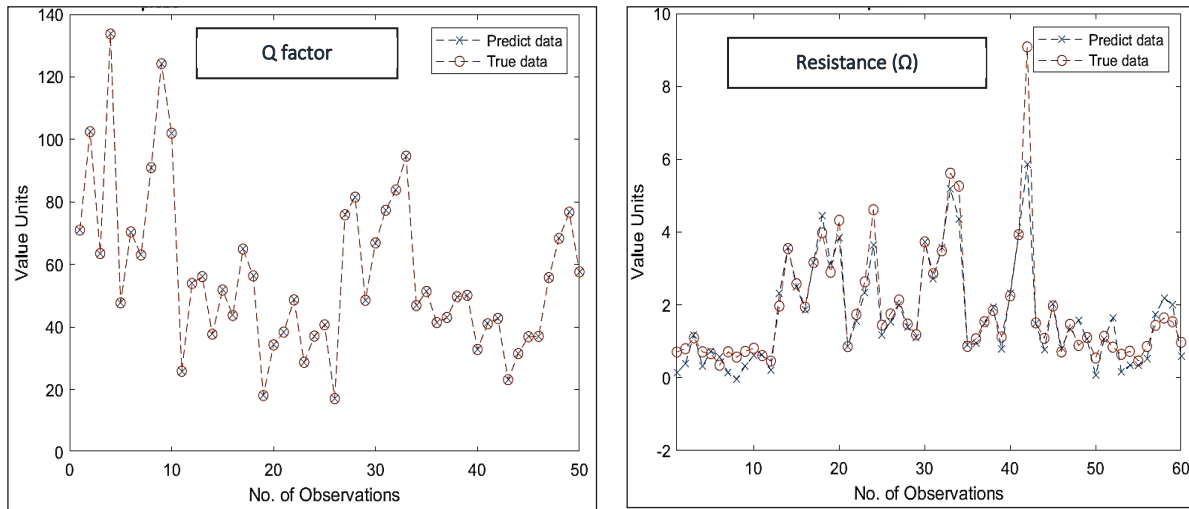


Fig. III. 43. The microprobe global Q factor and Resistance R prediction, after trial number optimization

In Fig. III. 43 we can also see that; the prediction of Resistance parameters of the microprobe adapts much better with the true value than in Fig. III. 41. Thus, we note an enhancement of the model prediction; even we still need to improve the model. Table III. 5 summarizes the performance of different AI models able to predict our microprobe's Resistance and Q factor.

Targets	ANN	RMSE	$\langle R^2 \rangle$ (%)
[R_probe Q_probe]	12 : 125 : 2	0.738	96.56
[Q_probe]	12: 52 : 1	0.032	99.79
[R_probe]	12 : 44 : 1	0.042	91.34

Table III. 5. The performance from the ANN architecture model for three target cases

As it is shown, our artificial intelligence algorithm (ANN) was validated to predict accurately the Q - factor of the microprobe (with $RMSE = 0.0322$ from test dataset), using a dataset of 6528 samples, which correspond to 99.79% of accuracy for the model prediction in term of to the test performance. Nonetheless, we need to enhance the model to predict the resistance parameters.

Conclusion

In this chapter, we proposed an electrical circuit that model the microprobe on a glass and silicon substrate. For that, we developed a 3D Transmission Line Extractor (TLE) platform; a homemade software dedicated to model the 3D transmission line (TL). Our goal was to model an NMR microprobe with a micro-coil, micro-TL, underpass, and vias structures. Thus, the effort was drawn on modelling and analysing the micro transmission lines and the TSV, simulated on a frequency range of 200 MHz to 900 MHz and then proposed the optimization in the designing to obtain a better-extracted value enhance the microprobe performance parameters (Q factor and Resistance value). The result obtained (Q factor of 110 for microprobe on a glass substrate, with a connecting wire solution – *airbridge* and a Q factor of 71 for a microprobe on a silicon substrate, with a connecting wire solution – *underpass & vias* with an optimized thickness $t_{und} = 10 \mu\text{m}$ instead of $0.5 \mu\text{m}$), We have validated these outcomes with ADS simulations; they were confirmed to be in good agreement (Table. III.2).

We also reported the training of an ANN model to predict the microprobe performances. Our study demonstrates how well ANN can help us to predict the microprobe performance based on its geometrical parameters, materials electrical properties and its own working frequency. The Q factor was accurately predicted (99.79% of accuracy which correspond to $RMSE = 0.0322$); while, the R_{probe} prediction accuracy was of 91% ($RMSE = 0.042$) which still need some improvements.

However, predicting the Q-factor that is correlated with the microprobe sensitivity remains a good opportunity to model the 3D Microprobe for NMR implanting before the microfabrication process and allow us to solve a complex problem that has been challenging for years.

Chapter IV

Manufacturing of the optimized microprobes and their characterizations in cleanroom

The chapter III already reported the optimization of planar microprobes (rectangular, square, circular and ellipsoidal) performances (Q factor and the equivalent resistance). We were able to determine the best geometry and dimensions suitable for an *in-vivo* application for monitoring changes in biomarker metabolites for an early diagnosis of Alzheimer's disease by MRS through an animal model.

Our optimization work led us to the micromanufacturing of the different microprobe prototypes on silicon and glass substrate. This also led us to propose masks fabrication with layout design by providing three types of connecting wire solution such as: *wire-bonding*, *underpass* & *vias* and *airbridge*.

The microfabrication requires implementing a relatively complex manufacturing process and some optimizations. It is therefore essential to present the main steps of the manufacturing process; described in detail in this chapter.

Firstly, we presented the specification required for the optimal microprobe, for our application. Then we recalled the main stages of microprobe fabrication. Furthermore, we reported the optimization steps that were performed to fabricate the final prototype. In the end, we performed some characterizations and we validated their suitability for our *in vivo* applications.

IV.1. Microprobe cleanroom manufacturing process

There is almost three methods for the fabrication of micro-systems [136] [137] such as : (i) Bulk micromachining, (ii) Surface micromachining and (iii) LIGA process, that is the Germanic abbreviation of Röntgenlithographie, Galvanoformung, Abformung representing different steps of the process [138]. The first two methods are the most widely used in the microsystem fabrication in silicon and glass substrates [139]. However, the fabrication of our microprobe prototypes was performed using the surface micromachine method, more precisely the copper electroplating technique.

It is known that, the implementation of the micro-probe for our application lead the choice of the manufacturing process, from the connecting wire solution until the choice of the substrate to be used in order to have the desired performances for our application. From our team, a state of the art of different fabrication processes of the microprobe on silicon and glass substrate was reported in the Thesis of J. Trejo Rosillo [37]. The most important points to highlight are: (i) Micro-coil fabricated by electrodeposition on glass silicon can achieve a good quality factor. Though, a glass substrate does not allow the embedding of an active or passive circuit as in the case of a silicon substrate. (ii) Micro-coil manufactured on the silicon substrate reach a poor Q factor when we work on the high-frequency domain. Several works from the literature reported different MEMS coil designs, optimizing their performance, mainly investigating their performance for different coil materials, substrates and different fabrications techniques to maximize the Q factor [140]. The glass substrate has been preferred compared to a silicon substrate for the fabrication of the NMR microprobe. The Glass substrate has a low conductivity (about 10 to 15 S/m) and is biocompatible for our application. For our study, we performed the fabrication of the microprobe prototype on both substrates: silicon and glass substrate.

IV.1.1. Specifications of the microprobe prototype fabrication

According to the optimal microprobe specification project, the following Tables summarises the provided microprobe geometries, dimensions, n (number of spires turns) and the quantity in the designed layout for *wire-bonding* in Table IV. 1 while *underpass & vias, and airbridge* in Table IV. 2. Note that we have provided ninety-six (96) rectangular geometry ($500 \times 1000 \mu m^2$) on the glass substrate which is widely more than enough for the required quantity for the biocompatibility test and validations characterizations and performance analysis (30 microprobes).

• <i>Micro-coil type</i>	Dimensions (μm^2)	Number of spire n	Number of μ probes
Square	500×500	4	64
	400×400	4	80
	300×300	4	32
	250×250	4	16
	1000×1000	6	2
Rectangular	500×250	4	32
	1000×300	4	16
	900×300	4	16
	1000×400	4	16
	1000×500	4	96
	1000×250	4	16
Ellipsoidal	1000×500	4	48
Circular	500×500	4	64
	1000×1000	6	2
Total	All		≈ 484

Table IV. 1. The microprobe geometry, dimensions and characteristics: *wire-bonding*

Micro-coil type	Dimensions (μm^2)	Number of tours	Number of μ probes
Square	500×500	4	60
	400×400	4	45
	300×300	4	30
	250×250	4	45
	1000×1000	6	4
Rectangular	500×250	4	75
	1000×300	4	15
	900×300	4	15
	1000×400	4	15
	1000×500	4	15
	600×300	4	45
	1000×250	4	15
Ellipsoidal	1000×500	4	15
Circular	500×500	4	60
	1000×1000	6	4
Total	All		≈ 458

Table IV. 2. The microprobe geometry, dimensions and characteristics: *underpass & vias and airbridge*

We provided two types of substrates (silicon and glass) and two mask layout designs with the following characteristics:

1. A glass substrate with 400 μm thickness (mask 1).
 - *Wire-bonding* for connecting micro-wire, and 40 μm for copper thickness
2. A silicon substrate with thickness of 500 μm , and 40 μm for copper thickness (mask 2)
 - *Underpass & vias* for connecting micro-wire
 - *Airbridge* for connecting micro-wire

Mask 1 was conceived with a unique layer level (Fig. IV. 1) corresponding to the copper strip line and specifically designed for the fabrication with a provided connecting micro-wire solution such as *wire-bonding*.

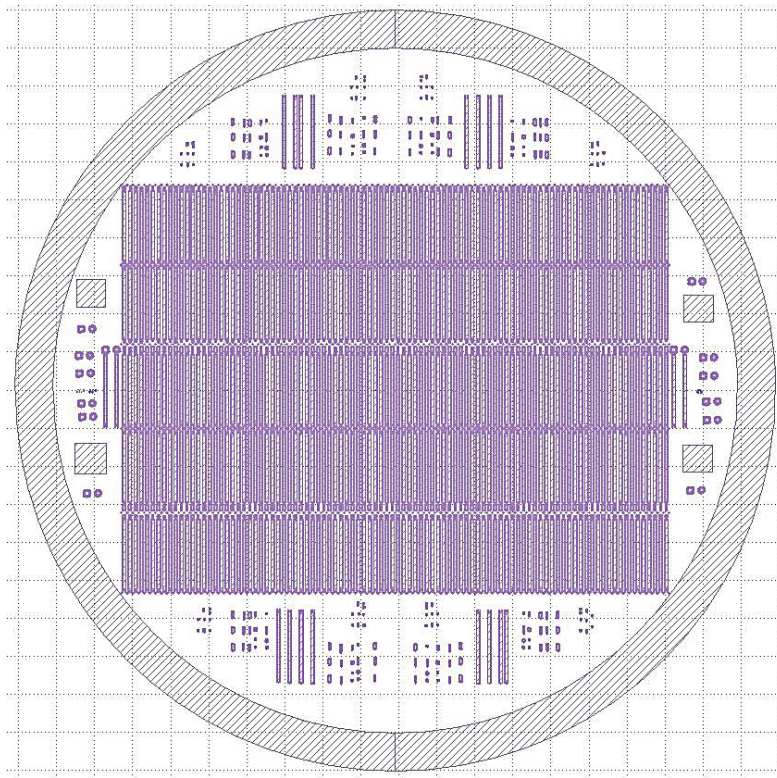


Fig. IV. 1. Layout designed for *wire-bonding* mask fabrication

On the *wire-bonding* layout, we provided at least the 30 microprobes prototype fabrication that should be useful for the biocompatibility study.

Mask 2 was developed with three-layer levels (Fig. IV. 2). First corresponds to the *underpass*, second to the *vias*, and third for the microprobe copper stripe line (Fig. IV. 3). This mask was also used for the *airbridge* connecting micro-wire.

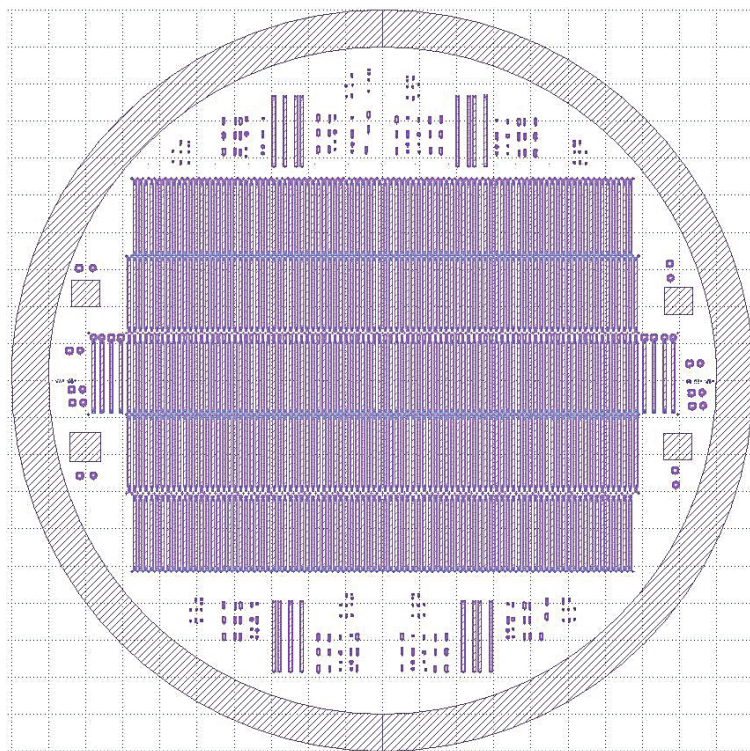


Fig. IV. 2. Layout designed for *underpass & vias* and *airbridge* mask fabrication

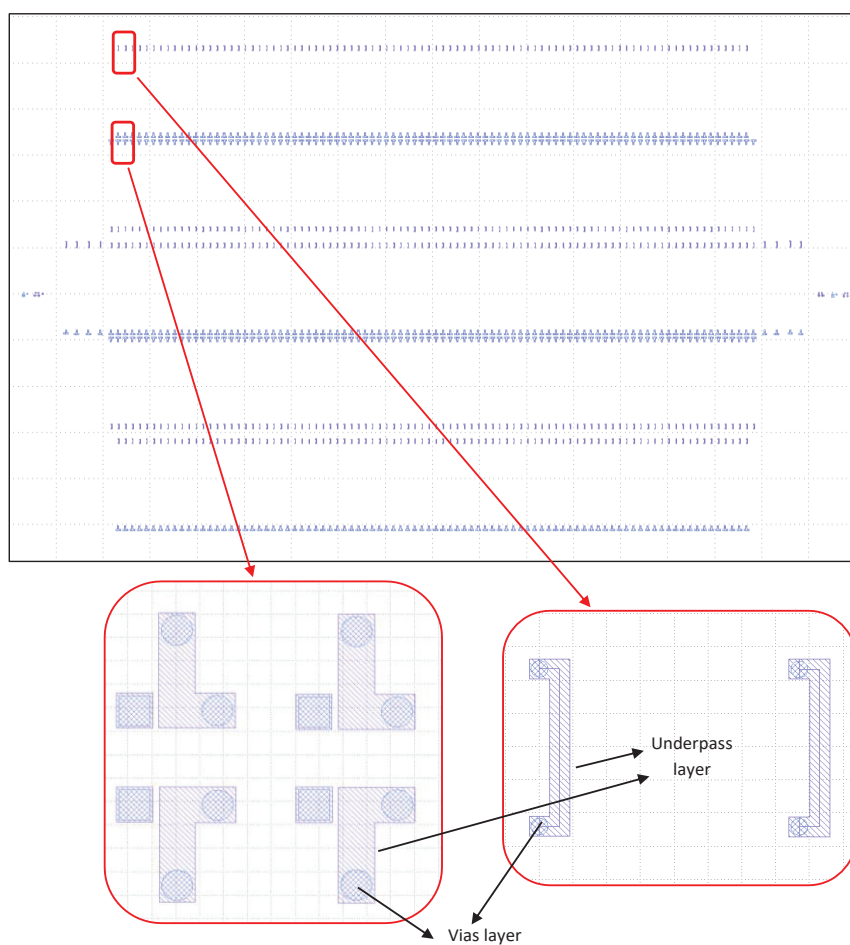


Fig. IV. 3. The *underpass and vias* layer of the designed layout

The two masks layout were designed using KLayout, which is open-source software. For the fabrication support, we used a standard wafer with a dimension of $10 \times 10 \text{ cm}^2$. The wafer was divided into five sections. Each one corresponds to hundreds of microprobes with its specific type of coils geometry and dimensions. Fig. IV. 4 shows the microprobes organized according to their dimension similarities.

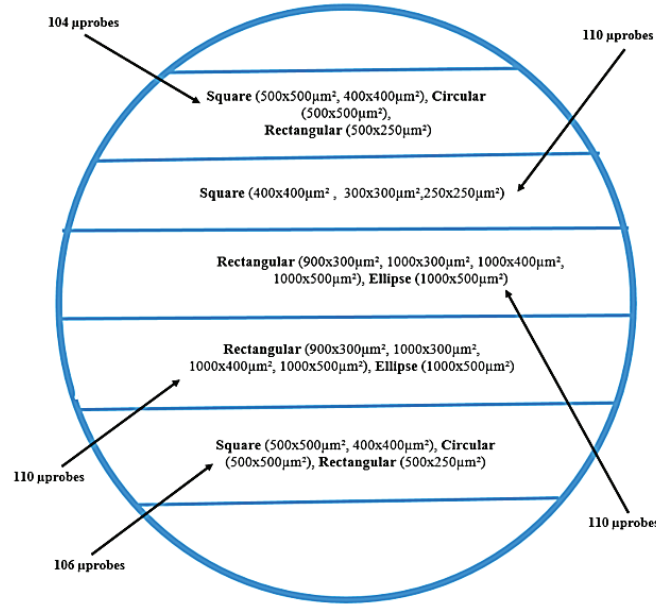


Fig. IV. 4. Layout design for the glass wafer: geometries, description of the number of the microprobes for each raw

IV.1.2. The main steps for the microprobe fabrication

In this section, we described the main five steps of the microprobe prototypes manufacturing on a glass substrate; as we reminded previously, it should be similar to the case of the silicon substrate. There will have a supplementary step, such as the preparation of SiO_2 layer (silicon micro thickness oxidation) to reduce the resistive losses of silicon in the case of use at the high-frequencies domain.

The microprobe fabrication was performed in the cleanroom of l' Ecole Supérieure d'Ingénieurs en Electrotechnique et Electronique (ESIEE), Paris. This is a working environment with a regulated temperature (20°C) and relative humidity (30 % — 40 % RH for year-round operation). It is permanently crossed by a flow of filtered air in slight overpressure, allowing the uninterrupted elimination of dust and gases that potentially can enter in the cleanroom. A cleanroom is characterized by a class that represents the number of dust particles inside, smaller than $4 \mu\text{m}$ contained in a volume equal to one cubic inch (one inch = 2.54 cm). The cleanroom of ESIEE Paris is a class 100 to 10000 (ISO 5 to 7), with 650 m^2 and has about 70 equipments

for micromanufacturing of MEMS and microelectronics technology. Our microprobe prototypes on the glass wafer were fabricated in there through the following steps.

IV.1.2.1. Stage 1: Thin film deposition (Sputtering and evaporation)

The vacuum deposition method is used to produce a thin film and coatings. It is characterized by a process in which the material goes from a condensed phase vapour phase to a thin film condensed phase. Due to a high electric field effect, the argon-ion is accelerated toward the material to deposit and then spray on the wafer surface. For our case, we used sputtering and evaporation, which are the most common.

Fig. IV. 5 shows the sputtering equipment (Cryogenic pump, SAS loading, DC spraying, RF, Bias, Cleaning by RF etching), we used for the thin film deposition.

Metal available: Aluminum (*Al*), Gold (*Au*), Chromium (*Cr*), Copper (*Cu*), Titanium / Tungsten (10 % *Ti* and 90 % *W*), Tungsten (*W*).

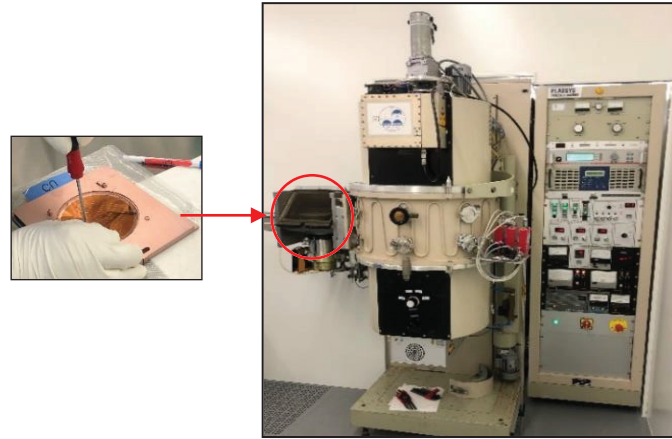


Fig. IV. 5. Sputtering equipment type SCM 600 (ALCATEL)

We started the microfabrication process by preparing the wafer, depositing the seed layer through the PVD (Physical Vapour Deposition) or cathodic pulverization technique (Fig. IV. 6). This vacuum technique allowed making the deposition of an adherence and conductor material. By this, we could reach a thin layer of 600 μm .

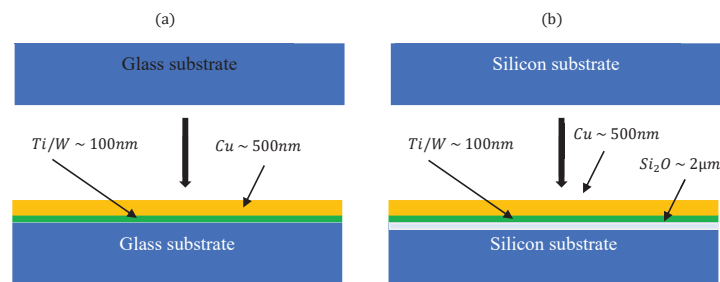


Fig. IV. 6. Seed layer preparing process a) Glass substrate and b) silicon substrate

Four our experiments, we prepared six glass wafers, knowing that most were used to optimize the fabrication process in the first trial.

- First, we plated a layer of *titanium/tungsten (Ti/W)* of 100 nm thickness to provide the cohesion of the next layer on the glass wafer.
- We could then deposit a 500 nm copper (*Cu*) thickness over the entire *Ti/W* layer by the same technique we used to deposit the 1st layer and pulverize using an *argon plasm*.

IV.1.2.2. Stage 2: Ultra Violet (UV) Photolithography

UV photolithography represents the etching of the mask layout pattern to the wafer surface after their preparation. This method could create extremely small patterns, down to a few tens of nanometers. The steps involved in the photolithography process are:

1. Wafer cleaning
2. Photoresist coating (spin coating)
3. Baking and relaxing,
4. Mask alignment, light exposure and development.

The main step of the Photolithography is shown in the following schematic representation (Fig. IV. 7):

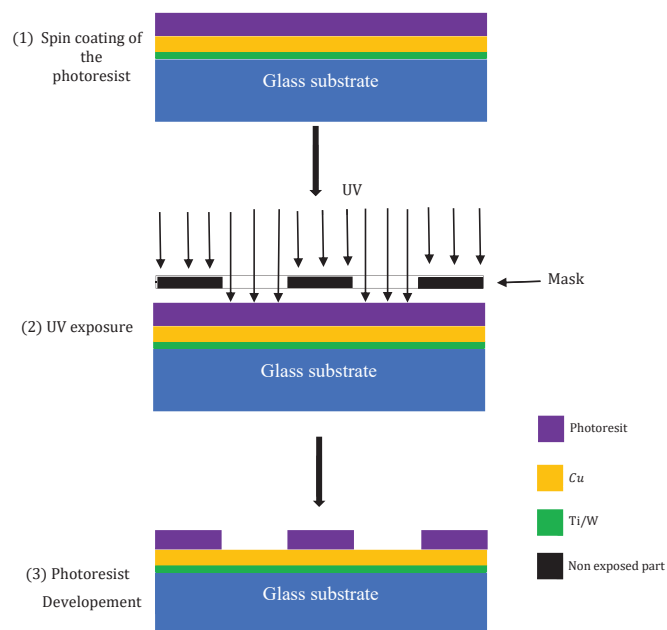


Fig. IV. 7. The main step of UV photolithography (Mask patterns etching)

Before the Spin coating, it was necessary to clean the wafer surface to remove the residual matter or any marks of inorganic, ionic and metallic impurities.

After the cleaning, we covered the copper seed layer uniformly with the photoresist through a spin coater machine (Fig. IV. 8). Photoresists were organic compositions consisting of light-sensitive polymers dissolved in one or more organic solvents. Generally, there are two types:

- Negative photoresist (*i.e.* SU-8, JSR), for which the area exposed to UV- light is photopolymerized and becomes insoluble in the developer solution. The developer used is the Methyl Ethyl Ketone (MEK) or Methyl-Isobutyl-Ketone (MIBK).
- Positive Photoresist (*i.e.* PFR, AZ 9260, AZ 4562, SJR 5740). When exposed to UV light, they become soluble in the developer solution.

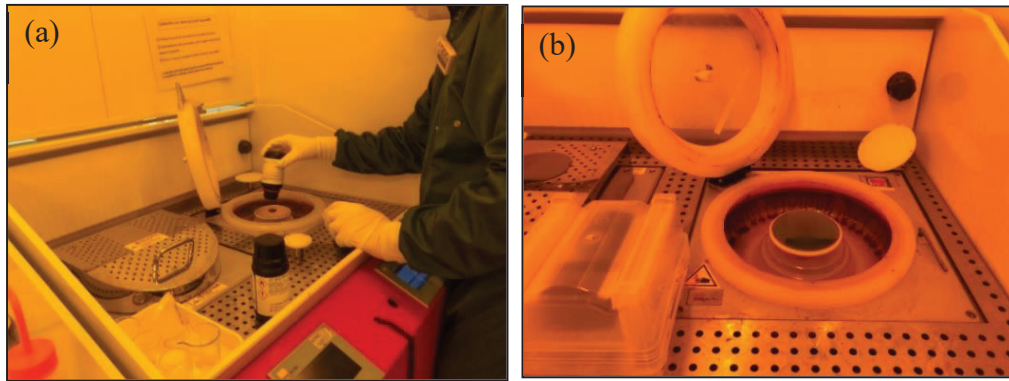


Fig. IV. 8. The spin coating, (a) before and (b) after the photoresist spreading out

The thickness of the spread photoresist depends mainly on its viscosity and the coater centrifuge rotation speed, which can be calculated by the equation below:

$$t = \frac{kp^2}{\sqrt{\omega}} \quad (\text{IV.1})$$

Where k is the centrifuge constant (between 80 and 100), p is the percentage of the photoresist viscosity, and ω is the speed in revolutions per minute divided by 1000.

To optimize the microfabrication process, we spread a positive photoresist (AZ4562) on the prepared wafer surface. We were able to reach a mould thickness of $50 \mu m$ maximum with a positive photoresist and $40 \mu m$ for a negative photoresist. Positive photoresist gradually is more widely used since they offer better process mastering for small geometry features [144]. Moreover, positive photoresist have the advantage of producing thick and resistant layers which can be used as a mould for the electrodeposition of metal [142].

Baking and relaxing: after the spin coating step, we kept the wafer relaxing for a few minutes to place and sequentially apply heat. We put on the electric heating plate of $64.3^\circ C$ (soft-backing) for *1 minute* and then $110^\circ C$ (hard-backing) for *2 minutes* to evaporate the

solvents contained in the photoresist (annealed). After backing on, we maintained the wafer again, relaxing for a few minutes.

The Soft-baking step improved the solvents removed from the photoresist coating. That had a very critical role in meaning that the photoresist became more photosensitive after a wafer soft-baking. An over soft-baking can degrade the resist photosensitivity by reducing the developer solubility (details in next paragraphs). **Hard-baking** was necessary to harden the photoresist and improve the photoresist adhesion to the wafer surface.

Light exposure and development consist of the photoresist exposing to the UV for the mask shape printing into the wafer surface and then removing the photoresist. The mask protects the photoresist against UV light at the desired location to obtain the micro-probe fingerprints on the positive photoresist surface. In this process step, the mask alignment was necessary; this task was performed by an automatized equipment (Fig. IV. 9 (a)).

After the light exposure, the wafer was immersed into a PRD 238 solution for 45 seconds to remove the soluble photoresist and reveal the microprobe patterns overprinted onto the wafer surface (areas not exposed to UV light) as in Fig. IV. 9 (b).

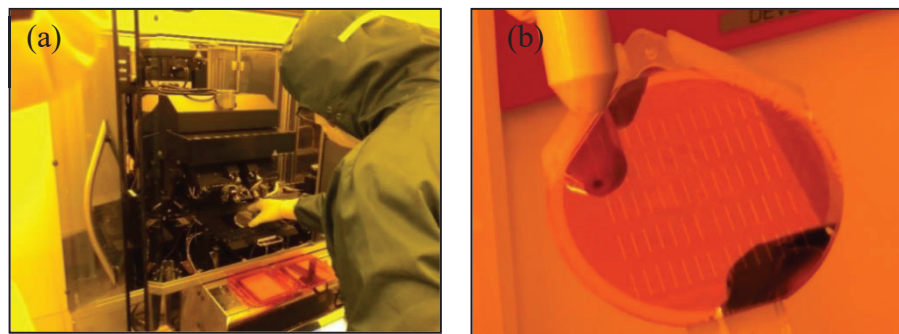


Fig. IV. 9. UV photolithography equipment (a): wafer mask alignment to the light exposure) and (b): the wafer after photoresist cleaning up

In the following figure (Fig. IV. 10), we have the characterization of the wafer (a) and the results of the micro-probe shape after wet etching of the Photoresist layer on the seed layer (b).

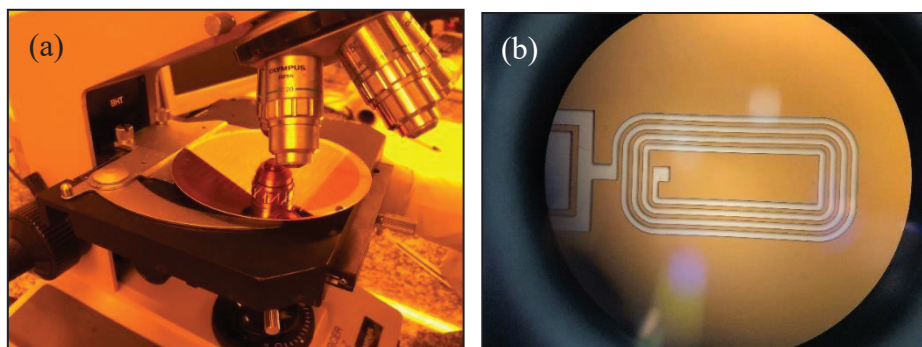


Fig. IV. 10. (a) The microscope to characterize the micro-coil shape, (b) Rectangular micro-coil geometry after the photoresist development and cleaning up

IV.1.2.3. Stage 3: Copper electroplating

Before the copper growing process, an intermediate stage was required to remove the leftovers of photoresist within the bottom of the moulds printing microprobe design. Precisely, we placed the wafer under an oxygen plasma to etch the photoresist residues. We can name this section as "*retro sputtering*".

The copper electroplating technique is based on the current density passage through the copper solution (Fig. IV. 11 b), which induces the copper ion Cu^{2+} to the metallic electrode. we submerged the wafer into the copper sulfate electrolyte bath $Cu^{2+}SO_4^{2-}$. Also, there was a small ionized water concentration; Since the presence of a current, the copper ions migrated and deposited onto the wafer regions with a pre-existing metal seed layer.

The seed layer needed to have a homogenous surface to improve the copper growing homogeneity. The contact of the copper on the seed layer was achieved using the electrode of the electrodeposition device and an aluminium layer (Fig. IV. 11 c), recovering the wafer back and attending the contact with the seed layer.

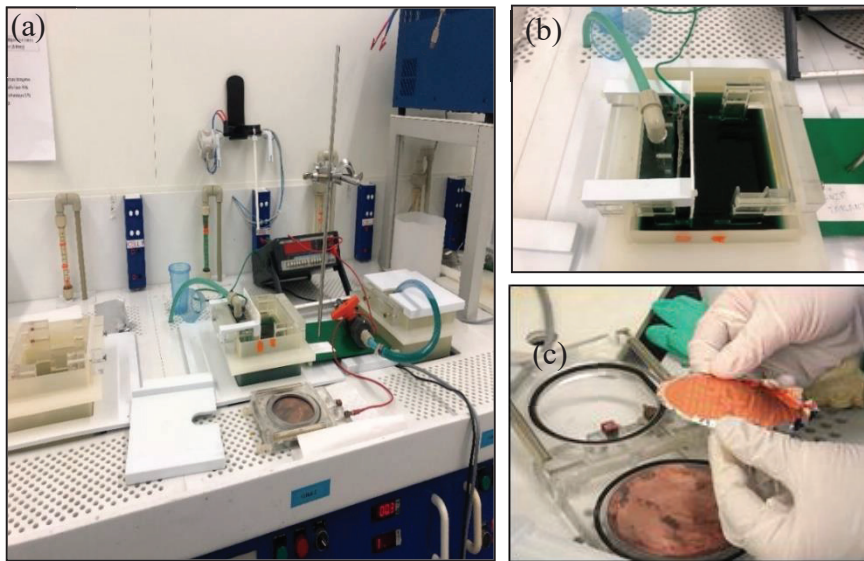


Fig. IV. 11. (a) Electro-planting system, (b) bath with an electrolyte solution, (c) preparing the wafer to fix in the cathode part.

The Fig. IV. 12 shows the schematic representation of the copper electrodeposited result.



Fig. IV. 12. The representation of the wafer after Cu electrodeposition

We ensured the copper growth into the microprobe etched patterns. The copper deposition rate depends on the current density and the flow rate of the ionic solution; the two elements allowed us to determine how much and quickly the copper was uniformly spread on the wafer surface. Thus, in our case, we used on the first trial of the fabrication process a current density of 200 mA/cm^2 and about a flow rate of 20 l/h . Then, we waited for 40 min , during which the copper layer was being deposited in the wafer, and it was reached a copper layer of $20 \text{ }\mu\text{m}$.

IV.1.2.4. Stage 4: The photoresist and seed layer removing (Lift-Off)

This step consisted of removing the insoluble photoresist and the unprotected seed layer (copper and Titanium layer) after the growth of the copper layer. To achieve this, we immersed the wafer into an acetone bath. The photoresist dissolution was also accelerated using an ultrasound tray.

So then, the seed layer removing; First, the copper layer was removed by dipping the wafer in a solution of 60 g from CN_{10} and 10 g oxide water (H_2O_2) during one minute. Secondly, the T_i/W layer was also removed by using the H_2O_2 solvent, for one minute.

The schematic representation of the Lift-Off step, before and after the process is shown in Fig. IV. 13.

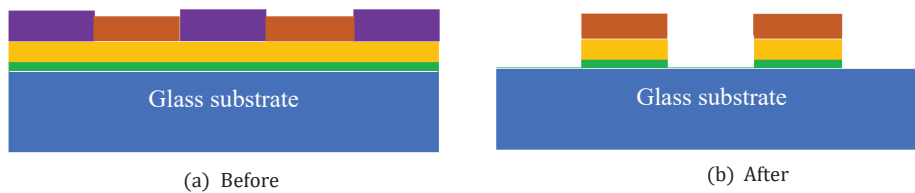


Fig. IV. 13. Wafer before (a) and (b) after photoresist and seed layer removing

Fig. IV. 14 shows the results of the process: (a) wafer before and (b) wafer after the Lift-Off process.

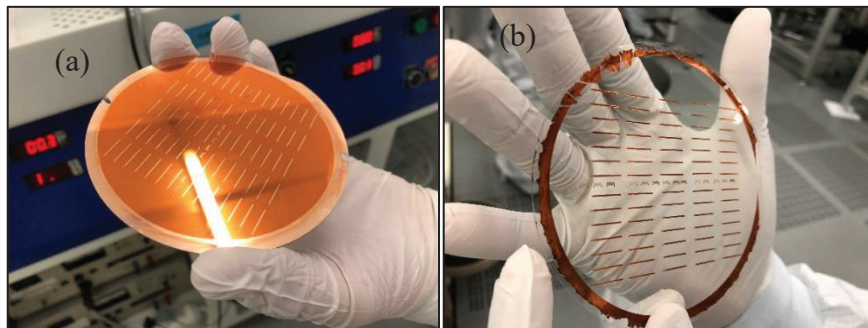


Fig. IV. 14. Wafer before (a) and (b) after photoresist and seed layer removing

This step was carefully carried out, and the time ultrasound tray was critical to ensure that the seed layer was completely removed while ensuring that all microstructures designed on the wafer did not get out to the wafer.

IV.1.2.5. Stage 5: Electroless gold plating

Electroless plating is defined as a coating process without applying an external current. It allows a uniform metallic coating regardless of the geometric shape of the surface after the sample is immersed in the solution. It is as if a chemical reaction occurs between the copper layer and the gold.

After removing the seed layer, the copper-plated on the wafer was exposed to an oxidation. To avoid this, we had to growth a gold layer on top of the copper layer by electroless gold plating; So, the wafer was immersed in a gold solution; In the Fig. IV. 15, we show a schematic illustrating the result after the electroless process. This section is often required at the end of the microprobe fabrication process.

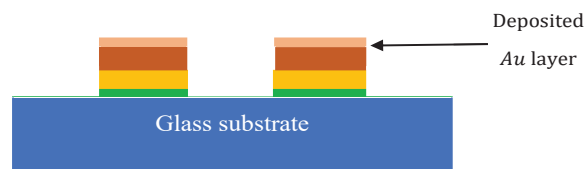


Fig. IV. 15. The prototype ended up after the electroless process

IV.1.3. Characterization of the fabricated microprobes: 1st trial

Whatever the manufacturing technique, a surface is never completely flat, its morphology depends crucially on the material deposited and the optimization of the manufacturing process. To examine and validate the fabrication process of the microprobe's prototypes, we performed their characterizations (morphological and electrical).

The morphological characterizations allowed us to check the shape of the prototypes, the impurities, the manufacturing defects (residuals resin and short-circuits) and this characterization allowed also examining the surface roughness and verify the thickness of the deposited copper layer. For this, we used two principal equipment: a microscope and a profilometer.

The electrical characterization allowed estimating the resistance and verifying the short-circuits. The measure of the microprobe resistance was carried out using a conventional multimeter equipped with two micro-tips.

In the following sections, we presented the results of the morphological (section IV.1.3.1) and electrical characterization (section IV.1.3.2) of the microprobe prototypes manufactured in the first trial of the fabrication process, as well as the equipment used.

IV.1.3.1. Morphological characterization

In the Fig. IV. 16 a), we showed the microscope used to examine the shape of the microprobe prototypes, and the impurities from residuals resin not completely removed, short-circuits between the microprobes strip-lines. Also, we showed in the, Fig. IV. 16 b) the Mechanical profilometer (Veeco Dektak 8 model (Bruker)) used to survey the surface roughness and measure the microprobe thickness.

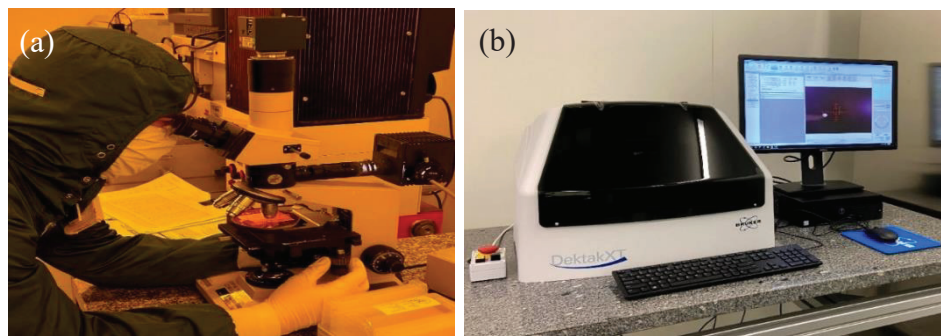


Fig. IV. 16. (a) The microscope (b) The optic profilometer

The profilometer consists of performing a displacement of a microtip along the surface in a pre-defined direction on the surface of the material (Ox or Oy direction) usually with a sensitive diamond tip. The tip follows the material irregularities by varying its vertical position. These variations are converted into electrical voltage to be analyzed and processed by the interface software. It is equipped with a $12.5\ \mu m$ long tip, with an exerting force of 0.03 to 10 mg which allowed us to measure the thickness in the range of 5 nm to 1 mm , in our case we chose the tip weight of 3 g . The device has a Charge Coupled Device (CCD) camera of different magnifications to facilitate the visualization of the sample spacing.

The Fig. IV. 17 shows the results of the microprobe characterization by microscopy (objective zoom of 10). Manufacturing defects are easily clustered. Note that the spacing between microstrip is smallest in the Fig. IV. 17. a), b) and d) ((1) (2): short-circuit), ((3) residual resin). The copper oxidation can be seen at different sides of the microprobe, more specifically on the corners.

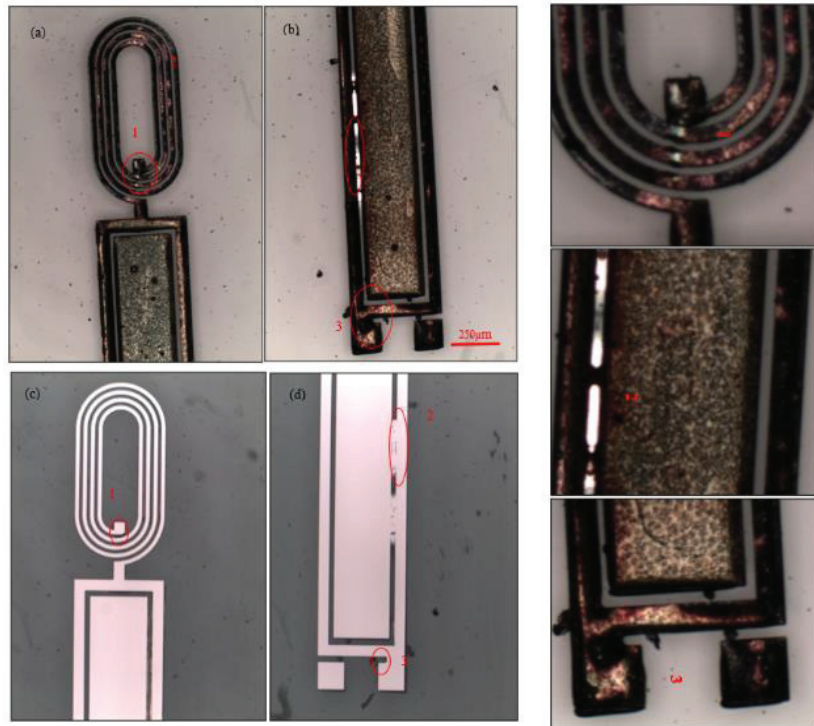


Fig. IV. 17. Checking different defects of the first prototype manufactured: short-circuit, residual resin

The Fig. IV. 18 and Fig. IV. 19 show the results of the measured thickness of the microprobe. We scanned along the micro-coil part, to obtain the micro-coil thickness measure (Fig.IV.19) and then to the transmission line part (Fig.IV.20), for the measurement of it thickness.

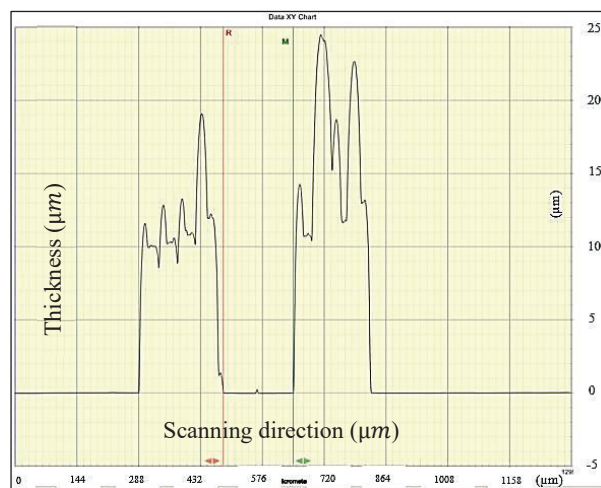


Fig. IV. 18. Profile of the micro-coil surface scanning

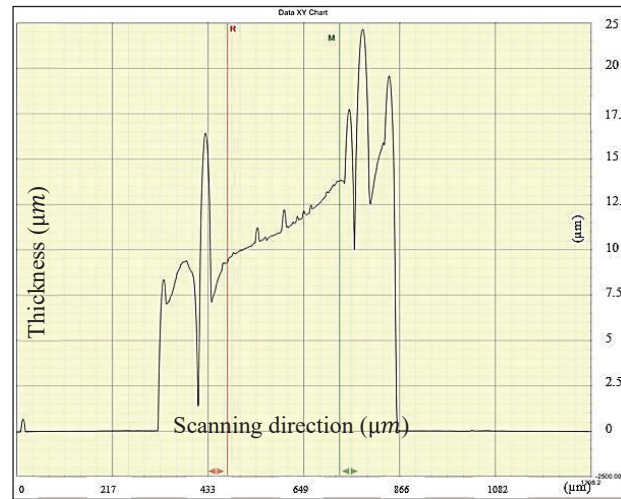


Fig. IV. 19. Profile of the micro-path surface scanning

In Fig. IV. 18 and Fig. IV. 19, one can notice a substantial difference between the two sides of the microprobe profile: 23 μm to 13 μm .

The thickness of the microprobe can also be measured, as shown in Fig. IV. 20 (b). This method was faster than the previous one, but the measurement of the prototype thickness was estimated less accurately. This method was more efficient when it was a question of measuring the thickness of each layer deposited during the manufacturing process, by that, we measured several times the thickness of the photoresist, the developed thickness, etc. This was required to investigate the performance of each section of the prototype fabrication.

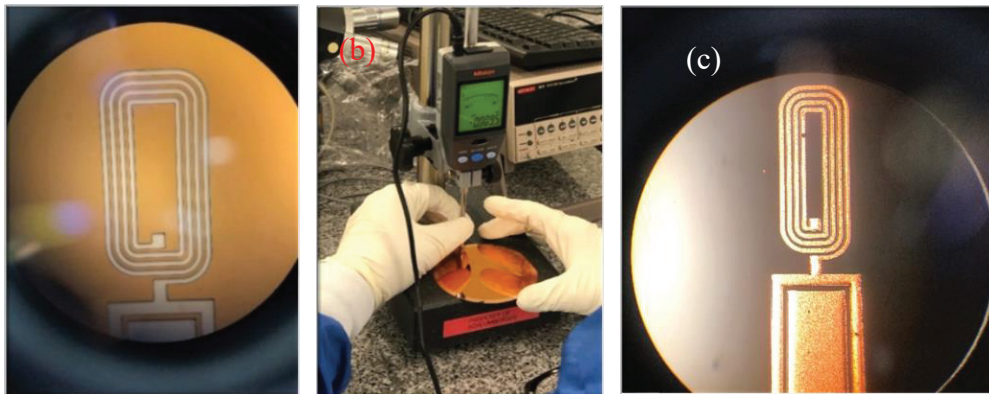


Fig. IV. 20. Profile of the microprobe surface scanning

All previous results from the characterization of the first test of fabrication represented a good asset to validate some steps of the microfabrication process and then optimize the fabrication process to obtain the optimal prototype as defined by the specification sheet of the project.

IV.1.3.2. Electrical parameters measurement

Fig. IV. 21 shows the experiment carried out to measure the microprobe resistance using a digital multimeter.

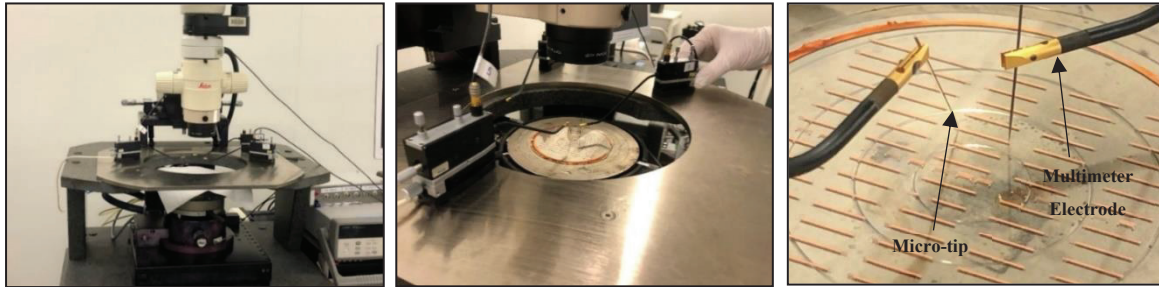


Fig. IV. 21. Two-point micro-structure resistance measurement

The Fig. IV. 22 shows the result of the measure of the resistance displayed on the multimeter (KEITHLEY 2100/220, 1kV3A, 6.5 digits). Note that the resistance of the microprobe measured is $R = (3.897 \pm 0.193) \Omega$.



Fig. IV. 22. Digital multimeter (KEITHLEY 2100, 1kV3A, 6.5 digits) used for Resistance measurement

After the morphological and resistance measurement of the microprobe prototype, we selected ten microprobe prototypes suitable for the rest of the experiment. Note that, on a set of 96 characterized microprobes in the first trial of the process fabrication, only 10 microprobes were suitable.

The following parts of the experiments were performed in collaboration with Icube laboratory, at Strasbourg. So, we set up ten microprobes (Fig. IV. 23 a) on PCB circuits. The experiment was performed using a NANO VNA ZVL (Rhode & Schwarz, 50 kHz to 2 GHz, frequency precision 0.5 ppm).

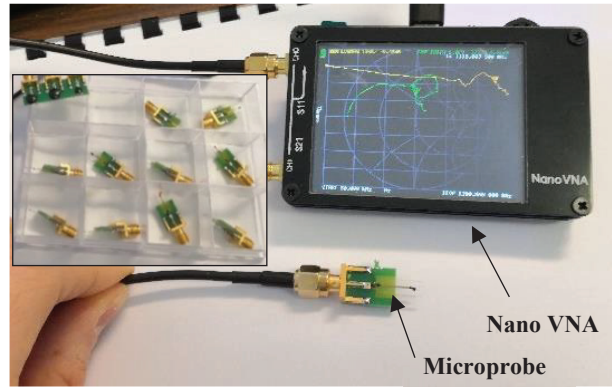


Fig. IV. 23. Then microprobe set up on the PCB, and the NANO VNA connected with a microprobe.

Fig. IV. 24 shows the three microprobes were suitable for the performance measurement of RLQ parameters, among the ten microprobes set up on the PCB.

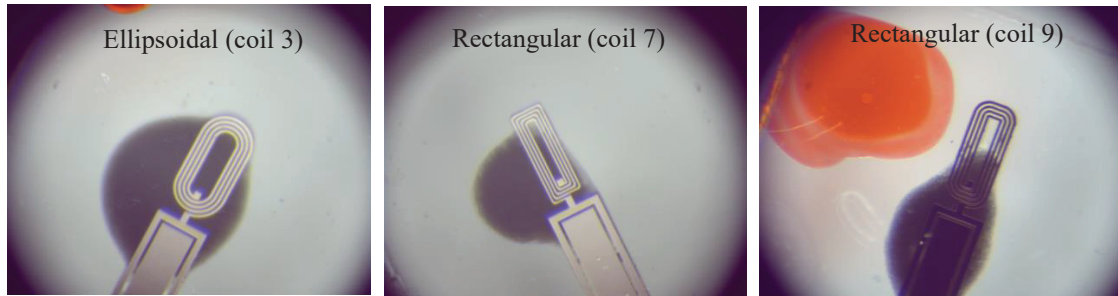


Fig. IV. 24. The geometries suitable for the performance measurements

The Table IV. 3 shows the results of the measurement of RLQ parameters of the three selected microprobes. All measurements were reported at frequency of 300 MHz . One can notice that our results are in good agreement with those of the simulations.

Microprobe type Geometry	Dimensions (μm^2)	Resistance (Ω)			Inductance (nH)			$Q - factor$		
		Meas.	Er%	Sim.	Meas.	Er%	Sim.	Meas.	Er%	Sim.
Rectangular (coil 9)	1000×400	6.12	2	1.51	22.75	6	26.88	4.12	8	33.30
Ellipsoidal (coil 3)	1000×500	11.6	3	1.45	25.52	4	26.26	4.12	7	34.16
Rectangular (coil 7)	1000×300	6.14	4	1.48	21.76	5	25.67	6.671	9	34.37

Table IV. 3. The measurement of RLQ parameters of microprobe on 300 MHz (1st trial of microfabrication)

What is interesting to emphasize in this section is that all these results show that the first trial of microprobe manufacturing still needs to be improved. Therefore, in the next section, we will show the steps that we improved and then carry out for the fabrication of the final prototype according to the required specifications.

IV.1.4. Optimization of Micro-manufacturing process

After the first trial of the microprobe prototype fabrication, all the obtained prototypes were characterized. We noticed some major defects on certain shapes of the microprobe, and sometimes the required thickness was not reached.

Based on these results, from the previous microprobe fabrication trial (1st trial), we have a focus on the optimization of the following process steps:

1. Photolithography (UV lighting time, Spin coating process)
2. Developing (timing, photoresist and baking time)
3. Copper electroplating (electroplating time and the applied current, homogeneity of the plating and the seed layer oxidation)

The Fig. IV. 25 a) shows the ten wafers prepared for the optimization of the process fabrication with the new fabricated mask (Fig. IV. 25 b)) and resin.

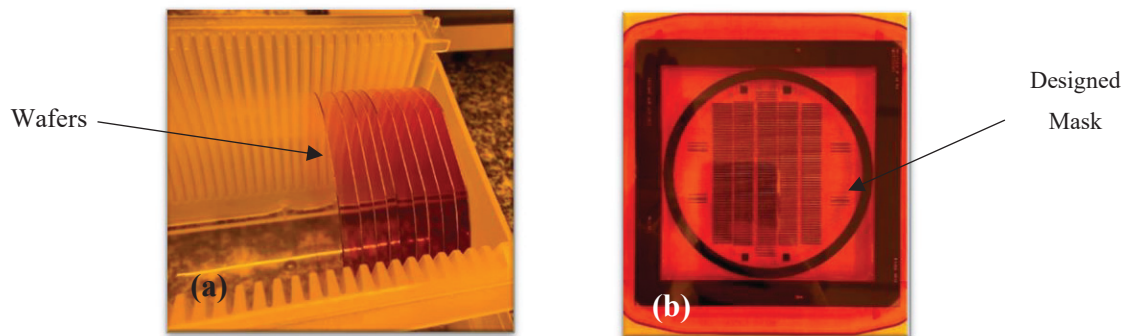


Fig. IV. 25. (a) Ten prepared wafers, (b) the optimized mask

IV.1.4.1. Photolithography Optimisation

We used a positive photoresist (AZ4562) on the previous trial fabrication, but we could not reach the required thickness ($40\text{ }\mu\text{m}$). Thus, we changed to a negative photoresist, and we also changed the mask. Note that the negative photoresist we get using for this experiment is suitable for spreading a thick mould layer.

Therefore, we aimed to define the optimal parameters for the spin coating equipment in the first place, knowing that it is needed to deposit at least $40\text{ }\mu\text{m}$ thickness of the photoresist. Then we optimized the baking time adapted to the resist and the UV insolation time to achieve the expected shape during the etching section.

For this experiment, we used a positive mask with some enhancement even for the optimization of the space on the wafer. In the following Fig. IV. 26, we have shown the spin coating section, where we spread the photoresist on the prepared wafer.

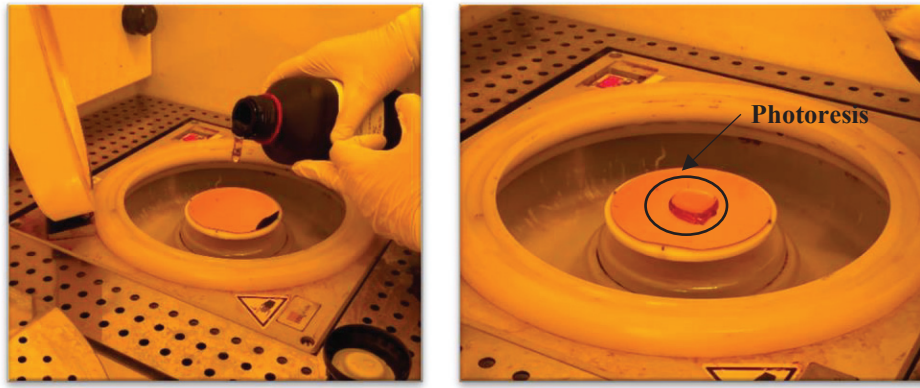


Fig. IV. 26. Spin coating section, placing the photoresist

The testing for the photolithography optimization was done with the characteristics of the following material:

- Adherence promotor (UN1992: hexamethyldisilane time: 1 *minute*)
- Spin coating parameters: Time: 30 *sec* speed: 3125 *m/s* *acc* : 500 *m/s*²

In the Table IV. 4, we have summarized the fundamental parameters of each step to optimize the photolithography process.

Trial	First trial			Second trial		
Step	Timing (<i>min</i>)	Temperature (°C)	Pressure (<i>mTorr</i>)	Timing (<i>min</i>)	Temperature (°C)	Pressure (<i>mTorr</i>)
Relaxing	15	20	X	25	20	X
Baking step	15	140	X	13	130	X
UV insulation	0.65	X	X	X	X	X
Development	6	20	X	8	20	X
Plasma	1.30	X	84	1.5	X	84

Table IV. 4. Fundamental parameters of the photolithography process optimization

So, we tested different parameters for the spin coating shown in the Table IV. 5.

Step	Speed (<i>m/s</i>)	Acc (<i>m/s</i> ²)	Time (<i>sec</i>)
1	3000	200	5
2	2400	200	2
3	2300	200	8

Table IV. 5. Photoresist planting (AZ 125 NXT – 10A)

Based on the photoresist datasheet information that we have reminded in the following Table IV. 6, for a standard thickness, with its corresponding UV insulation time. Thus, we could determine the tendency curve and get the optimal insulation time for our expected thickness.

AZ 152NXT, photoresist specifications	
Thickness x (μm)	Insolation time t (sec)
20	172
70	307

Table IV. 6. Standards parameters specifications of AZ 125 NXT – 10A photoresist

$$t [sec] = 2.7 \times x [\mu m] + 118 \quad R^2 = 1 \quad (IV.2)$$

Therefore, we determined the UV insolation time of 226 sec to reach 40 μm of photoresist plating.

Spin coating - For thick photoresists like AZ 152NXT – 10A, we had a big part of the solution spread out on the wafer board. The relaxation timing helped the photoresist become spatially homogeneous on all wafer zone.

Plasma - This step was crucial; it had to be achieved at the end of photolithography. It removed the photoresist residues and enhanced the shape designing, ultimately deep-drawing on the pattern of the microprobe stamped on the wafer surface.

IV.1.4.2. Electroplating Optimization

1. Plasma (Reactive Ion Etching)

Timing (sec)	Voltage (V)	Power (W)	Gas	Pressure ($mTorr$)
90	250	80	O_2	90

Table IV. 7. Parameters of the Oxygen plasma section to clean up the wafer before the copper electroplating

2. The wafer edge thickness characterization to measure the photoresist deposited.

Before the copper electroplating process, we need to verify the photoresist thickness after the plasma step. In the following figure, we have shown the measurement of the different deposition on the wafer (mould and copper layer)

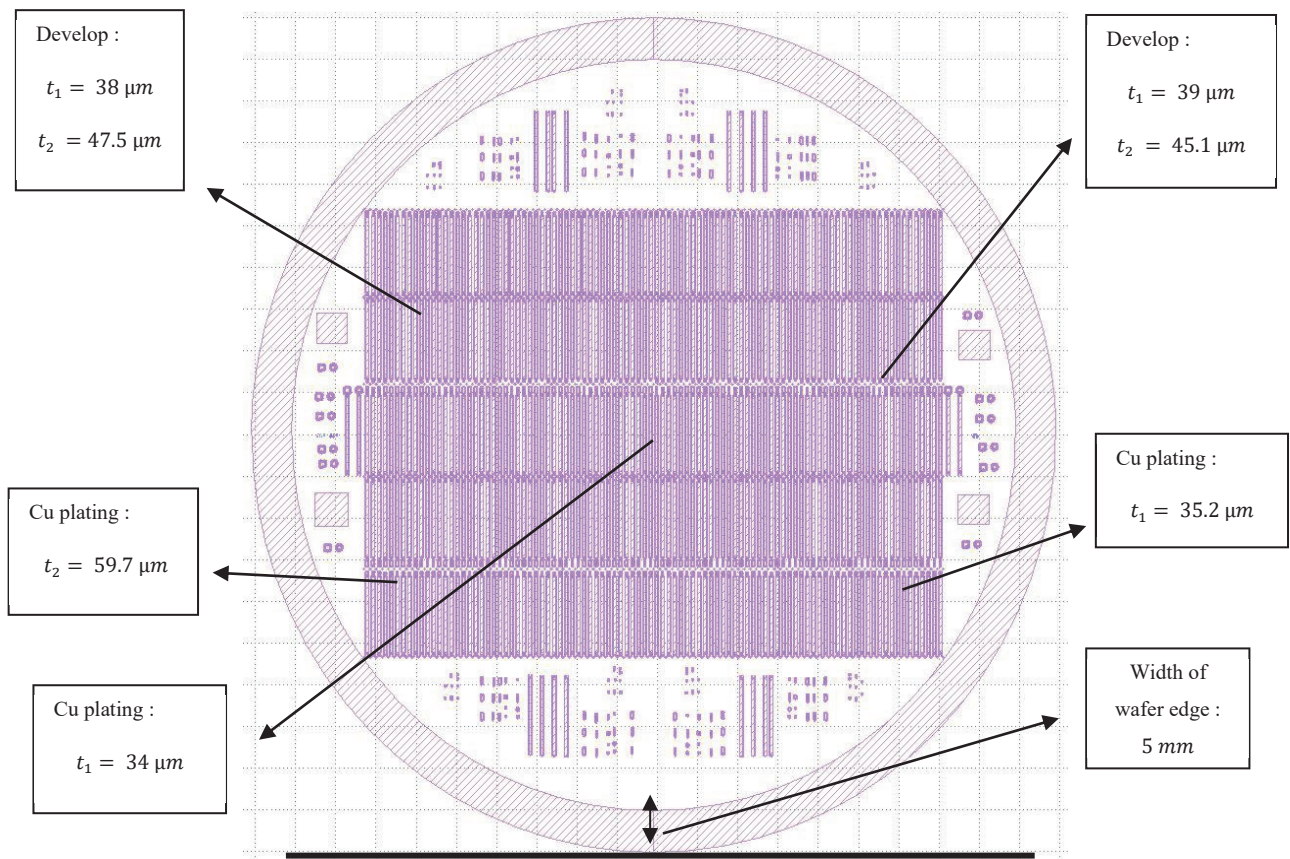


Fig. IV. 27. The thickness of the deposited resin and the copper layer at the different parts of the wafer

We can see in Fig. IV. 27 that we were not able to perform a uniform deposition either for the photoresist or the copper layer. Electroplating needed some improvement; that is why playing with all parameters was a fundamental option.

Dev: Measurement of the thickness for the photoresist layer.

Plating: Measurement of the thickness of the *Cu* electroplated layer

3. Copper electroplating is defined for the optimized process as follow in the table

Homogenizing speed (m/s)	t (min)	Current (mA)	Speed flow (l/h)
60	30	200	20

Table IV. 8. The setting parameters for the electroplating of the copper layer

4. Measurement of the *Cu* plating thickness

The electroplating was performed in two steps since it was unknown how to evaluate exactly the time required to reach the standard thickness with the new photoresist.

We first deposited *Cu* electroplating only $4 \mu m$ for 30 min to determine the rate of *Cu* plating on the wafer. So, to attend at least $30 \mu m$ (like $28 \mu m$), we restarted the electroplating

for $3h\ 30\ min$. After that, we could estimate the speed of the growth of the copper layer by about $8\ \mu m/h$. Which in Fig. IV. 27 was denoted by the t_1 . For wafer 2, we selected the same initial parameters defined in Table IV. 6, and we selected $5\ h$ for Cu electrodeposition to attend at least $40\ \mu m$ of thickness, which we denoted by t_2 in Fig. IV. 27.

IV.1.5. Manufactured microprobe after the optimization process

The optimized prototypes are shown in the following images of the micro-coil manufactured on silicon and glass substrate. These pictures were made using a microscope with an objective zoom of 10.

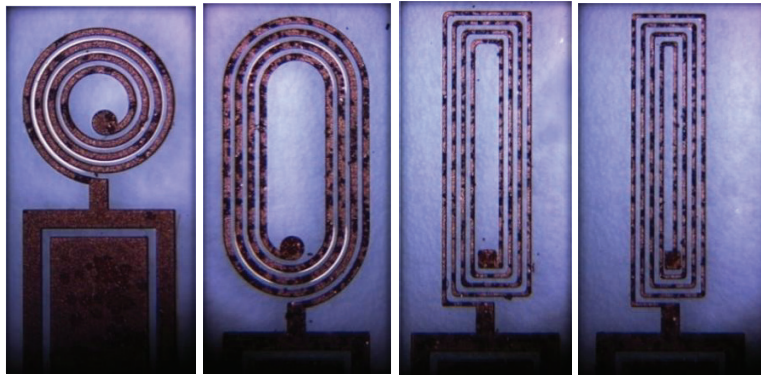


Fig. IV. 28. The geometry of some manufactured micro-coil: circular ($500 \times 500\ \mu m^2$), ellipsoidal ($1000 \times 500\ \mu m^2$), rectangular ($1000 \times 300\ \mu m^2$, $1000 \times 250\ \mu m^2$)

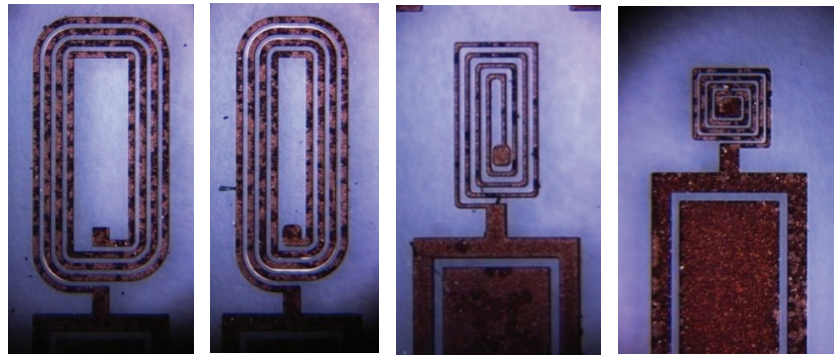


Fig. IV. 29. The geometry of some manufactured micro-coil: rectangular ($1000 \times 500\ \mu m^2$, $1000 \times 400\ \mu m^2$, $500 \times 250\ \mu m^2$), square ($250 \times 250\ \mu m^2$)

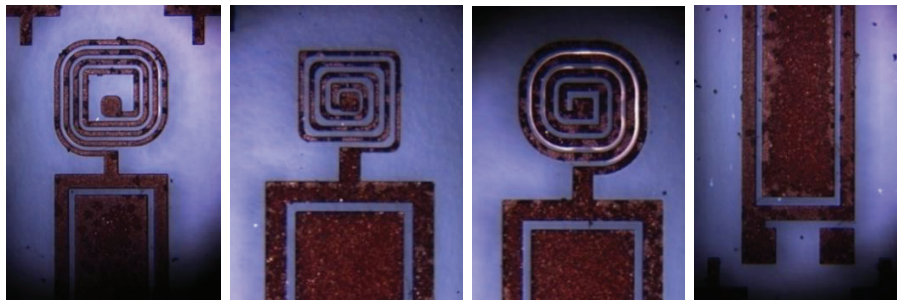


Fig. IV. 30. The geometry of some manufactured micro-coil: square ($500 \times 500\ \mu m^2$, $250 \times 250\ \mu m^2$, $400 \times 400\ \mu m^2$), micro-transmission line.

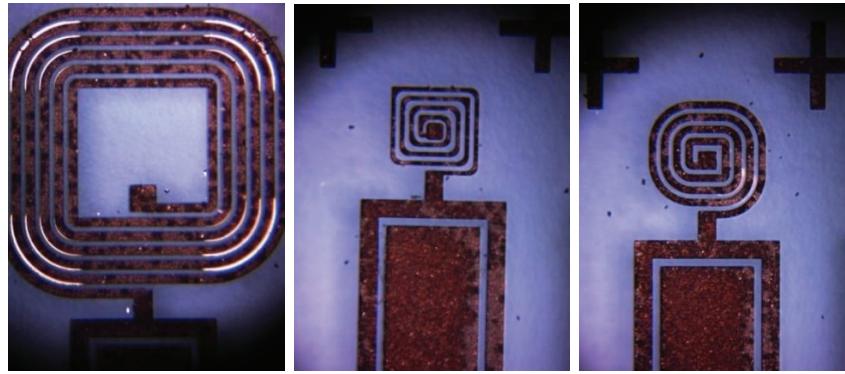


Fig. IV. 31. The geometry of some manufactured micro-coil: micro-coil: square ($1000 \times 1000 \mu m^2$, $250 \times 250 \mu m^2$, $400 \times 400 \mu m^2$).

Therefore, the pictures show how well we could optimize the microprobe fabrication process since the images show the micro-coil part without any defect compared to the previous one (1st trial of microfabrication). Thanks to this, we could fabricate microprobes whose characterization results will be presented in the next session.

IV.1.6. Characterization of the optimized prototype.

After the manufacturing process, the obtained microprobes were covered with a resin layer to protect and prevent them from peeling off the wafer support.

This photoresist layer needed to be removed before characterization of the microprobe. The removal process of the protective resin layer also needed to be optimized. So, first of all, we selected seven microprobes. The aim here was to find and validate the optimal time for the removal process of the resin.

The experiment was carried out by plunging the microprobe into the recipient with an acetone solution. 14min30 for microprobe (n° 1) and 10 min for microprobe (n° 3 to n° 7).

Microprobe (n° 1) resin removing without ultrasound, n°6 complete 10 minutes on the ultrasound, n° 4 was 5 minutes with and 5 minutes without and the rest of microprobe was 7 minutes without ultrasound and 3 minutes with (n° 2, 3, 5, and 7).

In Fig. IV. 32, we show the schematic distribution of the microprobe selected for the experiments (geometrical characteristics and their classification according to the resin removal results).

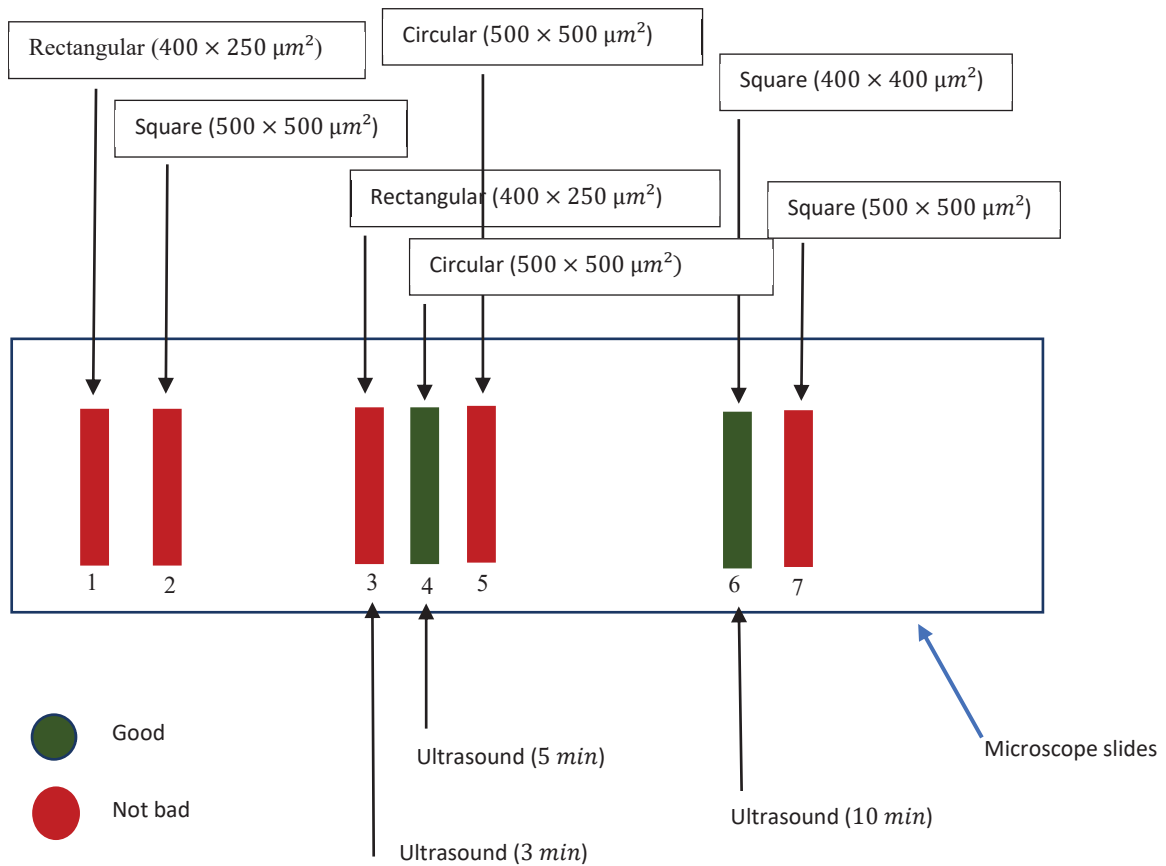


Fig. IV. 32. The seven-microprobes selected for the resin removing and their classification according to their observation using a microscope.

The characterisation of the shape of all microprobes allowed us to estimate the optimal time for microprobe resin removing. Therefore, we have fixed *5 minutes* to *10 minutes* in the ultrasound. This result was useful to characterise the rest of microprobes on the wafer as we will show in the next section.

IV.1.6.1. Measurement of the thickness on different sides of the wafer

This characterization work aims to identify the thickness of the microprobe on different positions of the wafer. The objective is to examine the uniformity of the copper depositing in the different parts of the wafer.

For this, we have chosen seven microprobes, selecting four on all corners (one for each one), and then 3 for both extreme middle lines and one on the centre area of the wafer (Fig. IV. 33).

We remove the resist of 7 microprobes, one by one for *5 minutes* on the ultrasonic cleaning (acetone) + *2 minutes* in isopropyl alcohol.

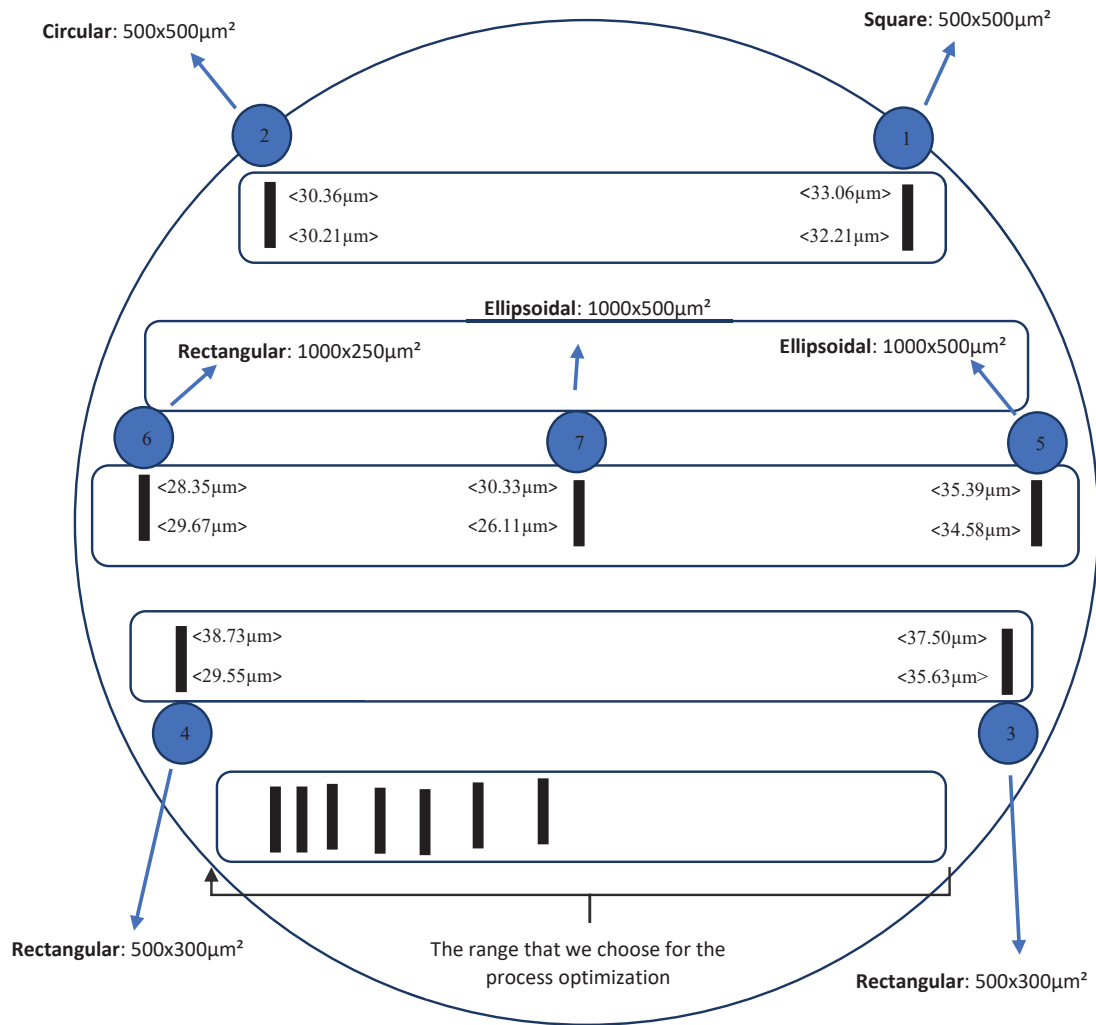


Fig. IV. 33. Microprobe thickness mapping on different parts of the wafer support

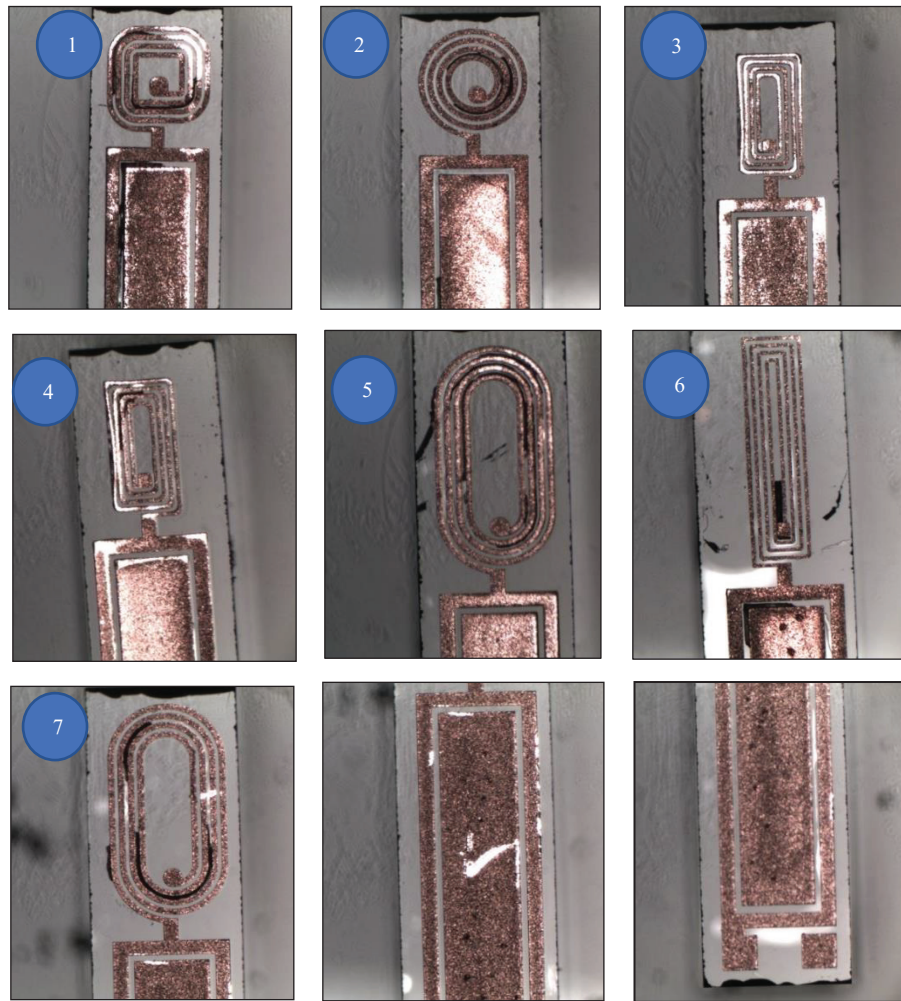



Fig. IV. 34. Confocal Raman Microscopy images of the microprobes selected for the wafer mapping

We have also shown the mean value of the deposited thickness, standard deviation and percentage of the error in order to estimate the deposited copper layer in each side of the wafer and deduce if it was deposited uniformly.

Table (IV. 9.1 to IV. 9.7) show the measurements of the cooper thickness from different areas of the wafer (microprobe n° 1 to n° 7).

Type of geometry (ID)	Micro-coil thickness (μm)	TL thickness (μm)
<div style="text-align: center;">  Square $500 \times 500 \mu m^2$ </div>	32.25	33.79
	32.12	30.09
	31.48	34.79
	32.76	30.53
	34.71	30.53
	35.01	30.53

Mean	33.06	31.78
std	1.33	1.86
Error %	3.12	4.90

Table IV.9.1:


Type of geometry (ID)	Micro-coil thickness (μm)	TL thickness (μm)
 Circular $500 \times 500 \mu m^2$	29.47	31.55
	29.19	31.46
	31.39	28.27
	30.28	31.55
	29.77	31.46
	29.92	28.27
	32.13	31.55
	31.99	31.46
	29.99	28.27
	29.43	28.27
Mean	30.36	30.21
std	1.03	1.59
Error %	2.66	4.67

Table IV.9.2:


Type of geometry (ID)	Micro-coil thickness (μm)	TL thickness (μm)
 Rectangular $500 \times 300 \mu m^2$	38.82	36.43
	37.09	35.94
	35.62	36.93
	39.56	33.20
	36.80	35.94
	37.66	36.93
Mean	37.50	35.63
std	1.30	1.28
Error %	2.51	2.30

Table IV.9.3:


Type of geometry (ID)	Micro-coil thickness (μm)	TL thickness (μm)
 Rectangular $500 \times 300 \mu m^2$	57.21	37.43
	29.76	37.29
	31.71	26.86
	32,71	23.84
	36.52	27.40
	50.51	26.09
Mean	39.73	29.82
std	11.35	5.97
Error %	23.69	16.86

Table IV.9.4:


Type of geometry (ID)	Micro-coil thickness (μm)	TL thickness (μm)
 Ellipsoidal $1000 \times 500 \mu m^2$	35.95	32.47
	35.38	35.00
	33.69	33.75
	37.62	36.65
	35.36	33.75
	35.45	34.71
Mean	35.39	34.58
std	1.31	1.70
Error %	2.52	3.99

Table IV.9.5:


Type of geometry (ID)	Micro-coil thickness (μm)	TL thickness (μm)
 Rectangular $1000 \times 250 \mu m^2$	28.10	29,90
	28.44	29.60
	28.55	29.50
	28.22	29.90
	28.55	29,60
	28.22	29.50
Mean	28.35	29.67
std	0.19	0.19
Error %	0.59	0.52

Table IV.9.6:


Type of geometry (ID)	Micro-coil thickness (μm)	TL thickness (μm)
 Ellipsoidal $1000 \times 500 \mu m^2$	29.70	26.33
	30.80	25.89
	30.50	26.33
	29.70	25.89
	30.80	26.33
	30.50	25.89
Mean	30.33	26.11
std	0.51	0.02
Error %	1.39	0.84

Table IV.9.7:

From our thickness measurements of the micro-coil part and transmission line on different positions of the wafer, we estimated that the average thickness of the microprobe was about $t_{coil} = (28.18 \pm 1.47) \mu m$ corresponding to measurement uncertainty of $error = 5.21 \%$, and $t_{TL} = (26.02 \pm 1.27) \mu m$ corresponding to measurement uncertainty of $error = 4.87 \%$.

IV.1.6.2. Electrical characterization of the fabricated microprobes

In the Fig. IV. 35, we show a microprobe set up on a PCB support with a wire-bonding connecting to a SMA connector type-N.

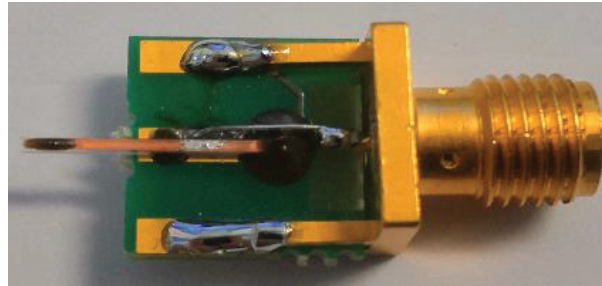


Fig. IV. 35. Microprobe fabricated in the glass substrate, with a connector on a PCB support, by *wire-bonding* connecting wire.

Measurement of the microprobes S_{11} parameters

The S_{11} parameters of the four microprobes were measured by a NANO VNA ZVL Rhode & Schwarz. We measured four micro-coil geometries such the square, circular, rectangular and ellipsoidal). The measurements were performed in the frequency range of 10 MHz to 6 GHz, calibrated for 4000 points of frequency to measure.

Fig. IV. 36. shows the results of S_{11} parameters measures that was done, for the four geometries of microprobe. We can note, that the four geometries do have a S_{11} value at least close to -10 dB. We could confirm that the four microprobes have almost the same self-resonance frequency, 4 GHz for many of them.

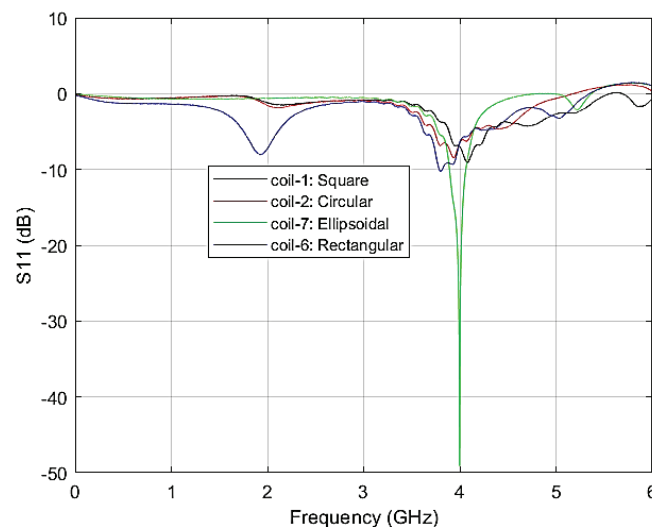


Fig. IV. 36. Measure of S_{11} parameter from four geometries of microprobe

Measurement of the microprobes Resistance and Inductance

The resistance and inductance measurement were done at the range of 10 MHz to 1.5 GHz. In the Fig.IV.37 we have their variation as function of frequency. Note that the resistance increase with the frequency and the Inductance is quietly constant.

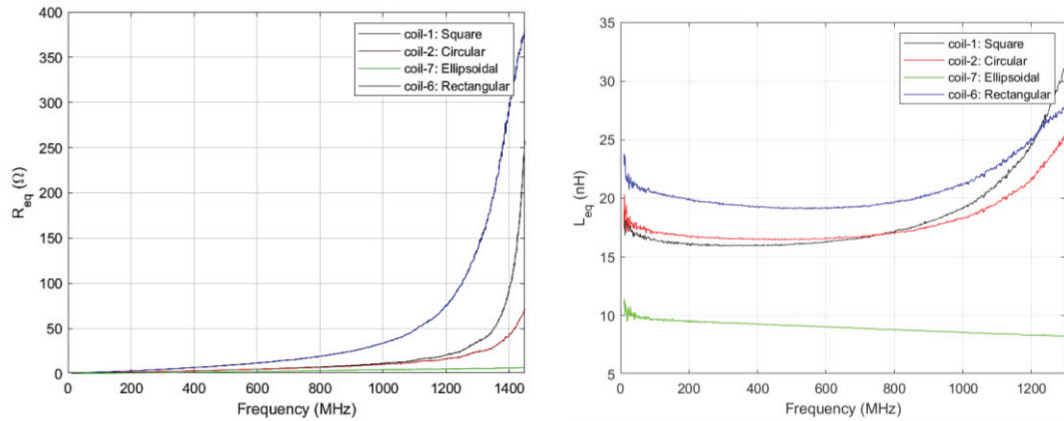


Fig. IV. 37. Measure of the resistance and inductance from four geometries of microprobe

In the following table we summarized the value of RL parameters of four geometries at 300 MHz and 500 MHz.

Coil n°	Geometry	Dimensions (μm^2)	300 MHz		500 MHz	
			R [Ω]	L[nH]	R [Ω]	L[nH]
1	Square	500×500	2.2	16.0	4.0	16.2
2	Circular	500×500	2.3	16.6	4.1	16.6
6	Rectangular	1000×250	4.7	19.6	8.8	19.5
7	Ellipsoidal	1000×500	1.1	9.4	2.3	9.3

Table IV. 10. The measurement of the microprobes RL parameters at 300 MHz and 500 MHz

In the Table IV.12, we compared the parameters of the ellipsoidal geometry determined by different approach.

Frequency (MHz)	R [Ω]				L _{self} [nH]				$\frac{B_z(z=0)}{i} \left[\frac{mT}{A\sqrt{\Omega}} \right]$
	Meas.	Calc.	COMSOL	ADS	Meas.	Calc.	COMSOL	ADS	
300	1.1	0.78	1.84	0.73	9.4	26.88	13.44	28.01	11.81
500	2.3	1.06	3.54	1.48	9.6	27.77	15.96	33.24	14.42

Table IV. 11. The measurement of the microprobes RL parameters at 300 MHz and 500 MHz

Note that the microprobe parameters are different according to the approach used, and mainly each is complementary to determine the RL parameters of the microprobe accurately.

Conclusion

In this chapter, we have described the processes of micro-antenna prototypes fabrication on glass or silicon substrates. Due to the inconvenience of previous connection points (*wire-bonding* or *underpass & vias*) between the centre of the micro-coil and the signal transmission tracks on the previous prototype (1st and 2nd) fabricated by our team, we have proposed a design of the microprobe with a connecting wire solution such *airbridge*. Thus, we presented the specifications of the microprobe characteristics for our fabrication.

Based on the defined specifications, we optimized the fabrication process, intending to reach the microprobe thickness ($t = 40 \mu m$). We mainly optimized the UV photolithography and the electroplating step, whose results are summarized in Fig. IV. 26 - Fig. IV. 31.

From the point of view of the microprobe fabrication step, we did two trials. The prototype was characterized by morphological information. The first trial was not suitable for our applications; that is why we have optimized the fabrication process in the second trial (final optimized prototype of the micro-antenna). So, the morphological characterization shows satisfactory results for our application (Fig. IV. 33). We enhance in the first place the thickness of the prototype from trial 1 to the second one (1st trial prototype thickness: $(15.71 \pm 3.12) \mu m$ and 2nd trial prototype thickness: $(27.10 \pm 1.37) \mu m$).

The measurement of the electrical characteristics of the prototypes fabricated during the first and second trial were carried out on the glass wafer. The results obtained show that the resistive and inductive losses measured match very well with the simulated results (Table IV. 3 and Table IV. 11). Furthermore, the final prototype after optimization of the process (second trial) should be suitable in terms of electrical performance due to great results of morphological characterization (no short-circuits, less residuals resin or impurities compared to the first trial, and the highest thickness, as well as the electrical characterization).

General Conclusions and Discussions

Based on the previous studies conducted by our team to develop implantable NMR micro-antenna, and by analysing the points not yet explored, this theoretical and experimental work comes as a complement to optimize the performances of the expected micro-antennas for our application.

In this work, we have proposed new methods to estimate the additional losses of all parts of the microprobe at the frequency range, 200 MHz to 900 MHz. Indeed, the analytical calculation of the resistance (R), inductance (L) and Q factor of the complete microprobe had been performed through an electrical circuit proposed in this work to model the microprobe in a silicon and glass substrate. Our approach takes into account all the constituents and characteristics of the systems: the skin, and proximity effect, the substrate, the intermediates layers (SiO_2) for the prototypes manufactured on the silicon substrate.

From our results, we could note that, at 300 MHz, the changes of microprobe substrate from glass to silicon provided an impact on the performance of the Q-factor (decreasing by 7 %). At 500 MHz, the Q-factor of the microprobe degraded by 27 % if used with silicon substrate instead of the glass substrate. Thus, the best working frequency for our application could be 500 MHz, for a microprobe on a glass substrate. We were sure that we could optimize considerable resistive loss due to the *underpass* & *vias* embedded on a silicon substrate or simply change the connecting wire type to *airbridge*, which requires an adaptation on the manufacturing process of the microprobe prototype.

By simulations, we could confirm that we could optimize the Q factor of microprobe ($Q = 71$ instead of $Q = 59$) by optimizing the thickness of the *underpass* & *vias* connecting wire ($t_{und} = 10 \mu m$ instead of $t_{und} = 0.5 \mu m$). The Q factor was also improved ($Q = 110$) using a connecting wire *airbridge* of $t_{airbridge} = 10 \mu m$ (see Table. III.3).

An AI approach, specifically ANN combined with 3D-TLE, is a method we developed to generalize the optimization of our highly complex multi-parametric system (micro-probe). Our ANN model was trained using the dataset generated by the simulation work done beforehand. Our last optimized ANN model allowed us to predict the Q-factor of the micro-probe with a test accuracy of 99.67% ($RMSE = 0.032$), the strength prediction with an accuracy of 91.34 % ($RMSE = 0.042$),

Considering the geometrical parameters of the μ -antennas that was defined from simulation work, the micro-moulding fabrication technique with electroplating was performed to obtain $40\text{ }\mu\text{m}$. We had carried out a UV photolithography optimization choosing 226 sec for the UV insolation with a new photoresist (AZ152NXT – Negative photo-resin). We also optimized the second trial of the microfabrication process, the electroplating step (5 h for copper electroplating, copper sulphate electrolyte bath ($\text{Cu}^{2+}\text{SO}_4^{2-}$) with a speed flow of about 20 l/h and applied current density of 200 mA/cm^2).

We have optimized the fabrication process of the microprobe in order to respect the specifications defined in the project (see section IV.1.1). Preliminary characterization results (morphological and electrical) obtained with the 1st prototype fabricated on glass substrates were reported. the 1st fabrication test allowed us to reach a microprobe thickness of $t = (18.90 \pm 5.25)\text{ }\mu\text{m}$ (Fig. IV. 18 & Fig. IV. 19), the resistance of the prototype in a glass substrate without a connector, was about $R = (3.897 \pm 0.193)\text{ }\Omega$, and with a connector soldered into a PCB, was $R = (6.12 \pm 0.12)\text{ }\Omega$. While, from the final optimized process, we were able to fabricate micro-probes with reduced micro-coils of dimensions up to $250 \times 250\text{ }\mu\text{m}^2$ (Fig. IV. 30) with a thickness of about $t = (27.10 \pm 1.37)\text{ }\mu\text{m}$ (Fig. IV. 33); dimensions never reached before by our team. Our characterization results are very promising for future in vivo applications.

Thanks to all these results, we strongly believe that 3D-TLE associated with the ANN approach can help establish a relationship between several microprobe geometric parameters, material properties, and the working frequency with the microprobe performances parameters (Resistance and Q factor).

Actually, our AI model can perform the prediction of microprobe performance in 2 minutes instead of 15 hours of computing time. Thus, this new optimization approach using AI tools combined with simulation tools (multi-parameter optimization work) implies an advance in biomedical research based on the development of NMR micro-sensors used for brain exploration, early diagnosis and treatment monitoring.

Finally, this thesis work also allowed us to demonstrate that we can design and fabricate optimized prototypes of different probes dedicated to the applications by knowing the desired performances, the working frequency and the materials needed for its fabrication.

Bibliography

- [1] A. D. International and M. University, World Alzheimer Report 2021: Journey through the Diagnosis of Dementia, (2021).
- [2] G. B. Frisoni, N. C. Fox, C. R. Jack, P. Scheltens, and P. M. Thompson, The Clinical Use of Structural MRI in Alzheimer Disease, *Nat. Rev. Neurol.* **6**, 67 (2010).
- [3] D. I. Hoult and R. E. Richards, The Signal-to-Noise Ratio of the Nuclear Magnetic Resonance Experiment, *J. Magn. Reson.* 1969 **24**, 71 (1976).
- [4] D. I. Hoult, The NMR Receiver: A Description and Analysis of Design, *Prog. Nucl. Magn. Reson. Spectrosc.* **12**, 41 (1978).
- [5] J. L. Griffin, A. W. Nicholls, H. C. Keun, R. J. Mortishire-Smith, J. K. Nicholson, and T. Kuehn, Metabolic Profiling of Rodent Biological Fluids via ^1H NMR Spectroscopy Using a 1 Mm Microlitre Probe, *The Analyst* **127**, 582 (2002).
- [6] T. M. Tsang, J. L. Griffin, J. Haselden, C. Fish, and E. Holmes, Metabolic Characterization of Distinct Neuroanatomical Regions in Rats by Magic Angle Spinning ^1H Nuclear Magnetic Resonance Spectroscopy, *Magn. Reson. Med.* **53**, 1018 (2005).
- [7] H. Rabeson, F. Fauvelle, G. Testylier, A. Foquin, P. Carpentier, F. Dorandeu, D. van Ormondt, and D. Graveron-Demilly, Quantitation with QUEST of Brain HRMAS-NMR Signals: Application to Metabolic Disorders in Experimental Epileptic Seizures, *Magn. Reson. Med.* **59**, 1266 (2008).
- [8] S. M. Wright and L. L. Wald, Theory and Application of Array Coils in MR Spectroscopy, *NMR Biomed.* **10**, 394 (1997).
- [9] T. Niendorf, C. Oezerdem, Y. Ji, E. Oberacker, A. Kuehne, H. Waiczies, and L. Winter, Radiative RF Antenna Arrays for Cardiac, Brain and Thermal Magnetic Resonance at Ultrahigh and Extreme Magnetic Field Strengths: Concepts, Electromagnetic Field Simulations and Applications, in 2017 International Conference on Electromagnetics in Advanced Applications (ICEAA) (IEEE, Verona, Italy, 2017), pp. 1567–1570.
- [10] M. Menéndez González, Atlas of Biomarkers for Alzheimer’s Disease (Springer International Publishing, Cham, 2014).
- [11] Les traitements de la maladie d’Alzheimer - ICM, <https://institutducerveau-icm.org/fr/alzheimer/traitement/>.

- [12] O. Querbes, Place des biomarqueurs dans le diagnostic précoce individuel de la maladie d'Alzheimer : une étude multicentrique, exercice, Université Toulouse III - Paul Sabatier, 2021.
- [13] R. C. Petersen, G. E. Smith, S. C. Waring, R. J. Ivnik, E. G. Tangalos, and E. Kokmen, Mild Cognitive Impairment: Clinical Characterization and Outcome, *Arch. Neurol.* **56**, 303 (1999).
- [14] P. J. Visser and D. S. Knopman, Amyloid Imaging in the Prediction of Alzheimer-Type Dementia in Subjects with Amnesic MCI, *Neurology* **73**, 744 (2009).
- [15] F. Ben Bouallègue, D. Mariano-Goulart, P. Payoux, and the Alzheimer's Disease Neuroimaging Initiative (ADNI), Comparison of CSF Markers and Semi-Quantitative Amyloid PET in Alzheimer's Disease Diagnosis and in Cognitive Impairment Prognosis Using the ADNI-2 Database, *Alzheimers Res. Ther.* **9**, 32 (2017).
- [16] A. Sörensen, G. Blazhenets, F. Schiller, P. T. Meyer, L. Frings, and for the Alzheimer Disease Neuroimaging Initiative, Amyloid Biomarkers as Predictors of Conversion from Mild Cognitive Impairment to Alzheimer's Dementia: A Comparison of Methods, *Alzheimers Res. Ther.* **12**, 155 (2020).
- [17] Diagnosed Mild Cognitive Impairment Due to Alzheimer's Disease with PET Biomarkers of Beta Amyloid and Neuronal Dysfunction, <https://journals.plos.org/plosone/article?id=10.1371/journal.pone.0066877>.
- [18] N. Smailagic, L. Lafortune, S. Kelly, C. Hyde, and C. Brayne, 18F-FDG PET for Prediction of Conversion to Alzheimer's Disease Dementia in People with Mild Cognitive Impairment: An Updated Systematic Review of Test Accuracy, *J. Alzheimers Dis.* **64**, 1175 (2018).
- [19] Using Machine Learning to Quantify Structural MRI Neurodegeneration Patterns of Alzheimer's Disease into Dementia Score: Independent Validation on 8,834 Images from ADNI, AIBL, OASIS, and MIRIAD Databases - Popuri - 2020 - Human Brain Mapping - Wiley Online Library, <https://onlinelibrary.wiley.com/doi/full/10.1002/hbm.25115>.
- [20] K. Popuri, D. Ma, L. Wang, and M. F. Beg, Using Machine Learning to Quantify Structural MRI Neurodegeneration Patterns of Alzheimer's Disease into Dementia Score: Independent Validation on 8,834 Images from ADNI, AIBL, OASIS, and MIRIAD Databases, *Hum. Brain Mapp.* **41**, 4127 (2020).

- [21] S. Basaia, F. Agosta, L. Wagner, E. Canu, G. Magnani, R. Santangelo, and M. Filippi, Automated Classification of Alzheimer's Disease and Mild Cognitive Impairment Using a Single MRI and Deep Neural Networks, *NeuroImage Clin.* **21**, 101645 (2019).
- [22] T. K. Khan, *Biomarkers in Alzheimer's Disease* (Academic Press is an imprint of Elsevier, London, United Kingdom ; San Diego, CA, USA, 2016).
- [23] W. E. Klunk et al., Imaging Brain Amyloid in Alzheimer's Disease with Pittsburgh Compound-B: Imaging Amyloid in AD with PIB, *Ann. Neurol.* **55**, 306 (2004).
- [24] S. A. Small, W. Y. Tsai, R. DeLaPaz, R. Mayeux, and Y. Stern, Imaging Hippocampal Function across the Human Life Span: Is Memory Decline Normal or Not?, *Ann. Neurol.* **51**, 290 (2002).
- [25] F. Hulstaert et al., Improved Discrimination of AD Patients Using γ -Amyloid(1-42) and Tau Levels in CSF, *Neurology* **52**, 1555 (1999).
- [26] M. Mapstone et al., Plasma Phospholipids Identify Antecedent Memory Impairment in Older Adults, *Nat. Med.* **20**, 415 (2014).
- [27] H. M. Snyder et al., Developing Novel Blood-Based Biomarkers for Alzheimer's Disease, *Alzheimers Dement.* **10**, 109 (2014).
- [28] C. Cudalbu, V. Mlynárik, and R. Gruetter, Handling Macromolecule Signals in the Quantification of the Neurochemical Profile, *J. Alzheimers Dis.* **31**, S101 (2012).
- [29] V. Govindaraju, K. Young, and A. A. Maudsley, Proton NMR Chemical Shifts and Coupling Constants for Brain Metabolites, *NMR Biomed.* **13**, 129 (2000).
- [30] P. T. Francis, A. M. Palmer, M. Snape, and G. K. Wilcock, The Cholinergic Hypothesis of Alzheimer's Disease: A Review of Progress, *J. Neurol. Neurosurg. Psychiatry* **66**, 137 (1999).
- [31] K. J. Reinikainen, H. Soininen, and P. J. Riekkinen, Neurotransmitter Changes in Alzheimer's Disease: Implications to Diagnostics and Therapy, *J. Neurosci. Res.* **27**, 576 (1990).
- [32] J. Puoliväli, L. Pradier, and P. Riekkinen Jr., Moderate Cortical EEG Changes in Apolipoprotein E-Deficient Mice during Ageing and Scopolamine Treatment but Not after Nucleus Basalis Lesion, *Psychopharmacology (Berl.)* **145**, 386 (1999).
- [33] P. A. Pahapill, The Pedunculopontine Nucleus and Parkinson's Disease, *Brain* **123**, 1767 (2000).
- [34] M. Steriade, F. Amzica, and I. Timofeev, Bases Cellulaires Des Transitions de l'état de Sommeil Aux Paroxysmes Épileptiformes, *Médecine/Sciences* **19**, 999 (2003).

- [35] Picciotto M., Alreja M., and Jentsch D, Acetylcholine, Neuropsychopharmacology, The Fifth Generation of Progress, (2002).
- [36] G. Paxinos, Paxino's and Watson's The Rat Brain in Stereotaxic Coordinates, Seventh edition (Elsevier/AP, Academic Press is an imprint of Elsevier, Amsterdam ; Boston, 2014).
- [37] J. T. Rosillo, Contribution à l'amélioration de la sensibilité d'un micro-récepteur RMN implantable, phdthesis, Université Claude Bernard - Lyon I, 2014.
- [38] R. Eisberg, R. Resnick, and J. Brown, Quantum Physics of Atoms, Molecules, Solids, Nuclei, and Particles, Phys. Today **39**, 110 (1986).
- [39] N. Bloembergen, E. Purcell, and R. Pound, Relaxation Effects in Nuclear Magnetic Resonance Absorption, Phys. Rev. **73**, 679 (1948).
- [40] R. J. Abraham, J. Fisher, and P. Loftus, Introduction to NMR Spectroscopy, Magn. Reson. Chem. **27**, 1004 (1989).
- [41] H. D. W. Hill and R. E. Richards, Limits of Measurement in Magnetic Resonance, J. Phys. [E] **1**, 977 (1968).
- [42] K. J. R. Rosman and P. D. P. Taylor, Isotopic Compositions of the Elements 1997 (Technical Report), Pure Appl. Chem. **70**, 217 (1998).
- [43] T. Truong-Cong, Optimisation Par Approche Physique Des Micro-Antennes RMN Fabriquées Par Techniques Microelectroniques : Etude Theorique et Experimentale, PhD Thesis, INSA de Lyon, 2014.
- [44] D. I. Hoult, The Principle of Reciprocity, J. Magn. Reson. **213**, 344 (2011).
- [45] L. Chi, M. Huang, A. R. Pfaff, J. Huang, R. E. Gerald, and K. Woelk, Capillary-Tube Package Devices for the Quantitative Performance Evaluation of Nuclear Magnetic Resonance Spectrometers and Pulse Sequences, Rev. Sci. Instrum. **89**, 123115 (2018).
- [46] D. L. Olson, T. L. Peck, A. G. Webb, R. L. Magin, and J. V. Sweedler, High-Resolution Microcoil 1H-NMR for Mass-Limited, Nanoliter-Volume Samples, Science **270**, 1967 (1995).
- [47] T. L. Peck, R. L. Magin, J. Kruse, and M. Feng, NMR Microspectroscopy Using 100 Mm Planar RF Coils Fabricated on Gallium Arsenide Substrates, IEEE Trans. Biomed. Eng. **41**, 706 (1994).
- [48] J. E. Stocker, T. L. Peck, A. G. Webb, M. Feng, and R. L. Magin, Nanoliter Volume, High-Resolution NMR Microspectroscopy Using a 60-Mm Planar Microcoil, IEEE Trans. Biomed. Eng. **44**, 1122 (1997).

- [49] J. D. Trumbull, I. K. Glasgow, D. J. Beebe, and R. L. Magin, Integrating Microfabricated Fluidic Systems and NMR Spectroscopy, *IEEE Trans. Biomed. Eng.* **47**, 3 (2000).
- [50] C. Massin, F. Vincent, A. Homsy, K. Ehrmann, G. Boero, P.-A. Besse, A. Daridon, E. Verpoorte, N. F. de Rooij, and R. S. Popovic, Planar Microcoil-Based Microfluidic NMR Probes, *J. Magn. Reson.* **164**, 242 (2003).
- [51] S. Eroglu, B. Gimi, B. Roman, G. Friedman, and R. L. Magin, NMR Spiral Surface Microcoils: Design, Fabrication, and Imaging, *Concepts Magn. Reson.* **17B**, 1 (2003).
- [52] B. Gimi, S. Eroglu, L. Leoni, T. A. Desai, R. L. Magin, and B. B. Roman, NMR Spiral Surface Microcoils: Applications, *Concepts Magn. Reson.* **18B**, 1 (2003).
- [53] R. Subramanian, M. M. Lam, and A. G. Webb, RF Microcoil Design for Practical NMR of Mass-Limited Samples, *J Magn Reson* **133**, 227 (1998).
- [54] R. Subramanian and A. G. Webb, Design of Solenoidal Microcoils for High-Resolution ^{13}C NMR Spectroscopy, *Anal. Chem.* **70**, 2454 (1998).
- [55] K. Ehrmann, M. Gersbach, P. Pascoal, F. Vincent, C. Massin, D. Stamou, P.-A. Besse, H. Vogel, and R. S. Popovic, Sample Patterning on NMR Surface Microcoils, *J. Magn. Reson.* **178**, 96 (2006).
- [56] N. BAXAN, Mise En Oeuvre de Microantennes RMN En Perspective d'étude in Vivo de Metabolites Par Spectroscopie, Université Claude Bernard - Lyon 1, 2008.
- [57] N. Baxan, H. Rabeson, G. Pasquet, J.-F. Châteaux, A. Briguet, P. Morin, D. Graveron-Demilly, and L. Fakri-Bouchet, Limit of Detection of Cerebral Metabolites by Localized NMR Spectroscopy Using Microcoils, *Comptes Rendus Chim.* **11**, 448 (2008).
- [58] A. Kadjo, Micro-Capteur Implantables : Etude Des Criteres de Performance En Vue de l'optimisation Des Acquisitions Par Spectroscopie RMN in Vivo, Ph. D. Thesis, Université Claude Bernard Lyon1, 2011.
- [59] N. Baxan, A. Briguet, D. Graveron-Demilly, L. Fakri-Bouchet, R. Cespuglio, and C. Rousset, In Vivo Animal NMR Studies Using Implantable Micro Coil, in *IEEE Imaging Systems and Techniques (IEEE, 2008)*, pp. 294–296.
- [60] M. Woytasik et al., Characterization of Flexible RF Microcoils Dedicated to Local MRI, *Microsyst. Technol.* **13**, 1575 (2007).
- [61] M. Weiger, D. Schmidig, S. Denoth, C. Massin, F. Vincent, M. Schenkel, and M. Fey, NMR Microscopy with Isotropic Resolution of 3.0 Mm Using Dedicated Hardware and Optimized Methods, *Concepts Magn. Reson. Part B Magn. Reson. Eng.* **33B**, 84 (2008).

- [62] H. Lee, E. Sun, D. Ham, and R. Weissleder, Chip–NMR Biosensor for Detection and Molecular Analysis of Cells, *Nat. Med.* **14**, 869 (2008).
- [63] K. Ehrmann, N. Saillen, F. Vincent, M. Stettler, M. Jordan, F. M. Wurm, P.-A. Besse, and R. Popovic, Microfabricated Solenoids and Helmholtz Coils for NMR Spectroscopy of Mammalian Cells, *Lab. Chip* **7**, 373 (2007).
- [64] M. Rivera, J. J. Vaquero, A. Santos, J. Ruiz-Cabello, and F. del Pozo, MRI Visualization of Small Structures Using Improved Surface Coils, *Magn. Reson. Imaging* **16**, 157 (1998).
- [65] C. S. Bosch and J. J. H. Ackerman, Surface Coil Spectroscopy, in *In-Vivo Magnetic Resonance Spectroscopy II: Localization and Spectral Editing*, edited by M. Rudin, Vol. 27 (Springer Berlin Heidelberg, Berlin, Heidelberg, 1992), pp. 3–44.
- [66] J.-C. Ginefri, A. Rubin, M. Tatoulian, M. Woytasik, F. Boumezbeur, B. Djemaï, M. Poirier-Quinot, F. Lethimonnier, L. Darrasse, and E. Dufour-Gergam, Implanted, Inductively-Coupled, Radiofrequency Coils Fabricated on Flexible Polymeric Material: Application to in Vivo Rat Brain MRI at 7T, *J. Magn. Reson.* **224**, 61 (2012).
- [67] J. Deborne, N. Pinaud, and Y. Crémillieux, Implantable NMR Microcoils in Rats: A New Tool for Exploring Tumor Metabolism at Sub-Microliter Scale?, *Metabolites* **11**, 176 (2021).
- [68] J. S. Schoeniger and S. J. Blackband, The Design and Construction of a NMR Microscopy Probe, *J. Magn. Reson. B* **104**, 127 (1994).
- [69] T. L. Peck, R. L. Magin, and P. C. Lauterbur, Design and Analysis of Microcoils for NMR Microscopy, *J. Magn. Reson. B* **108**, 114 (1995).
- [70] Charles Kittel, *Introduction to Solids Physics Book*, 8th ed. (Stuart Johnson, EUA, 2005).
- [71] H. Nyquist, Thermal Agitation of Electric Charge in Conductors, *Phys. Rev.* **32**, 110 (1928).
- [72] L. Darrasse, Perspectives with Cryogenic RF Probes in Biomedical MRI, *Biochimie* **85**, 915 (2003).
- [73] M. E. Lacey, R. Subramanian, D. L. Olson, A. G. Webb, and J. V. Sweedler, High-Resolution NMR Spectroscopy of Sample Volumes from 1 NL to 10 ML, *Chem. Rev.* **99**, 3133 (1999).
- [74] D. L. Olson, J. A. Norcross, M. O’Neil-Johnson, P. F. Molitor, D. J. Detlefsen, A. G. Wilson, and T. L. Peck, Microflow NMR: Concepts and Capabilities, *Anal. Chem.* **76**, 2966 (2004).

- [75] Micro-Capteur Implantables : Etude Des Critères de Performance En Vue de l'optimisation Des Acquisitions Par Spectroscopie Rmn in Vivo Kadjo - Recherche Google, (n.d.).
- [76] M. E. Lacey, J. V. Sweedler, C. K. Larive, A. J. Pipe, and R. D. Farrant, ^1H NMR Characterization of the Product from Single Solid-Phase Resin Beads Using Capillary NMR Flow Probes, *J. Magn. Reson.* **153**, 215 (2001).
- [77] G. Boero, *Integrated NMR Probe for Magnetometry*, (2005).
- [78] L. Renaud, M. Armenean, L. Berry, P. Kleimann, P. Morin, M. Pitaval, J. O'Brien, M. Brunet, and H. Saint-Jalmes, Implantable Planar Rf Microcoils for NMR Microspectroscopy, *Sens. Actuators Phys.* **99**, 244 (2002).
- [79] B. Sorli, J. F. Chateaux, M. Pitaval, H. Chahboune, B. Favre, A. Briguet, and P. Morin, Micro-Spectrometer for NMR: Analysis of Small Quantities in Vitro, *Meas. Sci. Technol.* **15**, 877 (2004).
- [80] T. Truong-Cong, J. Trejo-Rosillo, H. Phuc Dang, H. Huy Pham, A. Fakri, and L. Fakri-Bouchet, A Method for Improving the Performance of Implantable RF Microcoil Designed for MRI and MRS of Murine Brain at 4.7T, in *Materiaux et Applications Aux Dispositifs En Capteurs* (2012).
- [81] M. Bhattacharya, Analysis of Broadside Offset Coupled Strips for Broadband Filter Applications, in (IEEE, 2009), pp. 1–5.
- [82] P. M. Mendes, S. Sinaga, A. Polyakov, M. Bartek, J. N. Burghartz, and J. H. Correia, Wafer-Level Integration of on-Chip Antennas and RF Passives Using High-Resistivity Polysilicon Substrate Technology, in (IEEE, 2004), pp. 1879–1884.
- [83] L. Cadix et al., Modelling of Through Silicon Via RF Performance and Impact on Signal Transmission in 3D Integrated Circuits, in 2009 IEEE International Conference on 3D System Integration (IEEE, San Francisco, CA, USA, 2009), pp. 1–7.
- [84] J. U. Knickerbocker et al., Three-Dimensional Silicon Integration, *IBM J. Res. Dev.* **52**, 553 (2008).
- [85] H. B. Dwight, Proximity Effect in Wires and Thin Tubes, *J. Am. Inst. Electr. Eng.* **42**, 961 (1923).
- [86] S. Eroglu, G. Friedman, and R. L. Magin, Estimate of Losses and Signal-to-Noise Ratio in Planar Inductive Micro-Coil Detectors Used for NMR, *IEEE Trans. Magn.* **37**, 2787 (2001).
- [87] F. E. Neumann, *Ann. Phys. Chem.* **143**, 31 (1846).

- [88] E. B. Rosa, The Self-Inductance of a Toroidal Coil of Rectangular Section, *Bull. Bur. Stand.* **4**, 141 (1907).
- [89] E.B. Rosa., The Self and Mutual Inductances of Linear Conductors (Bulletin of the Bureau of Standards, 1908).
- [90] F. W. Grover, Inductance Calculations: Working Formulas and Tables (Instrument Society of America, 1973).
- [91] C. Hoer and C. Love, Exact Inductance Equations for Rectangular Conductors with Applications to More Complicated Geometries, *J. Res. Natl. Bur. Stand. Sect. C Eng. Instrum.* **69C**, 127 (1965).
- [92] T. N. Osborn, All-Copper Chip-to-Substrate Interconnects for High Performance Integrated Circuit Devices, (2009).
- [93] M. Schuettler and T. Stieglitz, Microassembly and Micropackaging of Implantable Systems, in *Implantable Sensor Systems for Medical Applications* (Elsevier, 2013), pp. 108–149.
- [94] B. D. Ducata, Chip Bonding Tools, Fine Ceramic & Machining Parts, <https://www.smallprecisiontools.com/products-and-solutions/chip-bonding-tools/bonding-capillaries/technical-guide/basics-of-ball-bonding-process/gold-ball-wire-bonding-Process/?oid=562&lang=en>.
- [95] S. M. Sze, *Physics of Semiconductor Devices*, 3rd ed (Wiley-Interscience, Hoboken, N.J, 2007).
- [96] J. Yan, B. Kim, and Y. G. Jeong, Thermomechanical and Electrical Properties of PDMS/MWCNT Composite Films Crosslinked by Electron Beam Irradiation, *J. Mater. Sci.* **50**, 5599 (2015).
- [97] A. Nabil, J. A. Bernardo, Y. Ma, M. Abouelatta, A. Shaker, L. F. Bouchet, H. Ragai, and C. Gontrand, Electrical Modeling of Tapered TSV Including MOS-Field Effect and Substrate Parasitics: Analysis and Application, *Microelectron. J.* **100**, 104797 (2020).
- [98] Y. Ma, *Modèles compacts électroniques du premier ordre et considération de bruit pour les circuits 3D*, Université de Lyon 1, INSA -Lyon, 2018.
- [99] C. Gontrand, *Towards a Modeling Synthesis of Two or Three-Dimensional Circuits Through Substrate Coupling and Interconnections* (Bentham Science Publishers, 2014).
- [100] J.-E. Lorival et al., An Efficient and Simple Compact Modeling Approach for 3-D Interconnects with IC's Stack Global Electrical Context Consideration, *Microelectron. J.* **46**, 153 (2015).

- [101] O. Valorge, F. Sun, J.-E. Lorival, M. Abouelatta-Ebrahim, F. Calmon, and C. Gontrand, Analytical and Numerical Model Confrontation for Transfer Impedance Extraction in Three-Dimensional Radio Frequency Circuits, **2012**, (2012).
- [102] T. Smedes, N. P. van der Meijs, and A. J. van Genderen, Extraction of Circuit Models for Substrate Cross-Talk, in Proceedings of IEEE International Conference on Computer Aided Design (ICCAD) (1995), pp. 199–206.
- [103] Numerically Stable Green Function for Modeling and Analysis of Substrate Coupling in Integrated Circuits | IEEE Journals & Magazine | IEEE Xplore, <https://ieeexplore.ieee.org/abstract/document/703820>.
- [104] Y. Ma, L. Fakri-Bouchet, F. Calmon, and C. Gontrand, Electrothermal Modeling for 3-D Nanoscale Circuit Substrates: Noise, IEEE Trans. Compon. Packag. Manuf. Technol. **6**, 1040 (2016).
- [105] C. Gontrand, F. Sun, J. Ricardo Cardenas-Valdez, Y. Ma, C. Plossu, F. Calmon, J. Cruz Nuñez-Perez, and J. Verdier, 3D Substrate Modeling; from a First Order Electrical Analysis, towards Some Possible Signal Fluctuations Consideration, for Radio Frequency Circuits, Microelectron. J. **45**, 1061 (2014).
- [106] Y. Cao, R. A. Groves, X. Huang, N. D. Zamdmer, J.-O. Plouchart, R. A. Wachnik, T.-J. King, and C. Hu, Frequency-Independent Equivalent-Circuit Model for on-Chip Spiral Inductors, IEEE J. Solid-State Circuits **38**, 419 (2003).
- [107] J. R. Long and M. A. Copeland, The Modeling, Characterization, and Design of Monolithic Inductors for Silicon RF IC's, IEEE J. Solid-State Circuits **32**, 357 (1997).
- [108] J. Aguilera, J. de No, A. Garcia-Alonso, F. Oehler, H. Hein, J. Sauerer, J. D. No, and A. G.-A. Ceit, A Guide for On-Chip Inductor Design in a Conventional CMOS Process for RF Applications, Appl. Microw. Wirel. (2001).
- [109] K. Okada and K. Masu, Modeling of Spiral Inductors, in Advanced Microwave Circuits and Systems, Chapt 14, edited by V. Zhurbenko (InTech, 2010).
- [110] C. P. Yue and S. S. Wong, On-Chip Spiral Inductors with Patterned Ground Shields for Si-Based RF ICs, IEEE J. Solid-State Circuits **33**, 743 (1998).
- [111] Applications of Deep Learning to MRI Images: A Survey, Big Data Min. Anal. **1**, 1 (2018).
- [112] Z. Akkus, A. Galimzianova, A. Hoogi, D. L. Rubin, and B. J. Erickson, Deep Learning for Brain MRI Segmentation: State of the Art and Future Directions, J. Digit. Imaging **30**, 449 (2017).

- [113] N. Yamanakkanavar, J. Y. Choi, and B. Lee, MRI Segmentation and Classification of Human Brain Using Deep Learning for Diagnosis of Alzheimer's Disease: A Survey, *Sensors* **20**, 3243 (2020).
- [114] Z. Wang et al., A Sparse Model-Inspired Deep Thresholding Network for Exponential Signal Reconstruction -- Application in Fast Biological Spectroscopy, 2020.
- [115] X. Qu, Y. Huang, H. Lu, T. Qiu, D. Guo, T. Agback, V. Orekhov, and Z. Chen, Accelerated Nuclear Magnetic Resonance Spectroscopy with Deep Learning, *Angew. Chem.* **132**, 10383 (2020).
- [116] K. Sharma and G. P. Pandey, Designing a Compact Microstrip Antenna Using the Machine Learning Approach, *J. Telecommun. Inf. Technol.* **4**, 44 (2021).
- [117] M. Sağık, O. Altıntaş, E. Ünal, E. Özdemir, M. Demirci, Ş. Çolak, and M. Karaaslan, Optimizing the Gain and Directivity of a Microstrip Antenna with Metamaterial Structures by Using Artificial Neural Network Approach, *Wirel. Pers. Commun.* (2021).
- [118] D. Erricolo, P.-Y. Chen, A. Rozhkova, E. Torabi, H. Bagci, A. Shamim, and X. Zhang, Machine Learning in Electromagnetics: A Review and Some Perspectives for Future Research, in 2019 International Conference on Electromagnetics in Advanced Applications (ICEAA) (IEEE, Granada, Spain, 2019), pp. 1377–1380.
- [119] E. Alpaydin, *Machine Learning* (2021).
- [120] R. S. Michalski and J. R. Anderson, *Machine Learning An Artificial Intelligence Approach* (1983).
- [121] J. Schmidhuber, Deep Learning in Neural Networks: An Overview, *Neural Netw.* **61**, 85 (2015).
- [122] G. E. Hinton, A Practical Guide to Training Restricted Boltzmann Machines, in *Neural Networks: Tricks of the Trade: Second Edition*, edited by G. Montavon, G. B. Orr, and K.-R. Müller (Springer, Berlin, Heidelberg, 2012), pp. 599–619.
- [123] S. Hochreiter and J. Schmidhuber, Long Short-Term Memory, *Neural Comput.* **9**, 1735 (1997).
- [124] J. J. DiCarlo, D. Zoccolan, and N. C. Rust, How Does the Brain Solve Visual Object Recognition?, *Neuron* **73**, 415 (2012).
- [125] W. S. McCulloch and W. Pitts, A Logical Calculus of the Ideas Immanent in Nervous Activity, *Bull. Math. Biophys.* **5**, 115 (1943).
- [126] F. Rosenblatt, The Perceptron: A Probabilistic Model for Information Storage and Organization in the Brain, *Psychol. Rev.* **65**, 386 (1958).

- [127] Figure 3. Diagram of the Artificial Neuron (Deep Learning). Source:..., https://www.researchgate.net/figure/Diagram-of-the-artificial-neuron-deep-learning-Source-created-by-Chrislb-CC-BY-SA_fig2_340603309.
- [128] Title: What Is Neuron and Artificial Neuron in Deep Learning? [MPLSVPN - Moving Towards SDN and NFV Based Networks, <https://www.google.com/imgres>.
- [129] B. Yegnanarayana, Artificial Neural Networks, 11. print (Prentice Hall of India, New Delhi, 2005).
- [130] B. Ding, H. Qian, and J. Zhou, Activation Functions and Their Characteristics in Deep Neural Networks, in 2018 Chinese Control And Decision Conference (CCDC) (IEEE, Shenyang, 2018), pp. 1836–1841.
- [131] A. Farzad, H. Mashayekhi, and H. Hassanpour, A Comparative Performance Analysis of Different Activation Functions in LSTM Networks for Classification, Neural Comput. Appl. **31**, 2507 (2019).
- [132] D. Jurafsky and J. H. Martin, Speech and Language Processing: An Introduction to Natural Language Processing, Computational Linguistics, and Speech Recognition, 2nd ed (Pearson Prentice Hall, Upper Saddle River, N.J, 2009).
- [133] J. Mueller and L. Massaron, Deep Learning (John Wiley and Sons, Inc, Hoboken, NJ, 2019).
- [134] K. Pasupa and W. Sunhem, A Comparison between Shallow and Deep Architecture Classifiers on Small Dataset, in 2016 8th International Conference on Information Technology and Electrical Engineering (ICITEE) (IEEE, Yogyakarta, Indonesia, 2016), pp. 1–6.
- [135] I. Goodfellow, Y. Bengio, and A. Courville, Deep Learning (2016).
- [136] N. Tangri, D. Ansell, and D. Naimark, Predicting Technique Survival in Peritoneal Dialysis Patients: Comparing Artificial Neural Networks and Logistic Regression, Nephrol. Dial. Transplant. Off. Publ. Eur. Dial. Transpl. Assoc. - Eur. Ren. Assoc. **23**, 2972 (2008).
- [137] M. Buscema, Back Propagation Neural Networks, Subst. Use Misuse **33**, 233 (1998).
- [138] SungJin Park, Suan Lee, and J. Kim, Time-Sensitive Multi-Dimensional Recommender in Database System, in 2017 IEEE International Conference on Big Data and Smart Computing (BigComp) (IEEE, Jeju Island, South Korea, 2017), pp. 284–287.
- [139] V. K. Varadan, K. J. Vinoy, and K. A. Jose, RF MEMS and Their Applications (John Wiley, Chichester, England; Hoboken, NJ, 2010).

- [140] V. Choudhary and K. Iniewski, MEMS: Packaging and Technology (2017).
- [141] W. Ehrfeld, The LIGA Process for Microsystems, in Micro System Technologies 90, edited by H. Reichl (Springer Berlin Heidelberg, Berlin, Heidelberg, 1990), pp. 521–528.
- [142] S. Sotnik, V. Lyashenko, and T. Shakurova, Nano Devices and Microsystem Technologies: Brief Overview, (2021).
- [143] O. F. Hikmat and M. S. Mohamed Ali, RF MEMS Inductors and Their Applications—A Review, J. Microelectromechanical Syst. **26**, 17 (2017).
- [144] C. Luo, C. Xu, L. Lv, H. Li, X. Huang, and W. Liu, Review of Recent Advances in Inorganic Photoresists, RSC Adv. **10**, 8385 (2020).
- [145] M. Brunet, T. O'Saposs\$Donnell, J. O\$apos\$Brien, P. McCloskey, and S. C. \$Oacute\$ Mathuna, Thick Photoresist Development for the Fabrication of High Aspect Ratio Magnetic Coils, J. Micromechanics Microengineering **12**, 444 (2002).
- [146] F. Ahamed, Field and Wave Electromagnetics - David K Cheng, (n.d.).
- [147] U. van Rienen, Numerical Methods in Computational Electrodynamics, Vol. 12 (Springer Berlin Heidelberg, Berlin, Heidelberg, 2001).
- [148] Regularization — ML Glossary Documentation, <https://ml-cheatsheet.readthedocs.io/en/latest/regularization.html#id7>.

APPENDICES

APPENDIX A

A.1. Maxwell's equations

Electromagnetic analysis on a macroscopic level is solving Maxwell's equations subject to certain boundary conditions. Maxwell's equations are a set of equations, written in differential or integral form, stating the relationships between the fundamental electromagnetic quantities. These quantities are:

- Electric field intensity \mathbf{E}
- Electric displacement or electric flux density \mathbf{D}
- Magnetic field intensity \mathbf{H}
- Magnetic flux density \mathbf{B}
- Current density \mathbf{J}
- Electric charge density ρ

Here, the equations have been formulated in differential form because it leads to differential equations that the finite element method can handle. For general time-varying fields, Maxwell's equations can be written as:

The first two equations are also referred to as Maxwell-Ampère's and Faraday's, respectively.

$$\nabla \times \mathbf{H} = \mathbf{J} + \frac{\partial \mathbf{D}}{\partial t} \quad (1)$$

$$\nabla \times \mathbf{E} = -\frac{\partial \mathbf{B}}{\partial t} \quad (2)$$

The next equations are two forms of Gauss' law: the electric and magnetic form, respectively.

$$\nabla \cdot \mathbf{D} = \rho \quad (3)$$

$$\nabla \cdot \mathbf{B} = 0 \quad (4)$$

Out of the five equations mentioned, only three are independent. The both altogether, with either the electric form of Gauss' law or the equation of continuity form such a separate system. The equations include constitutive relations that describe the macroscopic properties of the medium to obtain a closed system. They are given as:

$$\mathbf{D} = \epsilon_0(\mathbf{E} + \mathbf{P}) \quad (5)$$

$$\mathbf{B} = \mu_0(\mathbf{H} + \mathbf{M}) \quad (6)$$

$$\mathbf{J} = \sigma \mathbf{E} \quad (7)$$

where ϵ_0 is the permittivity of vacuum, μ_0 is the permeability of the vacuum, and σ is the electrical conductivity. In the SI system, the permeability of vacuum is chosen to be $\mu_0 = 4\pi \times 10^{-7}$ H/m. The velocity of an electromagnetic wave in a vacuum is given as c_0 and the permittivity of a vacuum is derived from the relation:

$$\epsilon_0 = \frac{1}{c_0^2 \mu_0} = 8.854 \times 10^{-12} \frac{\text{F}}{\text{m}} = \frac{1}{36\pi} \times 10^{-9} \frac{\text{F}}{\text{m}} \quad (8)$$

The electromagnetic constants ϵ_0 , μ_0 , and c_0 are available in COMSOL Multiphysics as predefined physical constants.

A consequence of Maxwell's equations is that changes in time of currents and charges are not synchronized with changes of the electromagnetic fields. The changes of the fields are always delayed relative to the changes of the sources, reflecting the finite speed of propagation of electromagnetic waves. Under the assumption that this effect can be ignored, it is possible to obtain the electromagnetic fields by considering stationary currents at every instant. This is called the quasi-stationary approximation. The approximation is valid because the magnetic field variations in time are small, and the studied geometries ($l_{probe} \approx 1\text{cm}$) are considerably smaller than the wavelength ($\lambda = 1\text{m}$) [146] [147].

A.2. Mesh

In finite element analysis, the resolution domain is discretized into subdomains called mesh elements. These elements are the elementary bricks whose mesh will represent the geometric system to be simulated. The elements are geometrical primitives composed of several nodes.

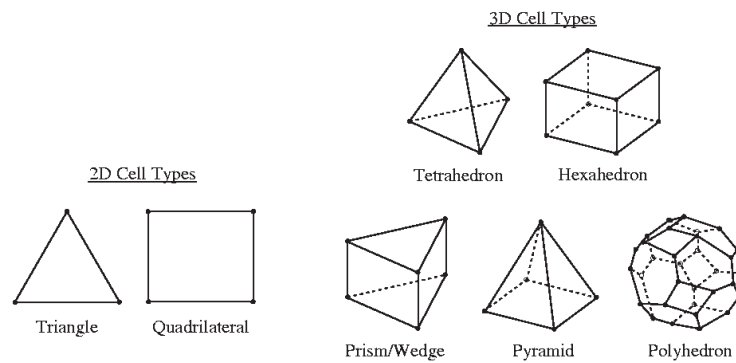


Fig.1: The shape elements type to mesh a geometry.

In COMSOL we have two types of mesh, physics-controlled mesh and user-controlled mesh.

Meshing considerations in COMSOL Multiphysics:

1. How to divide the geometry: sequence type
2. The shape used to divide the geometry: element type
3. Interpolation between nodes: Element order

A.3. Syntaxes of the *.txt* file to model TL part on a silicon substrate

*Modele CPW pour 240um mais avec Wgnd=60um et Wsig=320um

GROUP Umodel

#LAYERS

SUB 1 0 0 0 W=600u L=10000e-6 T=398e-6 rho=0.58 epsr=11.7

OXI 1 0 0 398e-6 W=600e-6 L=10000e-6 T=2e-6 epsr=6.2

BEOL 1 T=40u rho=1.72e-8

#COMPONENTS

LINE 1 BEOL 1 W=320u L=9500u ncells=10 inter OXI(1)->SUB(1)

LINE 2 BEOL 1 W=60u L=9590u ncells=10 inter OXI(1)->SUB(1)

#PATHS

LINE 2 gnd1 50e-6 0 400e-6 0 0 coupled

LINE 1 signal 140e-6 0 400e-6 1 2 coupled

LINE 2 gnd2 490e-6 0 400e-6 0 0 coupled

#COUPLINGS

LINE gnd1 LINE signal LINE gnd2

end group

end

A.4. Syntaxes of the *.txt* file to model *underpass & vias* within the silicon substrate

*Modele 2xTSV CHAIN 240um

GROUP Umodel

#LAYERS

RDL 1 T=0.5u rho=1.72e-8

RDL 2 T=0.1u rho=1.72e-8

SUB 1 0 0 0 W=1000u L=2000e-6 T=398e-6 rho=1e-4 epsr=11.7

OXI 1 0 0 398e-6 W=1000e-6 L=2000e-6 T=2e-6 epsr=5.8

OXI 2 469.9e-6 789.9e-6 358e-6 W=60.2u L=315.2e-6 T= -5u epsr=6.1

BEOL 1 T=1u rho=1.72e-8

#COMPONENTS

LINE 1 RDL 1 W=60u L=315u ncells=10 inter OXI(2)->subnode(1)

LINE 2 RDL 2 W=60u L=60u ncells=10

TSVPORT 1 BEOL 1 W=60u L=60u ncells=10

TSV 1 Rmet_top=32e-6 Rmet_down=31e-6 Tmet_top=31e-6 Tmet_down=30e-6 +

Toxi_top=0.1e-6 Toxi_down=0.09e-6 h=40e-6 rho=1.72e-8 epsr=6.5 +

ncells=10 updown BEOL(1)->RDL(1) inter TSVPORT(1)->OXI(1)

#PATHS

LINE 1 signal 470e-6 790e-6 357.4e-6 11 12

LINE 2 rdlin 470e-6 790e-6 357.9e-6 1 11

LINE 2 rdlout 470e-6 1044.8e-6 357.9e-6 12 2

TSV 1 tsv1 500e-6 820e-6 358e-6 in 1 101 102 coupled

TSV 1 tsv2 500e-6 1074.8e-6 358e-6 2 out 201 202 coupled

#COUPLINGS

TSV tsv1 TSV tsv2

end group

end

A.5. Netlist of SPICE file (*.sp*), with the results of the TL and Underpass & vias modelling within a silicon substrate

*Netlist generated from Umodel

.subckt network1 in1 out1 in2 out2 in3 out3

R1_gnd1 in1 x1_gnd1 0.0034042
L1_gnd1 x1_gnd1 x2_gnd1 5.4591e-10
L2_gnd1 x2_gnd1 x3_gnd1 5.4591e-10
R2_gnd1 x3_gnd1 out1 0.0034042
Coxgnd1 x2_gnd1 oxsub_gnd1 1.5638e-12

R1_signal in2 x1_signal 0.00063828
L1_signal x1_signal x2_signal 4.2487e-10
L2_signal x2_signal x3_signal 4.2487e-10
R2_signal x3_signal out2 0.00063828
Coxsignal x2_signal oxsub_signal 8.3402e-12

R1_gnd2 in3 x1_gnd2 0.0034042
L1_gnd2 x1_gnd2 x2_gnd2 5.4591e-10
L2_gnd2 x2_gnd2 x3_gnd2 5.4591e-10
R2_gnd2 x3_gnd2 out3 0.0034042
Coxgnd2 x2_gnd2 oxsub_gnd2 1.5638e-12

Rsub_1_2 oxsub_gnd1 oxsub_signal 87.8677
Rsub_2_3 oxsub_signal oxsub_gnd2 87.8677
Rsub_1_3 oxsub_gnd1 oxsub_gnd2 -2195.3718
Csub_1_2 oxsub_gnd1 oxsub_signal 6.8348e-13
Csub_2_3 oxsub_signal oxsub_gnd2 6.8348e-13
Csub_1_3 oxsub_gnd1 oxsub_gnd2 -2.7356e-14

K1_gnd1_vs_signal L1_gnd1 L1_signal 0.68645
K2_gnd1_vs_signal L2_gnd1 L2_signal 0.68645
Cinter_gnd1_signal x2_gnd1 x2_signal 6.9502e-14
K1_gnd1_vs_gnd2 L1_gnd1 L1_gnd2 0.48905
K2_gnd1_vs_gnd2 L2_gnd1 L2_gnd2 0.48905

K1_signal_vs_gnd2 L1_signal L1_gnd2 0.68645
K2_signal_vs_gnd2 L2_signal L2_gnd2 0.68645
Cinter_signal_gnd2 x2_signal x2_gnd2 6.9502e-14

.ends network1

X1_network1 0 n1_gnd1 1 n1_signal 0 n1_gnd2 network1
X2_network1 n1_gnd1 n2_gnd1 n1_signal n2_signal n1_gnd2
X3_network1 n2_gnd1 n3_gnd1 n2_signal n3_signal n2_gnd2
X4_network1 n3_gnd1 n4_gnd1 n3_signal n4_signal n3_gnd2
X5_network1 n4_gnd1 n5_gnd1 n4_signal n5_signal n4_gnd2
X6_network1 n5_gnd1 n6_gnd1 n5_signal n6_signal n5_gnd2
X7_network1 n6_gnd1 n7_gnd1 n6_signal n7_signal n6_gnd2
X8_network1 n7_gnd1 n8_gnd1 n7_signal n8_signal n7_gnd2
X9_network1 n8_gnd1 n9_gnd1 n8_signal n9_signal n8_gnd2
X10_network1 n9_gnd1 0 n9_signal 2 n9_gnd2 0 network1

.end

.subckt tsv1_tsv2 in1 out1 side1 side2 in2 out2 side3 side4

R1 in1 x1_tsv1 1.1049e-05
L1 x1_tsv1 x2_tsv1 3.2966e-13
L2 x2_tsv1 x3_tsv1 3.2966e-13
R2 x3_tsv1 out1 1.1049e-05
Coxtsv1_tsv1 x2_tsv1 p1_tsv1 2.4057e-13
Coxtsv2_tsv1 x2_tsv1 p2_tsv1 2.4057e-13
Coxgnd1_tsv1 p1_tsv1 side1 9.2394e-15
Coxgnd2_tsv1 p2_tsv1 side2 9.2394e-15

R3 in2 x1_tsv2 1.1049e-05
L3 x1_tsv2 x2_tsv2 3.2966e-13
L4 x2_tsv2 x3_tsv2 3.2966e-13
R4 x3_tsv2 out2 1.1049e-05
Coxtsv1_tsv2 x2_tsv2 p1_tsv2 2.4057e-13
Coxtsv2_tsv2 x2_tsv2 p2_tsv2 2.4057e-13
Coxgnd1_tsv2 p1_tsv2 side3 9.2394e-15
Coxgnd2_tsv2 p2_tsv2 side4 9.2394e-15

K1 L1 L3 0.094998
K2 L2 L4 0.094998

.ends tsv1_tsv2

X1_tsv1_tsv2 in n1_tsv1 101 102 2 n1_tsv2 201 202 tsv1_tsv2
X2_tsv1_tsv2 n1_tsv1 n2_tsv1 101 102 n1_tsv2 n2_tsv2 201 202 tsv1_tsv2
X3_tsv1_tsv2 n2_tsv1 n3_tsv1 101 102 n2_tsv2 n3_tsv2 201 202 tsv1_tsv2
X4_tsv1_tsv2 n3_tsv1 n4_tsv1 101 102 n3_tsv2 n4_tsv2 201 202 tsv1_tsv2
X5_tsv1_tsv2 n4_tsv1 n5_tsv1 101 102 n4_tsv2 n5_tsv2 201 202 tsv1_tsv2
X6_tsv1_tsv2 n5_tsv1 n6_tsv1 101 102 n5_tsv2 n6_tsv2 201 202 tsv1_tsv2
X7_tsv1_tsv2 n6_tsv1 n7_tsv1 101 102 n6_tsv2 n7_tsv2 201 202 tsv1_tsv2
X8_tsv1_tsv2 n7_tsv1 n8_tsv1 101 102 n7_tsv2 n8_tsv2 201 202 tsv1_tsv2
X9_tsv1_tsv2 n8_tsv1 n9_tsv1 101 102 n8_tsv2 n9_tsv2 201 202 tsv1_tsv2
X10_tsv1_tsv2 n9_tsv1 1 101 102 n9_tsv2 out 201 202 tsv1_tsv2

.end

A.6. The sequences of Microprobe Simulation for data-generating

1. Define the dimension choosing the D_{out} size. e.g: $D_{out} = 1000\mu m$
2. Define the w , s , n , t , t_{und} and h_{vias} sizes
3. Run the algorithms for each geometry (Circular, Ellipsoidal, Square and Rectangular) in both substrate cases (Glass and Silicon).
4. Then we change the t value, and we repeat the 3rd step.
 - a. $t = [40\ 38\ 20\ 10\ 2]\mu m$
 - b. We repeat the process until the last t value for all geometry and substrate cases (e.g: $t = 2\mu m$)
5. So, we change the t_{und} and h_{vias} both simultaneously, and then we repeat step four.
 - a. $t_{und} = [20\ 10\ 2\ 0.5]\mu m$
 - b. $h_{vias} = [2\ 1\ 1\ 1]\mu m$
 - c. We change the t_{und} and h_{vias} until the end value (e.g: $t_{und} = 0.5\mu m$ and $h_{vias} = 1\mu m$), getting back to the step .4 for each value.
6. So then, we start the change of w , s , taking into account the step. 3 to 5
7. We change the n value
 - a. $n = [6\ 5\ 4\ 3]$
 - b. We repeat the process from step three until step six for each n value until the end one.
8. Then we change the next D_{out} value
 - a. $D_{out} = [1000\ 900\ 800\ 700\ 600\ 500\ 400\ 300]\mu m$
9. (Add here please the next step)

A.7. The Microprobe characteristics for data simulated

- $D_{out} = 1000\mu m, n = 6$ (Circular and square geometry: $w = s = 30\mu m$ and $w = 22\mu m, s = 20\mu m$), $n = 5$ (all geometries $w = 22\mu m, s = 20\mu m$)
- $D_{out} = 900\mu m \& 500\mu m, n = 5$ (Ellipsoidal and Rectangular geometries):

A.8. Data regularization methods for generalization of the model

There are several techniques that can be used to avoid overfitting and improve the training model. In this section, we explain one of the more used ways very briefly when we have a small amount of dataset. Regularization is defined as a process of adding data with the aim to avoid a model overfitting. Here we are going to describe two standards methods of data regularization: augmentation and Dropout [145].

Having more data (dataset/samples) is the best way to get better consistent estimators (ML model). In the real world, getting a large volume of useful data for training a model is cumbersome, and labelling is extremely tedious. Data Augmentation is one of the interesting regularization techniques to resolve the above problem. The concept is very simple; this technique generates new training data from a given original dataset. Dataset Augmentation provides a cheap and easy way to increase the amount of your training data.

$$\text{New training data} = \text{Original training data} + \text{Noise data}$$

Dropout is a regularization technique for reducing overfitting in neural networks by preventing complex co-adaptations on training data. This consists of randomly selecting neurons to ignore them during training. They are "dropped out" randomly. This means that their contribution to the activation of downstream neurons is temporally removed on the forward pass, and any weight updates are not applied to the neuron on the backward pass. Simply, it is the process of ignoring some neurons, particularly forward or backward propagation. Dropout can be easily implemented by randomly selecting nodes to be dropped out with a given probability (e.g., .1%). Most importantly, Dropout is only used during a model's training and is not used when evaluating the model.

A.9. Epoch

An epoch is a term used in machine learning to indicate the number of passes of the entire training dataset the machine learning algorithm has completed. Datasets are usually grouped into batches (especially when the amount of data is very large). Some people use the term iteration loosely and refer to putting one batch through the model as an iteration.

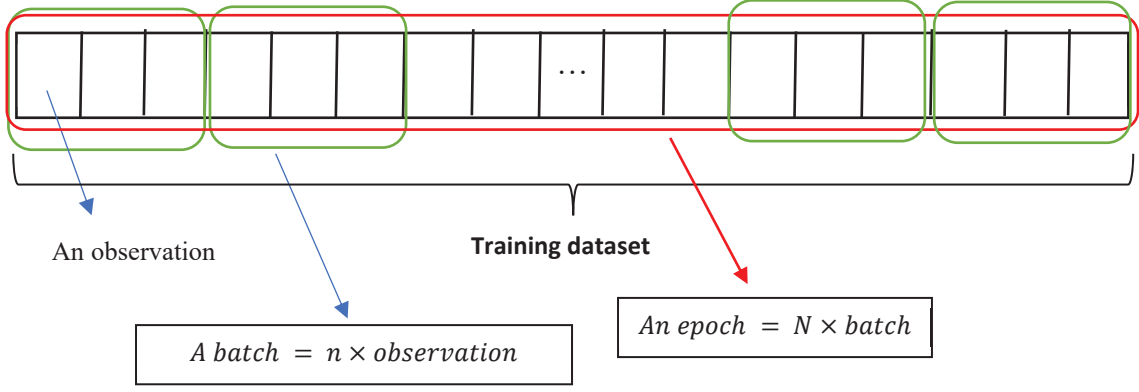


Fig.2: Graphical representation of epoch and batch in a dataset training.

If the batch size is the whole training dataset, then the number of epochs is the number of iterations. For practical reasons, this is usually not the case. Many models are created with more than one epoch. The general relation where dataset size is N , number of epochs is N_e , number of iterations is N_i , and batch size is n , the relationship would be as the following equation:

$$N \times N_e = N_i \times n \quad (8)$$

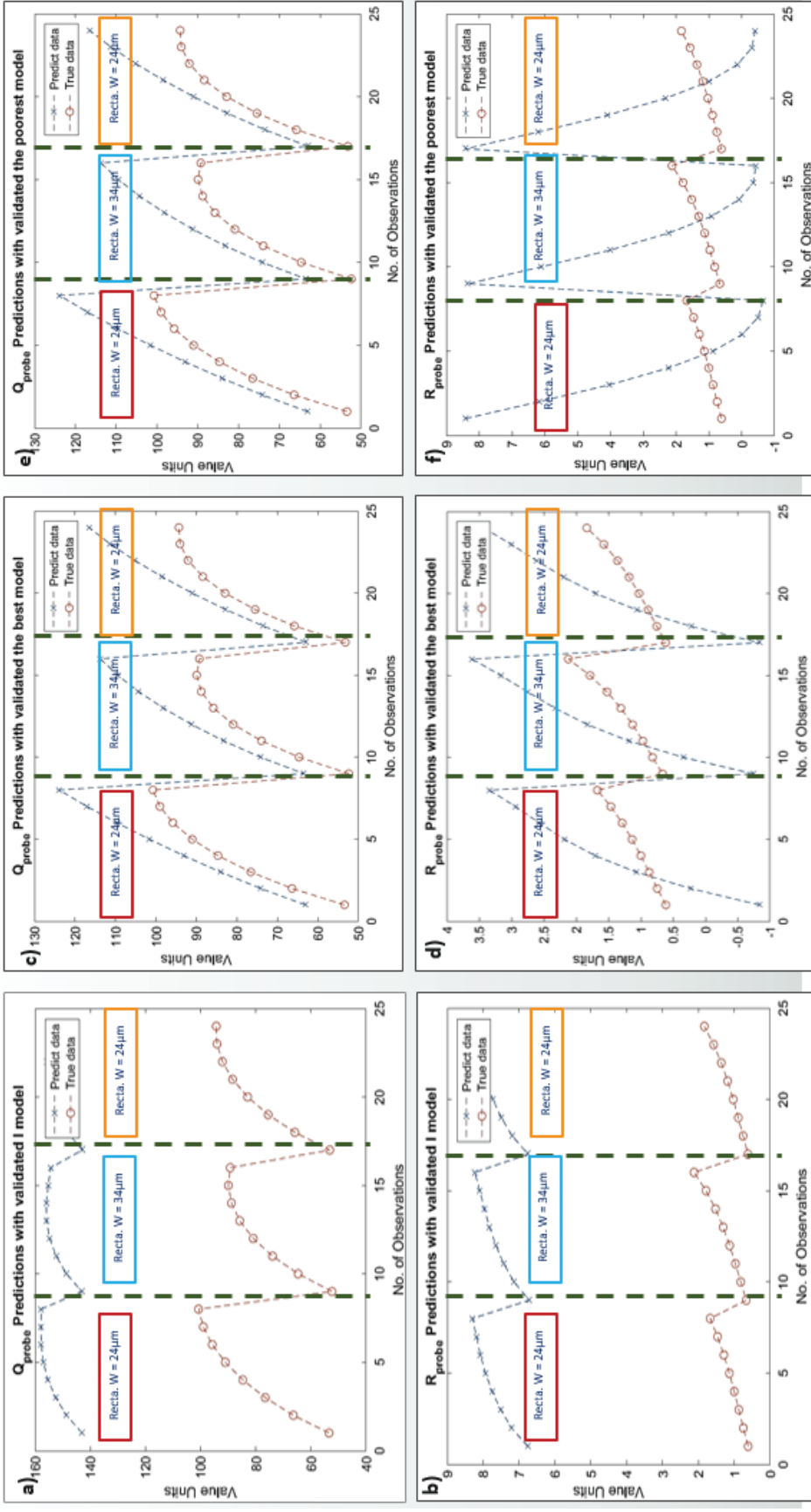
How many epochs a model should run to train is based on many parameters related to the dataset and the goal of the mode. So, while there have been efforts to turn this process into an algorithm, often a deep understanding of the data itself is indispensable, that why the pre-processing stage is crucial before the model training.

A.10. Algorithm selected for the optimization of the final model.

TRAINLM is a network training function that updates weight and predicts values according to Levenberg-Marquardt optimization. Levenberg Marquardt Algorithm (LMA) is a commonly used training algorithm in data classification. It is often the fastest backpropagation algorithm, although it does require more memory than other algorithms. The network performance function that is used is Mean Squared Error. It measures the network's performance according to the mean of squared errors. Mean Squared Error measures the network's performance according to the mean of squared errors. It is an average of the squares of differences between the actual observations and those predicted. The squaring of errors tends to heavily weigh statistical outliers, affecting the accuracy of the results. In mathematics and computing, the Levenberg–Marquardt algorithm (LMA or just LM), also known as the damped least-squares (DLS) method, is used to solve non-linear least squares problems. These minimization problems arise, especially in least-squares curve fitting.

The LMA is used in many software applications for solving generic curve-fitting problems. However, as with many fitting algorithms, the LMA finds only a local minimum, which is not necessarily the global minimum. The LMA interpolates between the Gauss-Newton algorithm (GNA) and the method of gradient descent. The LMA is more robust than the GNA, which means that in many cases, it finds a solution even if it starts very far off the final minimum. For well-behaved functions and reasonable starting parameters, the LMA tends to be slower than the GNA. LMA can also be viewed as Gauss-Newton using a trust-region approach.

A.11. Prediction of Resistance and Q factor using completely different dataset for three trained models.



APPENDIX B: List of personal publications

B.1. Scientific papers

- **J. A. Bernardo**, A. Rangel Trejo, Adam Adewolu, L. Werling, W. Uhring, L. Hebrad, Ch. Gontrand, L. Fakri-Bouchet, *New Methodology to improve an Implantable Micro-sensor for NMR Spectroscopy*, Sensors journal (**Submitted**).
- **J. A. Bernardo**, A. Rangel Trejo, L. Werling, W. Uhring, L. Hebrad, Ch. Gontrand, L. Fakri-Bouchet, *Machine learning approach to improve an NMR microprobe performance* (**In progress**).
- **J. A. Bernardo**, A. Rangel Trejo, Adam Adewolu, L. Werling, W. Uhring, L. Hebrad, Ch. Gontrand, L. Fakri-bouchet, *3D – Transmission Line Extractor for electrical circuits performance criteria simulation* (**In progress**).
- Amira Nabil, **J. A. Bernardo**, Yue Ma, Mohamed Abouelatta, Ahmed Shaker, Latifa Fakri-Bouchet, Christian. Gontrand, *Electrical modelling of tapered TSV including MOS-Field effect and substrate parasitics: Analysis and application*. Microelectronics journal. Vol 100, p.104797, (jun 2020). DOI: <https://doi.org/10.1016/j.mejo.2020.104797>
- A. Nabil, **J. A. Bernardo**, A. Rangel Trejo, M. Shaker, M. Abouelatta, L. Fakri-Bouchet, Ch. Gontrand, *Towards a Description Synthesis of the Entanglement of the Substrate with the Interconnection Networks, for Fast Modeling of 3D RF circuits*. Transactions on Networks and Communications. 9, 3 (May 2021), 36–54. DOI: <https://doi.org/10.14738/tnc.93.10196>
- A. Rangel Trejo, **J. A. Bernardo**, Leticia K., L. Fakri-Bouchet, *Ultra-Wideband Microstrip Patch Sensor Antenna Embedded into Bra for Comfortable Breast Cancer Microwave Imaging*, Sensors journal (**Submitted**).

B.2. International Congress papers with published proceedings: [O]
[eP]:

- **J. A. Bernardo**, Y José A. Bernardo, Abel Rangel-Trejo, Adam Adewolu, Lucas Werling, Wilfried Uhring, Luc Hebrard, Christian Gontrand, Latifa Fakri-Bouchet, *New Methodology to improve an Implantable Micro-sensor for NMR spectroscopy*. SENSORS 2021 congress ; 19 Avr.2021, 20-22 octobre 2021, Milan, Italie.[O], (**Available Online**: <https://hal.archives-ouvertes.fr/hal-03420639>)

- **José Antonio Bernardo**, Abel Rangel Trejo, Lucas Werling, Wilfried Uhring, Luc Hebrard, Youssef Wadghiri-Zaim, Christian Gontrand, Latifa Fakri-Bouchet, *New approach to Improve Sensitivity of Implantable NMR microprobe through Electrical Modelization*, International Society for Magnetic Resonance in Medicine (ISMRM2021) (**Online**), 15-20 Mai 2021, California, USA [**eP**] [**O**]
- **J. A. Bernardo**, Y. Ma, L. Werling, V. D. Nguyen, Ch. Gontrand, W. Uhring, Y. Wadghiri, L. Hebrard, L. Fakri-Bouchet, *Modèle Electrique de Micro Bobine RMN et Pertes Résistives*, MADICA 2018; 7-8 Nov. 2018, Madica, Tunisie. [**P**].
- A. Rangel Trejo, **J. A. Bernardo**, Leticia K., L. Fakri-Bouchet, *Ultra-Wideband Microstrip Patch Sensor Antenna Embedded into Bra for Comfortable Breast Cancer Microwave Imaging*.— congrès SENSORS 2021, le 20 – 22 octobre 2021, Milan, Italie. [**O**], (Available Online: <https://hal.archives-ouvertes.fr/hal-03420616>)
- L. Fakri-Bouchet, **J. A. Bernardo**, Y. Ma, L. Werling, V. D. Nguyen, Ch. Gontrand, W. Uhring, Y. Wadghiri, L. Hebrard, *Micro Bobine RMN et Pertes Résistives*, 13^{ème} édition du colloque international CETSIS, du 29 au 31 octobre 2018, Fès, Maroc, [**O**].

B.3. Presentation in a national conference and congress, Oral

[**O**]/Posters [**P**] [**eP**]

- **J. A. Bernardo**, Yue Ma, Latifa Fakri-Bouchet, *NMR Micro coil Electrical model and its resistive loss*, Petit déjeuner Scientifique ISA, 29/11/2018. (**P**)
- **J. A. Bernardo**, Y. Ma, L. Werling, D. Nguyen, W. Uhring, L. Hebrard, Ch. Gontrand, L. Fakri-bouchet, *Implantable miniaturized probe for NMR spectroscopy applications: Alzheimer disease detection and gliomes*, Journée des doctorants, ISA 4/02/2019. (**O**)
- **J. A. Bernardo**, Yue Ma, Latifa Fakri-Bouchet, *'Implantable miniaturized probe for NMR signal enhancement : Optimized resistive losses and electrical model'*, Petit déjeuner Scientifique ISA, 13/06/2019, Lyon, France. [**P**]
- **J. A. Bernardo**, A. Rangel Trejo, L. Werling, D. Nguyen, W. Uhring, L. Hebrard, Ch. Gontrand, L. Fakri-bouchet, *Implantable miniaturized probe for NMR spectroscopy*

applications in vivo: Alzheimer disease diagnosis, Journée des doctorants, ISA 02/12/2019, Lyon, France. [O]

- **José Bernardo**, Abel Rangel Trejo, Lucas Werling, Wilfried Uhring, Luc Hebrard, Christian Gontrand and Latifa Fakri-Bouchet, *Implantable NMR Microprobe Design using a Machine learning approach*, RJCIA 2021 (**Online**), 28 Juin au 02 Juillet 2021, Bordeaux, France. [eP], (Available Online: <https://hal.archives-ouvertes.fr/hal-03298735/>)
- **J. A. Bernardo**, Y. Ma, L. Werling, D. Vinh Nguyen, W. Uhring, L. Hebrard, Ch. Gontrand, L. Fakri-Bouchet, *Implantable miniaturized probe for NMR Signal enhancement: Optimized Resistive Losses and Electrical Model*. Journées Nationales du Réseau Doctoral en Micro-nanoélectronique JNRDM 2019 congress ; 6-7 Nov. 3-5 juin 2019, Montpellier, France. [O]
- **J. A. Bernardo**, Y. Ma, L. Werling, V. D. Nguyen, Ch. Gontrand, W. Uhring, Y. Wadghiri, L. Hebrard, L. Fakri-Bouchet, *Optimisation du RSB des Micro Bobine RMN, Modèle électrique et réduction de bruit*. 1ère Journée Thématique inter GDRs ; GDRs SoC2 et Réparer l'Homme, Dec. 2018, Paris, France. [P]
- Abel Rangel Trejo, **José Antonio Bernardo**, Leticia Konadu and Latifa Fakri-Bouchet, *AI's potential for Artificial Phantom Mimicking Tissue of the Human Breast Electrical Properties*, RJCIA 2021 (**Online**), le 28 Juin au 2 Juillet à Bordeaux, France. [eP], (available Online : <https://hal.archives-ouvertes.fr/hal-03298725/>)
- A. Rangel Trejo, **J. A. Bernardo**, L. Konadu, L. Fakri-Bouchet, *AI's potential for Artificial Phantom Mimicking Tissue of the Human Breast Electrical Properties*. CLARA : Cancéropôle Lyon Auvergne Rhône-Alpes 29 mars - 2 avril 2021, Lyon, France, (**Online**). [O][eP]
- A. Rangel Trejo, **J. A. Bernardo**, L. Konadu¹, L. Latifa-Bouchet, *AI's potential for Artificial Phantom Mimicking Tissue of the Human Breast Electrical Properties*, Deep Learning Medical Imaging School, LabEx PRIMES (Online) 19 – 23/04/2021. [eP]